Modelling transport and transformation of aerosols from ship exhausts

Dissertation

zur Erlangung des Doktorgrades der Naturwissenschaften

an der Fakultät für Mathematik, Informatik und Naturwissenschaften

Fachbereich Geowissenschaften

der Universität Hamburg

Vorgelegt von

Lea Fink

Hamburg, 2023

Universität Hamburg
DER FORSCHUNG | DER LEHRE | DER BILDUNG

Helmholtz-Zentrum hereon

Gutachter der Dissertation:

Prof. Dr. Bernd Leitl

Dr. Volker Matthias

Gutachter der Disputation:

Prof. Dr. Bernd Leitl

Dr. Volker Matthias

Prof. Dr. Annette Eschenbach

PD Dr. Thomas Pohlmann

Prof. Dr. Markus Quante

Datum der Disputation:

19.03.2024

Vorsitzender des Promotionsausschusses:

Prof. Dr. Hermann Held

Dekan der Fakultät MIN:

Prof. Dr.-Ing. Norbert Ritter

Eidesstattliche Versicherung

Hiermit erkläre ich an Eides statt, dass ich die vorliegende Dissertationsschrift selbst verfasst und keine anderen als die angegebenen Quellen und Hilfsmittel benutzt habe.

06.11.23 

Hamburg, den Unterschrift

Abstract

Emissions from shipping contribute significantly to the formation of air pollutants in the form of gases and atmospheric particles. Despite this negative impact on air quality, global maritime freight traffic is expected to continue to increase in the future. The Mediterranean region is an area with a high volume of shipping traffic both within Europe and for trade between Europe and Asia.
Air monitoring stations along the Mediterranean coast have recorded elevated levels of air pollution linked to ship emissions. In order to assess ship-related air pollution on a larger scale beyond monitoring points, the potential ship influence on air pollution can be simulated by using chemical transport models. The subsequent comparison of simulated with measured concentrations can help to assess the reliability of chemical transport models and reveal deviations from observed data.

This thesis emphases on simulating the formation, transport, chemical transformation and fate of gaseous as well as particulate air pollutants in the Mediterranean region using regional scale chemical transport models. The focus lays on emissions from ships and their input in coastal areas for the year 2015. A comparison of five different regional scale chemical transport models was carried out and their model performance was evaluated. Identical input emissions and grid size (12 x 12 km²) were used for all models in order to provide comparable conditions.
In a first step, the air pollution from the photooxidants O_3 and NO_2 was evaluated and $PM_{2.5}$ is investigated based on this with a focus on the inorganic components and precursors.
The model results were differing regarding the time series and pattern but shared the same outcome in underestimating NO_2 and overestimating O_3. The potential impact from ships to the total NO_2 concentration was especially high at the main shipping routes and coastal regions (25 % to 85 %). The potential impact from ships on the total O_3 concentration was lowest in regions with the highest NO_2 concentrations (reduction of down to -20 %).
Four of the five models underestimate measured $PM_{2.5}$ concentrations. This underestimation was attributed to model-specific mechanisms or underestimation of particle precursors. The potential impact of ships on the $PM_{2.5}$ concentration ranged from 15 % to 20 % at the main shipping routes. Regarding particle species, SO_4^{2-} was main contributor to the absolute ship-related $PM_{2.5}$ and to total $PM_{2.5}$ concentrations. In ship-related $PM_{2.5}$, a higher share of inorganic particle species was found when compared to the total $PM_{2.5}$. In most cases with high concentrations of both NH_4^+ and NO_3^-, lower SO_4^{2-} concentrations were simulated. Differences among the simulated particle species distributions trace back to the aerosol size distribution and how models distribute emissions among the coarse and fine mode ($PM_{2.5}$ and PM_{10}).
The underestimation of NO_2 and $PM_{2.5}$ from the actually measured concentrations can be explained by the direct dilution of emissions on a grid cell size of 12 x 12 km². The pollutants are directly diluted to a large volume, but this does not correspond to reality. Much higher values are found within the ship's exhaust plume.
Regarding particle formation, the results from the regional simulations showed the necessity of small-scale simulations to depict all physical and chemical processes in the exhaust plume and avoid underestimations. In the present work, the MAFOR box model was used for this purpose. It simulated the particle number and mass size distribution from the point of emission to the site of interest. The particle transformation was simulated concurrently with plume dispersion. The model input was based on measured data on emissions, concentration of air pollutants and meteorology. With help of the model results from MAFOR, the ship emissions were adjusted with regard to the particle

formation processes and the evolution of the particles in the ship exhaust plume. For this purpose, the emission factors of the volatile organic compounds (VOCs) as precursor substances were used as a link between the box model and the regional scale model.
This resulted in higher $PM_{2.5}$ concentrations in the simulations of the regional scale chemical transport model CMAQ. The effect is particularly noticeable in summer due to increased speed of chemical reactions at high temperatures and can lead to lower deviations between the modeled and measured $PM_{2.5}$ concentrations.

Zusammenfassung

Die Emissionen aus der Schifffahrt tragen maßgeblich zur Bildung von Luftschadstoffen in Form von Gasen und atmosphärische Partikeln bei. Trotz dieser negativen Auswirkung auf die Luftqualität wird erwartet, dass der weltweite maritime Güterverkehr zukünftig weiter ansteigt. Der Mittelmeerraum stellt dabei sowohl innerhalb Europas, als auch für den Handel zwischen Europa und Asien eine Region mit hohem Schiffverkehrsaufkommen dar.
Luftmessstationen entlang der Mittelmeerküste verzeichnen regelmäßig hohe Schadstoffkonzentrationen, die auf Schiffsemissionen zurückzuführen sind. Um diese Luftbelastung auf einer räumlich großen Skala und nicht nur an Messstationen abzuschätzen, kann der potenzielle Einfluss von Schiffen auf die Luftverschmutzung mithilfe von Chemikalientransportmodellen simuliert werden. Der anschließende Vergleich von gemessenen mit modellierten Konzentrationen hilft dabei, die Zuverlässigkeit chemischer Transportmodelle zu beurteilen und Abweichungen von beobachteten Daten aufzudecken.

In der vorliegenden Doktorarbeit werden die Bildung, den Transport, die chemische Umwandlung und den Verbleib sowohl von gas- als auch von partikelförmigen Luftschadstoffen für den Bereich des Mittelmeeres mit regionalskaligen Chemietransportmodellen untersucht. Dabei liegt der Schwerpunkt auf dem Einfluss der Schiffe auf Küstengebiete im Jahr 2015. Es erfolgt ein Vergleich von fünf verschiedenen regionalskaligen chemischen Transportmodellen, welche hinsichtlich ihrer Modellperformance evaluiert werden. Es werden für alle Modelle einheitliche Emissionen und Gitterzellengrößen (12 x 12 km²) verwendet, um vergleichbare Ausgangsbedingungen zu schaffen.
Im ersten Schritt werden die Photooxidantien O_3 und NO_2 untersucht. Darauf aufbauend wird $PM_{2.5}$ detailliert hinsichtlich der anorganische Partikelspezies und Partikelvorläuferstoffe analysiert.
Die in der vorliegenden Arbeit vorgestellten Ergebnisse zeigen, dass sich die Modellergebnisse bezüglich der Zeitreihen und der räumlichen Verteilung der Luftschadstoffe unterscheiden, jedoch alle fünf verwendeten regionalskaligen Chemietransportmodelle die Konzentrationen von O_3 überschätzen und NO_2 unterschätzen. Der potenzielle Einfluss von Schiffen auf die gesamte NO_2-Konzentration war an den Hauptschifffahrtsrouten und Küstenregionen besonders hoch (25 % bis 85 %). Der potenzielle Einfluss von Schiffen auf die gesamte O_3-Konzentration ist in den Regionen mit der höchsten NO_2-Konzentration am niedrigsten (bis zu -20 %).
Bei $PM_{2.5}$ unterschätzen vier der fünf Modelle die tatsächlich gemessene Konzentration. Diese Unterschätzung kann auf modellspezifische Mechanismen oder Unterschätzungen von Partikelvorläufern zurückgeführt werden. Der potenzielle Einfluss von Schiffen auf die $PM_{2.5}$-Konzentration liegt auf den Hauptschifffahrtsrouten zwischen 15 % und 25 %. In Hinblick auf einzelne Partikelspezies trägt hauptsächlich SO_4^{2-} zur $PM_{2.5}$-Konzentration bei. Für $PM_{2.5}$ aus Schiffsemissionen ist im Vergleich zum Gesamt-$PM_{2.5}$ ein höherer Anteil anorganischer Partikel zu finden.
In den meisten Fällen werden bei hohen Konzentrationen sowohl von NH_4^+ als auch von NO_3^- niedrigere SO_4^{2-}-Konzentrationen von den Modellen simuliert. Unterschiede zwischen den modellierten Partikelverteilungen könnten auf die Aerosolgrößenverteilung und die Art und Weise zurückzuführen sein, wie Modelle die Emissionen zwischen $PM_{2.5}$ und PM_{10} verteilen.

Die Unterschätzung von NO_2 und $PM_{2.5}$ kann mit der direkten Verdünnung auf die Gitterzellengröße von 12 x 12 km² erklärt werden. Die Schadstoffe werden direkt auf ein großes Volumen verdünnt, was jedoch nicht der Realität entspricht. Innerhalb der Schiffsabgasfahne liegen viel höhere Konzentrationen vor.
Um die Unterschätzung der regionalskaligen Chemietransportmodelle zu vermeiden, ist eine kleinskalige Betrachtung notwendig, um alle physikalischen und chemischen Prozesse in der Abgasfahne abbilden zu können. In der vorliegenden Arbeit wird dafür das Box-Modell MAFOR verwendet. Mit Hilfe dieses Modells kann die Partikelanzahl und –massengrößenverteilung vom Austrittspunkt der Emissionen bis zur gewünschten Distanz simuliert werden. Das Partikelwachstum wird dabei gleichzeitig mit der Verteilung der Abgasfahne berechnet. Der Modellinput basiert auf tatsächlich gemessenen Daten von Emissionen, Konzentrationen und Meteorologie. Mit Hilfe der Modellergebnisse aus MAFOR können die Schiffsemissionen hinsichtlich der Partikelbildungsprozesse und der Entwicklung der Partikel in der Schiffsabgasfahne angepasst werden. Dafür werden die Emissionsfaktoren der volatilen organischen Substanzen (VOCs) als Vorläufersubstanzen als Link zwischen dem Box-Modell und dem regionalskaliegen Chemietransportmodell verwendet. Die Anpassung der Prozesse in der Schiffsabgasfahne resultiert in höheren $PM_{2.5}$ Konzentrationen in den Simulationen des verwendeten regionalskaligen Chemietransportmodells CMAQ. Dies zeichnet sich vor allem im Sommer ab durch die erhöhte Geschwindigkeit chemischer Reaktionen bei hohen Temperaturen und führt zu einer besseren Übereinstimmung der modellierten und gemessenen Konzentrationen.

Table of contents

List of Figures

List of Tables

List of Abbreviations

0-D	zero-dimensional
1.5-D	1.5-dimensional
2-D	2-dimensional
3-D	3-dimensional
ABL	Atmospheric boundary layer
AI	Aitken mode
AQGs	Air quality guidelines
AS	Accumulation mode
ASOA	Anthropogenic secondary organic aerosol
BSOA	Biogenic secondary organic aerosol
BaP	Benzo(α)pyrene
BC	Black carbon
CAMx	Comprehensive Air Quality Model with Extensions
CBM-IV	Carbon bond mechanism (version IV)
CB05	Carbon Bond mechanism 05
CF	Climate and Forecast
CH_4	Methane
CMAQ	Community Multiscale Air Quality model
CO	Carbon monoxide
CO_2	Carbon dioxide
CTM	Chemical Transport Model
EC	Elemental carbon
ECA	Emission control areas
ECMWF	European Centre for Medium-Range Weather Forecasts
EEA	European Environment Agency
EF	Emission factor
EMEP	European Monitoring and Evaluation Programme model
EU	European Union
FINN	Fire INventory from NCAR
FMPS	Fast Mobility Particle Sizer
GEOS-5	Goddard Earth Observing System Model, Version 5

GEOS DAS	Goddard Earth Observing System Data Assimilation System
GHG	greenhouse gas
GNFR	Gridded Nomenclature for Reporting
GOCART	Global zone Chemistry Aerosol Radiation and Transport
HCl	hydrochloric acid
HFO	Heavy fuel oil
HNO_3	Nitric acid
HO_2	Hydroperoxyl radical
$HOSO_2$	Hydroxysulfonyl radical
H_2SO_4	Sulfuric acid
IFS-CAMS	Integrated Forecasting System – Copernicus Atmosphere Monitoring Service
LNG	Liquefied natural gas
LMDz-INCA	Laboratoire de Météorologie Dynamique General Circulation Model INteraction with Chemistry and Aerosols
MAFOR	Multicomponent Aerosol FORmation
MARS	Model for an Aerosol Reacting System
MCIP	Meteorology-Chemistry Interface Processor
MEGAN	Model of Emissions of Gases and Aerosols from Nature
MELCHIOR	Modele Lagrangien de Chimie de l'Ozone a l'echelle Regionale
MEPC	Marine Environment Protection Committee
MERRA	Modern-Era Retrospective Analysis for Research and Applications
MDO	Marine diesel oil
MSC-W	Meteorological Synthesizing Centre – West
NECA	Nitrogen emission control area
NH_3	Ammonia
NH_4^+	Ammonium
NH_4NO_3	Ammonium nitrate
$(NH_4)_2SO_4$	Ammonium sulfate
NH_4HSO_4	Ammonium bisulfate
NMB	Normalized mean bias
NMVOC	Non-methane volatile organic compound
N_2O	Nitrous oxide
NO	Nitrogen oxide
NO_2	Nitrogen dioxide
NO_3^-	Nitrate

NO_x	Nitrogen oxides
NU	Nucleation mode
O_3	Ozone
OC	Organic carbon
OH	Hydroxyl radical
OPS	Optical Particle Sizer
PM	particulate matter
$PM_{0.1}$	particulate matter < 0.1 µm
$PM_{2.5}$	particulate matter < 2.5 µm
PM_{10}	particulate matter < 10 µm
PNC	particle number count
POA	primary organic aerosol
POC	primary organic carbon
PSAT	Particulate Source Apportionment Technology
R	Spearman's correlation coefficient
RADM-AQ	Regional Acid Deposition Model−Aqueous Chemistry
RMSE	root mean square error
SCIPPER	Shipping contribution to Inland Pollution - Push for the Enforcement of Regulations
SECA	Sulfur emission control area
SOA	Secondary organic aerosol
SOAP	Secondary Organic Aerosol Processor
SO_2	Sulfur dioxide
SO_4^{2-}	Sulfate
SO_x	Sulfur oxides
STEAM	Ship Traffic Emission Assessment Model
TPPM	Total primary particulate matter
UFP	ultrafine particles
VBS	volatility basis set
VOC	volatile organic compound
WHO	World Health Organization

Publications

The following publications are part of the present thesis:

Fink, L., Karl, M., Matthias, V., Oppo, S., Kranenburg, R., Kuenen, J., Moldanova, J., Jutterström, S., Jalkanen, J.-P., and Majamäki, E.:

Potential impact of shipping on air pollution in the Mediterranean region – a multimodel evaluation: comparison of photooxidants NO_2 and O_3

Atmos. Chem. Phys., 23, 1825–1862, https://doi.org/10.5194/acp-23-1825-2023, 2023.

The supplementary material for this publication (mainly Section 5.1) is indicated as "Supplements 1" and is attached to the thesis as well as accessible under: Supplement of Atmos. Chem. Phys., 23, 1825–1862, https://doi.org/10.5194/acp-23-1825-2023-supplement, 2023.

Fink, L., Karl, M., Matthias, V., Oppo, S., Kranenburg, R., Kuenen, J., Jutterström, S., Moldanova, J., Majamäki, E. and S., Jalkanen, J.-P.:

A multimodel evaluation of the potential impact of shipping on particle species in the Mediterranean Sea

Atmos. Chem. Phys., 23, 10163–10189, https://doi.org/10.5194/acp-23-10163-2023, 2023.

The supplementary material for this publication (mainly Section 5.2) is indicated as "Supplements 2" and is attached to the thesis as well as accessible under: Supplement of Atmos. Chem. Phys., 23, 10163–10189, https://doi.org/10.5194/acp-23-10163-2023-supplement, 2023.

The following publication is a co-authorship and was prepared during the time of the PhD, but is not part of the present thesis

Matthias, V., Quante, M., Arndt, J. A., Badeke, R., Fink, L., Petrik, R., Feldner, J., Schwarzkopf, D., Link, E.-M., Ramacher, M. O. P., and Wedemann, R.:

The role of emission reductions and the meteorological situation for air quality improvements during the COVID-19 lockdown period in central Europe

Atmos. Chem. Phys., 21, 13931–13971, https://doi.org/10.5194/acp-21-13931-2021, 2021.

1 Introduction

1.1 Adverse effects of air pollution

Air pollution is one of the main threats to public health all over the world. The WHO has stated that worldwide 4.2 million premature deaths annually are caused by exposure to ambient air pollution (WHO, 2022).

Although air pollutant emissions have significantly decreased in the European Union (EU) in recent decades, their concentrations in the lower troposphere are still very high. It has been reported that most people in urban areas in the EU living are exposed to key air pollutants at harmful levels that cause health damage (EEA, 2023). These key air pollutants include particulate matter < 2.5 µm ($PM_{2.5}$), particulate matter < 10 µm (PM_{10}), O_3 (ozone), nitrogen dioxide (NO_2), benzo(α)pyrene (BaP) and SO_2 (sulfur dioxide).

The negative effects of air pollution on human health have already been thoroughly investigated (Kampa and Castanas, 2008; Cesaroni et al., 2014). The negative effects on human health depend on the duration and intensity of exposure. Both short- as well as long-term exposure conditions have been related to decreased life expectancy and increased morbidity. Under short-term exposure to high concentrations and long-term exposure to low concentrations, all air pollution types are harmful to the neurological, reproductive, and respiratory systems and can cause cancer and death (Kampa and Castanas, 2008). The health effects of exposure to air pollutants at high concentrations are more severe for people with respiratory or cardiovascular problems as well as for young children or elderly individuals (Manisalidis et al., 2020).

The focus of this thesis will be on O_3, NO_2 and $PM_{2.5}$. NO_2 pollution is linked to several diseases such as diabetes mellitus, hypertension, stroke, chronic obstructive pulmonary disease and asthma (Schneider et al., 2018). In addition, NO_2 takes a crucial part in the formation of O_3 as well as in the deposition of reactive nitrogen compounds (Crutzen, 1979). O_3 can cause inflammation and damage to the respiratory system, render the lungs more vulnerable to infection and lead to intensification of lung diseases (EPA, 2021).

Exposure to $PM_{2.5}$ likely leads to certain diseases affecting the lungs, cancer, or type 2 diabetes (Heusinkveld et al., 2016; Chen et al., 2016; Gao and Sang, 2020). Even smaller particles, so called ultrafine particles (UFPs), can penetrate deeper into the respiratory tract than larger particles. The physical properties of UFPs might be independent to those of $PM_{2.5}$ (Oberdörster et al., 2005; Rückerl et al., 2011). These small particles have high biological reactivity, are poorly recognized by the human immune system, can be removed from the lungs less effectively than larger particles and can enter the bloodstream (Kendall and Holgate, 2012; Miller et al., 2017).

Moreover, air pollution exerts negative impacts on the environment. Wildlife are harmed by toxic airborne pollutants, which can result in reproductive failure. Acid rain is the term for precipitation containing high levels of nitric or sulfuric acids that can damage trees and can acidify water and soil. A high input of nutrients (mainly nitrogen) could cause an imbalance in the ecosystem, stimulate algae blooms in water and cause the replacement of plants in low-nutrient habitats. These nutrients enter ecosystems from the atmosphere via wet or dry deposition, even though the atmosphere is not the main source of nutrients (Pacyna, 2008).

In addition to these negative impacts, the production of greenhouse gases (GHGs) as a side effect of air pollution, namely, carbon dioxide (CO_2) and CO_2 equivalents, leads to climate warming. The Earth's radiation budget, defined as the overall balance between the incoming and outgoing radiant

energy, is affected by GHGs. However, not only CO_2 but also particulate matter (PM) resulting from human activities impact the radiation budget (Granados-Muñoz et al., 2019; Meloni et al., 2018; Kok et al., 2017; Otto et al., 2007).

1.2 Air pollution from shipping

Ships release a variety of air pollutants into the environment because of numerous onboard combustion and energy transformation activities. After entering the atmosphere, these emissions travel hundreds of kilometers, with 70 % of shipping-related emissions being found less than 400 kilometers from the shore (Eyring et al., 2010; Endresen et al., 2003). The adverse effect of shipping-related emissions on the concentration of air pollutants has been noted in a number of previous studies. These emissions play a role as GHGs, impacting human health or contributing to acidification and eutrophication (Tysro and Berge, 1997; Corbett and Fischbeck, 1997; Corbett et al., 1999). Mainly in coastal areas, maritime transport accounts for a substantial share of air pollution (Viana et al., 2014, Karl et al., 2019a, Matthias et al., 2010). The influence of international shipping to global anthropogenic PM emissions is comparable to that of road traffic (Klimont et al., 2017).

Fuel combustion, as a ship activity, is a source for the production of aerosols and gases such as CO_2, nitrogen oxides (NO_x) and sulfur oxides (SO_x). The combustion process also produces carbon monoxide (CO) and volatile organic compounds (VOCs). In addition to gas processes, ship exhaust similarly contains particles, including the emission of PM such as soot, ash, and other fine particles.

In terms of the percentages of the total national EU emissions stemming from all economic sectors, the maritime transport industry in the EU was responsible for 24 % of NO_x, 24 % of SO_x, and 9 % of $PM_{2.5}$ emissions in 2018 (EMSA, 2023).

Total shipping-related GHG emissions (including CO_2), methane (CH_4), and nitrous oxide (N_2O) increased approximately 10 % between 2012 and 2018. Long-term economic and energy scenarios project that ship emissions could increase from +90 % to +130 % in 2050 over 2008 levels (IMO, 2019). This shows the urgency of regulating emissions with mitigation strategies for air pollutants.

1.3 Regulatory measures for air pollution

1.3.1 General air pollution limits

The WHO started to address the air pollution problem in Europe in 1987 (WHO, 1987) by delivering health-based air quality guidelines for the principal health-damaging air pollutants: PM, O_3, NO_2 and SO_2. These guidelines are not legally binding, but they provide an important base for governments and civil societies. Air pollution limits are frequently adjusted based on actual studies on their health hazards and potential levels that could be considered safe for human health.

With this as a base, the air pollution problem can be analyzed, and policies can be formulated aiming at mitigating the health effects of air pollution. The earlier versions of the WHO air quality guidelines provided a foundation for legislation targeting air quality, particularly for European countries. The Ambient Air Quality Directive (2008/50/EC) of 2008 established limitations on major air pollutants in the EU and was updated in 2015 (EU Parliament and Council, 2015). The directive also established legally enforceable limits for a variety of pollutants (PM, NO_2, O_3, SO_2, and CO).

The recommended WHO levels are lower than the limits established by the EEA (Table 1). In addition, for $PM_{2.5}$, there are limit values, although there is no level below which the concentration of this pollutant could be considered safe (Anderson et al., 2012). Due to the ongoing problem of air pollution, the Commission proposed revising the Ambient Air Quality Directives in 2022 as part of the European Green Deal (European Commission, 2022). This modification should yield air quality

requirements that are closer to WHO recommendations. For example, the yearly limit value for $PM_{2.5}$ will be cut in half.

In addition to the Ambient Air Quality Directive, the zero-pollution action plan was accepted in May 2021 by the European Commission. It aims to decrease the number of premature deaths caused by fine particulate matter exposure by 55 % until 2030 from 2005 levels. In 2020, the premature mortality due to fine PM exposure decreased by 45 % compared to 2005. Nevertheless, to reach the goal of zero pollution and to attain levels that are no longer considered harmful to health, increased efforts are necessary. To achieve this goal, the proposed directive will establish 2030 air quality criteria that are more closely linked with the WHO AQGs (EEA, 2023; Table 1).

Table 1: WHO air quality guideline and current EU limits for air pollutants as well as revised limits for 2030 (Hoffmann et al., 2021; Halleux, 2023; European Commission, 2022; EU Parliament and Council, 2015). These values are limit values except for O_3. Limit values are legally binding when they enter into force, whereas for target values the obligation is to take all necessary measures to reach compliance.

Pollutant (legal nature)	Averaging period	EU current standard value (µg/m³)	EU revised standard values for 2030 (µg/m³)	WHO air quality guideline (µg/m³)
$PM_{2.5}$	24 hours	-	25	15
(limit)	Annual mean	25	10	5
PM_{10}	24 hours	50	45	45
(limit)	Annual mean	40	20	15
O_3	Maximum 8-hour daily mean	120	120	100
(target)				
NO_2	24 hours		50	25
(limit)	Annual mean	40	20	10
SO_2	10 minutes	-		500
(limit)	1 hour	350		-
	24 hours	125	50	40

1.3.2 Regulations for shipping

For the reduction of ship-related air pollution, the regulations in Annex VI to the MARPOL Convention of 1997 by the MEPC (Marine Environment Protection Committee) took effect in 2005 (IMO MEPC, 1997). Existing EU laws specify standards that Member States must fulfill with respect to a variety of pollutants concerning marine water and air quality.

The most important adjustments to MARPOL Annex VI included the establishment of emission control areas (ECAs). In ECAs, the regulations are more stringent in terms of reducing SO_x, NO_x, and particulate matter emissions in specific maritime zones, as well as achieving a global reduction in SO_x, NO_x, and particulate matter emissions.

The global sulfur cap for marine vessels was implemented in the amended MARPOL Annex VI in January 2020. It states that the sulfur content in any fuel oil used by ships must not exceed 0.5 % m/m, with the exception of ships that employ equivalent compliance mechanisms to reduce sulfur emissions, such as scrubbers (IMO, 2016). Reductions in precursor gases can also cause a decrease in PM. Viana et al. (2020) concluded that stricter regulations could lower the number of $PM_{2.5}$ (PM < 2.5 µm)-related premature deaths by an average of 15 % in southern European coastal cities. The limits applicable in ECAs for SO_x (SECAs) were reduced to 0.1 % m/m from 01.01.2015 (IMO, 2016).

Due to existing regulations, NO_x shipping-related emissions in the North and Baltic Seas will steadily decrease. This primarily occurs because ships constructed on or after 01.01.2021, and driving in EU nitrogen emission control areas (NECAs) in the North and Baltic Seas will be subject to the stricter MARPOL Annex VI NO_x standards (tier III; EMSA, 2023).
In contrast to the regulations effective in the North and Baltic Seas, the Mediterranean Sea has not yet been designated as an ECA. The Mediterranean Sea was designated as an ECA in terms of sulfur emissions in 2025 by the contracting parties of the Barcelona Convention, which could lead to a decrease in SO_2 emissions. Nevertheless, no regulations on NO_x emissions originating from ships in the Mediterranean Sea are currently planned. Under a future scenario of Cofala et al. (2018), it was predicted that without regulation, the NO_x emissions stemming from ships will likely exceed emissions stemming from land-based sources after 2030.

2 Scientific questions & structure of the thesis

2.1 Scientific questions

Although ship emissions significantly impact air pollution in the Mediterranean Sea (Viana et al., 2020), few regional scale chemical transport modeling studies have focused on this domain. A review of the research assessing how shipping-related pollutants affect the quality of the air in European coastal areas by Viana et al. (2014) could indicate that studies on shipping-related emissions in the Mediterranean Sea focus on PM levels and their chemical composition rather than on gaseous pollutants. They further noted that the highest $PM_{2.5}$ contributions were found in the Mediterranean Sea and North Sea.

Aksoyoglu et al. (2016) studied the O_3 and $PM_{2.5}$ atmospheric concentrations in the Mediterranean Sea region followed by a comparison of two models. They found an increase in the O_3 and $PM_{2.5}$ concentrations in the Mediterranean Sea due to ship traffic. The impacts predicted for the Mediterranean region are greater than those reported in previous studies.

Other investigations of air pollution in the Mediterranean region have focused on smaller domains over the Iberian Peninsula (Baldasano et al., 2011; Nunes et al., 2020), the eastern part of the Mediterranean Sea with the Arabian Peninsula (Večeřa et al., 2008; Tadic et al., 2020; Celik et al. 2020; Friedrich et al., 2021) or urban-scale and harbor cities (Schembari et al., 2012; Donateo et al., 2014; Prati et al., 2015). The results of regional scale chemical transport models were compared for the Baltic Sea and for all of Europe (Karl et al., 2019a; Im et al., 2015a,b).

High air pollution concentrations have been measured in the western Mediterranean region (Nunes et al., 2020). This region will be investigated in detail in the present work.

The regional chemical transport models (CTMs) used for this investigation usually consider $PM_{2.5}$ but do not divide PM into smaller particles or consider UFPs (Frohn et al., 2021). Physical processes such as the physical transformation of particles, including nucleation, condensation, evaporation, coagulation, cloud processing and particle growth, are important for detailed investigation of PM (Frohn et al., 2021).

González et al. (2011) found inland transport of UFPs from ship plumes in Santa Cruz de Tenerife, with ship emissions accounting for a share of 65 % to 70 % of the total UFP number concentration. Pirjola et al. (2014) also reported an increase in UFP concentrations due to ship emissions in European coastal cities.

Although the issue of shipping impact on the air quality has been largely addressed in the aforementioned studies, there remain open questions to be investigated and answered. None of these studies focused on analyzing the potential impact of ships on a regional scale with a subsequent model comparison of different regional scale CTMs over the western part of the Mediterranean Sea in regard to different air pollutants. Furthermore, ship emissions in regional scale CTM systems are usually directly diluted into one grid cell, thus not considering small-scale plume chemistry.

In this thesis, regional air quality model results were validated through intercomparison of five regional scale CTM systems and their model internal mechanisms. The intercomparison and the research in this PhD thesis were conducted as part of the Horizon 2020 project Shipping Contribution to Inland Pollution - Push for the Enforcement of Regulations (SCIPPER). The overarching aim of this project was to obtain further insights into the capability of several monitoring approaches for shipping emissions. Embedded in this project was the modeling of the impact of ships on air pollution

as well as the evaluation of the effect of shipping-related emissions on the air quality under various regulatory enforcement scenarios (https://www.scipper-project.eu/, 2023).

In the second part, observations derived from a measurement campaign in the SCIPPER project were used for small-scale modeling of particles in ship plumes and plume dilution for more detailed investigation of in-plume processes.

The following specific research (sub)questions are addressed in this PhD thesis:

(1) What is the influence of ships on air pollution in coastal areas concerning the photooxidants NO_2 and O_3 as well as $PM_{2.5}$ and inorganic aerosol species?

a. How much do regional scale CTMs deviate from each other when simulating air pollutants and deposition, and how well do they perform compared with observed data?

b. What is causing the uncertainty in regional scale models when one uncertainty factor, namely, emissions, is the same across all models?

(2) How large is the influence on results of regional scale CTM simulations when the plume development is considered?

a. How can ship plumes be represented in atmospheric chemical models?

b. How can the output of a box model be implemented in a 3-D regional scale CTM?

These questions should be assessed via simulations and comparison of five regional scale CTM systems. The simulated model outputs were validated against concentration measurements. For a representation of the changes in the particle number and mass size distribution from emission exhaust to the location of interest, particle transformation should be simulated in parallel with plume dispersion. Because the particle size and composition change quickly, studying the evolution close to the source with high spatial and temporal resolutions is important.

2.2 Structure of the thesis

After introducing the problem of air pollution and the arising research questions, this thesis is structured as follows:

Section 3 contains the scientific background on atmospheric chemistry, accounting for gaseous and particulate air pollutants as well as their sources and sinks. Additionally, in this section, the fundamentals of chemical transport models are explained.

Section 4 contains an explanation of the methods used in studies. This serves as a basis for the results, and the research outcome of this thesis is described in the publications. Both the first and second publications provide the results of an intercomparison study. This study was conducted as part of the SCIPPER project and aims to quantify the ship impact on the Mediterranean Sea, simulated by different CTM systems. In the third publication, the $PM_{2.5}$ ship emissions for regional scale CTM simulations are adjusted based on the output of the Multicomponent Aerosol FORmation model (MAFOR). With the adjusted emissions, a new regional scale CTM simulation for the Mediterranean Sea was adopted. An increase in the $PM_{2.5}$ concentration coming from ships is indicated after emission adjustment.

Section 5 includes the results and discussion of the three studies. Section 5.1 contains the first part of the intercomparison study and a comparison and evaluation of the five CTMs concerning their predictions of air pollutant dispersion and transformation. The focus of this investigation is to compare the model simulation results regarding the potential ship impact on atmospheric concentrations and NO_2 and O_3 dry deposition. In this section, the important differences in photochemical processing between CTMs in regard to ships are highlighted. Section 5.2 contains results and discussion on simulated potential ship impact on $PM_{2.5}$ concentration as well as on inorganic particle species. This section completes the model intercomparison by providing an overview of gaseous and particulate substances. To achieve this overview, the same CTM simulations are considered. In addition, aerosol precursors and inorganic particle species are investigated.
Based on the results of the second study, the particle formation and processes in the small-scale area are considered in detail in the third study (Section 5.3). As such, the ship exhaust plume and dilution are considered, and ship emissions are adjusted as input for CTMs based on the observed data from a measurement campaign. Finally, one CTM simulation is performed with adjusted ship emissions, and the changes in the total $PM_{2.5}$ concentration are calculated.

The last part (Section 6) of the thesis contains the overarching conclusions and a summary of the main findings, and an outlook on future investigations on this topic is provided therein.

3 Background

3.1 The atmosphere and its chemistry

The Earth's atmosphere is characterized by changes in temperature and pressure that vary with height. The change in the average temperature profile with altitude provides a basis for identifying the various atmospheric layers. The troposphere is the lowest layer of the atmosphere. It extends from the Earth's surface to the tropopause, which varies in height depending on the season and latitude and is characterized by a temperature decrease with height and fast vertical mixing (Seinfeld and Pandis, 2006). The atmospheric boundary layer (ABL) is the lowest part of the troposphere. Due to its contact with the Earth's surface, its behavior is directly influenced by surface processes, such as turbulent mixing, which is influenced by temperature, humidity, and wind speed. The ABL is characterized by stable or unstable stratification, depending on the difference in the temperature between the surface and the air above it (Hayden and Pielke, 2016). However, the free atmosphere is the region of the atmosphere that is located above the boundary layer. In this region, the properties of the air are more uniform and less influenced by the underlying surface.

During the daytime, the Earth's surface is heated, and the air in the ABL is mixed by convection. The thickness of this layer depends on the intensity of surface heating and the amount of evaporated water. Generally, the height of the ABL increases with increasing surface heat. Over deserts, it can reach a height up to 5000 m, whereas over ocean areas, the height of the top remains well below 1000 m (Hayden and Pielke, 2016). Air pollution originating from anthropogenic sources such as ships usually occurs in the ABL (Figure 1).

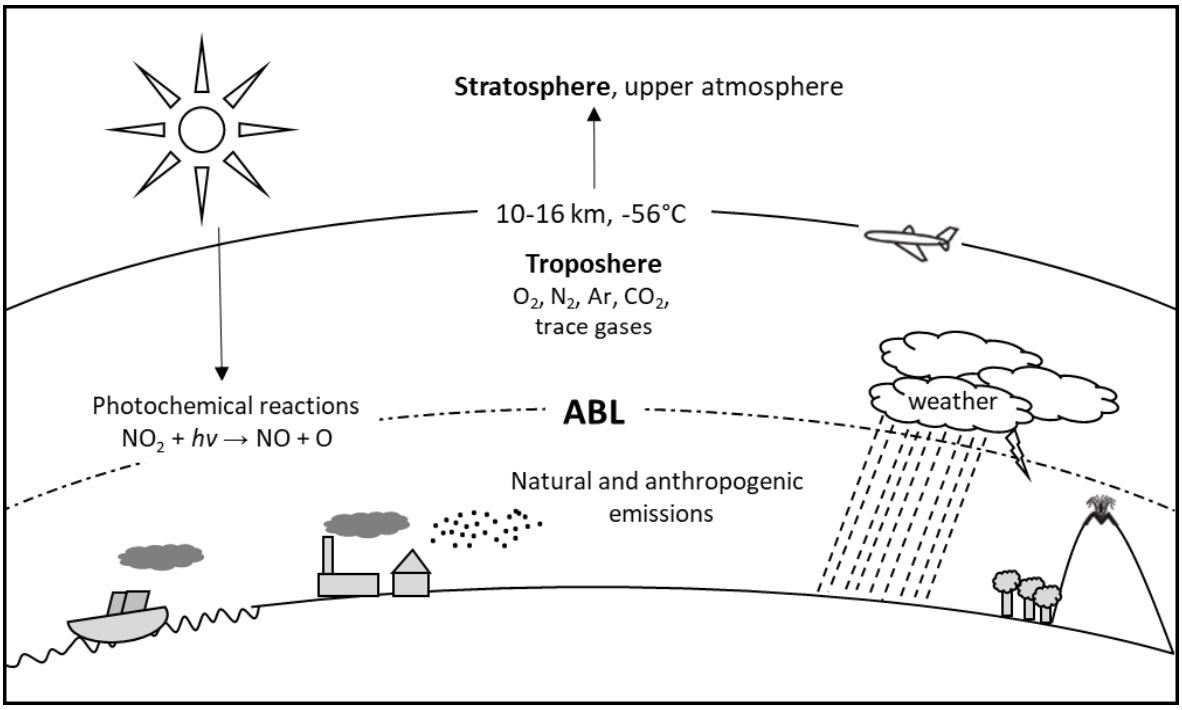

Figure 1: The lowest layer of the atmosphere (troposphere), which contains the atmospheric boundary layer (ABL). It is the layer with most air pollution phenomena. Adjusted from Manahan (2011).

Air pollutants in the atmosphere can be classified as primary or secondary pollutants. Primary pollutants are directly emitted into the atmosphere. Through a combination of chemical reactions and microphysical processes involving precursor pollutants, secondary pollutants are formed in the atmosphere. Depending on their sources or the sources of their precursors, air pollutants might have a natural, anthropogenic, or mixed origin.
Primary air pollutants are primary PM components (e.g., sea salt, black carbon, and trace metals), SO_x, NO_x, ammonia (NH_3), CO, CH_4, volatile organic compounds (VOCs), and certain metals and polycyclic aromatic hydrocarbons. Secondary air pollutants include particulate matter formed in the atmosphere via secondary particle formation, O_3, NO_x, and various oxidized VOCs.
SO_2, NO_x, NH_3, and VOCs are important precursor gases for secondary PM. VOCs are organic trace gases and carbon-containing compounds, excluding EC, CO and CO_2. VOCs exhibit a vapor pressure higher than 10 Pa at 25 °C, a boiling point of up to 260 °C under atmospheric pressure and 15 or fewer carbon atoms. Any compounds not fitting this definition are labeled semivolatile organic compounds (SVOCs; Williams and Koppmann, 2007).
In the atmosphere, gases SO_2 and NO_x can be oxidized into SO_4^{2-} (sulfate) and NO_3^- (nitrate), respectively, which produce two and one H^+ atoms, respectively. The reaction between NH_3 and H^+ may produce ammonium (NH_4^+).
To obtain a better understanding of the underlying pollutant chemistry, the most important photochemical processes and particle formation are explained in the following sections.

3.1.1 OH radical

The most significant oxidant in the lowest part of the atmosphere is the hydroxyl radical (OH). It initiates the removal of noxious substances such as CO, radiatively active gases such as CH_4, tropospheric ozone precursors such as VOCs and NO_x, and stratospheric ozone-depleting chemicals from the atmosphere (Levy, 1971).
OH is formed in a clean atmosphere during the day by the photolysis of ozone and a reaction of ozone with H_2O (g). $O(^1D)$ can only be formed by shortwave radiation and is an oxygen atom in an electronically excited state, which is more reactive than an oxygen atom in the ground state:

$$O_3 + h\nu \rightarrow O_2 + O(^1D) \qquad (\lambda < 310\ nm) \qquad \text{(Eq. 3.1)}$$

$$O(^1D) + H_2O \rightarrow 2\,OH \qquad \text{(Eq. 3.2)}$$

3.1.2 O_3-NO_x chemistry

NO_x and O_3 chemistries are strongly connected. Although O_3 is not directly emitted, it is an important compound in photochemistry. NO_x is primarily emitted as nitrogen oxide (NO) and formed in thermal combustion reactions at high temperatures (USEPA, 1999):

$$N_2 + O_2 \rightarrow 2\,NO \qquad \text{(Eq. 3.3)}$$

In the presence of sunlight during the daytime, NO rapidly establishes an equilibrium with NO_2 and O_3. After the formation from NO, NO_2 is photolytically decomposed. Part of this photon energy is then transferred to a neutral collision partner M, which is mostly molecular oxygen or nitrogen:

$$NO + O_3 \rightarrow NO_2 + O_2 \qquad \text{(Eq. 3.4)}$$

$$NO_2 + O_2 + M + h\nu \rightarrow NO + O_3 + M \qquad \text{(Eq. 3.5)}$$

In a further reaction of NO_2 with the OH radical, nitric acid (HNO_3) is formed:

$$NO_2 + OH + M \rightarrow HNO_3 + M \quad \text{(Eq. 3.6)}$$

Nitrogen dioxide can also form a base for a photostationary equilibrium of O_3:

$$NO_2 + h\nu \rightarrow NO + O \quad (\lambda < 424\ nm) \quad \text{(Eq. 3.7)}$$

$$O + O_2 \rightarrow O_3 \quad \text{(Eq. 3.8)}$$

At night, the concentration of photochemically produced OH is virtually zero; thus, NO_x is removed through different reactions. NO is oxidized into NO_2, which reacts with O_3 and forms NO_3 in the next step:

$$NO_2 + O_3 \rightarrow NO_3 + O_2 \quad \text{(Eq. 3.9)}$$

Freshly emitted NO can also be oxidized into NO_2 at night by the NO_3 oxidant

$$NO_3 + NO \rightarrow 2\ NO_2 \quad \text{(Eq. 3.10)}$$

NO_3 can also react with nitrogen dioxide:

$$NO_3 + NO_2 \leftrightarrow N_2O_5 \quad \text{(Eq. 3.11)}$$

$$N_2O_5 + H_2O \rightarrow 2\ HNO_3 \quad \text{(Eq. 3.12)}$$

During the day, NO_3 formed during the night is quickly photolyzed by solar radiation:

$$NO_3 + h\nu \rightarrow NO + O_2 \quad (\lambda < 700\ nm) \quad \text{(Eq. 3.13)}$$

$$NO_3 + h\nu \rightarrow NO_2 + O \quad (\lambda < 580\ nm) \quad \text{(Eq. 3.14)}$$

where the second reaction is more efficient.
Nitric acid (Eq. 3.12) is very soluble in water. This usually results in its washing out from the atmosphere before it undergoes photolysis. HNO_3 can also be converted into particulate nitrate in the presence of NH_3 (Eq. 3.25).

3.1.3 VOC- and NO_x-limited regimes

In addition to the dependency on NO_x, the concentration of tropospheric O_3 depends on the reactions of VOCs or CO, as they are important sources of hydroperoxyl radicals (HO_2) due to their reactivity. Furthermore, additional O_3 is present when NO is transformed into NO_2 by molecules other than O_3. HO_2 is formed by the oxidation of CO or VOCs through OH radicals. The reaction of VOCs can be compared to the reaction of CO:

$$CO + OH + O_2 \rightarrow CO_2 + HO_2 \quad \text{(Eq. 3.15)}$$

When NO is oxidized by HO_2 instead of O_3, the O_3 concentration increases:

$$HO_2 + NO \rightarrow NO_2 + OH \quad \text{(Eq. 3.16)}$$

HO_2 can also react with another HO_2 radical to form hydrogen peroxide:

$$HO_2 + HO_2 \rightarrow H_2O_2 + O_2 \quad \text{(Eq. 3.17)}$$

Hydrogen peroxide functions as a reservoir for HO_x species. It can be photolytically decomposed into OH:

$$H_2O_2 + h\nu \rightarrow 2\ OH \qquad \text{(Eq. 3.18)}$$

or be separated into HO_2 and water:

$$H_2O_2 + OH \rightarrow HO_2 + H_2O \qquad \text{(Eq. 3.19)}$$

Within this context, tropospheric O_3 concentrations are greatly influenced by the proportion of NO_2 produced during VOC oxidation. The VOC:NO_x ratio that corresponds to the peak production of O_3 in the troposphere depends on environmental parameters such as the temperature or the NO_2:NO ratio (National Research Council, 1991). High mixing ratios of VOC and NO_x combined with constant sunny weather can lead to the formation of summer smog where high concentrations of O_3 are possible. This is visualized in the empirical kinetic modeling approach (EKMA) developed by Dodge (1977). It is an approach for estimating environmental O_3 concentrations based on the generation of O_3 concentration isopleths depending on the NO_x and VOC concentrations (Figure 2). The highest O_3 concentration is reached when the VOC:NO_x ratio is 8:1.

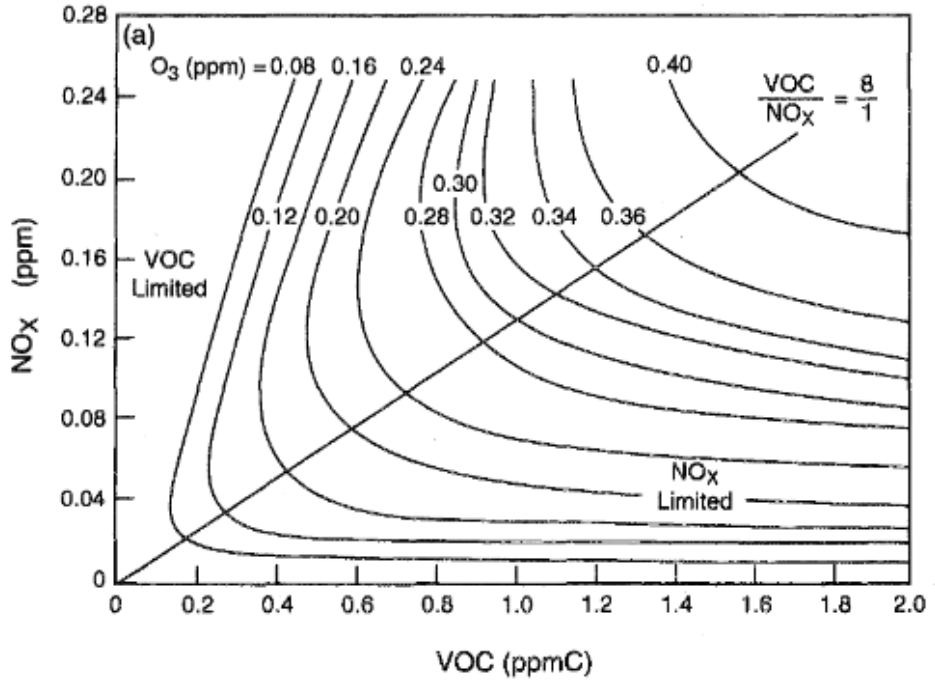

Figure 2: NO_x- and VOC-limited regimes for ozone production are displayed by typical ozone isopleths (Dodge; 1977).

3.1.4 Aerosols and aerosol precursors

Atmospheric PM stems from a number of sources (natural and anthropogenic). Natural sources of atmospheric PM include dust and sea salt particles resulting from natural events such as wind erosion and ocean spray, dust (airborne soil, also called crustal material), secondary sulfate, pollen, black carbon from wild fires, and volcanic ash. PM stemming from anthropogenic sources includes emissions from vehicles (road dust and break wear), soot from ship exhaust, power plants, and factories. Diesel engines and wood stoves are significant sources of fine particulate matter. In addition, agricultural activities such as plowing, harvesting, and livestock production can contribute to particulate matter generation, as well as forest fires and the burning of biomass for cooking and heating. All these are primary particles released into the air.

Secondary particles are created in the atmosphere by particle formation mechanisms. Secondary atmospheric particulate matter is formed through chemical reactions in the atmosphere involving precursor gases such as SO_2, NO_x, and VOCs.
The formation of secondary particulate matter is also influenced by meteorological factors like temperature, humidity, and atmospheric stability (Sun et al., 2022). PM is usually described by its diameter, which is divided into <10, <2.5, and <0.1 µm fractions (PM_{10}, $PM_{2.5}$, and $PM_{0.1}$, respectively; Anderson et al., 2012).
The gas-to-particle conversion process is responsible for most secondary fine PM thermodynamic equilibrium chemical reactions. They include the nucleation mode (< 0.1 µm) and the accumulation mode (0.1 to 2.5 µm). The accumulation mode is formed when various atmospheric gases condense to form new aerosol masses. Coagulation is the process that can drive particles from nucleation into accumulation. This process describes the collision between two particles that lead to the formation of a new particle of a larger size. The size distribution changes in favor of larger particles.
The most prevalent species in secondary inorganic aerosols are sulfate (SO_4^{2-}), nitrate (NO_3^-), ammonium (NH_4^+) and water. The two main acidic gases in the atmosphere, sulfuric acid (H_2SO_4) and nitric acid (HNO_3), are produced by the oxidation of SO_2 and NO_x, respectively. The main gaseous alkaline species, NH_3, may neutralize these acid gases in the atmosphere in addition to influencing the acidification and eutrophication of ecosystems (Koziel et al., 2006).

The homogenous or ion-induced nucleation of H_2SO_4 generated during the oxidation of SO_2 and OH radicals is likely the cause of new particle formation (Kulmala et al., 2004). H_2SO_4 is created by condensing on already existing accumulation mode particles or nucleating to generate new particles. The reaction of sulfuric acid with NH_3 produces atmospheric aerosol compounds such ammonium sulfate ($(NH_4)_2SO_4$; Eq. 3.23) and ammonium bisulfate (NH_4HSO_4).
Different aerosol modes and size distributions will be explained in Section 3.1.5. Because the concentrations are too low for coagulation to occur, accumulation mode particles typically do not move into the coarse mode because they were previously deposited (Koziel et al., 2006). The scheme in Fig. 3 shows the incorporation routes of chemical species into atmospheric PM.

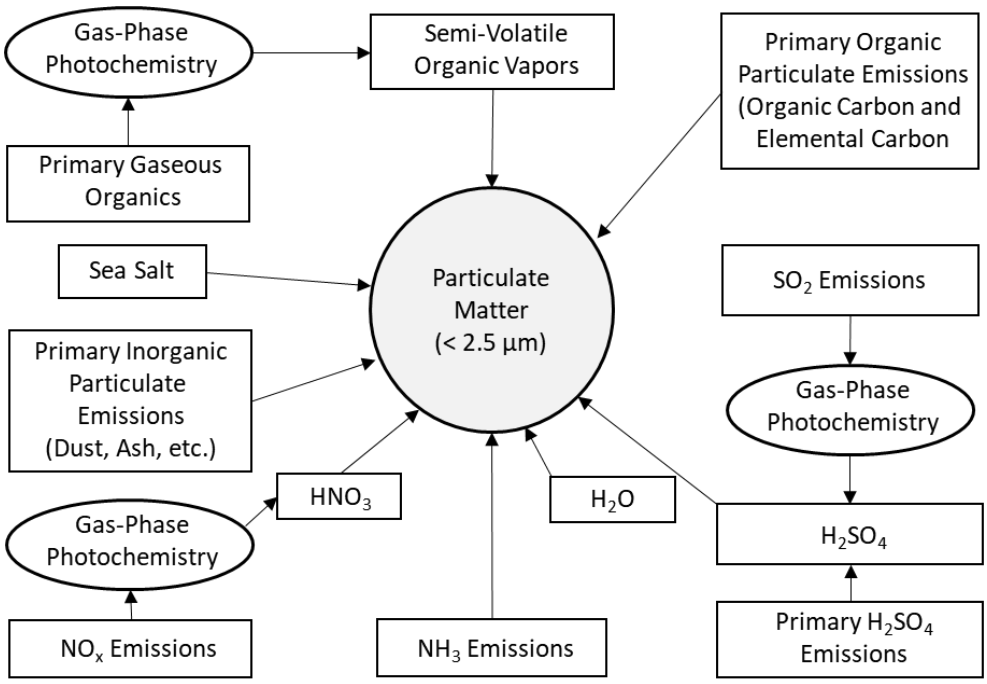

Figure 3: The incorporation of chemical species into atmospheric particulate matter (Koziel et al., 2006).

Sulfur enters the atmosphere mainly in the form of SO_2, which is released largely during human activities such as fossil fuel burning, petroleum refining, and metal smelting (Zhong et al., 2020). Gas-phase oxidation of SO_2 is initiated mainly by the OH radical:

$$SO_2 + OH + M \rightarrow HOSO_2 + M \qquad \text{(Eq. 3.20)}$$

When the hydroxysulfonyl radical ($HOSO_2$) becomes stable, it reacts with O_2 to form SO_3 (Eq. 3.21), which then undergoes hydrolysis to form H_2SO_4 (Eq. 3.22):

$$HOSO_2 + O_2 \rightarrow HO_2 + SO_3 \qquad \text{(Eq. 3.21)}$$

$$SO_3 + (H_2O)_n \rightarrow H_2SO_4 + (H_2O)_{n-1} \qquad \text{(Eq. 3.22)}$$

H_2SO_4 can initiate particle formation by reacting with basic trace gases such as NH_3 or condensing on existing particles. As such, it contributes to aerosol formation, growth, and cloud droplet nucleation (Sun et al., 2022).
Sulfuric acid is simply removed from the atmosphere by wet deposition. Similar to nitric acid, it can condense to form particles, e.g., in the presence of NH_3. Ammonia originates mainly from soils, animal waste, fertilizers and industrial emissions and neutralizes sulfuric acid as follows:

$$2NH_3\,(g) + H_2SO_4\,(g) \rightarrow (NH_4)_2SO_4\,(s) \qquad \text{(Eq. 3.23)}$$

HNO_3 originates from the conversion of NO_x and is removed from the atmosphere by wet or dry deposition:

$$NO_2 + OH \rightarrow HNO_3 \qquad \text{(Eq. 3.23)}$$

Nitric acid may also be removed from the atmosphere through a reaction with NH_3:

$$NH_3\ (g) + HNO_3\ (g) \leftrightarrow NH_4NO_3\ (s) \qquad \text{(Eq. 3.25)}$$

NH_4NO_3 (Ammonium nitrate) and $(NH_4)_2SO_4$ are essential components of PM in polluted air (Finlayson-Pitts and Pitts, 2000). Both substances may undergo dry or wet deposition by which they are removed from the atmosphere.

3.1.5 Particle size distribution

The size distribution of particles is usually represented as curves, of which the peaks are referred to as modes, attributed to various source and sink mechanisms. Particles continuously change in size due to condensation, evaporation, coagulation and fragmentation; thus, the size spectra of these modes overlap (Figure 4). The smallest particles are formed by gas-to-particle conversion (nucleation mode) and increase through condensation of gases and water vapor. The particle diameter first increases rapidly (Aitken mode) and then slowly by coagulation, from 50 to 100 nm (accumulation mode). When the particle size exceeds 100 nm, the efficiency of thermodynamic and mechanical sink processes (e.g., sedimentation and wet deposition) is enhanced (Seinfeld and Pandis, 2006).

Particles can be formed by nucleation, which then may grow by condensation (e.g., SO_3 in Eqs. 3.20 to 3.22). Aitken particles are formed by the nucleation mode or incomplete combustion (e.g., soot), accumulation mode particles are formed by Aitken growth, and coarse particles are formed from accumulation mode particles and moderate mechanical processes (e.g., abrasion of mineral dust, volcanic ash, and sea spray; Guevara, 2016).

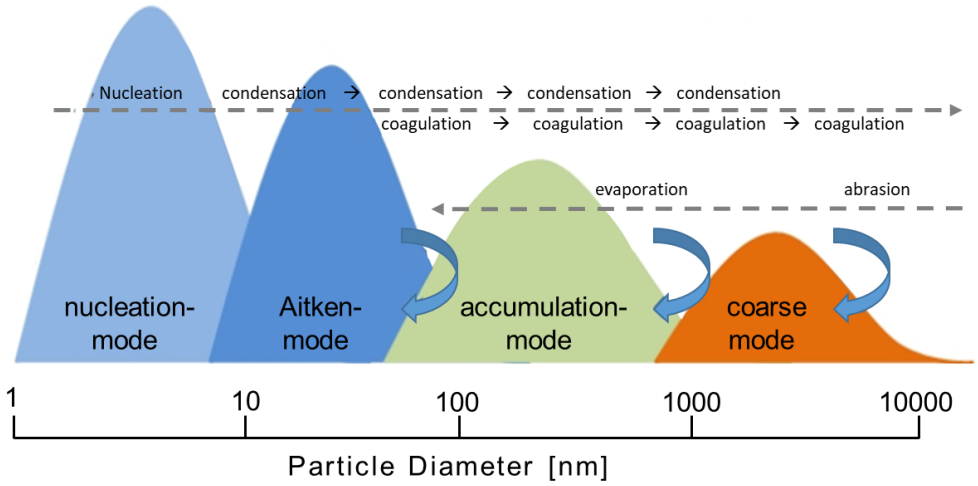

Figure 4: Schematic particle size distribution with transformations between the modes. Adjusted from Deutscher Wetterdienst (DWD, n.d.).

The size distribution can be mathematically described approximately by logarithmic normal distributions, with the best fit for single-source aerosols. When aerosols are measured or modeled, they are usually counted in bins or channels. These contain particles of certain size classes. To ensure a more meaningful shape of the plotted curve, the size distribution function can be expressed as:

$$\frac{dN}{dlogD_p} = \frac{dN}{logD_{p,u} - logD_{p,l}} \qquad \text{(Eq. 3.26)}$$

where dN denotes the particle concentration, D_p is the midpoint particle diameter, $D_{p,u}$ is the upper channel/bin diameter and $D_{p,l}$ is the lower channel/bin diameter, which refers to channels also used in measurement instrumentation. The unit used for dN is usually 1/cm³, and that for $D_{p,}$ is µm.

From the above, the particle concentration can be obtained as:

$$dN = \frac{dN}{logD_{p,u} - logD_{p,l}} * (logD_{p,u} - logD_{p,l}) \quad \text{(Eq. 3.27)}$$

The above is usually not plotted as dN since the x-axis (D_p) generally exhibits a logarithmic scale. The size distribution can encompass any aerosol property and can also display, e.g., the mass $dM/dlogD_p$ or volume $dV/dlogD_p$. The maximum particle number can usually be found in the nucleation mode, whereas the maximum particle mass can be found in the accumulation or coarse mode.

The size distributions of particles emitted by marine diesel engines can cover ranges from the nucleation mode across the Aitken mode to the accumulation mode. These modes are applicable to both ship plumes and fresh emissions. However, shipping-related emissions mainly occur as fine $PM_{2.5}$ particles, which are created from primary and secondary particulate matter (Moldanova et al., 2013; Viana et al., 2020).

3.2 Sources and sinks of atmospheric pollutants

Plants, the ocean, and soil are examples of pollutant sinks since they can absorb more pollutants from the atmosphere than they can emit. A source, however, is anything that emits more pollution into the atmosphere than it absorbs, e.g., anthropogenic activities, such as the combustion of fossil fuels, and natural sources, such as volcanic eruptions.

3.2.1 Ship emissions as sources of atmospheric pollutants

Tropospheric O_3 is formed from the emissions of NO_x and other ozone precursors from shipping, which also affect the level of OH and the lifespan of CH_4. SO_4^{2-} is the primary aerosol component produced by ship emissions and is created by the oxidation of SO_2 (Eyring et al. 2010; Karjalainen et al.; 2022).

The particle processes and particle sizes in ship exhaust can vary depending on the fuel type used and the engine type. When heavy fuel oil (HFO) is burned in a ship engine, PM is produced including soot, ash, and other fine particles. The size of these particles can range from less than 0.1 µm (ultrafine particles) to several µm. The particle size distribution can vary depending on the combustion conditions, with larger particles typically produced under incomplete combustion conditions. In addition, the burning of marine diesel oil (MDO) produces PM, but the particle size distribution tends to be smaller than that of the particles produced from the burning of HFO. The size of the particles can range from smaller than 0.1 µm to approximately 1.0 µm. When MDO is combusted, the SO_x and PM emissions are lower than those when burning HFO, but the NO_x emissions can still be significant. Liquefied natural gas (LNG) is considered a cleaner fuel than HFO and MDO and produces lower levels of PM upon combustion. However, PM can still be produced in the combustion process. The size of these particles can range from smaller than 0.1 µm to approximately 0.5 µm. In addition, LNG still produces GHG emissions, primarily CO_2 and CH_4 (Corbin et al., 2020; Winnes and Fridell, 2009).

The amount of emissions produced by pollutant sources can be calculated by emission models, which can then provide emission inventories that are fed into CTM systems. Information on emissions is needed for CTM systems to accurately calculate the chemical composition and physical state of the

atmosphere (Matthias et al., 2018). The ship emission model used in this thesis is the Ship Traffic Emission Assessment Model (STEAM; a detailed description is provided in Sect. 4.1.4.2). The Finnish Meteorological Institute (FMI) calculates ship emissions with the STEAM based on ship activity and emission factors (EFs) as follows:

$$\text{Ship emissions} = \text{ship activity} * \text{EF} \quad \text{(Eq. 3.28)}$$

3.2.2 Sinks of atmospheric pollutants

Sinks are processes that result in the removal of substances and pollutants from the atmosphere. One major sink for gases and particles in the atmosphere is deposition. It can either occur as dry deposition, which entails uptake at the surface (soil, water or vegetation), or as wet deposition, in which substances are absorbed into droplets followed by precipitation or impaction (e.g., fog droplets; Zannetti, 1990). Dry deposition determines the net flux of pollutants at the Earth's surface (Galmarini et al., 2021). Since deposition is a significant loss mechanism connected with concentrations near to the ground, accurate estimations for accurate projections of atmospheric concentrations are required (Emerson et al., 2020; Vivanco et al., 2018). NO_2 deposition contributes to eutrophication, followed by biodiversity loss, whereas O_3 dry deposition could result in damage to plant tissues and a reduction in plant productivity (Vivanco et al., 2018; Clifton et al., 2020). Wet deposition, however, can deliver indications regarding the fate of particles.
Furthermore, chemical reactions can function as sinks for gases. Atmospheric gases can react with other substances to form new compounds that are more stable and less likely to remain in the atmosphere, such as particles. Some gases in the atmosphere can dissolve in water bodies, leading to their removal from the atmosphere. Plants and trees can absorb certain gases, such as CO_2, during photosynthesis, leading to their removal from the atmosphere (Farrelly et al., 2013).

Overall, the sinks for gases and particles in the atmosphere play an important role in maintaining the balance of the Earth's atmosphere and regulating the concentrations of pollutants and GHGs (Olivier and Berdowski, 2001).

3.3 Chemical transport model systems

In the previous sections, only a few of the various chemical processes that occur in the atmosphere were described. These processes are relevant for the work in this thesis.
Measurements only provide partial insights into the complex atmospheric conditions at a certain moment and location. Thus, the transformation and movement of chemical substances in the atmosphere as well as their spatial distribution can be calculated by using CTMs to obtain a simplified version of the real conditions. One advantage of using chemical transport models over measurements is the capability of considering chemical reactions and tracking the contribution of emission sources to air pollutants. Another advantage over measurements is the spatial coverage. Measurements cannot fully cover the entire domain. In addition, they are usually limited in the number of detected air pollutants. Chemical transport models can be used to calculate the concentration of a large number of chemicals. Nevertheless, this could also constitute a disadvantage since these models could involve a highly simplified chemistry and cannot be employed to describe all the complex physical and chemical processes within the atmosphere. This could lead to deviations from the actual atmospheric composition.
Many CTMs with diverse approaches have been developed and applied. In this thesis, the Lagrangian and Eulerian model types are used. In addition to the type, models can be characterized by their dimensionality. In the Lagrangian approach, the change in the chemical composition within one or

many specific air parcels transported through the atmosphere can be simulated. In the Eulerian approach, a grid of fixed computational cells is assumed. In the Lagrangian modeling framework, there is no mass exchange between the air parcel and its surroundings since it flows in local wind. The exceptions are species emissions permitted to enter the air parcel through its base. The model can be employed to simulate concentrations at various locations and periods since air parcel are considered to travel continuously. Often, all air parcels are averaged to determine the percentage chance in the likelihood of cells moving along a certain direction. The Eulerian modeling framework does not move in space. Species enter and leave each cell through its walls, and the model simulates the species concentration at all locations as a function of time (Seinfeld and Pandis, 2006; Figure 5 a).
Another aspect for characterizing chemical transport models is their dimensionality, but the model complexity increases with dimensionality.
The zero-dimensional (0-D) box model is the simplest approach. The atmospheric domain (the area to be investigated) is represented by one simple box. A parcel model is a box model that travels through space along the wind direction. Emissions enter the box at various times and locations. A parcel model is also known as a Lagrangian trajectory model since it travels in a Lagrangian sense (Figure 5 b).
Three-dimensional (3-D) models can be used to simulate the entire concentration field with latitude, longitude, altitude and time. A 3-D model provides the advantage that dynamics and transport can be accurately represented but demands substantially more computation time and memory than a model with fewer dimensions (Seinfeld and Pandis, 2006; Chipperfield and Arnold, 2015).
The five different regional scale Eulerian models used for this thesis are part of Sect. 4.1. In Sect. 4.2, the 0-D Lagrangian-type MAFOR model (Karl et al., 2011, Karl et al., 2022) is described in detail. The results obtained with the MAFOR model are shown and evaluated in Sect. 5.3.

The domain of a 3-D CTM is the area chosen for the model simulations. This domain can range from a few hundred meters to thousands of kilometers with a different meteorology or resolution of the results on each scale. The model domain is usually defined as spaced boxes in which the atmospheric conditions are reproduced. These boxes form the domain grid, and in these boxes, transport and chemical transformation are numerically solved (Figure 5 a; Chipperfield and Arnold).

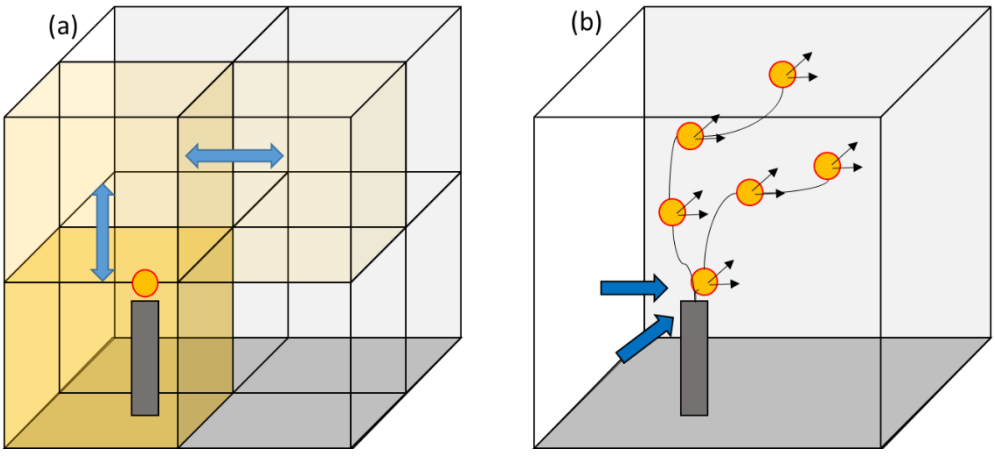

Figure 5: (a) Eulerian Model approach with simulating the species concentration coming from an emission source within fixed computational cells; (b) Lagrangian Model approach simulating the species concentration at different locations at different time based on a moving air parcel. The gray rectangle symbolizes the emission source, the orange circle represents the air pollutant, which is either diluted to grid cell size (a) or being moved as an air parcel (b).

Before starting a regional scale model simulation, the domain and grid size must be defined. Furthermore, the initial conditions in the modeling domain and the boundary conditions at the border of the domain must be given. These boundary conditions contain the meteorology originating from outside the domain and the concentration of substances at the border of the domain. Regarding the regional scale CTMs in this study, these conditions are provided by larger-scale (global) models with a lower resolution than that of the small-scale model, while the smaller-scale model provides detailed output used for evaluation. This process is referred to as nesting. Biogenic and anthropogenic emissions as well as meteorological data must be provided to initiate a CTM simulation.

The scheme in Fig. 6 shows the general flows of the input data and model setup for mathematical atmospheric models, such as Eulerian CTM systems. The models are based on a similar concept but differ in the internal mechanisms. This indicates the importance of comparing the model outputs to obtain indications regarding the range of deviations among various CTM systems.

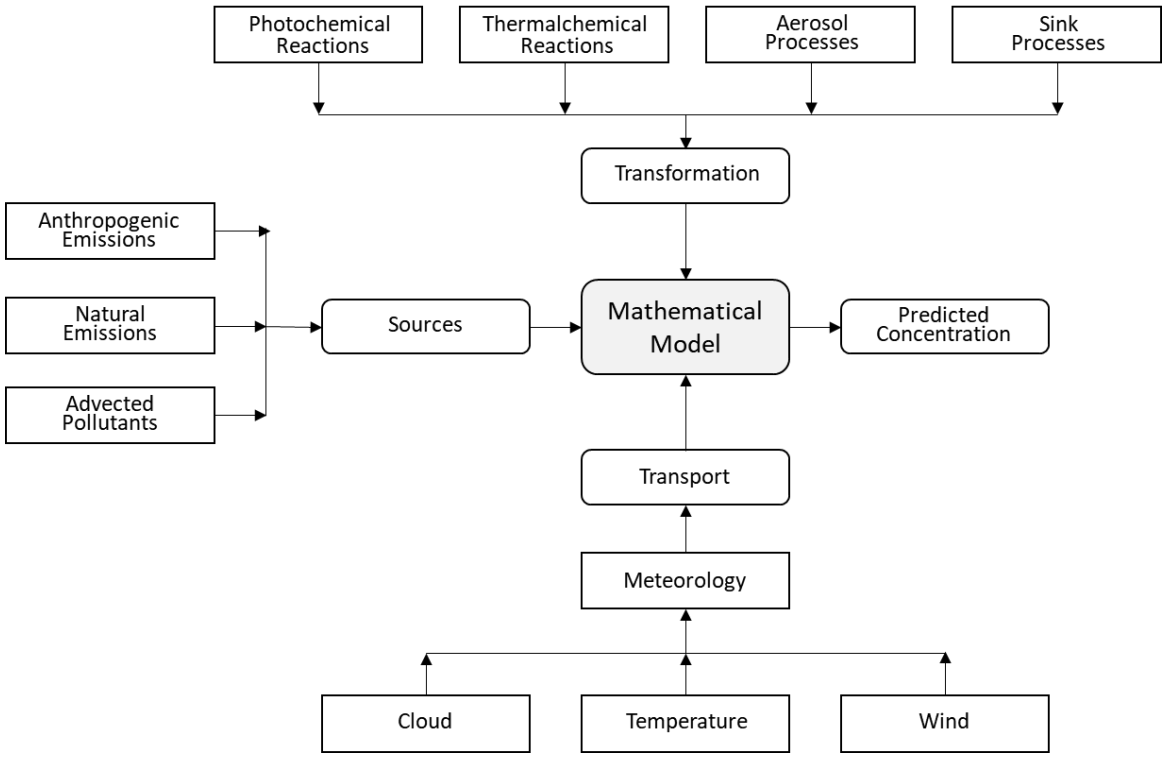

Figure 6: Scheme of main components of a mathematical atmospheric model. Simplified from Seinfeld & Pandis (1998).

4 Methods

This section is based on the methods adopted from the publications used for this thesis. Since the methods used in the first two studies are very similar, they are summarized in the Methods. This section is divided into a first part (Section 4.1), where the applied Eulerian models and relevant methods are described. This part is retrieved from published studies, as presented before the Introduction. The second part (Section 4.2) contains a description and methods of the study considering the Lagrangian box model MAFOR. The third part (Section 4.3) contains an explanation of the model evaluations for both model approaches.

4.1 Eulerian regional scale model systems

4.1.1 Model parameters and setup

Five different regional scale CTMs were used for the model intercomparison within this thesis. The CTM systems were run by four institutions: Comprehensive Air Quality Model with Extensions (CAMx) and CHIMERE by AtmoSud, Community Multiscale Air Quality (CMAQ) by Helmholtz-Zentrum Hereon, European Monitoring and Evaluation Programme (EMEP) by IVL Swedish Environmental Research Institute and LOTOS-EUROS by TNO Netherlands Organization for applied scientific research.

The goal was to have a model setup as similar as possible for all models to receive comparable simulations. As a base, an inner and outer domain with grid resolution was established. Additionally, the emissions were provided for one year. Especially of importance in the present study was the method for calculating the potential ship impact.

An overview of the input data is shown in Table 2. Input data were the same for shipping emissions using STEAM (version 3.3.0.; Jalkanen et al., 2009; Jalkanen et al., 2012; Johansson et al., 2013; Johansson et al., 2017), land-based emissions (CAMS-REG, v2.0) as well as projection (WGS84_lonlat), domain (Mediterranean Sea), resolution (0.1° x 0.1°, 12 x 12 km) and the modeled year (2015). Input data were different for meteorological input data, boundary and initial conditions because the CTMs used their standard setup.

The model domains covered the largest part of the Mediterranean Sea, with a spatial extent ranging in longitude from -0.95° to 29.95° and in latitude from 33.8° to 44.95° (Figure 7). The appointed grid cell size was 12 × 12 km² interpolated on a 0.1° × 0.1° grid nested in a 36 × 36 km² grid (except EMEP). The extent of computational domains for each model are in Supplements 1, Table S1.

The model simulations should all contain NO_2 and O_3 in µg/m³ at an hourly resolution on a 2D grid from the lowest layer and be provided as a netcdf file following Climate and Forecast (CF) conventions. The lowest layer on the ground was used in the present study.

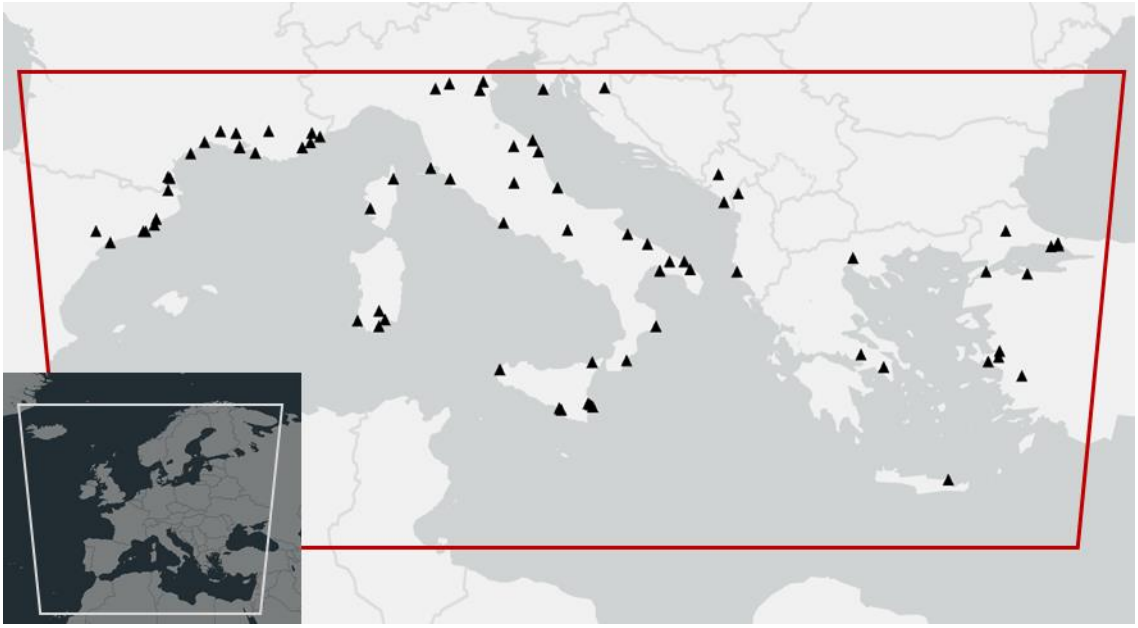

Figure 7: Domains and measurement stations. Red trapeze displays the 12 x 12 km² domain resolution, black triangles are locations of measurement stations. On bottom left the larger 36 x 36 km² domain resolution is displayed. Map source: ArcGIS Pro 2.7.1 © 2020 Esri Inc.

With all CTMs, a reference run for the current air quality situation was performed, including all emissions (base case). Furthermore, all models did one run without the emissions from shipping (noship case). The difference between the calculations with all emissions and the calculation without shipping emissions is used to determine the potential impacts of ships to the ambient pollutant concentration. This method shows the change of an emission reduction and the maximal effect, by having a complete switch-off from shipping activity in the noship run. Thus, it is referred to as zero-out method. This was done for all five models.

Table 2: Main model parameters and input data for the five chemical transport models.

Model parameter	CAMx	CHIMERE	CMAQ	EMEP	LOTOS-EUROS
Grid resolution inner domain	12x12 km²	12x12 km²	12x12 km²	0.1°x 0.1°	0.1°x 0.1°
Grid resolution outer domain	36x36 km²	36x36 km²	36x36 km²	none	0.5°x 0.25°
Meteorological driver	WPS/WRF	WPS/WRF	COSMO-5 CLM	ECMWF (IFS)	ECWMF (IFS)
Boundary conditions	Mozart-4 output is used and downscaled for time- and space-variable boundary conditions	Gaseous species: LMDz-INCA model (Folberth et al., 2006), with climatology as average monthly fields Aerosols: Global Ozone Chemistry	IFS_CAMS cycle45r1	provided with the open source model distribution for year 2015; Simple functions for prescribing concentrations in terms of latitude and time-of-year, or time-of-day.	CAMS C-IFS global forecast (lateral and top)

		Aerosol Radiation and Transport model GOCART (Ginoux et al., 2001)		(Simpson et al 2012). Boundary conditions of ozone are developed from climatological ozone-sonde datasets as in EMEP Status report 1/2022	
Land-based emissions	CAMS-REG v2.2.1	CAMS-REG v2.2.1	CAMS-REG v2.2.1	CAMS-REG v2.2.1	CAMS-REG v2.2.1
Shipping emissions	STEAM v3.3.0	STEAM v3.3.0	STEAM v3.3.0	STEAM v3.3.0	STEAM v3.3.0
Biogenic emissions	MEGAN Model v2.03 output for the year 2015	MEGAN Model v2.04 output for the year 2015	MEGAN Model v3 output for the year 2015	Calculated online: Emissions of isoprene and monoterpenes following Guenther et al. (1993, 1995). Soil NO emissions from soils of seminatural ecosystems are specified as a function of the N-deposition and temperature	Calculated online: Emissions of isoprene and monoterpenes following Guenther et al. (1993), using actual meteorological data. Emission of NO from soil as in Manders-Groot et al. (2016)
Sea salt emissions	Calculation based on Ovadnevaite et al. (2014)	Calculation based on Monahan et al. (1986)	Calculation based on Kelly et al. (2010)	Calculation based on Monahan et al. (1986) and Mårtensson et al. (2003)	Calculation based on Monahan et al. (1986) and Mårtensson et al. (2003)
Dust emissions	Based on approach used in global EMAC (ECHAM/ MESSy; Klingmueller et al., 2018; Astitha et al., 2012).	Calculated online: After parametrization of Marticorena and Bergametti (1995) and Alfaro and Gomes (2001)	Not considered	Key parameter is wind friction velocity. The parameterization after Marticorena and Bergametti (1995), Marticorena et al. (1997), Alfaro and Gomes (2001), Gomes et al. (2003), Zender et al. (2003).	Calculated online: Emissions after Marticorena and Bergametti (1995) with soil moisture as described by Fécan et al (1999). Dust from re-suspension by traffic and agriculture as

				Daily emissions from forest and vegetation fires from "Fire INventory from NCAR version 1.0" (Wiedinmyer et al., 2011)	in Schaap et al. (2009)
Chemical mechanism	CB05	MELCHIOR2	CB05	EmChem 19a	CBM-IV
Aerosol size distribution	$PM_{2.5}$; PM_{10}	8 bins: 40 nm to 10 µm	Trimodal size distribution (0.03µm, 0.3µm, 6µm; Binkowski and Roselle, 2003)	$PM_{2.5}$; $PM_{2.5-10}$	$PM_{2.5}$; $PM_{2.5-10}$
Inorganic aerosol module	ISORROPIA (Nenes et al., 1998)	ISORROPIA (Nenes et al., 1998)	ISORROPIA II (Fountoukis and Nenes, 2007)	MARS (Binkowski and Shankar, 1995)	ISORROPIA II (Fountoukis and Nenes, 2007)
Organic aerosol module	SOAP semivolatile scheme (Strader et al., 1999)	Described in Pun et al. (2006)	Updates on SOA as described in Pye et al. (2017)	For SOA the volatility basis set (VBS) approach (Robinson et al. 2007; Donahue et al. 2009; Bergström et al. 2012) is used	No organic aerosols in the simulations
Wet deposition scheme	Scavenging model for gases and aerosols (Seinfeld and Pandis, 1998)	The wet deposition in CHIMERE follows the scheme proposed by Loosmore and Cederwall (2004).	Wet deposition is calculated within CMAQ's cloud module as descriped by Roselle and Binkowsk (1999)	Calculation as described in Emberson et al. (2000); parametrization for different surfaces as in Simpson et al. (2012)	Wet deposition is divided between in-cloud and below-cloud scavenging. The in-cloud scavenging module is based on the approach described in Seinfeld and Pandis (2006) and Banzhaf et al. (2012).
Dry deposition scheme	Resistance model of Zhang et al. (2003)	Dry deposition is as in Wesely (1989)	Dry deposition scheme M3Dry (Pleim et al., 2001)	As described in Simpson et al. (2012)	Resistance approach following Erisman et al. (1994)

4.1.2 Model description

4.1.2.1 CAMx

CAMx is a Eulerian photochemical dispersion model developed by Ramboll Environ. Version CAMx v6.50 of the model was used in the present study.

For this study, a first domain with a 36 km resolution was defined at the European scale. A second nested domain was defined, named MEDI12 (147x249 points), and covered the center of Europe with a resolution of 12 km. Both meteorological and chemical transport simulations were provided for these domains. WRFv3.9 was run for the simulation of meteorological conditions with 28 vertical layers up to 50 hPa, with FNL data for initial conditions.

For the CAMx simulation, boundary conditions from the Mozart-4 was used. Sea salt emissions are calculated in the SEASALT pre-processor of CAMx. This program generates aerosol emissions of sodium, sulfate and chloride, and gaseous emissions of chlorine using CAMx-ready meteorological and landuse files. The sea salt emissions program calculates the flux of sea salt over the open ocean using parameterizations developed by Ovadnevaite et al. (2014). The surf zone aerosol flux is calculated by using Gong (2003) open ocean approach with an assumed 100 % whitecap coverage. Biogenic emissions were calculated separately with the Model of Emissions of Gases and Aerosols from Nature, version 2.03 (MEGANv2.03; Guenther et al., 2006) and then included in the land-based emissions. WBDUST pre-processors delivers dust emissions in CAMx and generates gridded windblown dust emissions. The scheme is based on an updated approach used in the global EMAC (ECHAM/MESSy) atmospheric chemistry-climate model (Klingmueller et al., 2018; Astitha et al., 2012). The mechanism for lightning NO_x was not activated in CAMx.

The gas phase chemical mechanism is Carbon Bond 5 (CB05), in which the NMVOC emissions are split into 13 species (TERP, ISOP, XYL, TOL, ETOH, MEOH, IOLE, OLE, ETH, ALD2, PAR, ETHA and FORM) and describe approximately 156 reactions. For semivolatile inorganic species (SO_4^{2-}, NO_3^-, and NH_4^+), the equilibrium concentration is calculated using the thermodynamic model ISORROPIA (Nenes et al., 1998). Fourteen vertical levels are simulated with a first layer height of approximately 10 m.

CAMx includes algorithms for inorganic aqueous chemistry (RADM-AQ), inorganic gas-aerosol partitioning (ISORROPIA), and two organic gas-aerosol partitioning and oxidation approaches, volatility basis set (VBS) or Secondary Organic Aerosol Processor (SOAP). Using gas-phase processes, these approaches produce sulfate, nitrate, and condensable organic gases. The hybrid 1.5-D (1.5-dimensional) VBS is applied to provide a unified framework for gas-aerosol partitioning and the chemical aging of both primary and secondary atmospheric organic aerosols (Ramboll Environment and Health, 2020). One crucial assumption in Particulate Source Apportionment Technology (PSAT) is that PM is allocated to the primary precursor for each type of particulate matter (i.e., PSO_4 is apportioned to SO_x emissions, PNO_3 is apportioned to NO_x emissions, and PNH_4 is apportioned to NH_3 emissions).

4.1.2.2 CHIMERE

CHIMERE is an offline chemical transport model developed by LMD-IPSL/CNRS (Menut et al., 2013). The CHIMERE2017r4 version of the model was used in this study.

Weather Research and Forecasting Model (WRFv3.9) was run for the simulation of meteorological conditions with 28 vertical layers up to 50 hPa, with FNL data for initial conditions.

Concerning CHIMERE simulation, boundary conditions are monthly mean climatologies taken from the Laboratoire de Météorologie Dynamique General Circulation Model – INteraction with Chemistry and Aerosols (LMDz-INCA model; Schulz et al., 2009) for gaseous species and from the

Global zone Chemistry Aerosol Radiation and Transport model (GOCART; Ginoux et al., 2001) for aerosols (desert dust, carbonaceous species and sulfate). Sea salt emissions were calculated as described in Monahan (1986). MEGAN Model v2.04 calculated biogenic emissions (Guenther et al., 2006). MEGAN is running directly by CHIMERE code and biogenic emissions are just generated before the air quality run. The mineral dust emissions are calculated on-line. The soil is represented by relative percentages of sand, silt and clay with the USGS soil texture (www.usgs.gov; accessed: 01.08.2023). The aeolian roughness length used in CHIMERE is the Global Aeolian Roughness Lengths from ASCAT and PARASOL (GARLAP) dataset as in Prigent et al. (2012). There is no treatment of NO_x lightning in CHIMERE.
The gas phase chemical mechanism is Modele Lagrangien de Chimie de l'Ozone a l'echelle Regionale (MELCHIOR2), in which the NMVOC emissions are split into 10 species (C2H6, NC4H10, C2H4, C3H6, C5H8, OXYL, HCHO, CH3CHO, CH3COE and APINEN) and describe approximately 120 reactions. For semivolatile inorganic, the equilibrium concentration is calculated using the thermodynamic model ISORROPIA (Nenes et al., 1998). Nine vertical levels are selected with a first layer height at 20 m to 25 m.
The full description of CHIMERE's inorganic and organic modules can be found in Menut et al. (2013). CHIMERE's sectional aerosol module includes emitted total primary particulate matter (TPPM), secondary species such as nitrate, sulfate, ammonium, and SOAs. Natural dust and sea salt aerosols can also be produced as passive tracers or interactive species in equilibrium with other ions. Organic matter and elemental carbon (EC) can be speciated if an inventory of their emissions is supplied. The utilized models include the aqueous, gaseous, and particulate phases of ammonia, ammonium, nitrate, and sulfate. For instance, in accordance with the ISORROPIA thermodynamic equilibrium model, the model species pNH_3 represents an equivalent ammonium in the particulate phase as the sum of the NH_4^+ ion, NH_3 liquid, NH_4NO_3 solid, and other salts (Nenes et al., 1998).

4.1.2.3 CMAQ

The CMAQ Model v5.2 with the aero6 model calculates on the basis of emission input data air concentration as well as deposition fluxes of atmospheric gases and aerosols (Byun and Schere, 2006; Appel et al., 2017). Atmospheric chemistry is used by the chemical CB05 mechanism (Yarwood et al., 2005) cb05tucl with updated toluene chemistry (Whitten et al., 2010), including the chlorine chemistry extension (CB05-TUCL; https://www.airqualitymodeling.org/index.php/CMAQv5.0_Chemistry_Notes, accessed May 2021). The aerosol scheme AERO6 is used for the formation of secondary inorganic aerosols. H_2SO_4, HNO_3, hydrochloric acid (HCl) and NH_3 gas phase – aerosol partition equilibrium is solved by the ISORROPIA mechanism (Fountoukis and Nenes, 2007; Nenes et al., 1998). Contained within is the formation of secondary organic aerosol (SOA) from isoprene, terpenes, benzene, toluene, xylene and alkanes (Carlton et al., 2010; Pye and Pouliot, 2012).
Sea salt emissions were calculated as described in Kelly et al. (2010). Biogenic emissions (NMVOC from vegetation and soil NO) were calculated previously with the MEGAN Model v3 (Guenther et al., 2012) and then included into the land-based emissions. Emissions of windblown dust were not considered. CMAQ models 30 vertical layers, with the lowest layer from 0 m to 42 m and the second layer from 42 m to 85 m. The NO_x lightning treatment in CMAQ was not activated for the present study.
The COSMO model simulated the meteorological data for CMAQ, applying the version COSMO5-CLM16 (Schultze and Rockel, 2018; Petrik et al., 2021). The Meteorology-Chemistry Interface Processor (MCIP) processed meteorological model output into the input format required for CMAQ. The vertical resolution of the meteorological model was 40 terrain-following geometric height levels up to 22 km. The Boundary Condition driver used was Integrated Forecasting System – Copernicus

Atmosphere Monitoring Service (IFS-CAMS cycle45r1; Inness et al., 2019) with a vertical resolution of 60 sigma levels up to 65 km.
To prevent the effects from initial conditions on the simulated atmospheric concentrations in 2015, the model run started with a spin up run in mid-December 2014. The grid size of the Mediterranean Sea domain was 12 x 12 km², nested in a 36 x 36 km² domain covering all of Europe.
CMAQ represents aerosol formation and growth using three log-normal distributed modes: the Aitken and accumulation modes are generally less than 2.5 μm in diameter, while the coarse mode contains significant amounts of mass above 2.5 μm. $PM_{2.5}$ and PM_{10} can be obtained from the model-predicted mass concentration and size distribution information.
The CMAQ aerosol scheme AERO6 was employed; this scheme expands the chemical speciation of PM by the species aluminum, calcium, iron, silicon, titanium, magnesium, potassium, and manganese. H_2SO_4, HNO_3, HCl (hydrochloric acid) and NH_3 gas phase – aerosol partition equilibrium is solved by the ISORROPIA II mechanism (Fountoukis and Nenes, 2007; Nenes et al., 1998). Contained within this scheme is the formation of SOA from isoprene, terpenes, benzene, toluene, xylene and alkanes (Carlton et al., 2010; Pye and Pouliot, 2012). CMAQ allows for dynamic mass transfer of semi-volatile inorganic gases to coarse mode particles, which facilitates the replacement of chloride by NO_3^- in sea salt aerosols (Foley et al., 2010).

4.1.2.4 EMEP

The European Monitoring and Evaluation Programme, Meteorological Synthesizing Centre – West (EMEP MSC-W, https://www.emep.int/mscw/index.html, accessed: 01.06.2021) model is a limited area, terrain-following hybrid coordinate model designed to calculate air concentrations and deposition fields for major acidifying and eutrophying pollutants, photooxidants and particulate matter (Simpson et al., 2012; Simpson et al., 2020).
In this study, a 0.1° x 0.1° resolution grid on long–lat projection and with 20 vertical levels was used. The meteorological input data are based on forecast experiment runs with the Integrated Forecast System (IFS), a global operational forecasting model from the European Centre for Medium-Range Weather Forecasts (ECMWF). The meteorological fields are retrieved on 0.1° x 0.1° long–lat coordinates. Vertically, the fields on 60 eta (η) levels from the IFS model are interpolated onto the 20 EMEP eta levels.
The model version used was rv4.34 with chemical mechanism EmChem 19a (Simpson et al., 2012; Simpson et al., 2020). The mechanism builds on surrogate VOC species (Simpson et al., 2012; extended with benzene and toluene) and has 171 gas phase and heterogeneous reactions. The model always assumes equilibrium between the gas and aerosol phases using the MARS equilibrium module of Binkowski and Shankar (1995). For SOA, a VBS approach (Robinson et al., 2007; Donahue et al., 2009; Bergström et al., 2012) is used. All primary organic aerosol (POA) emissions are treated as nonvolatile to keep emission totals of both PM and VOC components the same as in the official emission inventories, while the semivolatile ASOA and BSOA species are assumed to oxidize (age) in the atmosphere by OH reactions (Simpson et al., 2012).
The generation of sea salt aerosol over oceans is driven by the surface wind, and the EMEP model's parameterization scheme for calculating sea salt generation is based on two source functions, those of Monahan et al. (1986) and Mårtensson et al. (2003). The following natural emissions are calculated in the model for each grid cell and at every model time step: Biogenic emissions of isoprene and monoterpenes use near-surface air temperature and photosynthetically active radiation. Soil NO emissions from soils of seminatural ecosystems are specified as a function of N deposition and temperature. The key parameter driving dust emissions is wind friction velocity. Additionally, daily emissions from forest and vegetation fires are taken from the Fire INventory from NCAR version 1.0

(FINNv1; Wiedinmyer et al., 2011). Emissions of NO_x from lightning are included as monthly averages of global 3-D fields on a T21 (5.65° ×5.65°) resolution (Köhler et al., 1995). For this study, the initial and boundary conditions provided with the open source model distribution for 2015 were used.

The EMEP MSC-W model version used was rv4.34 with chemical mechanism EmChem 19a (Simpson et al. 2012; Simpson et al. 2020). The mechanism builds on surrogate VOC species (as in Simpson et al. 2012, but extended with benzene and toluene) and has 171 gas-phase and heterogeneous reactions. The model always assumes equilibrium between the gas and aerosol phases using the MARS equilibrium module of Binkowski and Shankar (1995). For SOAs a VBS approach is used (Robinson et al. 2007; Donahue et al. 2009; Bergström et al. 2012). The semivolatile ASOA and BSOA species are considered to oxidize (age) in the atmosphere via OH reactions, whereas all POA emissions are treated as nonvolatile to maintain the emission totals of both the PM and VOC components from the official emission inventories (Simpson et al., 2012). The aerosol module of the EMEP model distinguishes five classes of fine and coarse particles (fine-mode nitrate and ammonium, other fine-mode particles, coarse nitrate, coarse sea-salt, and coarse dust); for dry-deposition purposes, these particles are assigned mass-median diameters (D_p), geometric standard deviations (σ_g), and densities (ρ_p). The aerosol components that are taken into account include sea salt, SO_4^{2-}, NO_3^-, NH_4^+, and anthropogenic main PM. Aerosol water is also considered.

4.1.2.5 LOTOS-EUROS

LOTOS-EUROS is an Eulerian chemical transport model (Manders et al., 2017). The model simulates air pollution in the lower troposphere and is of intermediate complexity, allowing ensemble-based simulations and assimilation studies. LOTOS-EUROS performs hourly model output using ECMWF meteorological data. The gas phase chemistry follows the TNO CBM-IV scheme (Schaap et al., 2008).

For sea salt two parametrizations are used for online calculation of emissions, Mårtensson et al. (2003) for fine particles, and Monahan et al. (1986) for coarse particles. Biogenic emissions are calculated online during the CTM run. For isoprene, a tree species-dependent emission factor was used (Schaap et al., 2009; Beltman et al., 2013). NO emissions from soil were calculated as in Novak and Pierce (1993). Dust emissions are also calculated online for three sources of dust. Desert dust following Mokhtari et al. (2012) and road resuspension and dust from agricultural processes following a module developed by Schaap et al. (2009). There is no treatment of NOx lightning in LOTOS-EUROS.

LOTOS-EUROS has a dynamical vertical layer structure with five layers in total. The first layer is at 25 m, while the second layer follows the meteorological boundary layer. On top of that, up to 3500 m and one top layer up to 5000 m above sea level two evenly distributed reservoir layers are defined. The model has participated in multiple model intercomparison studies (Bessagnet et al., 2016; Colette et al., 2017), showing overall good performance.

LOTOS-EUROS uses the TNO CBM-IV scheme, which is a modified version of the original CBM-IV scheme (Whitten et al., 1980). N_2O_5 hydrolysis is described explicitly based on the available (wet) aerosol surface area (Schaap et al., 2004). The aqueous phase and heterogeneous formation of sulfate is described by a simple first-order reaction constant (Schaap et al., 2004; Barbu et al., 2009). Aerosol chemistry is represented using ISORROPIA II (Fountoukis and Nenes, 2007).

4.1.3 CTM deposition mechanisms

The deposition is one major sink for gases and particles in the atmosphere. The deposition mechanisms for dry and wet deposition differ among chemical transport models. For a better

understanding of differences occurring between the models, detailed explanations of the model internal deposition mechanisms are given in the following.

4.1.3.1 Dry deposition

Deposition velocities for gaseous species in CHIMERE, CMAQ and LOTOS-EUROS are based on the formula introduced by Wesely (1989). This formula is the reciprocal sum of aerodynamic resistance (R_a), quasi-laminar sublayer resistance (R_b) and surface resistance (R_c). Nevertheless, all models differ in calculating the single variables. R_a depends on meteorology and surface roughness, which is model dependent. R_b is determined by the friction velocity, depending on the surface type. R_c is the bulk surface resistance, containing different components, i.e., leaf stomata, soil, leaf litter, etc. All of these components use input data that are unique for each model.

In CHIMERE, R_b is estimated following Hicks et al. (1987). The resistance R_c formulation follows Erisman et al. (1994) and the developments made in the EMEP model (Emberson et al., 2000; Simpson et al., 2003; Simpson et al., 2012). It uses a variety of additional resistances, mostly to account for stomatal and surface processes, both of which are depending on the land use type and season. In CMAQ, the "m3dry" mechanism was used, which takes R_a and R_b from the provided meteorological data. R_c is calculated in CMAQ as described in Pleim and Ran (2011).

In EMEP quasi-laminar layer resistance R_b is following Hicks et al. (1987). Surface resistance, R_c Surface (or canopy) resistance is the most complex variable in the deposition model of which the calculation is described in Simpson et al. (2012).The resistance R_b in LOTOS-EUROS is described following the EDACS system (Erisman et al., 1994). In van Zanten et al. (2010), the parametrizations of different resistances R_c that contribute to resistance for dry deposition of NO_2 and O_3 are described, depending on land use type. The Deposition of Acidifying Compounds (DEPAC) 3.11 module was used in LOTOS-EUROS, following the resistance approach (van Zanten et al., 2010; Wichink Kruit et al., 2012).
CAMx uses the gas resistance model of Zhang et al. (2003), which is very similar to the Wesely formulations with regard to R_a and R_b. However, the R_c is expressed as several more serial and parallel resistances, based on Wesely (1989) but with some adjustments within CAMx (Ramboll Environment and Health, 2020).

4.1.3.2 Wet deposition

The CAMx wet deposition model uses a scavenging method in which the local concentration change rate inside or under a precipitating cloud is determined by a scavenging coefficient. From the top of the precipitation profile to the surface, wet scavenging is estimated for each layer inside a precipitating grid column. The scavenging coefficients of gases and PM are calculated differently depending on the correlations given by Seinfeld and Pandis (2006; Ramboll Environment and Health, 2020).
The wet deposition process in CHIMERE follows the scheme proposed by Loosmore and Cederwall (2004).
In CMAQ, wet deposition is calculated in cloud chemistry treatments. The resolved cloud model calculates the contribution of each model layer to the precipitation. Based on a normalized profile of precipitating hydrometeors, CMAQ operates a simple algorithm to assign precipitation amounts to individual layers (Foley et al., 2010).
The EMEP model's parameterization of wet deposition processes covers both the in-cloud and sub-cloud scavenging of gases and particles. The parameterization of wet deposition is described in Berge and Jakobsen (1998).

There are two types of wet deposition in LOTOS-EUROS: below-cloud scavenging and in-cloud scavenging. The technique is described in Seinfeld and Pandis (2006), and Banzhaf et al. (2012) served as the foundation for the in-cloud scavenging module.

4.1.4 Emissions

4.1.4.1 Land-based emissions

Annual anthropogenic land-based gridded emissions for 2015 obtained from the CAMS-REG v2.2 emission inventory were used as input by all five compared models. Gridded emission files contain Gridded Nomenclature for Reporting (GNFR) emission sectors for each country for the air pollutants NO_x, SO_2, NMVOC, NH_3, CO, PM_{10}, $PM_{2.5}$, and CH_4. The emissions are provided at a spatial resolution of 1/10° x 1/20° in longitude and latitude (i.e., ~ 6 x 6 km over central Europe).

The height distribution of emissions per GNFR sector was determined as described in Bieser et al. (2011b). The temporal distribution was determined by separating the annual emissions of each sector into hourly emission data with data splitting as described in Granier et al. (2019). PM was split as described in Bieser et al. (2011a); NO_x was split according to Manders-Groot et al. (2016). NMVOC emissions were given for different sectors, using the GNFR and were separated countrywise. This split was used as provided in the CAMS-REG v2.2 emission inventory (Granier et al., 2019). The species were afterwards split within each CTM according to their chemical mechanism. Information on biogenic emission totals for the whole model domain can be found in Supplements 1, Table S20.

4.1.4.2 Ship emissions

The shipping emission dataset produced with STEAM has a spatial resolution of 10 x 10 km² and a temporal resolution of 1 hour. The STEAM emissions are divided into two vertical layers (0 m to 36 m; 36 m to 1000 m) and are provided for mineral ash, CO, CO_2, EC, NO_x, organic carbon (OC), $PM_{2.5}$, particle number count (PNC), SO_4, SO_x and VOC. VOC emissions were split by FMI into four groups based on their characteristics as a function of engine load to limit the number of produced emission and the computing resources required to run the STEAM model. The VOC groups contain reactive (volatile) VOCs as well as organic compounds of different volatility. VOC emission factors in STEAM are calculated using average values from previous publications (Agrawal et al., 2008; Agrawal et al., 2010; Sippula et al., 2014; Reichle et al., 2015).

In CAMx, all shipping emissions are put in the first layer. For CHIMERE, all shipping emissions above 36 m and 88 % of the emissions below 36 m have been added to the second layer. Only 12 % of the emissions below 36 m were emitted in the first layer of the model. This was calculated based on the STEAM emission dataset and therein contained stack heights. Additionally, in CMAQ, shipping emissions were distributed in the two lowest layers, emissions below 36 m were attributed to the lowest layer, and emissions above 36 m were in the second layer. For EMEP simulations, the STEAM emissions were summed from hourly to daily emissions and attributed to the lowest layer (up to 90 m). In LOTOS-EUROS, emissions below 36 m are assigned ~ 70 % to the first layer, which is 25 m thick, and ~ 30 % to the second layer. Emissions above 36 m are divided over different height classes 30 % between 36 m and 90 m, 30 % between 90 m and 170 m, 30 % between 170 m to 310 m and 10 % between 310 cm and 470 m. Due to the dynamic second model layer (following the meteorological boundary layer), those emissions are put in the second and/or third model layer. In the case of a well-mixed and vertically extended meteorological boundary layer (above 470 m), all

emissions are in this second layer, whereas when the boundary layer is shallow, some emissions are put in the third layer.

4.2 Lagrangian Multicomponent Aerosol FORmation model – MAFOR

The open source MAFOR v2.1.0 model is a zero-dimensional Lagrangian type sectional aerosol box model (Karl et al., 2011; Karl et al., 2022) that combines gas and aqueous phase chemistry as well as aerosol dynamics (available on Github: https://github.com/mafor2/mafor). The mass and composition size distributions of a multicomponent aerosol is produced along an air parcel trajectory. The fixed sectional approach is used in MAFOR to solve the temporal evolution of the particle number and mass concentration distribution. For dealing with continuous nucleation, which is necessary for modeling new particle formation, the fixed sectional approach is computationally efficient and useful (Karl et al., 2020; Karl et al., 2022). The model consists of three basic modules: a chemistry module, an aerosol dynamic module, and a plume dispersion module (Figure 8).

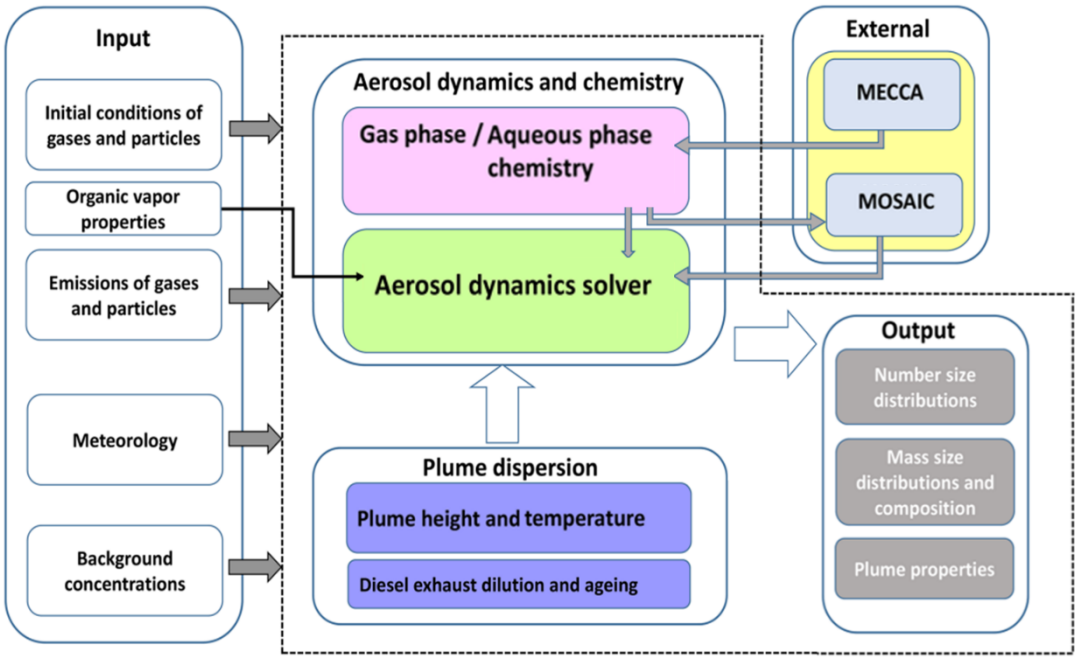

Figure 8: Illustration of the model structure. The dashed outline contains the MAFOR model. External modules are not part of MAFOR. Adjusted from Karl et al. (2022).

The model has three different types of operation. In the present work, the plume dispersion module was activated. This simulation considers a single exhaust plume along one dimension with the evolution of the particle number and mass composition distributions. The transformation of emitted gases, condensing vapors, and particles are treated simultaneously with the dilution with background air (Karl et al., 2022).

The calculation of MAFOR plumes run on a number of required input data that is based on actually measured data. Necessary files contain general data, information on the model configuration, gas phase, emission aerosols, background aerosols, organics and the dispersion. Detailed explanation of the model configuration is given in Sect. 4.2.2. The spatial coordinate in MAFOR is the downwind distance from the ship stack. The ship plume's centerline, which corresponds to the time-averaged wind direction of a Gaussian plume, is followed in time as an air parcel (Karl et al., 2020).

4.2.1 Measurements to initialize a MAFOR run

The MAFOR model run is initialized by using measurement data as input data. The measurements of ship emissions were done on board the Stena Germanica which is a Passenger/Ro-Ro Cargo Ship powered by four-stroke Wärtsilä 8ZAL40S engines with a maximum continuous rating (MCR) of 6000 kW and a nominal speed of 510 rev/min. All primary engines have SCR catalysts and are converted to dual-fuel engines that can run on methanol or regular marine fuels. The initial gases (CO_2, NO, NO_2, SO_2, CO, NH_3) in the ship plume were measured in the ship stack by the Aeromon BH-12 sensor (Nordic Drones, 2023). The measurement device was located in the stack after the catalyst. Measurements were carried out in different sampling phases. These were set by the researchers carrying out the measurement campaign and were depending on the used fuel as well as an appointed engine load during which measurements were taken during the campaign.

Particle number and mass size distribution from the Stena Germanica was measured at a resolution of one second by an Engine Exhaust Particle Sizer (EEPS; size distribution: 6.04 nm – 523.3 nm) as well as Electrical Low Pressure Impactor (ELPI; size distribution of 10.81 nm – 6.3 µm). The measurement point was in the stack after the Selective Catalytic Reduction (SCR) and the sample was diluted with an eDiluter with a dilution ratio of 90 before measuring.

The plume used as base for the aerosol formation model MAFOR was measured in the SCIPPER measurement campaign on 03.09.2021 in Laboe at the Kieler Förde (54.392809, 10.209186; Figure 9). The plume arrived the measurement station at 17:41:37 UTC. The evolution of the plume and the decrease in particle number over time was used to determine the time of plume peak (i.e., when the total concentration is highest; Appendix A1) and the time when only background particles were measured. The wind direction was 284° (± 15° in one hour).

For measuring the particles on shore a Fast Mobility Particle Sizer (FMPS; size distribution: 5.6 nm – 560 nm) was used for small particles. Larger particles were measured by OPS (Optical Particle Sizer; size distribution: 300 nm – 10 µm). The used air intake system for both particle measurement devices was the Sampling System for Atmospheric Particles from TSI for particles up to 10 µm.

Gases and meteorological parameters were measured at the station at Laboe close to Kiel with an airpointer 4D measurement system for NO_x, O_3, SO_2 and a weather station. The peak of measured NO_x concentrations after the passing of the ships are shown in Appendix A2.

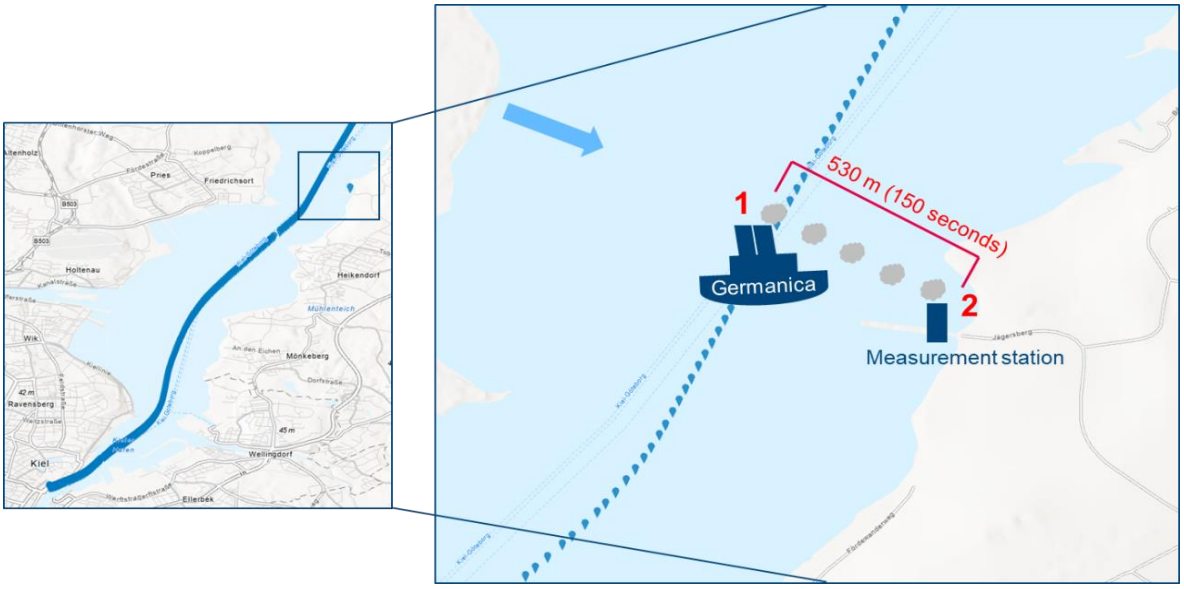

Figure 9: Shipping lane (blue dots), measurement station (single blue dot) and the direction of wind (blue arrow) from 283.5. The distance from the ship lane to the point of measurement is 530 m.

4.2.2 Input data and model configuration

The model relies on a number of input data files that include general data (meteorological data, time and location), configuration (processes that are used in the model), initial aerosol size distribution (in terms of mass) gas phase (Concentration), emission and background aerosols (particle mass concentration), organics (properties of the organic vapors) and dispersion (plume dispersion parameterization). The gas measurements and meteorology data obtained at the measurement station on shore were used in the MAFOR and defined the air parcels trajectory. The following processes were considered in the MAFOR run:

Dry deposition over water surface (Schack et al., 1985), nucleation, condensation of organics and of water and coagulation. The coagulation of particles was considered by Brownian coagulation process. The dilution of the plume into the background air with low particle concentration was done with the dispersion of ship plumes under convective conditions in the open sea. This dispersion is based on the parameterization by Chosson et al. (2008) and a plume height approximation following a formulation of von Glasow et al. (2003).

The dispersion was verified by plotting the dilution against measured data in and on the stack, measurements at the Sniffer station and in background air. Starting concentrations for H_2SO_4 in the stack were set according the concentrations received from Karl et al. (2020), with a value of 0.17×10^{11} cm^{-3}. The consideration of H_2SO_4 is of importance as it is important for atmospheric nucleation (Kulmala et al., 2004).

The emission factor (EF) of NO_x was measured on board in the exhaust stack and was used to calculate the EF for other gases. The measurements were too close to the emission source for the MAFOR model to start (it starts usually 1 second after the plume left the stack), therefore a dilution ratio for the gases of 1:8 was used as described in Karl et al. (2020).

The SOA concentrations are simulated using a hybrid method of condensation/evaporation and absorptive partitioning into an organic liquid (according to Kerminen et al., 2000) and using a 2-D VBS set (Donahue et al., 2011) consisting of nine organic compounds with different volatility.

To start the MAFOR simulation, the particle mass initial at the stack was calculated from the measured particle number size distribution. For this, the particles in sizes from 6.04 nm to 523.3 nm measured by EEPS (32 bins) and larger particles with size from 764.4 nm to 6.3 µm (4 bins) measured by ELPI were used. The resulting 36 bins were assigned to the four modes in MAFOR (NU: nucleation mode, AI: Aitken mode, AS1: accumulation mode 1, AS2: accumulation mode 2) and the mass was calculated as sum within those by assuming a density of 1.0 g/cm^3. The fourth mode is rather a second accumulation mode than a coarse mode; therefore, it was divided into a first and second accumulation mode. Emissions in the MAFOR model are mass-based and are subsequently converted to number by using assumptions on their densities (Karl et al., 2022). The median of 366 particle number and mass measurements on 03.09.2021 between 17:49:00 UTC to 22:54:30 UTC was calculated for each bin as input data for the ship plume aerosol. The received measured aerosol mass was transferred into a MAFOR input file that provides the initial aerosol size distribution. The total aerosol mass concentration is divided into the four modes (NU, AI, AS1, AS2). The aerosol initial mass composition is subsequently converted to a number based on the material densities of the different aerosol components, assuming spherical particles to ensure consistency in terms of mass and number (Karl et al., 2022). The calculation of particle number and mass concentrations in the model is then done using a sectional size representation of the aerosol. The chemical composition was based on a former observation for the Stena Germanica (Timonen et al., 2022). The total mass was divided into H_2SO_4, OC, NH_4, NO_3, Methane Sulfonate (MSAp), salt, primary organic material (POA), EC and ash.

For background aerosols, the particle mass calculated from particle number was used. The particle number size distribution was received from FMPS and OPS devices situated on shore. To avoid any influence of ship emissions, the median of measured particle number size distribution of half an hour before arrival of the plume was calculated for the background aerosol data. The distribution of the plume aerosol mass and background aerosol mass in the four modes is displayed in Table 3. The mass was distributed to fit the particle number distribution of the respective measurement.

Because of multicomponent condensation and particle coagulation, the composition of particles in the size bins may vary over time. MAFOR calculates rapid changes of the aerosol size distribution every 0.1 second. The simulation of the ship plume starts one second after release from the ships stack. The distance from the stack to the measurement station was 530 meter (corresponding to 150 seconds travel time of the ship plume).

Table 3: Mass distribution for background and ship aerosols; Mass is displayed in ng/m³; MSAp = (Methane Sulfonate); PBA = Primary biological material; v = volatile; nv = non-volatile; modes: NU= Nucleation (Dp < 10 nm); AI = Aitken (10 nm < Dp < 50 nm); AS1 = Accumulation 1 (50 nm < Dp < 500 nm); AS2 = Accumulation 2 (> 500 nm).

MODE	Dp (m)	SIG	H_2SO_4	OC	NH_4	NO_3	MSAp	SALT	PBA	EC	ASH	MTOT
			v	v	v	v	v	nv	nv	nv	nv	
BACKGROUND AEROSOL												
NU	9.90E-09	1.70	0.001	0.002	0	0	0	0	0	0	0	0.0025
AI	2.3E-08	1.52	0	0	0	0	0	0	0	0	0	1.38
AS1	1.0E-07	1.75	5	4	3	3	0	1	0	4	3	22.953
AS2	7.0E-07	2.10	14	11	7	7	0	3	0	12	7	60.59
SHIP AEROSOL												
NU	9.6E-09	1.65	0	0.026	0	0	0	0	0.011313	0	0	0.05
AI	1.5E-08	1.35	283	989.9	57	38	0	0	424.2393	94.3	0	1885.51
AS1	1.3E-07	1.75	1206	3657	241	161	0	0	1567.472	563	643	8038.32
AS2	7.5E-07	2.10	10726	32535	0	0	0	0	13943.78	3575	10726	71506.55

4.3 Model evaluation and analysis

4.3.1 Evaluation of regional scale CTM systems

4.3.1.1 Analysis of model results

Model results for total surface concentrations of NO_2 and O_3 from the five CTMs were evaluated against available measurements of the air quality monitoring network taken from the download service of Air quality of the European Environment Agency EEA (https://discomap.eea.europa.eu/map/fme/AirQualityExport.htm, accessed: 01.03.2021). NO_2 concentrations were monitored at 62, O_3 at 48 and $PM_{2.5}$ at 28 background stations. Figure 7 shows the locations of the measurement stations, and detailed information on the stations is given in Appendix B.

The stations were chosen based on the following criteria: i) the station type was "background," ii) the station elevation was less than 1000 meters, and iii) the station recorded data for more than one of the following pollutants: NO_2, O_3, or $PM_{2.5}$. Since simulating the potential impact of ships was the main focus of this work, stations near the sea were preferably chosen. There was no exact threshold of distance to the coastline assumed, but preferably stations at a distance < 30 km from the coast were chosen. Some stations further inland were chosen to check the model performance. Furthermore, the domain was divided into four parts for the analysis of NO_2 and O_3 (“west”, “north”, “south”, “east”), and a roughly equal number of stations should be in each parcel (map in Supplements 1, S2). The measured concentrations at the stations were compared against the results of simulations of the CTMs. For this purpose, the grid cell of the respective monitoring station was determined, and modeled concentrations were taken from there.

To compare the predicted daily mean concentrations to the measurements recorded at representative sites, time series were employed. In addition, based on hourly data, the yearly mean potential ship impact was determined. Boxplots based on yearly values obtained from hourly data at each station were used to graphically compare the model performances using the statistical analysis as described in Sect. 4.3.1.2. Annual mean values based on hourly data were utilized for the intercomparison maps. Based on hourly data, the correlations between models were determined for each grid cell.

4.3.1.2 Statistical Analysis

To prove that a model performs well, model output data are statistically analyzed. This often means that the output data are compared with observational data with statistical measures. These are in the presented studies the normalized mean bias (NMB), root mean square error (RMSE) and correlation (R). To compare the simulated model outputs from the different CTMs the correlation between the each grid cell for the annual mean values was calculated.

The statistical measures are defined as follows:

$$\mathrm{NMB} = \frac{\sum_1^n (M-O)}{\sum_1^n (O)} \qquad \text{(Eq. 4.1)}$$

$$\mathrm{R} = \frac{1}{(n-1)} \sum_1^n \left(\left(\frac{O-\overline{O}}{\sigma_o} \right) * \left(\frac{M-\overline{M}}{\sigma_m} \right) \right) \qquad \text{(Eq. 4.2)}$$

$$\text{RMSE} = \sqrt{\frac{\sum_1^n (M-O)^2}{n}} \quad \text{(Eq. 4.3)}$$

Where *M* and *O* stand for model and observation results, respectively. The time average is indicated over n time intervals (number of observations). The time average is done for one year.
NMB is the measure of normalized variables that may be used to compare scores from time series of varying durations, such as those created over various locations and time spans.
R is a measure of associativity that permits determining if trends are caught and is not biased.
RMSE is a measure of accuracy and allows prediction errors of different models to be compared for a particular dataset.
A categorization scheme for the correlations was established as described in Schober et al. (2018), with weak (0.00-0.39), moderate (0.40-0.69) and strong (0.70-1.00) correlations.

4.3.2 Evaluation of MAFOR model output

4.3.2.1 Comparison simulated against measured data

The comparison between modeled and measured data was done by comparing particle number concentrations and mean diameter for different size classes on which the measured and the modeled bins were mapped. These classes were set following the size distribution classification for the urban case presented in Karl et al. (2022) by adapting the modeled size distribution with the size classes (bins) of the measured size distribution. The result were classes in the ranges S1:1-10 nm; S2: 10-20 nm; S3: 20-50 nm; S4: 50-100 nm; S5: 100-300 nm; S6: 300-600 nm; S7: > 600 nm. The mean diameter of each size class was calculated as follows:

$$\overline{d_n} = \frac{\sum_i (N_i \cdot d_i)}{\sum_i N_i} \quad \text{(Eq. 4.4)}$$

where d_n denotes the mean diameter per size class, N_i is the number of particles, and d_i is the midpoint of the size class; index i is running over the size bins.

4.3.2.2 Ship emissions and VOC emission factor scaling

The ship emission dataset received from STEAM (see Section 4.1.4.2) was taken as base for the ship emissions adjustments.
The initial VOC emission factor for input in MAFOR is based on the VOC EF received from a previous Stena Germanica model run (Timonen et al., 2022).
The approach to receive a new VOC EF is presented in Fig. 10. The NO_x emission factor $NO_x\ EF_{new}$ was the only EF received for the present measurements. Therefore, a changing factor for all emission factors (EF_{all}) was calculated based on the initial NO_x EF (Eq. 4.5). The initial $VOC\ EF_{init}$ from the previous Stena Germanica model run was multiplied with the changing factor CF_NO_x (Eq. 4.6):

$$CF_{NO_x} = \frac{NO_x\ EF_{new}}{NO_x\ EF_{init}} \quad \text{(Eq. 4.5)}$$

$$CF\_NO_x * VOC\ EF_{init} = VOC\ EF_{new} \quad \text{(Eq. 4.6)}$$

The particle size distribution obtained from MAFOR simulations for the plume at the sniffer site for VOC was evaluated by comparing against the measured particle size distribution and mean diameter, as described in Sect. 4.3.2.1 (Eq. 4.4).

Calculations with different scenarios were carried out to investigate changes in the model performance in connection with the change in VOC emission factor (Sect. 5.3.3 Table 14). This was done because no VOC EF was available for the present plume and it can be assumed that the changes in the NO_x EF are not the same magnitude as the changes in the EF for VOC. The scenarios contained the newly calculated *VOC* EF_{new} multiplied with a correcting factor *CF*:

$$VOC\ EF_{new} * CF\ =\ VOC\ EF_{new,corr} \qquad \text{(Eq. 4.7)}$$

The sensitivity cases are named after the used correction factor (i.e. 0.9 means *VOC* EF_{new} * 0.9) and range from 0.5 to 2.0. With changing VOC EF the size distribution of particles changes. With higher VOC EF, there will be more larger particles, which are formed primarily by the growth of smaller particles through condensation. The particle number size distribution computed by MAFOR was compared to the measurement results. The modeled particle number size distribution was divided into seven size classes (described in Sect. 5.3.3).
The best fitting CF value was chosen for the size classes S2 - S5 by calculating the sum of absolute differences between MAFOR simulations to measurements (Table 14, Sect. 5.3.3). These size classes were chosen, since they contain the most reliable values. The optimal CF is the value where the sum of absolute relative differences is lowest. The *VOC* $EF_{new,corr}$ with the lowest deviation from simulations to measurements serves as a base for comparison with the EF used in STEAM.

The emission factors for VOCs from MAFOR were obtained from Stena Germanica with 50 % engine load. Since the aim was to derive a new VOC emission factor for the STEAM emission dataset, the EF used in STEAM for VOCs for vessels at 50 % engine load had to be related to the EFs for VOCs that were found in the optimization procedure using MAFOR (i.e., *VOC* $EF_{new,corr}$). The ratio between the two emission factors was calculated and the STEAM ship emissions for VOCs were adjusted by this factor *f_STEAM* for the CMAQ run:

$$\frac{VOC\ EF_{new,corr}}{VOC\ EF_{STEAM}} = f\_STEAM \qquad \text{(Eq. 4.8)}$$

The STEAM data was used as ship emissions and for the comparison run with the regional scale chemical transport model CMAQ, which is described in detail in Sect. 4.1.2.3.

CMAQ ran two simulations: one run was carried out with the ship emission data as provided by STEAM and a second run was performed with the ship emissions of the VOC groups adjusted by the adjustment factor derived from MAFOR.

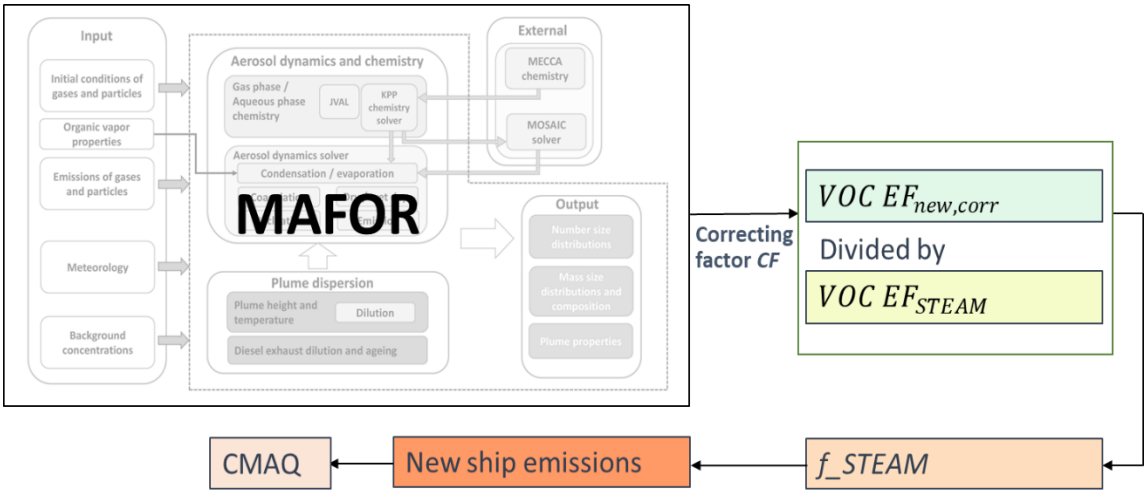

Figure 10: Approach of receiving ship emissions with adjusted VOC emission factors.

5 Results & Discussion

5.1 Publication I: Potential impact of shipping to air pollution in the Mediterranean region – a multimodel evaluation: Comparison of photooxidants NO_2 and O_3

The following chapter corresponds to results and discussion in the publication of the same name authored by:

Lea Fink, Matthias Karl, Volker Matthias, Sonia Oppo, Richard Kranenburg, Jeroen Kuenen, Sara Jutterström, Jana Moldanova, Elisa Majamäki, Jukka-Pekka Jalkanen

and published in Atmospheric Chemistry and Physics (ACP):

Potential impact of shipping on air pollution in the Mediterranean region – a multimodel evaluation: comparison of photooxidants NO_2 and O_3, Atmos. Chem. Phys., 23, 1825–1862, https://doi.org/10.5194/acp-23-1825-2023, 2023.

The Supplements, which are referred to in the Sect. 5.1 are indicated as "Supplements 1" and attached to this thesis as well as accessible under:

Supplement of Atmos. Chem. Phys., 23, 1825–1862, 2023 https://doi.org/10.5194/acp-23-1825-2023-supplement

In the following, the results for NO_2 and O_3 model performance and spatial distribution will be shown. Afterward, O_x and NO_x will be displayed for a more detailed investigation of the photochemistry and lifetime of the species. The results of dry deposition of NO_2 and O_3 will be considered in Sect. 5.1.4.

5.1.1 Model Performance and Intercomparison

To evaluate the performance of the CTMs, simulated concentrations considering all emission sectors (base case) for annual values of 2015 were compared against measured data of NO_2 and O_3. Based on the results of the five models for the cases with (base case) and without shipping emissions (noship case), potential impacts of the shipping sector to the NO_2 and O_3 concentrations were estimated. Figures of spatial distribution display the annual mean values for 2015 and the potential relative ship impacts. With this setup, the model performance and potential ship impact of the different models can be directly compared.

5.1.1.1 NO_2 Model Performance

Table 4 contains R, NMB and RMSE based on the annual time series for NO_2 at all stations. The highest correlation across all 62 stations showed LOTOS-EUROS followed by CMAQ with a slightly lower correlation (LOTOS-EUROS: R = 0.45; CMAQ: R = 0.42), whereas for CHIMERE, EMEP and CAMx, no to weak correlation was found (R = 0.08 to R = 0.10). The NMB suggests that all five CTMs underestimate the annual mean concentrations at most measurement sites; the NMB for all

stations is negative for all models. The RMSE is within the same range for all models (RMSE = 15.6 µg/m³ to 19.5 µg/m³; Table 4).
Time series for three example stations show the temporal variations between measured and modeled data (Appendix C). The supplements provide an overview of the mean values of stations in each map parcel ("west", "north", "south", "east"; Supplements 1, S2). Fig. C1 displays a time series at an urban background station in France (fr08614, "Gauzy", latitude: 43.8344, longitude: 4.374219), which was chosen because southern France will be investigated in greater detail as part of this study. Fig. C2 shows a rural background station in Italy (it1773a, "Genga – Parco Gola della Rossa", latitude: 43.46806, longitude: 12.95222), which was chosen due to its central location in the domain and the high number of stations in Italy. Fig. C3 displays the time series at a station in Greece (gr0035a, "Lykovrysi", latitude: 38.06963, longitude: 23.77689) to include a station in the eastern part of the domain.
Measurements at the French station show the highest NO_2 values in winter, with peaks between 40 µg/m³ and 55 µg/m³ (Figure C1). LOTOS-EUROS and EMEP underestimate the values throughout the year. Moderate correlation was calculated for CMAQ (R = 0.6) and LOTOS-EUROS (R = 0.65) at this station. The simulated ship impact has annual mean values from 0.2 µg/m³ (EMEP, CAMx) to 0.6 µg/m³ (CMAQ) at station fr08614. Shipping emissions have a potential relative impact between 1.8 % (EMEP) and 6.7 % (CMAQ) to the total concentration in the annual mean. The highest potential ship impact at this station was modeled by CMAQ. At the Italian station, 1773a lower NO_2 concentrations were measured compared to the station in France. The highest peaks are approximately 20 µg/m³ in winter. At station it1773a, the potential ship impact to the total NO_2 concentration has annual mean values between 0.07 µg/m³ (LOTOS-EUROS) and 0.5 µg/m³ (CAMx). The highest relative potential ship impact was 7.9 % and was modeled by CAMx. At station gr0035a, the lowest simulated values are shown by CMAQ and LOTOS-EUROS. The highest values display EMEP at this station, also with the highest correlation between measured and simulated data (R = 0.55). The potential ship impact at the Greek station is between 5.0 % (EMEP) and 15.3 % (CAMx), which is higher than the potential ship impact at the other two stations.
All CTMs underestimate the observed total NO_2 values at both stations, except for LOTOS-EUROS in Italy. None of the models is able to model matching peak values. Neither at the station in France, Italy nor Greece models showed seasonal variation in concentrations, whereas NO_2 usually has higher values in winter and lower values in summer, mainly because of lower photolytical degradation and suppressed vertical mixing, as described, i.e., in Ordóñez (2006).
Differences in potential ship impacts between the stations are caused by the location and station type (fr08614 = urban background; it1773a = rural background; gr0035a = suburban background). At the French station, the traffic-related NO_2 concentration might supersede the ship-related NO_2. The station in Italy is not located in a city, so the NO_2 concentration caused by ships comes to the fore. The highest potential ship impact was simulated at the station in Greece because it is suburban but close to the Port of Piraeus, which is one of the largest ports in the Mediterranean Sea. As expected, the average potential ship impact is low at stations that are not directly located at the coast or to a harbor.
To compare the correlation R, NMB and RMSE at all measurement stations for all models, the results of the comparison are divided by country and displayed in boxplots (Figure 11). Each dot displays one measurement station. The correlation measured against the simulated annual mean NO_2 is highest for LOTOS-EUROS and CMAQ in all countries, reflecting the results shown in Table 4 for correlation. Nevertheless, boxplots for NMB and, in particular, for RMSE visualize that differences among countries are larger than differences among the models (Figure 11 b, c). This means that all

models show good or bad performance at some stations, which was not found to be statistically relevant.

Underestimations by models of NO_2 at urban sites were found in other studies (Karl et al., 2019a; Giordano et al., 2015), despite differences in grid size. Karl et al. (2019a) used a grid resolution of 4 km, and Giordano et al. (2015) used a grid resolution of ~ 0.25° (27 km to 28 km). The underestimation might be due to too low emissions in the inventory used by the models and the heterogeneity of emissions. Regional CTMs cannot display small-scale spatial heterogeneity; coarse grid cells are not representative of the measurement location. Giordano et al. (2015) suggested in their study that the underestimation of NO_2 could be caused by either an underestimation of the chemical lifetime of NO_x, excessively high dry deposition, an underestimation of natural emissions at rural and remote stations or a combination of these factors. Differences in radical concentrations and reactive nitrogen might be additional reasons for underestimation (Knote et al., 2015).

The model performance of NO_2 has shown that differences in time series between the models occur, caused by the differences in meteorology and large grid size. Large grid sizes can cause errors insofar as in simulations the land areas are not seen as such but as water areas. This is especially problematic when having measurement stations located close to the sea.

Table 4: Correlation (R), normalized mean bias (NMB), root mean square error (RMSE), observational (obs) and simulated (sim) mean values of NO_2 for 2015: first data were averaged station wise and then averaged for all 62 stations.

	R	NMB	RMSE (µg/m³)	sim (µg/m³)	obs (µg/m³)
CAMx	0.08	-0.32	19.5	8.1	
CHIMERE	0.10	-0.52	18.5	5.8	
CMAQ	0.42	-0.56	17.3	6.7	16.6
EMEP	0.10	-0.40	18.8	7.1	
LOTOS-EUROS	0.45	-0.52	15.6	7.6	

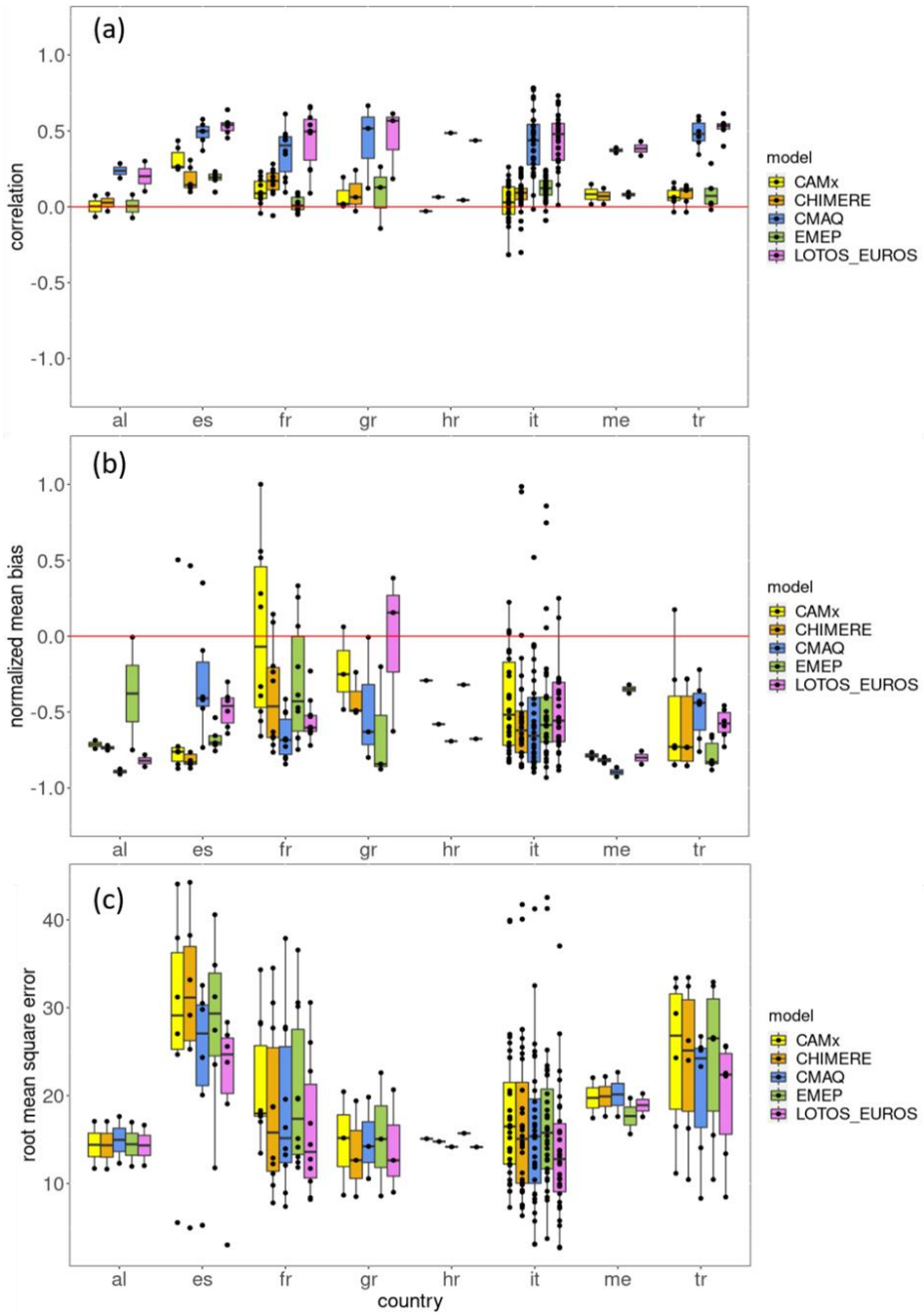

Figure 11: (a) = Correlation, (b) = NMB, (c) = RMSE for annual mean NO_2 concentration based on hourly data. Dots display annual mean values at measurement stations for the respective countries (al = Albania; es = Spain; fr =France; gr = Greece; hr = Croatia; it = Italy; me = Montenegro; tr = Turkey). Boxplots are for the models with the boxes displaying the interquantile range (IQR) between the 25th (Q1) and 75th (Q3) percentile, the black line displays the median (Q2), whiskers are calculated as Q1–1.5*IQR (minimum) and Q3 + 1.5*IQR (maximum).

5.1.1.2 NO_2 Spatial Distribution

The simulated annual mean NO_2 concentrations considering all emission sectors are similar for all CTMs, with most values between 0.0 µg/m³ and 2.0 µg/m³ (Figure 13). CAMx and CHIMERE have the largest areas, with values exceeding 5.0 µg/m³, especially along the main shipping routes and in urban areas. The CMAQ, EMEP and LOTOS-EUROS figures look similar, which is in good agreement with the displayed time series in Sect. 5.1.1.1., where the results are within the same range. Over land area, all model simulations display a concentration pattern ranging within one order of magnitude. Nevertheless, the frequency distributions of the CMAQ, EMEP and LOTOS-EUROS simulations show the highest frequency between 1.0 µg/m³ and 2.0 µg/m³, whereas for CAMx and CHIMERE, they are more equally distributed. Higher values of NO_2 concentrations simulated by CAMx and CHIMERE might indicate a longer lifetime of NO_2 in the atmosphere. NO_2 reacts quickly with hydroxyl radicals (OH) and forms HNO_3, or NO_2 photolysis creates O_3 during the daytime. The annual mean HNO_3 concentrations are between 2.0 µg/m³ to 5.0 µg/m³ for CAMx and CHIMERE over water areas and are 0.8 µg/m³ to 2.0 µg/m³ over water areas for CMAQ, EMEP and LOTOS-EUROS (Supplements 1, S11). Over land areas, the HNO_3 concentrations are within one range for all models. A lower HNO_3 concentration is expected for CTMs with longer lifetime of atmospheric NO_2. Nevertheless, there can be a misinterpretation when both concentrations are high. Therefore the data was normalized by using the HNO_3:NO_2 ratio (Supplements 1, S12). Especially along the main shipping routes differences are displayed. There, values are lower in CAMx and EMEP compared to the other models. This can be explained by the lower HNO_3 formation by these models along the shipping routes.

Also the meteorology might influence the vertical mixing of NO_2. This leads to differences between the models or explains the similarity between CAMx and CHIMERE due to the usage of the same meteorology. Nevertheless, this point will not discussed here in detail since in the present study only the lowest layer was considered and the vertical mixing processes were not evaluated.

The correlation between the models for total NO_2 concentration was calculate based on hourly data (Table 5). The highest correlation was found between CAMx and CHIMERE (R = 0.80). Weak correlations were found between LOTOS-EUROS and CAMx (R = 0.31) and LOTOS-EUROS and CHIMERE (R = 0.36). This weak correlation is due to the differences in frequency distribution, with LOTOS-EUROS showing most values below 1.0 µg/m³, whereas for CAMx and CHIMERE, more values are located in the higher value ranges. Overall, the models can give a robust estimate regarding the base run of the annual mean of NO_2.

The highest potential impact of ships to total NO_2 concentrations was found at the main shipping routes, with values > 85 % (Figure 14). Similar values were found for the Baltic Sea (Karl et al., 2019a) and for the Iberian Peninsula (Nunes et al., 2020). CHIMERE and CAMx model the highest values over the sea region, with a potential ship impact to NO_2 between 60 % and 85 %. CMAQ, LOTOS-EUROS and EMEP have similar patterns for ship impacts over the sea.

On the Mediterranean coastline, CMAQ, CHIMERE, LOTOS-EUROS and EMEP simulate a similar potential impact, with 25 % to 45 % potential ship impacts to total NO_2. Merico et al. (2017) found similar results in a study with NO_2 shipping impact up to 32.5 % regarding four port-cities in the Adriatic-Ionian Sea. CAMx reveals a higher impact with > 85 % at the coastline. The potential ship impact displayed in the time series in Sect. 5.1.1.1 was lower, although the measurement stations were not far from the coast. This shows that although the potential impact from ships reaches regions far from the coast, the highest impact is over the sea area. The frequency distribution for the relative ship impact shows that all models simulate most values between 0 % and 5.0 % of the ship potential impact. Interestingly, the distribution is lowest at values between 20 % and 40 % (CMAQ, EMEP,

LOTOS-EUROS) and 60 % (CAMx, CHIMERE) and then increases again at higher values, showing a bimodal distribution. This is due to large areas with high potential impacts over water and large areas with low potential impacts over land or near harbors.
Over land in the northeast area of the domain, slightly negative potential ship impacts are derived from the CMAQ, CAMx, LOTOS-EUROS and EMEP results. CHIMERE shows only very few negative values, but in the same region. Negative potential ship impacts to NO_2 concentrations may arise when the zero-out method is applied. They are a consequence of the nonlinear NO_x gas phase chemistry. Especially in areas where the impact of NO_x emissions from shipping is very low, less NO oxidation takes place because the additional NO from shipping in other areas already consumed the oxidants (e.g. O_3).
The boxplots in Fig. 12 display the annual mean values for the whole model domain of NO_2. Model results vary for the base run but also for the potential ship impact. This variability needs to be taken into account when the predictive power of CTMs is considered. The “all_mean” boxplot displays the mean of all models and displays that in comparison with other models, CAMx has high values. It further helps to show which CTM tends to simulate higher or lower values compared to others. The “all_mean” boxplots show similar ranges as boxplots for CMAQ and EMEP, particularly regarding absolute and relative potential ship impacts. Additionally, models simulating a higher overall concentration of pollutants also tend to simulate a higher potential ship impact. The relative potential ship impact is highest for CAMx and CHIMERE and lowest for LOTOS-EUROS.

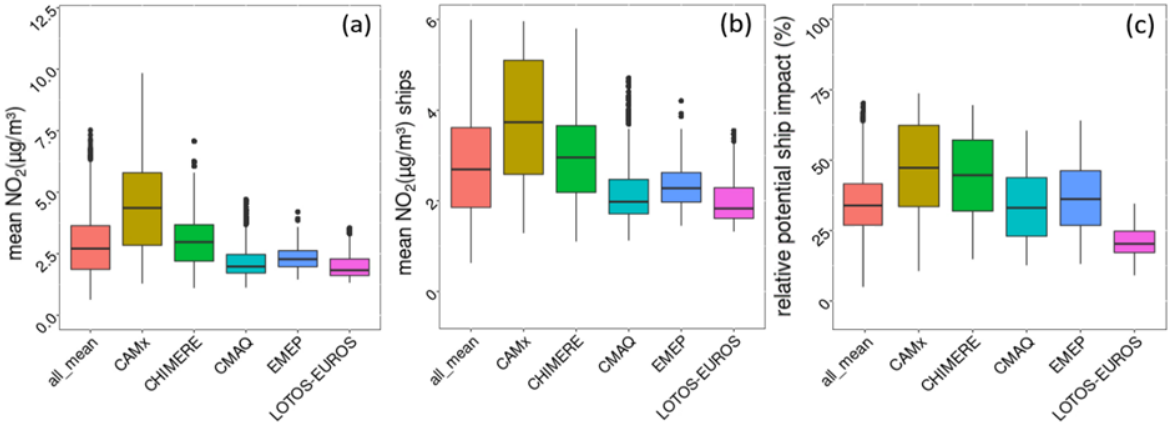

Figure 12: Annual mean for all grid cells in the whole model domain. (a) = mean NO_2 for all emission sectors (base case), (b) = mean NO_2 for shipping only, (c) = relative potential ship impact to total NO_2 concentration. All_mean is the mean value of all models, with a median of (a) = 2.8 µg/m³, (b) = 0.7 µg/m³ and (c) = 27.7 µg/m³.

Table 5: Correlation for the NO_2 base run between models for the whole domain (all grid cells), based on hourly data for NO_2 total concentration.

all	CAMx	CHIMERE	CMAQ	EMEP	LOTOS-EUROS
LOTOS-EUROS	0.31	0.36	0.71	0.73	-
EMEP	0.39	0.44	0.73	-	
CMAQ	0.39	0.43	-		
CHIMERE	0.80	-			
CAMx	-				

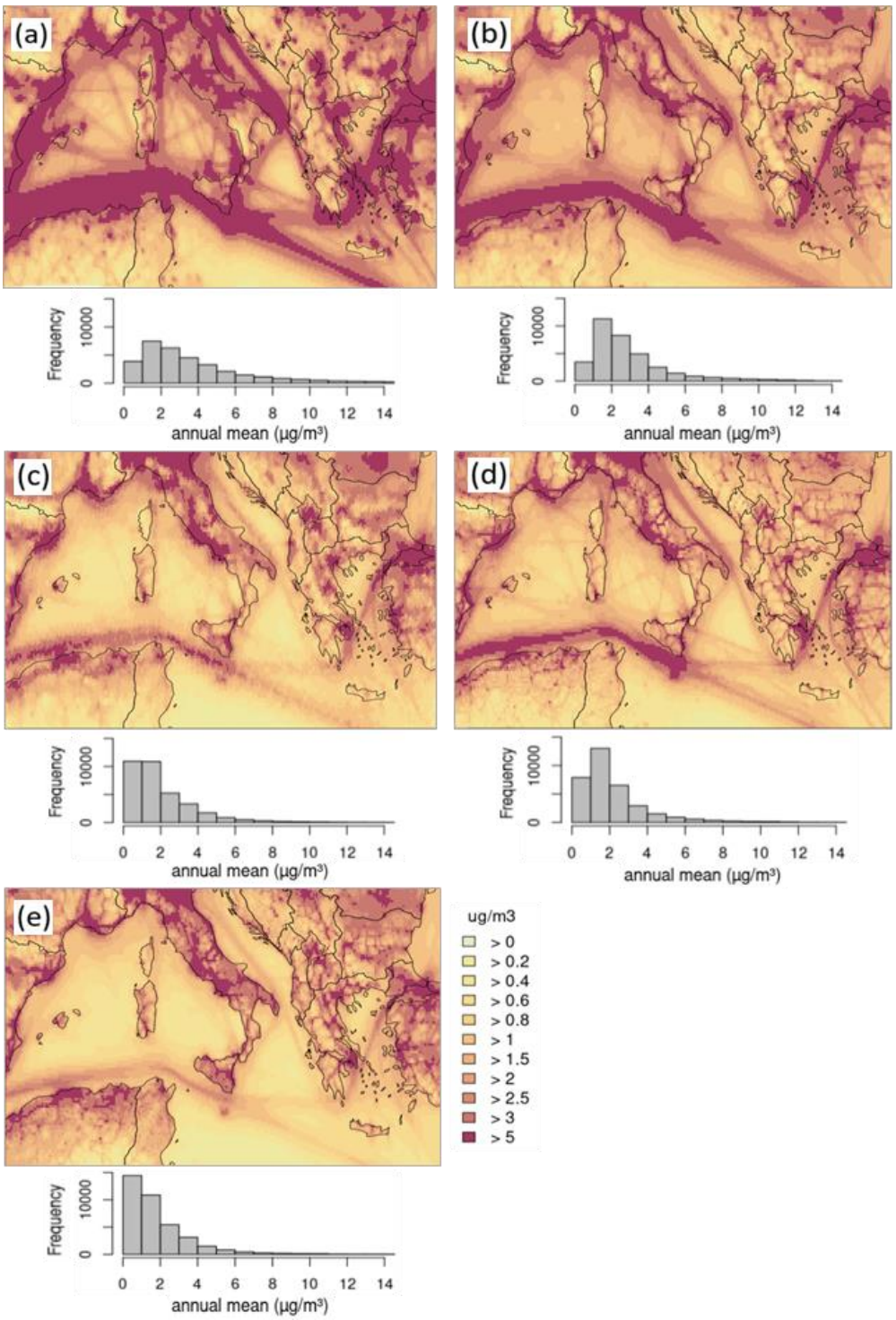

Figure 13: Annual mean NO_2 total concentration. (a) = CAMx, (b) = CHIMERE, (c) = CMAQ, (d) = EMEP, (e) = LOTOS-EUROS. Below the domain figure is the respective frequency distribution displayed for the annual mean NO_2 concentration, referred to the whole model domain.

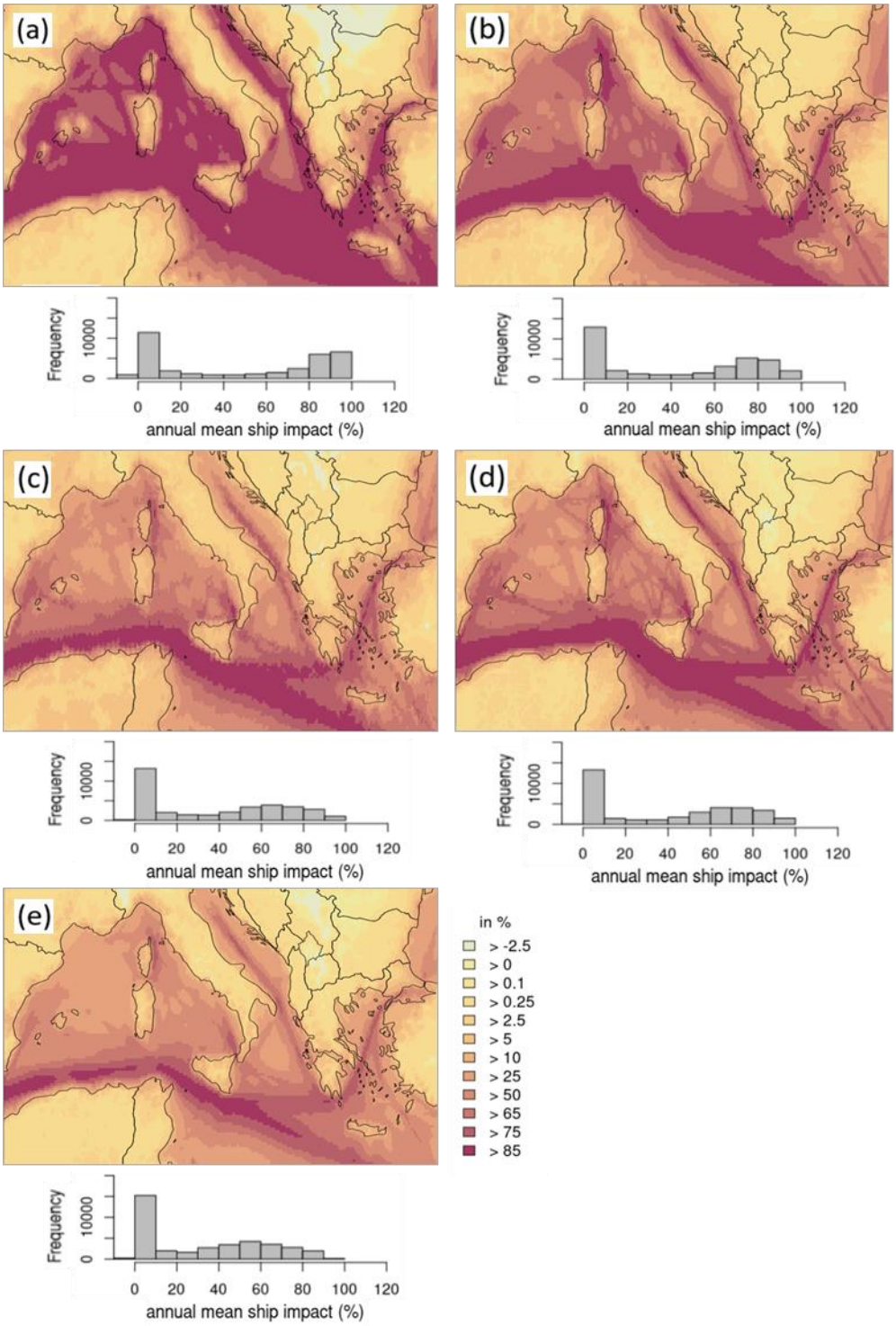

Figure 14: Annual mean NO_2 potential ship impact. (a) = CAMx, (b) = CHIMERE, (c) = CMAQ, (d) = EMEP, (e) = LOTOS-EUROS. Below the domain figure is the respective frequency distribution displayed for the annual mean NO_2 potential ship impact, referred to the whole model domain.

5.1.1.3 O_3 Model Performance

The tropospheric O_3 concentrations are strongly connected to the NO_2 concentration and to the oxidized nitrogen chemistry in the atmosphere. O_3 can be both an initiator and a product of photochemistry; thus, it is crucial in tropospheric chemistry.

Simulated versus measured data of one year daily mean O_3 time series show a weak (EMEP: R = 0.38) to moderate correlation (CAMx: R = 0.40; CHIMERE: R = 0.47; CMAQ: R = 0.60; LOTOS-EUROS: R = 0.69; Table 6).

Selected time series represent these differences in correlation (Appendix D). Nevertheless, for the first months of the year CHIMERE, CAMx and CMAQ overestimate the measured O_3 values (Figure D1: station fr08614; Figure D2: station it1773a; Figure D3: gr0035a).

During summer months, O_3 shows the highest values due to increased photochemical activity. The simulated potential ship impact is between 1.1 µg/m³ (CAMx) and 2.8 µg/m³ (LOTOS-EUROS) at station fr08614 and has a relative potential impact between 1.3 % (CAMx) and 4.0 % (CHIMERE) to the total concentration. At station it1773a, the mean O_3 potential ship impact is between 1.0 µg/m³ (CAMx) and 3.0 µg/m³ (CHIMERE), and the relative potential impact ranges from 1.1 % (CAMx) to 3.5 % (LOTOS-EUROS). The potential ship impact of station gr0035s ranges from -0.1 µg/m³ (CAMx) to 3.7 µg/m³ (CMAQ; LOTOS-EUROS), which is a relative potential impact of -0.1 % (CAMx) and 3.7 % (CMAQ).

The O_3 potential ship impact is within the same range at both stations and for all five CTMs. Fig. 6 shows that CMAQ has the smallest bias compared to the other models (NMB = 0.28), followed by LOTOS-EUROS (NMB = 0.36). The RMSE is lowest for CMAQ (RMSE = 31.2 µg/m³) and LOTOS-EUROS (RMSE = 32.6 µg/m³), along with the lower NMB compared to the other models. The performance analysis revealed that all five models predict higher O_3 concentrations than those measured at almost all stations (NMB > 0). The overestimation of observed O_3 by the models is in line with results from previous studies (Karl et al., 2019a; Appel et al., 2017; Im et al., 2015a; Im et al., 2015b). Im et al. (2015a) showed that O_3 concentrations above 140 µg/m³ are underestimated, while concentrations below 50 µg/m³ are overestimated by 40 % to 80 % in all considered models. This overestimation of O_3 by the models is likely linked to the chemical boundary conditions used in the regional CTMs. Analyses of the boundary conditions revealed that, especially in winter, O_3 levels are mostly driven by transport instead of local production due to limited photochemistry (Giordano et al., 2015).

CHIMERE uses boundary conditions from monthly mean climatologies simulated with the LMDz-INCA model, CAMx uses Mozart-4 output, LOTOS-EUROS and CMAQ use IFS-CAMS reanalysis data and the EMEP model uses ozone boundary conditions provided with the open source model distribution for 2015. These differences in input for the boundary conditions can be seen as the reason for the varying results in O_3 (Supplements 1, S13-S16).

All CTMs performed relatively well and are able to represent the course of the year, with higher values in summer and lower values in winter. Nevertheless, in some cases, the values in spring are overestimated.

Table 6: Correlation (R), normalized mean bias (NMB), root mean square error (RMSE), observational (obs) and simulated (sim) of O_3 as the mean values for 2015: the first data were averaged station wise and then averaged for all 48 stations.

	R	NMB	RMSE (µg/m³)	sim (µg/m³)	obs (µg/m³)
CAMx	0.40	0.41	40.5	90.4	
CHIMERE	0.47	0.57	45.4	100.7	
CMAQ	0.60	0.28	31.2	82.2	66.5
EMEP	0.38	0.37	39.0	87.6	
LOTOS-EUROS	0.69	0.36	32.6	87.7	

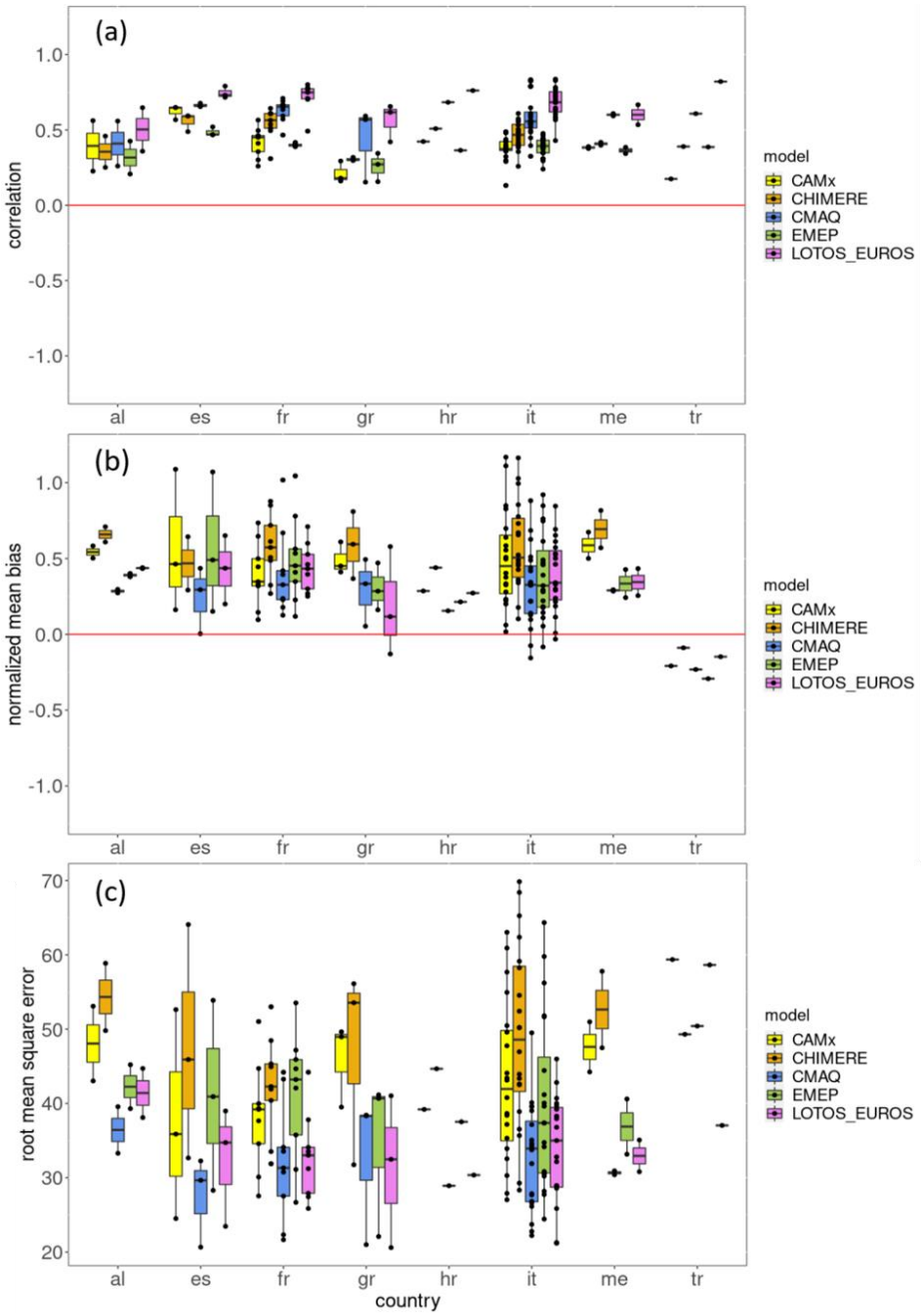

Figure 15: (a) = Correlation, (b) = NMB, (c) = RMSE for annual mean O_3 concentration. Dots display values at measurement stations for the respective countries (al = Albania; es = Spain; fr =France; gr = Greece; hr = Croatia; it = Italy; me = Montenegro; tr = Turkey). Boxplots are for the models with the boxes displaying the interquantile range (IQR) between the 25th (Q1) and 75th (Q3) percentile, the black line displays the median (Q2), whiskers are calculated as Q1–1.5*IQR (minimum) and Q3 + 1.5*IQR (maximum).

5.1.1.4 O_3 Spatial Distribution

The annual mean concentration of O_3 considering all emission sectors is between 60 µg/m³ and 120 µg/m³ for all models (Figure 17). This is consistent with the measurements displayed in the time series in Sect. 5.1.1.3. CHIMERE, CAMx and LOTOS-EUROS show particularly high O_3 concentrations over the sea. Interestingly, EMEP results are similarly high over the sea area, but in comparison with other CTMs, concentrations are lower over land, and even values below 60 µg/m³ can be seen in the Po valley (Figure 17, d). Regarding the correlation between the models for total concentration over the whole domain, it is highest between CMAQ and EMEP (R = 0.71) and lowest for CAMx and LOTOS-EUROS (R = 0.42), but predominantly moderate correlations were found among the models (Table 7).

In general, all CTMs show high annual mean concentrations over the sea areas and low annual mean concentrations over land areas. This is due to lower dry deposition over sea and the overall higher emissions over land. Furthermore, high values of O_3 are expected to enter the domain from the eastern part of the Mediterranean Sea. The frequency distribution of the annual mean total concentration of O_3 has a bimodal distribution for CHIMERE, CMAQ and EMEP. This reflects photochemical O_3 depletion or production, with high values over water areas and lower values over land. Over water, low O_3 depletion is expected during the night. A comparison of diurnal cycles of O_3 over water and over land shows that this presumption is reflected by CMAQ and EMEP results, showing more pronounced cycles of O_3 in grid cells over land (Supplements 1, S17). However, the diurnal cycles of CAMx, CHIMERE and LOTOS-EUROS do not show differences in amplitude over land and water. Despite this, over water, all models show a higher spread of values within diurnal cycles, displaying that there is more variability in the course of the year over water than over land.

The potential relative impact of ships to total O_3 concentrations is lowest in areas with a high potential impact of shipping to total NO_2 (Figure 18). It decreases to -20 % in areas with high NO_2 concentrations in all model results, displaying a local scale titration of O_3 by NO, which is emitted by ships. This reverse relationship between NO_2 and O_3 was already shown in other studies (e.g., Karl et al., 2019b). Measurement studies also indicate that emissions of NO lead to local reduction of O_3 concentration and showed that there could be an increase at larger distances (Merico et al., 2016). Consequently, the largest areas with O_3 destruction for the CAMx and CHIMERE coincide with areas where the models show the highest potential impact of shipping to NO_2. The comparison with the time series shows the highest potential ship impact to the total O_3 concentration in summer. Likewise, in Fig. 18 lowest potential ship impact was found for CAMx.

Fig. 16 shows boxplots with annual mean values of the models for the whole domain. It displays that CAMx, CHIMERE and LOTOS-EUROS are within one range regarding the annual mean total concentration. The CMAQ and EMEP simulations are lowest for the annual mean O_3 total concentration. Regarding potential ship impact, all CTMs except CAMx are within one range.

The present study does not contain the parts of the Mediterranean Sea furthest east due to the focus of the project on the western Mediterranean Sea with its harbor cities as well as due to the limited extent of the WRF domain. A more detailed investigation of the boundary conditions of CMAQ has shown high O_3 values in the eastern part of the domain. A high O_3 production over the eastern Mediterranean Sea and a steep west-east gradient of O_3 were described in previous studies (i.e. Doche et al., 2014; Safieddine et al., 2014; Liu et al., 2009). This production influences the amount of O_3 in the western part of the Mediterranean Sea. Safieddine et al. (2014) found an increase of up to 22 % in O_3 in the eastern part of the Mediterranean basin compared to the middle of the basin. Doche et al. (2014) described a steep west–east O_3 gradient with the highest concentrations over the eastern part of the Mediterranean basin.

Overall, all models showed a relatively good performance for O_3 but differed in simulating spatial distribution and potential ship impact mainly over water. Although boxplots for annual mean values of O_3 differ, for relative potential ship impact they show that CHIMERE, CMAQ, EMEP and LOTOS-EUROS are within one range. Diurnal cycles did not reveal differences in O_3 depletion over water and land among the models.

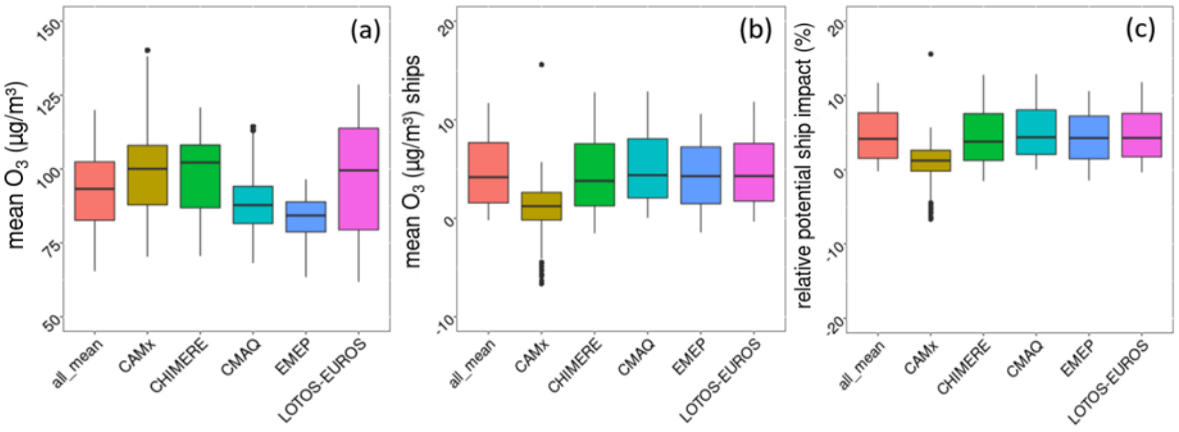

Figure 16: Annual mean for the whole model domain. (a) = mean O_3 for all emission sectors (base case), (b) = mean O_3 for shipping only, (c) = relative potential ship impact to total O_3 concentration. All_mean is the mean value of all models, with a median of (a) = 92.4 µg/m³, (b) = 4.0 µg/m³ and (c) = 4.2 µg/m³.

Table 7: Correlation between models for the whole domain (all grid cells) based on hourly data for O_3 total concentration.

all	CAMx	CHIMERE	CMAQ	EMEP	LOTOS-EUROS
LOTOS-EUROS	0.42	0.59	0.58	0.59	-
EMEP	0.44	0.58	0.71	-	
CMAQ	0.50	0.56	-		
CHIMERE	0.63	-			
CAMx	-				

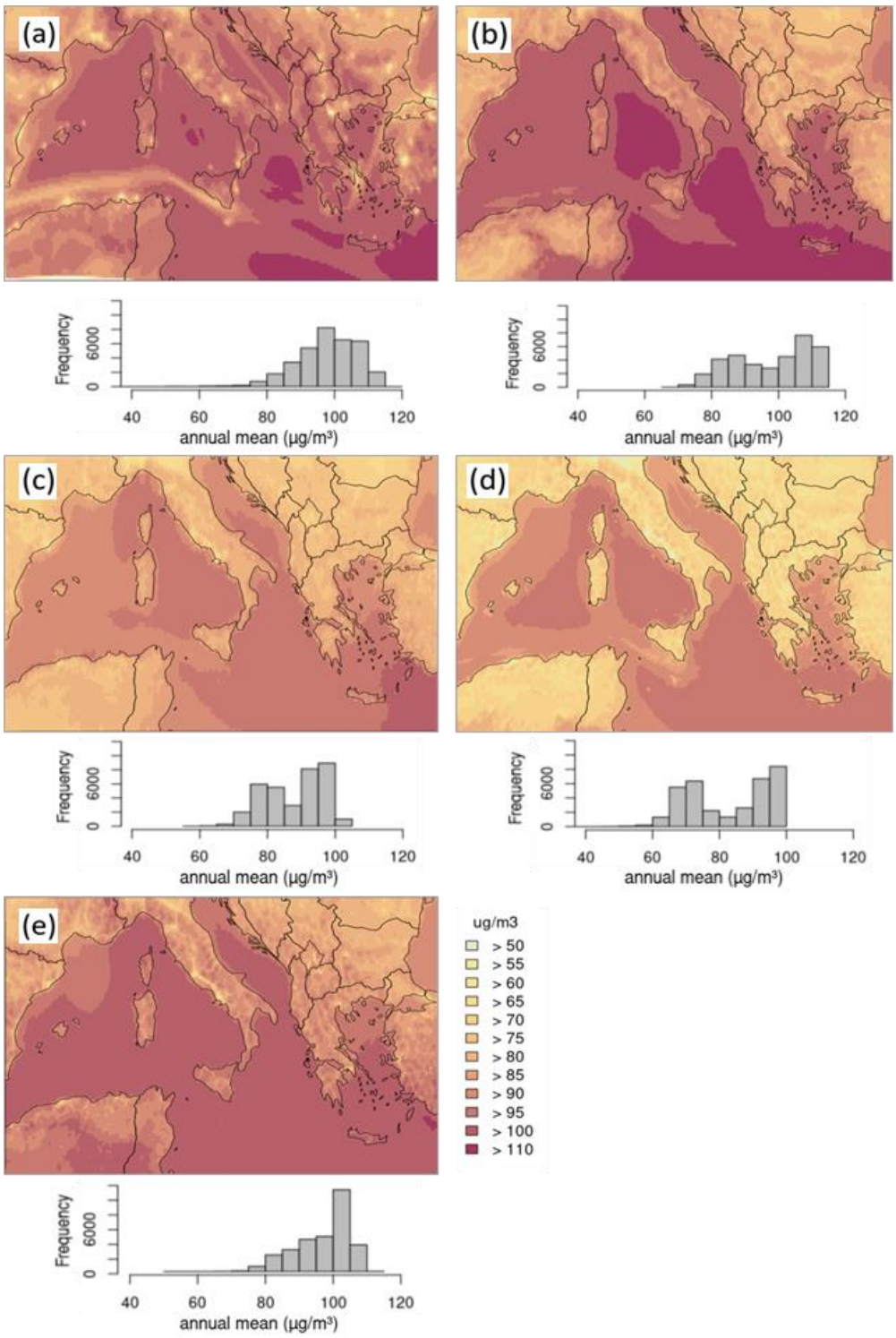

Figure 17: Annual mean O_3 total concentration. (a) = CAMx, (b) = CHIMERE, (c) = CMAQ, (d) = EMEP, (e) = LOTOS-EUROS; emisbase spatial distribution, annual mean value, white areas contain values below 60 µg/m³. Below the domain figure is the respective frequency distribution displayed for the annual mean O_3 concentration, referred to the whole model domain.

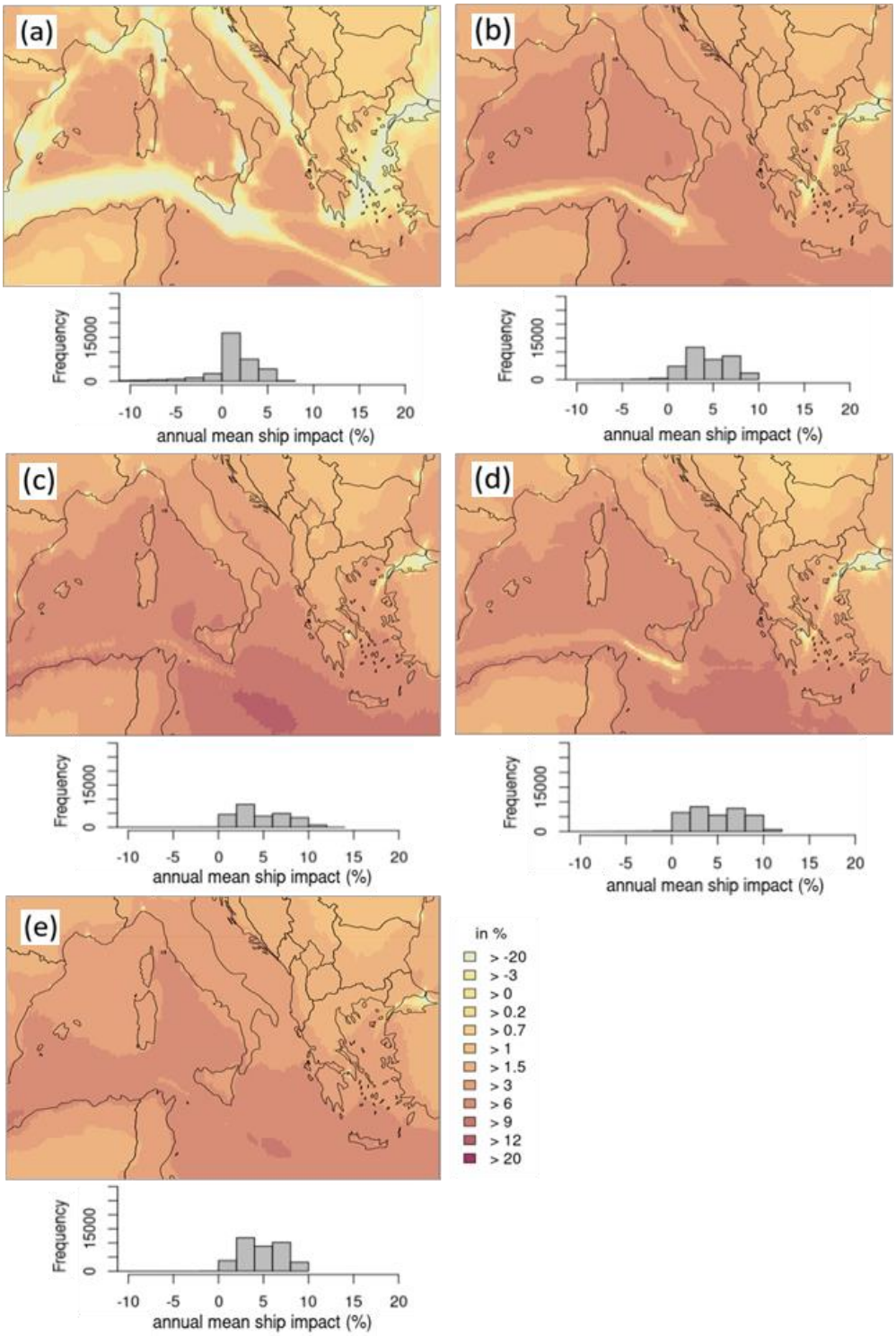

Figure 18: Annual mean O_3 potential ship impact. (a) = CAMx, (b) = CHIMERE, (c) = CMAQ, (d) = EMEP, (e) = LOTOS-EUROS; white areas display values below -20 %. Below the domain figure is the respective frequency distribution displayed for the annual mean O_3 potential ship impact, referred to the whole model domain.

5.1.2 O_x Spatial Distribution

The oxidation of VOCs produce O_3 in the troposphere when nitrogen oxides and sunlight are present. Central to understanding this production is the photostationary state formed between NO, NO_2, and O_3 in sunlight. In emission-free air, a steady equilibrium would be expected; nevertheless, emission sources disturb this equilibrium. In areas with high NO emissions, O_3 destruction is expected, resulting in lower O_3 concentrations along the main shipping routes, in urban areas and in harbor cities.

The results show that all five CTMs tend to underestimate NO_2 and overestimate O_3, but at different magnitudes. For a better understanding of photochemical air pollution and chemical coupling, the oxidant levels ($O_x = O_3 + NO_2$) were calculated and displayed for all emission sources and for the potential ship impact. Clapp and Jenkin (2001) showed that the concentration of O_x levels can be described as a NO_x-independent regional impact, where the O_x impact equates to the O_3 background, and a NO_x-dependent local impact. The NO_x-dependent impact correlates with the primary pollution, coming from direct NO_2 emissions or VOC, which promote conversion from NO to NO_2 (Clapp and Jenkin, 2001).

In comparison with the O_3 spatial distribution and frequency distribution, the annual mean concentration of O_x displays a similar pattern between the results (Figure 19). As it was the case for O_3, CHIMERE and CAMx show the highest values over the sea area, and EMEP shows the lowest values over land areas. The frequency distribution shows bimodal distributed values for CHIMERE, CMAQ and EMEP, as for O_3. Thus, O_x levels are mainly NO_x-independent.

Nevertheless, NO_x-dependent O_x formation can also be seen in the potential ship impact to the total O_x concentration (Figure 20). The relative potential impact of O_x displays how much substances from ships are added to the atmosphere. O_x shows a strong conversion of NO_2 and O_3, thus the shipping lanes are no longer visible. High O_x potential impacts over water areas for CHIMERE, CMAQ, EMEP and LOTOS-EUROS indicate the local potential impact from shipping emissions (NO_2 and VOC), which cause high O_x levels in these areas. For CAMx, the O_x potential impact was lower. This might be traced back to the overall higher concentration of NO_2 and O_3 in CAMx, leading to a lower proportion of other substances. Also, the differences between the O_x results among the models can occur due to the difference in O_3 that in turn results from the input from the boundaries. Here, CAMx displays an overall high input of O_3 from the boundary.

5.1.3 NO_x Spatial Distribution

To gain further insight into the differences in the lifetime of NO_2 in the models, NO_x was calculated and displayed (Appendix E). Differences in NO_x give a hint on the lifetimes because of the reaction of NO_2 with OH to HNO_3. The latter forms ammonium nitrate aerosol together with ammonia; thus, NO_2 is no longer in the gaseous phase. Another explanation is the dry deposition of NO_2, which also causes a loss and consequently differences in the NO_x pattern due to different deposition mechanisms. The spatial distribution of the annual mean NO_x and potential ship impact to the total NO_x concentration have shown a very similar pattern as for NO_2. The values of CAMx and CHIMERE are within one range, displaying higher values compared to CMAQ, EMEP and LOTOS-EUROS. These three models show results within one range.

To see the chemical fate of NO_2 the dry deposition could give a hint and will be considered in the following Sect 5.1.4.

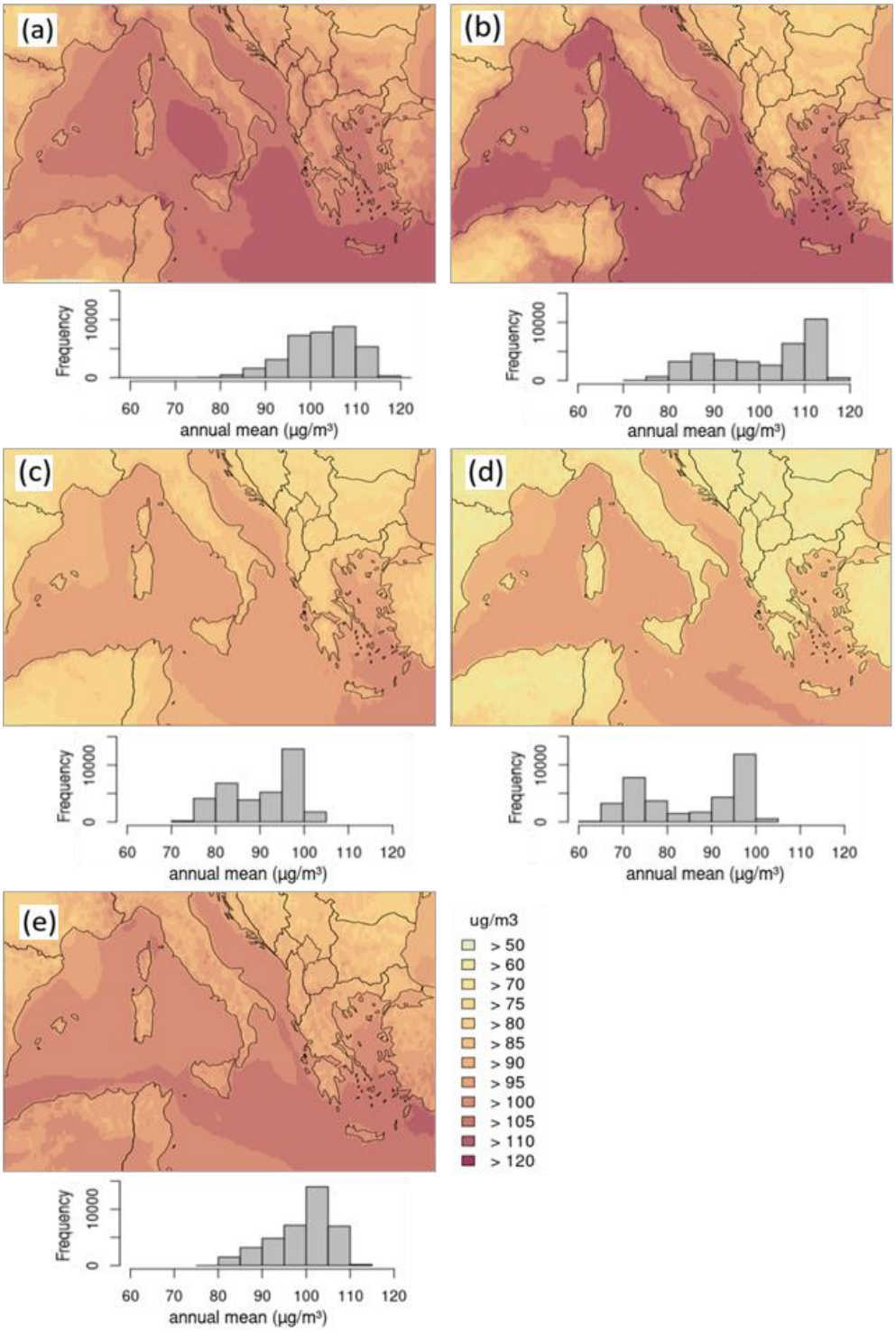

Figure 19: Annual mean O_x (= NO_2 + O_3) concentration. (a) = CAMx, (b) = CHIMERE, (c) = CMAQ, (d) = EMEP, (e) = LOTOS-EUROS. Below the domain figure is the respective frequency distribution displayed for the annual mean O_x concentration, referred to the whole model domain.

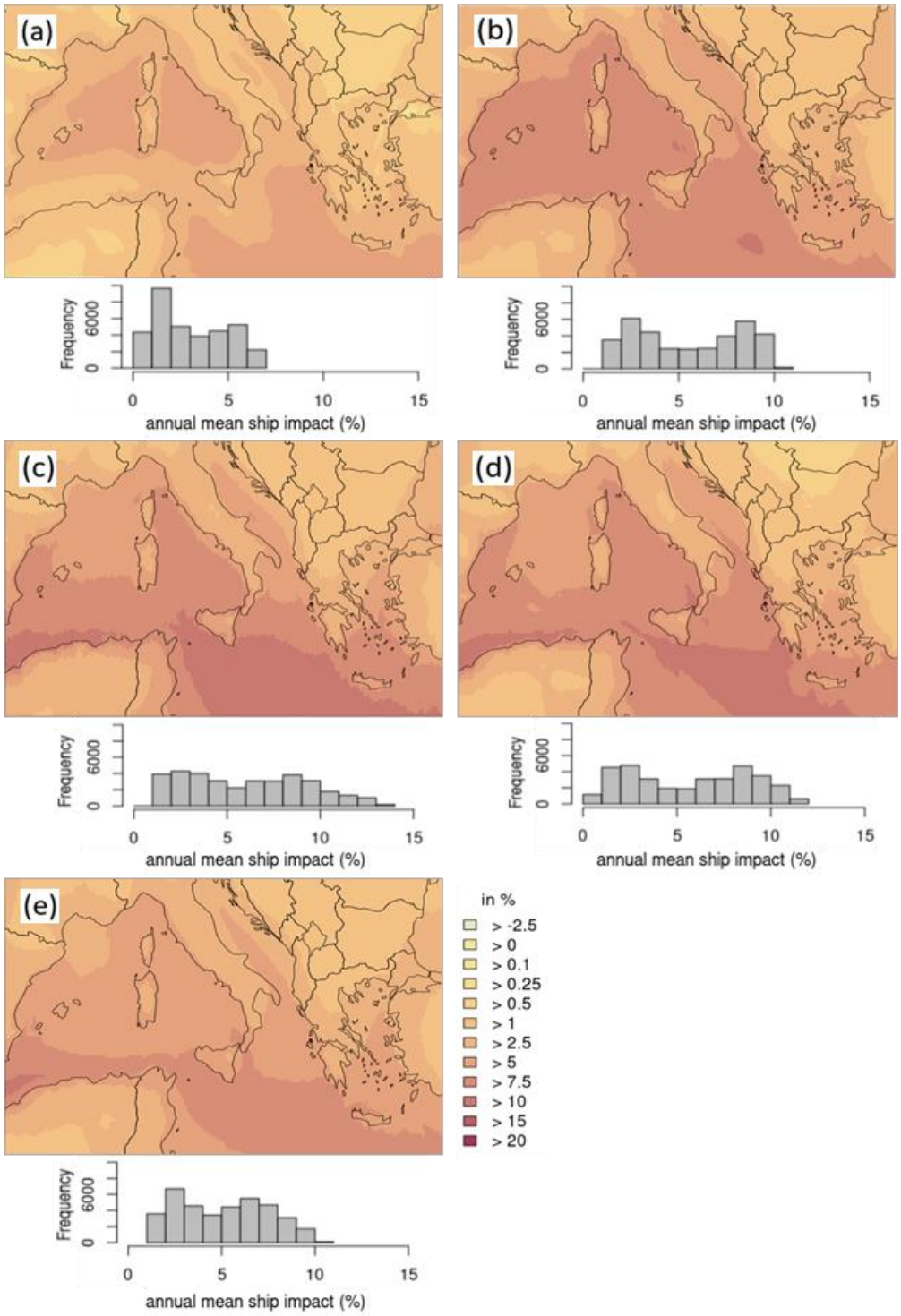

Figure 20: Annual mean O_x (= NO_2 + O_3) potential ship impact. (a) = CAMx, (b) = CHIMERE, (c) = CMAQ, (d) = EMEP, (e) = LOTOS-EUROS. Below the domain figure is the respective frequency distribution is displayed for the annual mean O_x potential ship impact, referred to the whole model domain.

5.1.4 Dry Deposition

In the present study, dry deposition of NO_2 and O_3 are displayed for the base and the no ship case for CAMx, CHIMERE, CMAQ and LOTOS-EUROS. EMEP does not deliver separate NO_2 and O_3 deposition files but does deliver oxidized and reactive nitrogen. Thus, EMEP is not considered in this chapter.

5.1.4.1 Dry Deposition of NO_2

The annual mean NO_2 dry deposition of all four compared CTMs displays similar values over land areas (Figure 21). In cities and densely populated regions, all models show high NO_2 dry deposition, with values over 300 mg/m²/year. Nevertheless, the frequency distribution of all values shows that this is mainly the case for CAMx and LOTOS-EUROS. Additionally, over the sea, the pattern of annual mean dry deposition of NO_2 is also similar for CAMx and LOTOS-EUROS.

Table 8 shows that the correlation was strongest between CHIMERE and CAMx (R = 0.72). Similarities and strong correlations in the output of both models were also found for the NO_2 concentration in Section 5.1.1.2. This can be traced back to the same meteorology data that were used by both CTMs.

The relative potential ship impact to the annual dry deposition of NO_2 is displayed in Fig. 22. The lowest potential ship impact to NO_2 dry deposition is simulated by CMAQ and LOTOS-EUROS. In particular, CMAQ shows large areas with negative (-2.5 %) potential ship impacts over land. The CHIMERE simulations looks similar to the CAMx simulations over land. Along the coastline, CMAQ and LOTOS-EUROS show a potential impact of ships between 10 % and 25 %; CAMx and CHIMERE expect a potential ship impact to the total annual deposition of 25 % to 75 %. The highest potential impact is displayed by CAMx.

Differences in NO_2 dry deposition model results can be due to the dry deposition velocities but also due to the different meteorology data used by the models (Wichink Kruit et al., 2014). Dry deposition velocities of NO_2 (Supplements 1, S18) display that deposition velocities of CHIMERE and CMAQ are within one range and are lower compared to CAMx and LOTOS-EUROS deposition velocities. Velocities of the latter two are within one range. High deposition velocities might lead to higher deposition rates, leading to high annual mean deposition. This is reflected in the annual dry deposition of NO_2, where CAMx and LOTOS-EUROS simulate highest values. Overall, the models have more differences in NO_2 dry deposition than in air concentration. As was the case for NO_2 concentration, CAMx simulated the highest values in dry deposition. The lowest values in NO_2 dry deposition are displayed by CMAQ. In addition, the correlation between CMAQ and the other models was lowest.

High NO_2 deposition over water areas caused by ships contributes to eutrophication (Vivanco et al., 2018). A study by Im et al. (2013) showed values of approximately 500 kg (N) m^{-2} per year (≙ 50000 mg/m²/year) over the Mediterranean Sea, which means an exceedance of the critical load of 2 g to 3 g (N) m^{-2} per year (≙ 2000 to 3000 mg/m²/year) to marine and coastal habitats (Bobbink and Hettelingh, 2011). The present study focused on NO_2 dry deposition; thus, a direct comparison with critical load levels or with other studies regarding total N deposition would not be possible. A subsequent calculation of N showed that the simulated values in the present study do not exceed the critical loads (Appendix F). Nevertheless, NO_2 dry deposition from ships contributes to the total N deposition budget, thus increasing with ship traffic and affecting the ecosystems in the Mediterranean Sea.

Table 8: Correlation between models for the whole domain (all grid cells) based on daily data for NO_2 total dry deposition.

all	CAMx	CHIMERE	CMAQ	LOTOS-EUROS
LOTOS-EUROS	0.48	0.55	0.22	-
CMAQ	0.22	0.27	-	
CHIMERE	0.72	-		
CAMx	-			

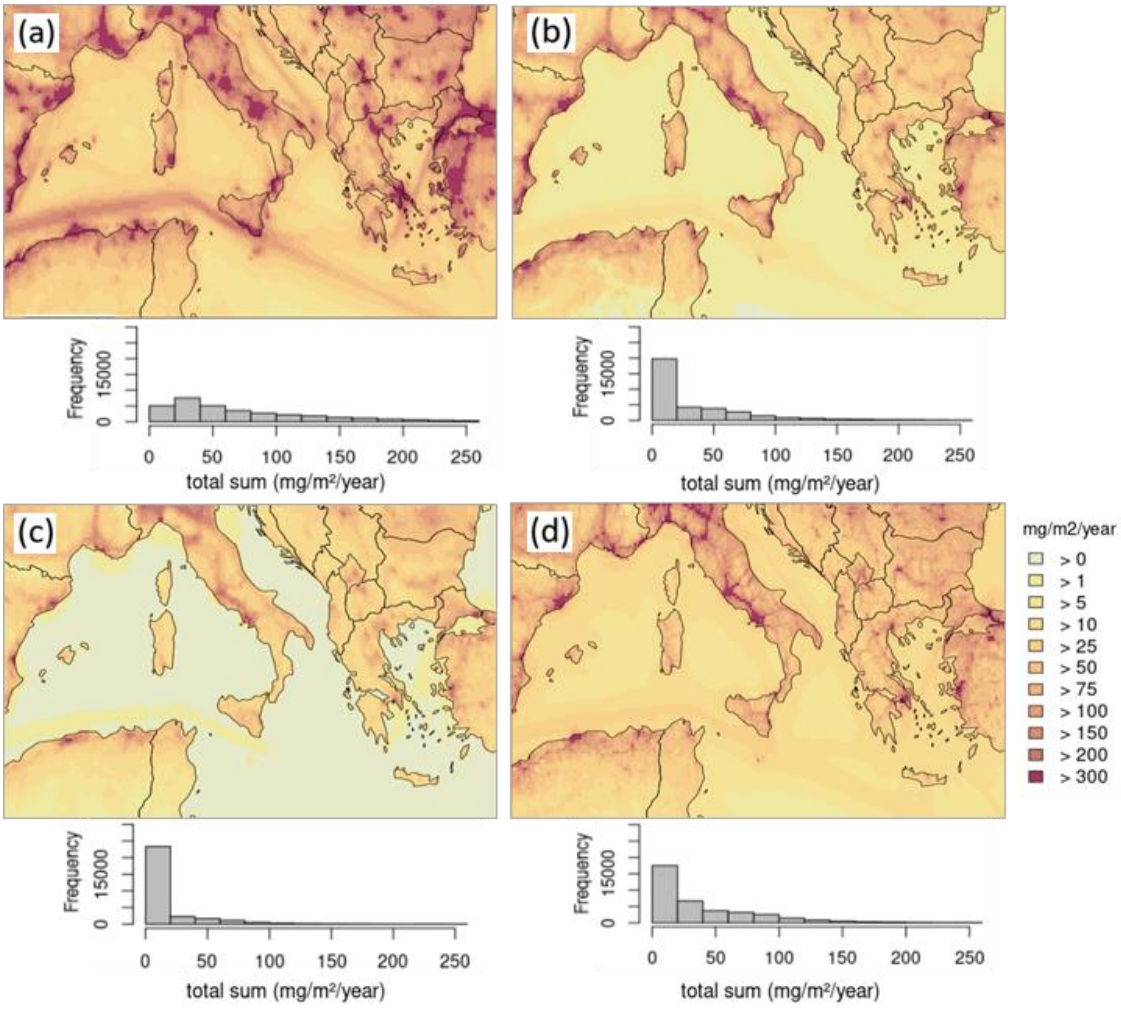

Figure 21: Annual total dry deposition of NO_2. (a) = CAMx, (b) = CHIMERE, (c) = CMAQ, (d) = LOTOS-EUROS. Below the domain figure is the respective frequency distribution displayed for the annual mean NO_2 dry deposition, referred to the whole model domain.

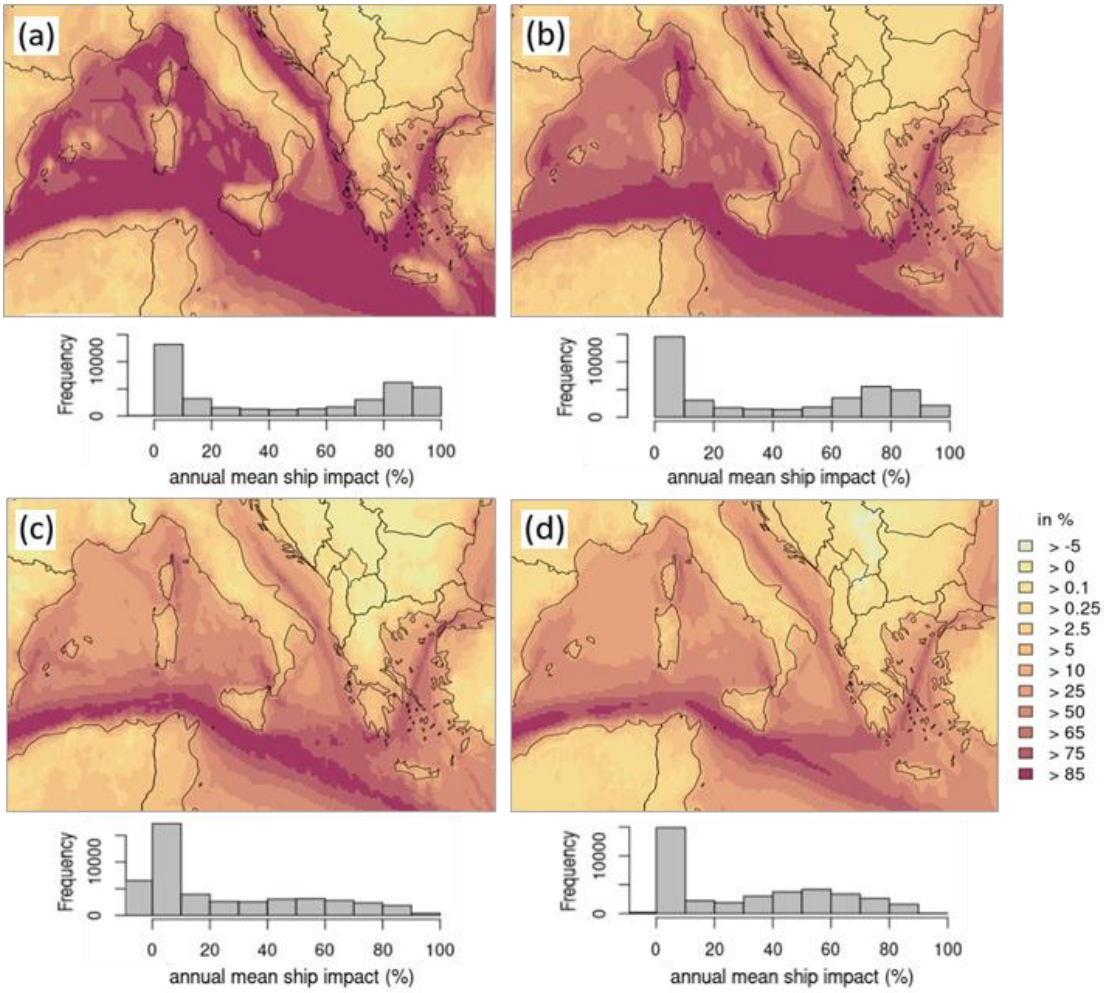

Figure 22: Annual mean dry deposition of NO_2 relative potential ship impact. (a) = CAMx, (b) = CHIMERE, (c) = CMAQ, (d) = LOTOS-EUROS. Below the domain figure is the respective frequency distribution displayed for the annual mean NO_2 dry deposition potential ship impact, referred to the whole model domain.

5.1.4.2 Dry Deposition O_3

Dry deposition is a major sink for O_3 in the lowest model layer. O_3 has high destruction rates on vegetated surfaces through plant stomata and lower rates on surfaces such as water or snow (Clifton et al., 2020). Spatial patterns of annual total O_3 dry deposition confirm this distribution. Over sea annual totals are lower (250 mg/m²/year to 1000 mg/m²/year) compared to values over land (2500 mg/m²/year to 10000 mg/m²/year; Figure 23). The correlation for the annual total concentration of O_3 dry deposition is highest between CHIMERE and CAMx, showing a moderate correlation (R = 0.57; Table 9).

Fig. 24 shows the potential ship impact to the total dry deposition of O_3. CMAQ and LOTOS-EUROS are within a similar range, with potential impacts of ships of 5 % to 10 % over water surfaces. The lowest potential impact of -5 % at the main shipping lanes is simulated by CAMx, showing a similar pattern as for the O_3 potential ship impact. Over land areas, ships contribute to dry O_3 deposition from 0.25 % to 2.5 %.

In addition to the impact of O_3 dry deposition on plant stomata, it is important to explain differences in surface O_3 concentration results. The O_3 concentration is sensitive to the deposition velocity (Clifton et al., 2020), which differs among the four CTMs. This can be confirmed by studies comparing deposition schemes, where differences in O_3 concentration between models are caused by the variety of processes (Clifton et al., 2020). In particular, the variability in deposition velocities across models, as discussed in Sect. 5.1.1.1, is seen as an originator leading to uncertainties in tropospheric O_3 (Wild, 2007). Deposition velocities for the models in the present study (Supplements 1, S19) show lowest velocities for CMAQ. Highest velocities were found for CAMx over land areas. The deposition velocities go along with the annual dry deposition, with high velocities in areas with high dry deposition.

A model comparison study with 15 models by Hardacre et al. (2015) found the greatest differences in total O_3 dry deposition occurring in areas where deposition velocities and O_3 concentrations are highest.

Additionally, soil moisture has an important impact on O_3 deposition and concentration. An evaluation study within the CHIMERE model found that especially in southern Europe, where soil is close to wilting point during summer and affects stomatal opening, O_3 dry deposition declines (Anav et al., 2018). This in turn affects the concentration of gases in the lower atmosphere and thus has an impact on O_3 concentrations.

Table 9: Correlation between models for the whole domain (all grid cells) based on daily data for O_3 total dry deposition.

all	CAMx	CHIMERE	CMAQ	LOTOS-EUROS
LOTOS-EUROS	0.14	0.42	0.20	-
CMAQ	0.26	0.27	-	
CHIMERE	0.57	-		
CAMx	-			

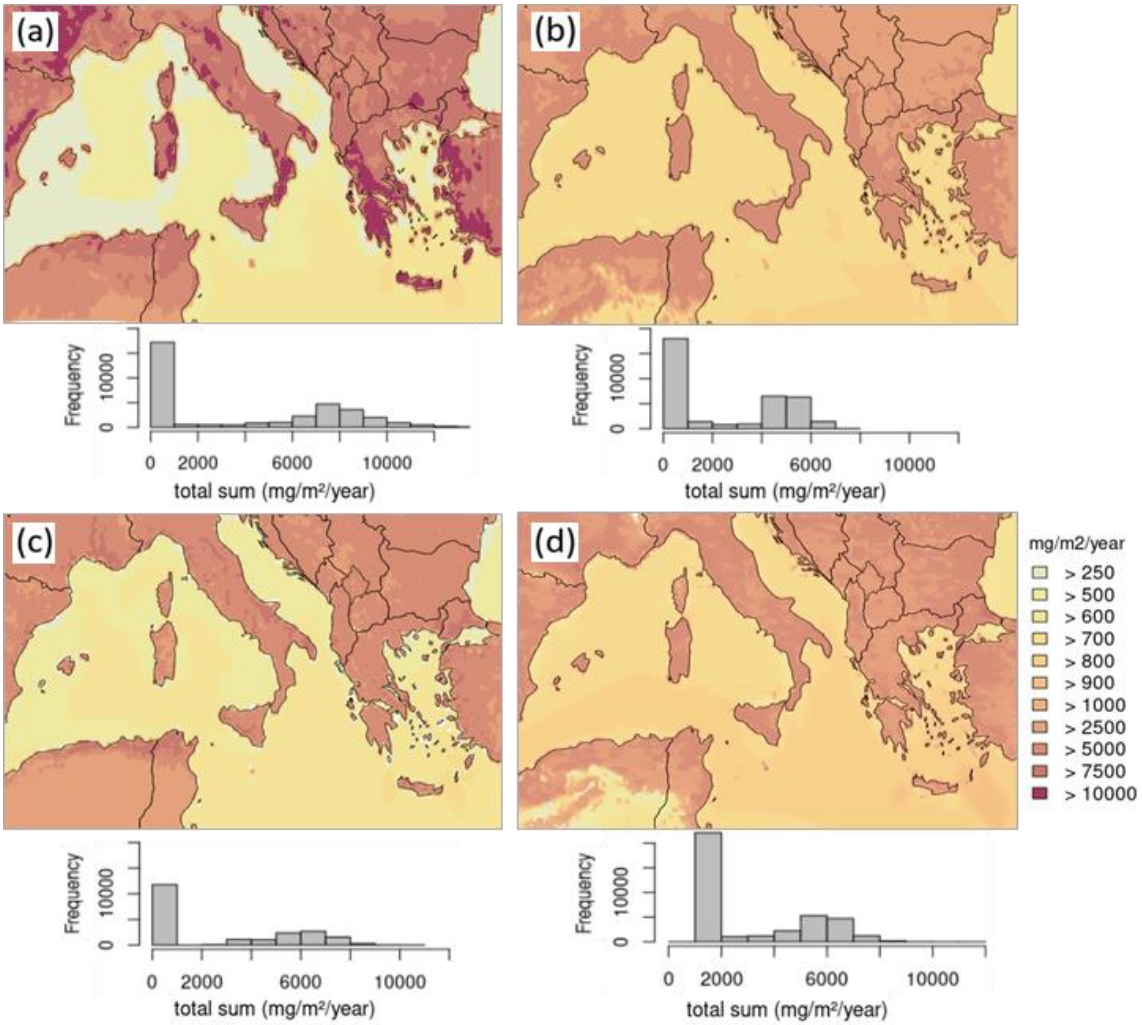

Figure 23: Annual total dry deposition of O_3. (a) = CAMx, (b) = CHIMERE, (c) = CMAQ, (d) = LOTOS-EUROS. Below the domain figure is the respective frequency distribution displayed for the annual mean O_3 dry deposition, referred to the whole model domain.

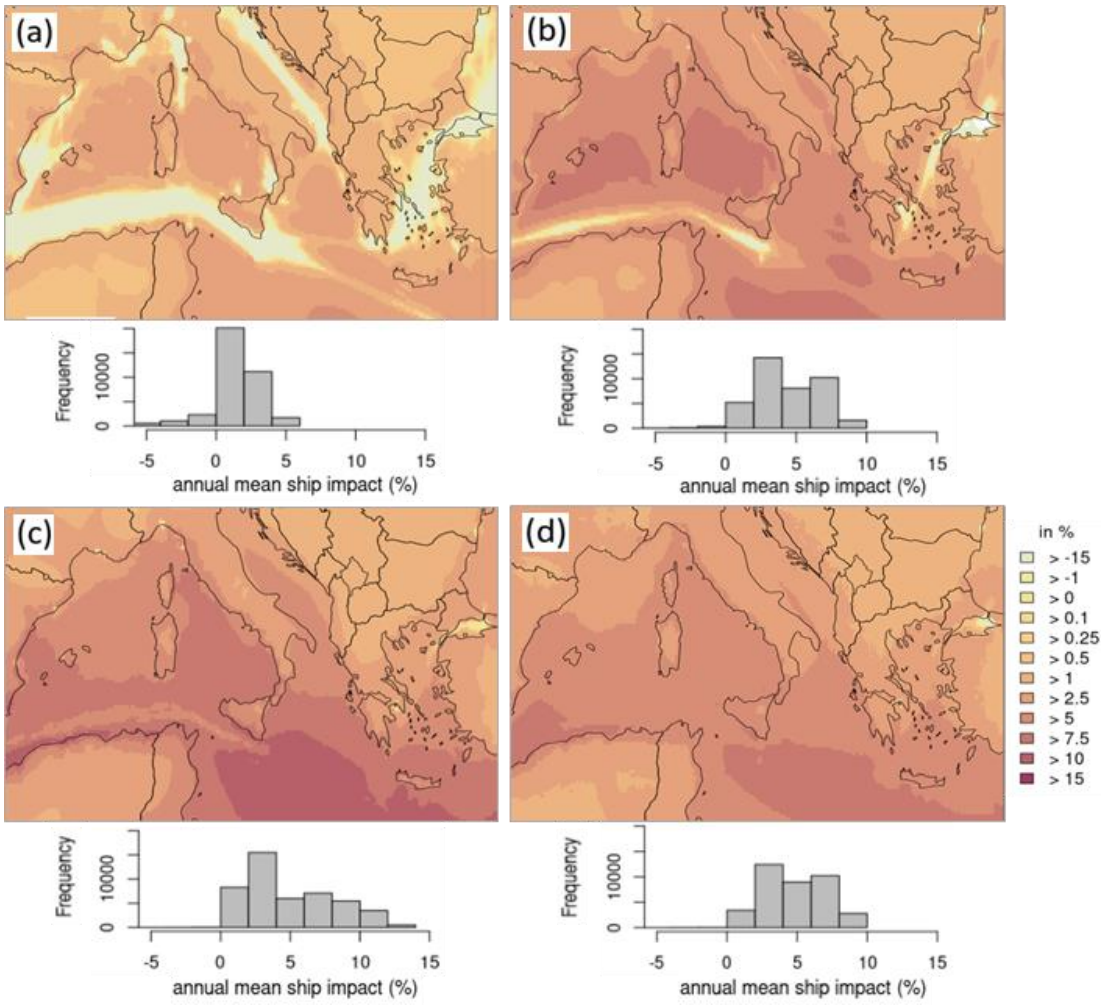

Figure 24: Annual mean dry deposition of O_3 relative ship potential impact. (a) = CAMx, (b) = CHIMERE, (c) = CMAQ, (d) = LOTOS-EUROS. Below the domain figure is the respective frequency distribution displayed for the annual mean O_3 dry deposition ship potential impact, referred to the whole model domain.

5.2 Publication II: A multimodel evaluation of the potential impact of shipping on particle species in the Mediterranean Sea

The following chapter corresponds to results and discussion in the publication of the same name authored by:

Lea Fink, Matthias Karl, Volker Matthias, Sonia Oppo, Richard Kranenburg, Jeroen Kuenen, Sara Jutterström, Jana Moldanova, Elisa Majamäki, Jukka-Pekka Jalkanen

and published in Atmospheric Chemistry and Physics (ACP):

A multimodel evaluation of the potential impact of shipping on particle species in the Mediterranean Sea, Atmos. Chem. Phys., 23, 10163–10189, https://doi.org/10.5194/acp-23-10163-2023, 2023.

The Supplements, which are referred to in the Sect. 5.2, are indicated as “Supplements 2” and attached to this thesis as well as accessible under:

Supplement of Atmos. Chem. Phys., 23, 10163–10189, https://doi.org/10.5194/acp-23-10163-2023-supplement

In the following, the results $PM_{2.5}$ model performance and spatial distribution will be shown. Afterward, the aerosol precursors will be investigated in detail, followed by analyzing the inorganic aerosol species. The results of the present publication will be discussed in Sect. 5.2.5.

5.2.1 $PM_{2.5}$ Model Performance

Regarding the model performance, time series can give an overview of the performance throughout the whole year. Fig. 25 displays the average values at all 28 measurement stations. CAMx, CMAQ, EMEP and LOTOS-EUROS underestimate the measured data. The largest underestimations are found for CMAQ (NMB = -0.42) and LOTOS-EUROS (NMB = -0.54). Contrary to the other CTM systems, CMAQ does not consider dust contribution, which can cause underestimations in $PM_{2.5}$. However, the correlations between the modeled and measured data is strongest for these models (CMAQ: R = 0.50, LOTOS-EUROS: R = 0.54; Table 10). No correlation can be found between the measured and modeled data for CHIMERE (R = 0.02), on the other hand CHIMERE displays only a slight overestimation of the observed values (NMB = 0.06). The simulated potential impacts of ships at all measurement stations are between 5.7 % (CMAQ) and 13.8 % (CAMx; Table 10) as annual average. The simulated ship impacts on $PM_{2.5}$ concentration are within the ranges stated in other studies. In a review of studies regarding the impact of shipping emissions on coastal regions, Viana et al. (2014) reported $PM_{2.5}$ impacts of shipping between 5 % and 14 %. Aksoyoglu et al. (2016) found $PM_{2.5}$ concentrations between 10 % and 15 % along coastal areas due to ship traffic. Ship impacts of approximately 20 % in the southern coastal region of the Iberian Peninsula were found by Nunes et al. (2020). Although in this study, the utilized models underestimated the measured total $PM_{2.5}$ concentrations, they slightly overestimated the relative potential ship impact on $PM_{2.5}$ compared to previous measurement studies. Donateo et al. (2014) measured a proportion of 7.4 % of ships to total $PM_{2.5}$; Pandolfi et al. (2011) measured a proportion of shipping in the bay of Algeciras to $PM_{2.5}$ concentrations between 5 % and 10 %. Argawal et al. (2008) monitored $PM_{2.5}$ at the harbor

of Los Angeles and found $PM_{2.5}$ contributions from ships up to 8.8 %. Predominating secondary particles in $PM_{2.5}$ for potential ship impact in the present study can explain the deviations to the measurement studies.

The RMSE is very similar for all models with a value between 10.7 µg/m³ and 12.2 µg/m³. However, the RMSE is strongly determined by high concentrations and can be biased by outliers. This might explain the similar RMSE derived from CHIMERE despite the lack of correlation. The mean RMSE from different models for $PM_{2.5}$ in Europe found in the AQMEII intercomparison study by Im et al. (2015b) was 6.19 for rural stations and 10.26 for urban stations and is similar as the RMSE calculated in the present study.

The underestimation of $PM_{2.5}$ concentrations by four out of five models is consistent with results by Im et al. (2015b) who reported an underestimation of particulate matter for all participating models, with largest underestimations observed in the Mediterranean region. They stated that the representation of dust and sea-salt emissions had a large impact on the simulated PM concentrations and that uncertainties remain when trying to identify the reasons for the model bias (Im et al., 2015b). Additionally, in a study by Gašparac et al. (2020), underestimations were also found when using EMEP and WRF-Chem to model $PM_{2.5}$ at rural stations in Europe. Solazzo et al. (2012) performed an operational model evaluation for ten models and found that the models underestimated the monthly mean $PM_{2.5}$ surface concentrations in Europe in most cases.

Table 10: Correlation (R), normalized mean bias (NMB), root mean square error (RMSE), observational (obs) and modeled (mod) mean $PM_{2.5}$ values for 2015 over all 28 stations. Observed mean value for all stations is 14.6 µg/m³.

	R	NMB	RMSE (µg/m³)	Mod (µg/m³)	Absolute potential ship impact (annual mean average at all stations) in µg/m³	Relative potential ship impact (annual mean average at all stations) in %
CAMx	0.19	-0.33	11.5	8.9	1.2	13.8
CHIMERE	0.02	0.06	11.1	14.3	1.8	13.2
CMAQ	0.50	-0.42	10.7	8.3	0.5	5.7
EMEP	0.17	-0.33	12.2	8.9	0.9	9.1
LOTOS-EUROS	0.54	-0.53	10.9	6.8	0.6	9.5

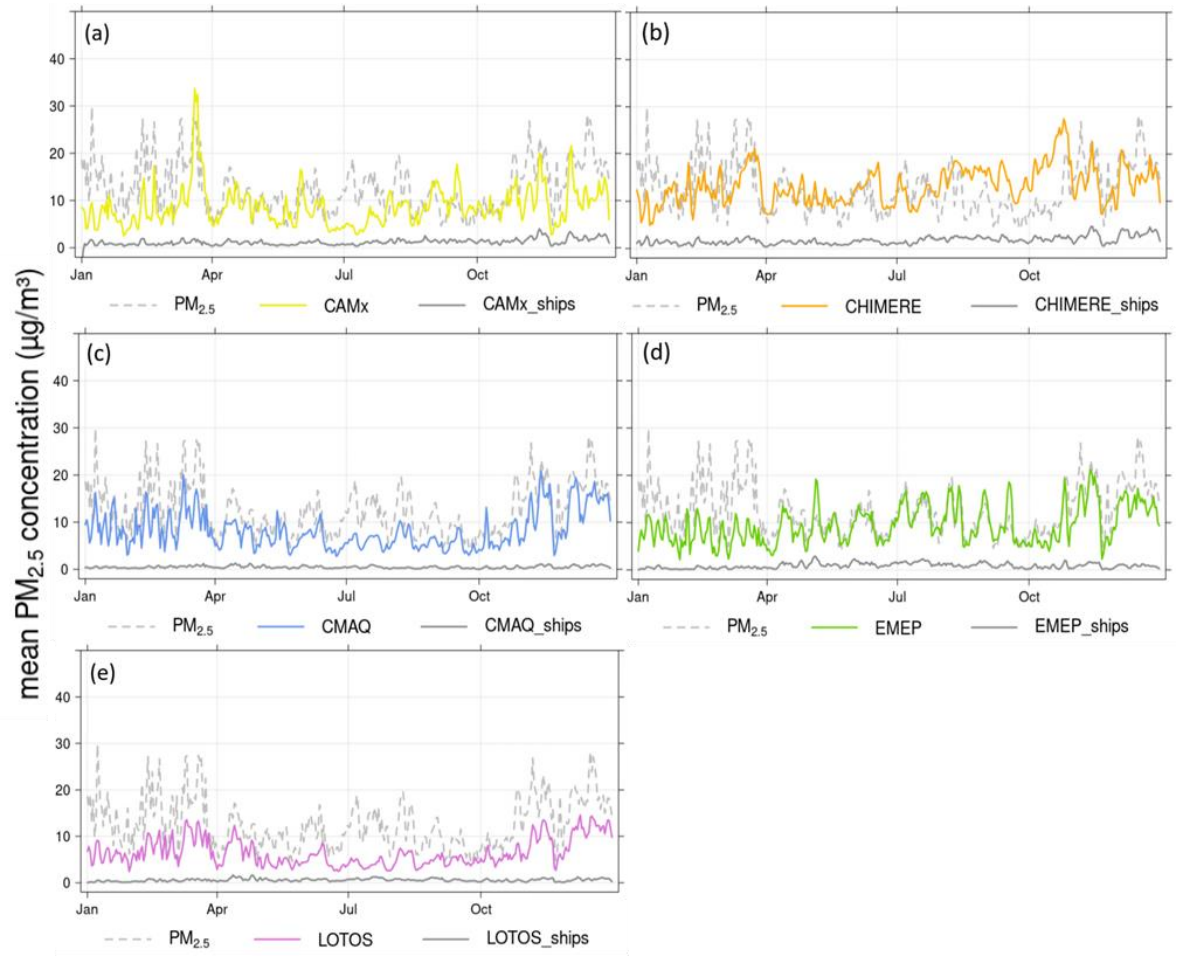

Figure 25: Time series with daily mean $PM_{2.5}$ concentration in 2015, averaged for all stations and the respective grid cells of the models. (a) = CAMx, (b) = CHIMERE, (c) = CMAQ, (d) = EMEP, (e) = LOTOS-EUROS. Dashed gray line = measured data, colored lines = modeled data, gray line = modeled potential ship impact.

5.2.2 $PM_{2.5}$ Spatial Distribution

The highest $PM_{2.5}$ values are simulated by all five models in northern Italy, the Balkan Peninsula and northern Africa (Figure 26). The $PM_{2.5}$ annual mean concentration results show that CHIMERE has the highest annual mean values of 13 µg/m³ to 15 µg/m³ for the eastern part of the domain and over water, whereas LOTOS-EUROS displays the lowest values with 2.0 µg/m³ to 4.0 µg/m³ in most regions (Figure 26). CMAQ, CAMx and EMEP show similar model $PM_{2.5}$ outputs with diverse values distributed between 2.0 µg/m³ and 11 µg/m³ over the domain. The ensemble mean value over the whole domain is 8.6 µg/m³ (Figure 32 a). All five models display high $PM_{2.5}$ concentrations of >15 µg/m³ in the Po valley. In this area, Kiesewetter et al. (2015) and Clappier et al. (2021) also simulated high values between 20 µg/m³ and 45 µg/m³ for 2015. As demonstrated in Table 11, the correlation between the base-run model results with all emissions is strongest between EMEP and CMAQ (R = 0.59) and CAMx and CMAQ (R = 0.42). In Fink et al. (2023) a high correlation was found between CAMx and CHIMERE simulated NO_2 and O_3 concentration because both models used the same meteorology. Nevertheless, the present study reveals that particle chemistry causes more differing results due to a higher complexity in the calculations.

The potential impacts of $PM_{2.5}$ from ships simulated by CAMx, LOTOS-EUROS and EMEP have the largest areas with values up to 25 % at the main shipping routes (Figure 27). CMAQ and CHIMERE have a potential shipping impact of 15 % along the main shipping lines close to the African coast. This impact is lower than that shown in other studies. Aksoyoglu et al. (2016) found the highest impacts of 25 % to 50 % of total $PM_{2.5}$ concentrations when using CAMx along main shipping routes. Sotiropoulou and Tagaris (2017) used CMAQ for simulations and stated that emissions from shipping are likely to increase $PM_{2.5}$ concentrations during winter by up to 40 % over the Mediterranean Sea, while during summer, they simulated an increase of more than 50 %. In both studies, the modeled year is 2006, which might explain the deviation to the present study using a different year. Regarding coastal areas in the present study, potential shipping impacts reaching to 12 % to 15 % are simulated.

Regarding the absolute potential impacts of ships at the main shipping routes, CAMx, CHIMERE and EMEP show values of 2.0 µg/m³, and the values simulated by CMAQ and LOTOS-EUROS are between 0.5 µg/m³ and 1.0 µg/m³ (Figure 28). The median of the ensemble mean is 0.85 µg/m³ (Figure 28 & 32). Aksoyoglu et al. (2016) simulated similar shipping impacts with CAMx, with values mainly between 0.5 µg/m³ and 1.0 µg/m³.

The sea salt concentrations might partly give an explanation for the differing $PM_{2.5}$ concentration distribution among the models. The annual mean sea salt (NaCl) concentration in fine and coarse showed the highest values for CHIMERE, which might be an explanation for the high $PM_{2.5}$ absolute concentration (Supplements 2, S1). The LOTOS-EUROS sea salt displayed lowest concentrations, also the overall $PM_{2.5}$ concentration is lowest compared to the other CTMs. The sea salt concentration was highest (up to 7.0 µg/m³) over sea in areas with high surface wind speed for CHIMERE, CMAQ, EMEP and LOTOS-EUROS (Supplements 2, S2). This can be confirmed by the correlation for wind speed and sea salt at several points over water for CMAQ, EMEP and LOTOS-EUROS (Supplements 2, S3 & Table S1). CAMx is excluded from the analysis since sea salt is only present in fine PM.

Solazzo et al. (2012) demonstrated that the chemical components SO_4^{2-}, NO_3^- and NH_4^+ were better reproduced by nine CTMs than total $PM_{2.5}$. They concluded from this result that other components (e.g., organic aerosols) could be simulated with less accuracy than inorganic components.

Table 11: Correlations between models for the $PM_{2.5}$ base runs of the whole domain (all grid cells), based on daily $PM_{2.5}$ total concentration data.

All	CAMx	CHIMERE	CMAQ	EMEP	LOTOS-EUROS
LOTOS-EUROS	0.07	0.00	0.26	0.06	-
EMEP	0.32	0.17	0.59	-	
CMAQ	0.42	0.19	-		
CHIMERE	0.40	-			
CAMx	-				

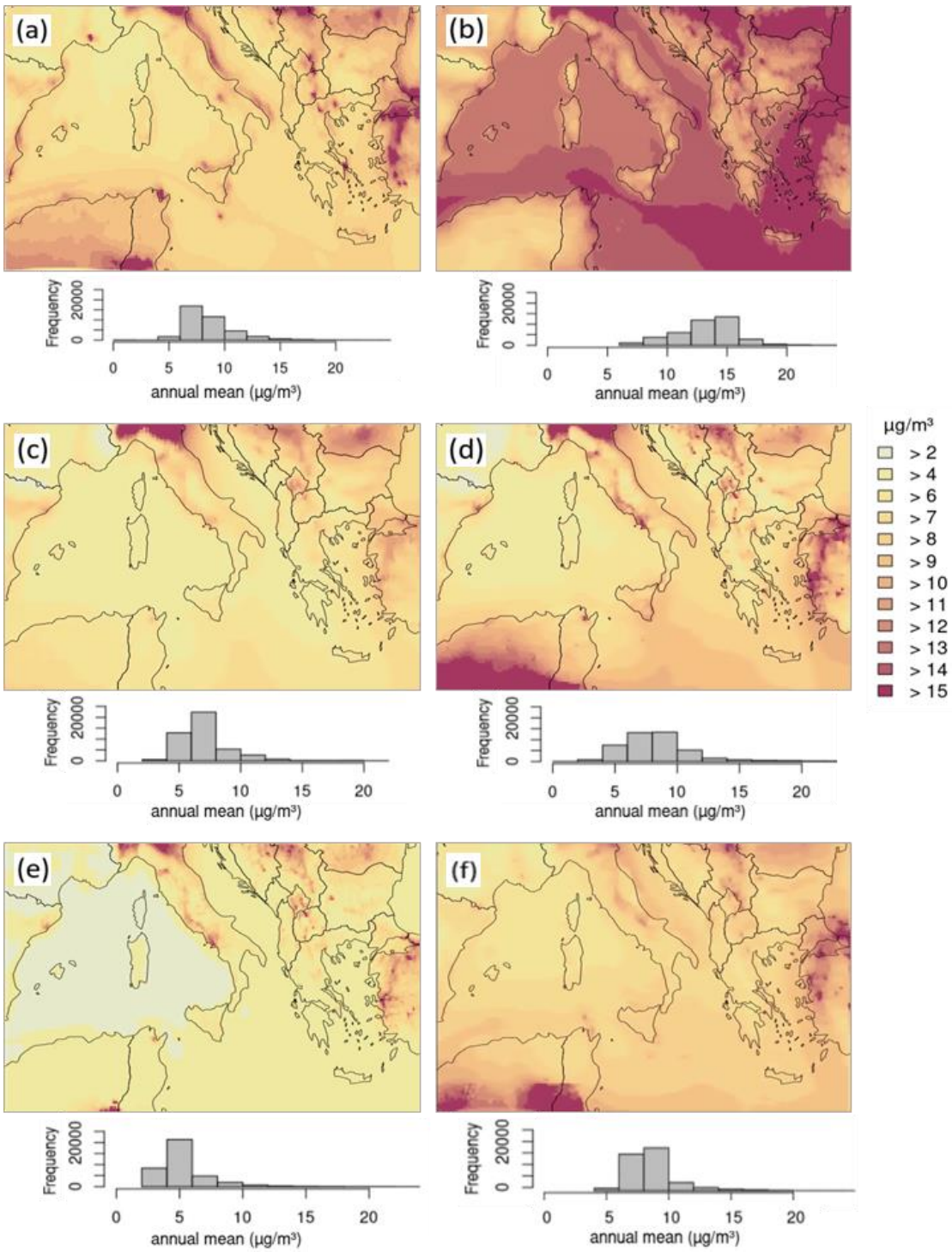

Figure 26: Annual mean $PM_{2.5}$ total concentration. (a) = CAMx, (b) = CHIMERE, (c) = CMAQ, (d) = EMEP, (e) = LOTOS-EUROS, (f) = ensemble model mean. Below the domain figure is the respective frequency distribution displayed for the annual mean $PM_{2.5}$ concentration, referred to the whole model domain.

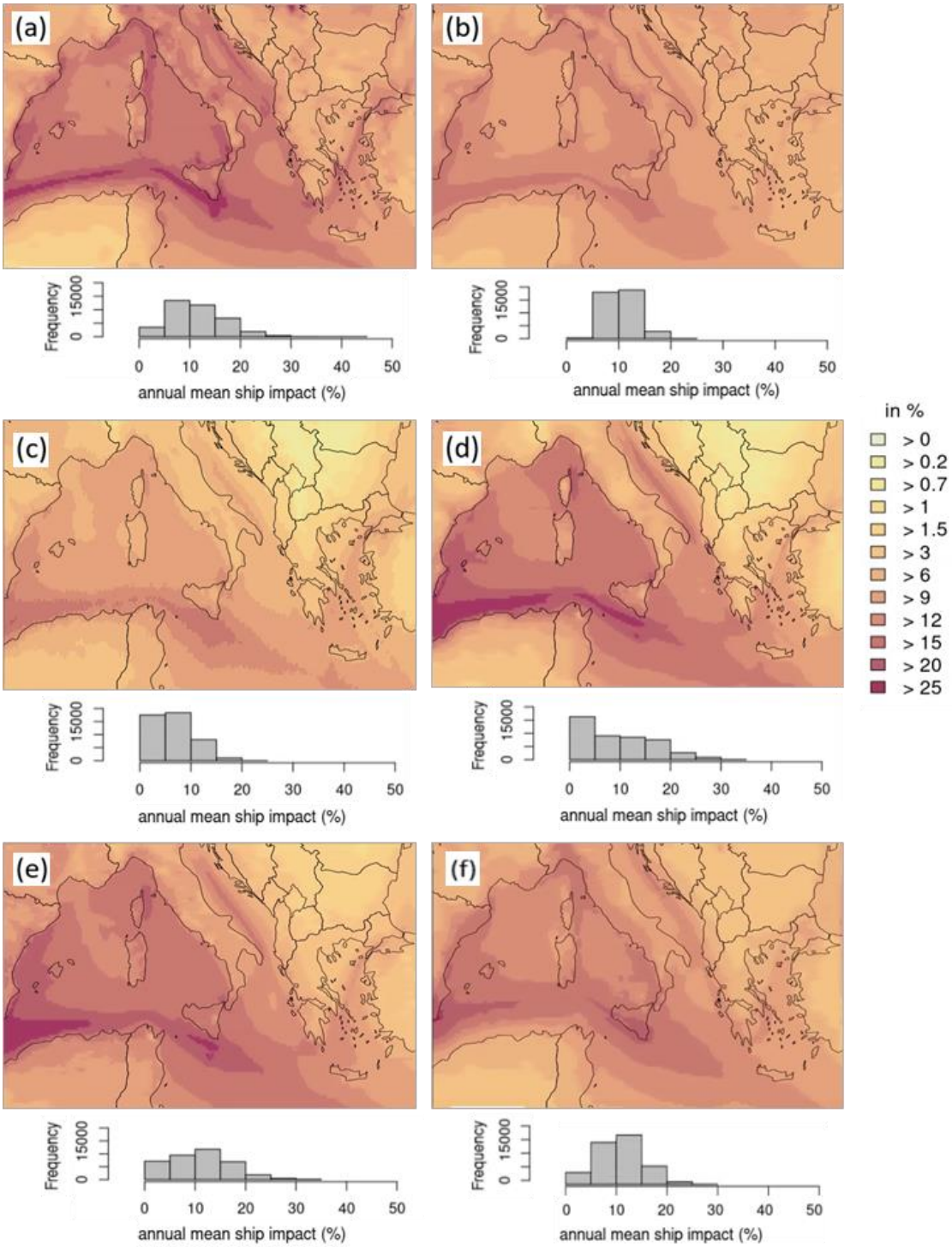

Figure 27: Annual mean $PM_{2.5}$ relative potential ship impact. (a) = CAMx, (b) = CHIMERE, (c) = CMAQ, (d) = EMEP, (e) = LOTOS-EUROS, (f) = ensemble model mean. Below the domain figure is the respective frequency distribution displayed for the annual mean $PM_{2.5}$ potential ship impact, referred to the whole model domain.

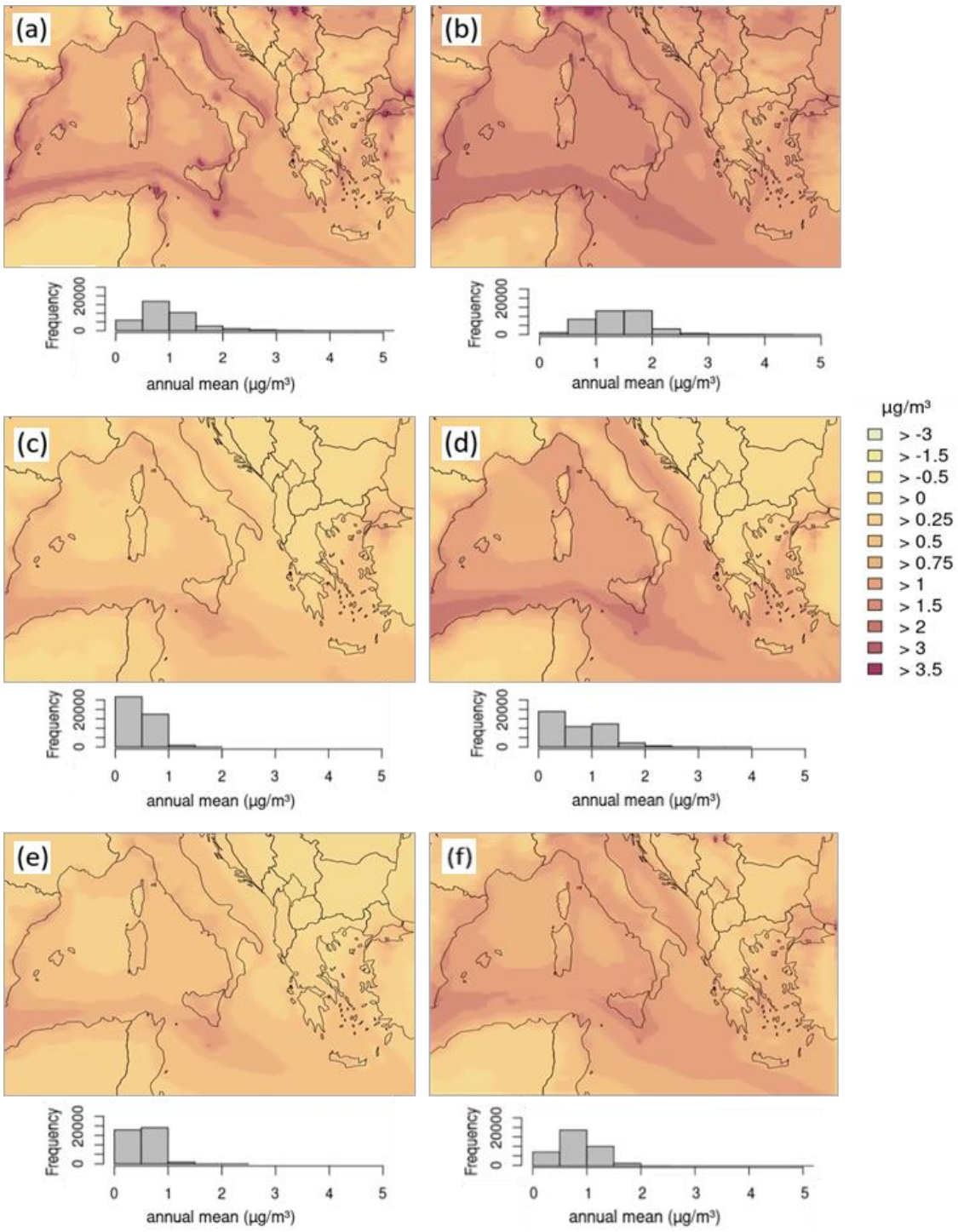

Figure 28: Annual mean $PM_{2.5}$ absolute potential ship impact. (a) = CAMx, (b) = CHIMERE, (c) = CMAQ, (d) = EMEP, (e) = LOTOS-EUROS, (f) = ensemble model mean. Below the domain figure is the respective frequency distribution displayed for the annual mean $PM_{2.5}$ potential ship impact, referred to the whole model domain.

5.2.3 Precursors

High amounts of NH_3, HNO_3, SO_2 and NO_2 are expected to lead to higher values of the aerosol particles composed of NH_4^+, NO_3^- and SO_4^{2-}. The modeled spatial distributions of these precursors can be found in Supplements 2 (HNO_3: S4-S6; NH_3: S8-S10; SO_2: S11-S13; and NO_x: S14-S16).

The highest annual mean HNO_3 concentration among the base runs is found in the CAMx and the CHIMERE simulations over water (2.0 µg/m³ to 5.0 µg/m³); over land, the values are between 0.0 µg/m³ and 1.5 µg/m³, and those in coastal areas reached 2.0 µg/m³ (Supplements 2, S4). The absolute potential ship impact is also highest in CAMx and CHIMERE at the main shipping routes and over water areas (1.0 µg/m³ to 3.0 µg/m³). The relative potential ship impact on total HNO_3 ranges from 60 % to 85 % along the main shipping routes simulated by CAMx, CMAQ and EMEP (Supplements 2, S4). These impacts are slightly lower for CHIMERE and LOTOS-EUROS (60 % to 75 %).

The high HNO_3 concentrations simulated by CAMx and CHIMERE might be traced back to the NO_2 concentrations; these two models also show higher NO_2 concentrations than the other CTMs (Figure 13 in Sect. 5.1.1.2). This can be explained by the fact that HNO_3 is a major NO_2 sink, especially during daytime. NO_2 is primarily emitted from anthropogenic fossil fuel burning but also comes from natural sources (i.e., soil emissions, biomass burning, lightning). During daytime, the main NO_2 removal mechanism is oxidation by hydroxyl (OH) radicals to form HNO_3 (Seinfeld and Pandis, 1998).

It can be concluded that in areas with shipping, more NO_2 enters the atmosphere, the total NO_2 concentration increases, and as a result of the subsequent reactions, the HNO_3 concentration also increases. The HNO_3:NO_2 ratio can be used to normalize the data (Supplements 2, S7). The ratio displays low values over land and along main shipping routes, indicating that in these areas, both the HNO_3 and NO_2 concentrations are high. Low HNO_3:NO_2 ratio could also mean that only a small amount of OH is present, especially in areas with low O_3 concentration.

After its formation, HNO_3 can react with NH_3 to be neutralized and form particles when NH_3 is in excess. The annual mean NH_3 for the base case show very similar patterns and values among all models (Supplements 2, S8). The highest concentrations of NH_3 with all emission sources are located over land areas with values up to 2.5 µg/m³, which can be traced back to agriculture, the main source of NH_3 emissions (Behera et al., 2013). Over water areas, the NH_3 concentration is very small, typically between 0.0 µg/m³ and 0.3 µg/m³, except for the slightly higher results modeled by LOTOS-EUROS, with values between 0.2 µg/m³ and 0.8 µg/m³. Negative potential ship impacts (-0.01 µg/m³ to -1.0 µg/m³ and -2.5 % to -150 %; Supplements 2, S9 & S10) are found for the whole domain in all five models. The relative ship impacts are lowest at the main shipping routes for CAMx and EMEP. The spatial distribution of the NH_3 relative ship impact is opposite to the simulated HNO_3 values; at the main shipping routes with low NH_3 and high HNO_3 values. These results indicate that available NH_3 reacts directly with HNO_3 to form particles (i.e., NH_4NO_3). Thus, NO_x emissions from shipping lead to HNO_3 formations and subsequent NH_3 consumption, e.g. shipping impacts on NH_3 concentrations are usually negative.

The CAMx simulations show highest SO_2 concentrations with more than 10 µg/m³ in some areas in Western Turkey, in urban areas and along major shipping lanes (Supplements 2, S11). The results from the other four CTMs display high values around the Bosporus and in some areas over the Balkan Peninsula with values of 11 µg/m³ and much lower concentrations along the main shipping routes. The potential ship impacts are similarly high in CAMx and CHIMERE (1.0 µg/m³; 85 % to total concentration; Supplements 2, S12 & S13), with the highest values along the major shipping route north of the African coast. The CMAQ, EMEP and LOTOS-EUROS results display similarly high values but only in small areas. The modeled year is 2015, so the global 0.5 % sulfur cap of marine

fuels was not yet effective. Heavy fuel oils with sulfur contents reaching 3.50 % were used until 2020 to power ships; thus, the SO_2 emitted from ships in the present study is still high and it can be expected that it has a large impact on secondary particle formation.

5.2.4 Inorganic Aerosol Species

5.2.4.1 Concentrations

In the Northern Hemisphere, secondary inorganic ammonium, sulfate and nitrate aerosols represent a large fraction of the $PM_{2.5}$ composition (Jimenez et al., 2009). Ammonium preferentially binds to SO_4^{2-} in atmospheric aerosols in the form of $(NH_4)_2SO_4$. NH_4NO_3, on the other hand, is formed in areas characterized by high NH_3 and HNO_3 conditions and low H_2SO_4 conditions. The results of the CTMs with regard to these three particle species and their potential ship impacts are considered in the following section. The spatial distributions of the total concentrations and absolute potential ship impacts of the individual species can be found in Supplements 2 (NH_4^+: S17 & S18; SO_4^{2-}: S19 & S20; and NO_3^-: S21 & S22), spatial distribution of relative potential ship impact is shown in Fig. 29 to Fig. 31.

The spatial distribution of NH_4^+ shows that the lowest total annual mean can be found mainly in the southwestern part of the domain (approximately 0.0 µg/m³) and the highest in the Po Valley and Bosporus (1.5 µg/m³, Supplements 2, S17). The relative ship impacts are very similar for all models (0.25 % to 5.0 % over land, 10 % to 25 % over water; Figure 29) as well as for the absolute ship impact (Supplements 2, S15). Aksoyoglu et al. (2016) simulated NH_4^+ values between 0.0 µg/m³ and 0.2 µg/m³ in the Mediterranean region, with higher concentrations (0.4 µg/m³) in the Po valley. This is within the same range of concentrations in the present study. Ge et al. (2021) used the EMEP model to simulate global particle species concentrations and compared them to measured concentrations. They showed in their study that the NH_4^+ concentrations simulated in Europe in 2015 were overestimated by factor 2 compared to the observed NH_4^+ concentrations. The measurements displayed a mean of 0.45 µg/m³. The ensemble mean for NH_4^+ in the present study (0.6 µg/m³, Figure 32 a) is in good agreement with these measurements. However, a previous study on measured compared with simulated aerosol distribution with the CMAQ model displayed a slight underestimation of NH_4^+ (Matthias, 2008).

The NH_4^+ proportion to total $PM_{2.5}$ is similar among all models (5.6 % to 7.8 %; Figure 32 a, Table 12), and only LOTOS-EUROS displayed a relatively high share (12.2 %). This pattern is similar for the ship impacts, where all models show proportions between 9.1 % and 12.6 %, but higher values are simulated by LOTOS-EUROS (23.5 %; Figure 32 b, Table 13).

SO_4^{2-} is the oxidation product of SO_2, which is primarily emitted by anthropogenic processes such as fossil fuel combustion, petroleum refining, and metal smelting (Zhong et al., 2020). In the present study, SO_4^{2-} is the main contributor to total $PM_{2.5}$ mass (Figure 32, Table 12). Especially in the model ensemble mean for the absolute ship-related concentrations, SO_4^{2-} makes up 44.6 % of $PM_{2.5}$ (Figure 32 b, Table 13). The annual mean SO_4^{2-} total concentration is highest for CHIMERE in the eastern part of the domain, reaching 6.0 µg/m². EMEP displays a SO_4^{2-} concentration within the ranges of the other models CAMx, CMAQ and LOTOS-EUROS in the western part of the domain. These models show very similar spatial distributions with concentrations up to 2.0 µg/m³. The median ensemble mean for the run with all emission sources is 2.0 µg/m³. This ensemble mean is low in comparison with the results of Solazzo et al. (2012); they found a mean value of 6.0 µg/m³ but considered a larger European area that included the areas with highest SO_4^{2-} concentrations in Europe. For this larger area, Solazzo et al. (2012) found that the used models underestimated SO_4^{2-} by 7 % to 17 %.

In the present study, the relative potential ship impact on total SO_4^{2-} is lowest over land, with 0 % to 3.0 %, and higher in coastal areas, with values from 6 % to 20 % (Figure 30). Along the main shipping routes it is highest, reaching 50 % for CAMx, EMEP and LOTOS; for CHIMERE and CMAQ, it is lower with values reaching 30 %. Aksoyoglu et al. (2016) showed similar relative potential ship impacts of 50 % to 60 % in the western Mediterranean. In their study, values were between 0.0 µg/m³ to 1.0 µg/m³ over land areas, but over water along the main shipping routes they were highest at 2.2 µg/m³.

Mallet et al. (2019) traced back higher SO_4^{2-} in the eastern part of the domain due to westerly winds. In the present study, we found this higher concentration for SO_4^{2-} in the eastern part of the Mediterranean as well. On Lampedusa, they found ammonium sulfate contributed 63 % to PM_1 mass, followed by organics (Mallet et al., 2019). In our study, the organics/others had highest share on total $PM_{2.5}$ when considering all emission sources, followed by sulfate and ammonium.

In the present study, CTM systems simulated lower values for ship impacts; over land, they are 0.0 µg/m³ to 0.03 µg/m³, and along the main shipping routes, they reached 0.9 µg/m³. Regarding the absolute ship impacts on SO_4^{2-}, the model simulations displayed similar concentrations and are slightly lower for CMAQ and LOTOS-EUROS (Supplements 2, S20) compared to the other models. Especially over water areas, large areas with considerable SO_2 and SO_4^{2-} concentrations can be seen. Because NH_4^+ is preferably bound to SO_4^{2-} in atmospheric aerosols to form $(NH_4)_2SO_4$, in areas over water, less NH_4NO_3 forms.

Im et al. (2015b) suggested in their intercomparison study that over Europe, SO_4^{2-} levels were underestimated by most models; only a few models overestimated SO_4^{2-} concentrations in Europe. The underestimating models were WRF-CHEM models, and the SO_4^{2-} underestimations were attributed to the absence of SO_2 oxidation in cloud water in the heterogeneous phase.

The highest annual mean NO_3^- total concentrations is simulated over land areas especially over Italy and in the Balkan states (> 2 µg/m³; Supplements 2, S18), lowest concentration are over sea. CAMx, CMAQ and LOTOS-EUROS show higher concentrations compared to results derived from CHIMERE. The concentrations over water are lower than those over land. The ensemble median of all CTMs over the whole domain is 0.63 µg/m³ (median value; Figure 32 a). The absolute potential impacts of ships on the total NO_3^- concentrations are similar among all models, displaying values mainly between -0.005 µg/m³ and 0.15 µg/m³; only CMAQ demonstrates relatively low values along the main shipping routes (-0.5 µg/m³), and CAMx has higher values (1.0 µg/m³) in some coastal areas (Supplements 2, S19). This can be explained by higher SO_4^{2-} concentrations derived from SO_2 emissions. Sulfate replaces nitrate as long as ammonia concentration is low. In model simulations with ships, NO_3^- can decrease because ammonia is already taken from sulfur emissions from ships. Aksoyoglu et al. (2016) found similar results for the Mediterranean Sea considering the NO_3^- concentrations, with values between 0.0 µg/m³ and 0.2 µg/m³. Im et al. (2015b) showed that simulated NO_3^- levels were overestimated by most of the CTMs by more than 75 %. Higher concentration over water than over land due to NH_4NO_3 formation are found in areas characterized by high NH_3 and HNO_3 conditions and low H_2SO_4 conditions. In the present study, the relative potential ship impacts on NO_3^- displays contradicting tendencies among the models (Figure 31). The CAMx, EMEP and LOTOS model results are similar, with relative potential ship impacts over land of 0.0 % to 5.0 % (in the Balkan states), those in coastal areas and Italy of 10 % to 25 % and those along main shipping routes of 50 % to 65 % or even up to 85 %. CHIMERE and CMAQ display lower relative potential ship impacts. For CMAQ, the impact is even negative along the main shipping routes, at -25 %. Sulfur dioxide or ammonia, might lead to negative NO_3^- impact, because the NO_2 emissions from ships would make a positive contribution to nitrate formation. Therefore, without ships, a $(NH_4)_2SO_4$

should be formed, which is more stable than NH_4NO_3. These low values in the aerosol species for CMAQ but higher values for EMEP, CAMx and LOTOS represented the $PM_{2.5}$ ship impacts and might partly explain the deviations in $PM_{2.5}$. Furthermore, in CMAQ the coarse mode in nitrate and ammonium has a larger share compared to the other CTMs. A more detailed discussion will be given in Sect. 5.2.5.

Regarding the $PM_{2.5}$ composition, the share of other particles, which contain mainly organics but also e.g. sea salt, is highest compared to the inorganic species (Figure 32). Nevertheless, the particle composition revealed varying distributions in the ship-related $PM_{2.5}$ concentration. Here, inorganic particle species have relatively high percentages compared to organic aerosols. In some cases, sulfate has an even higher share of the total $PM_{2.5}$ than other particles.

The seasonal variability in particle species shows that NO_3^- is more temperature-dependent than SO_4^{2-} and NH_4^+. NO_3^- is higher in winter and spring but lower in summer and autumn. This pattern can be found in all CTM simulations. For $PM_{2.5}$, on the other hand, no discernible pattern is found regarding seasonal variability. In particular, the ensemble mean $PM_{2.5}$ concentration remained within the same range in all seasons.

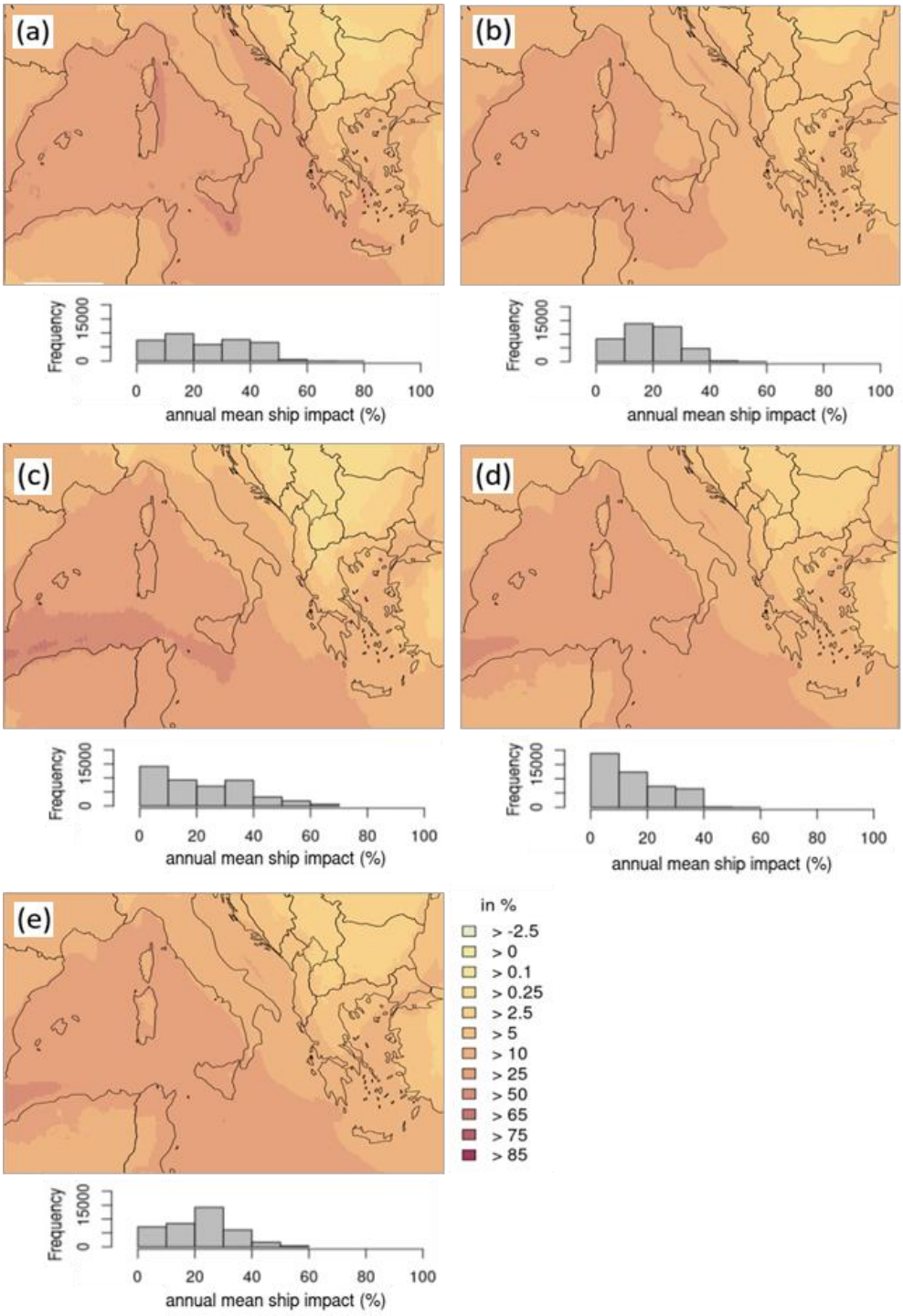

Figure 29: Annual mean NH_4^+ relative potential ship impact. (a) = CAMx, (b) = CHIMERE, (c) = CMAQ, (d) = EMEP, (e) = LOTOS-EUROS. Below the domain figure is the respective frequency distribution displayed for the annual mean NH_4^+ potential ship impact, referred to the whole model domain.

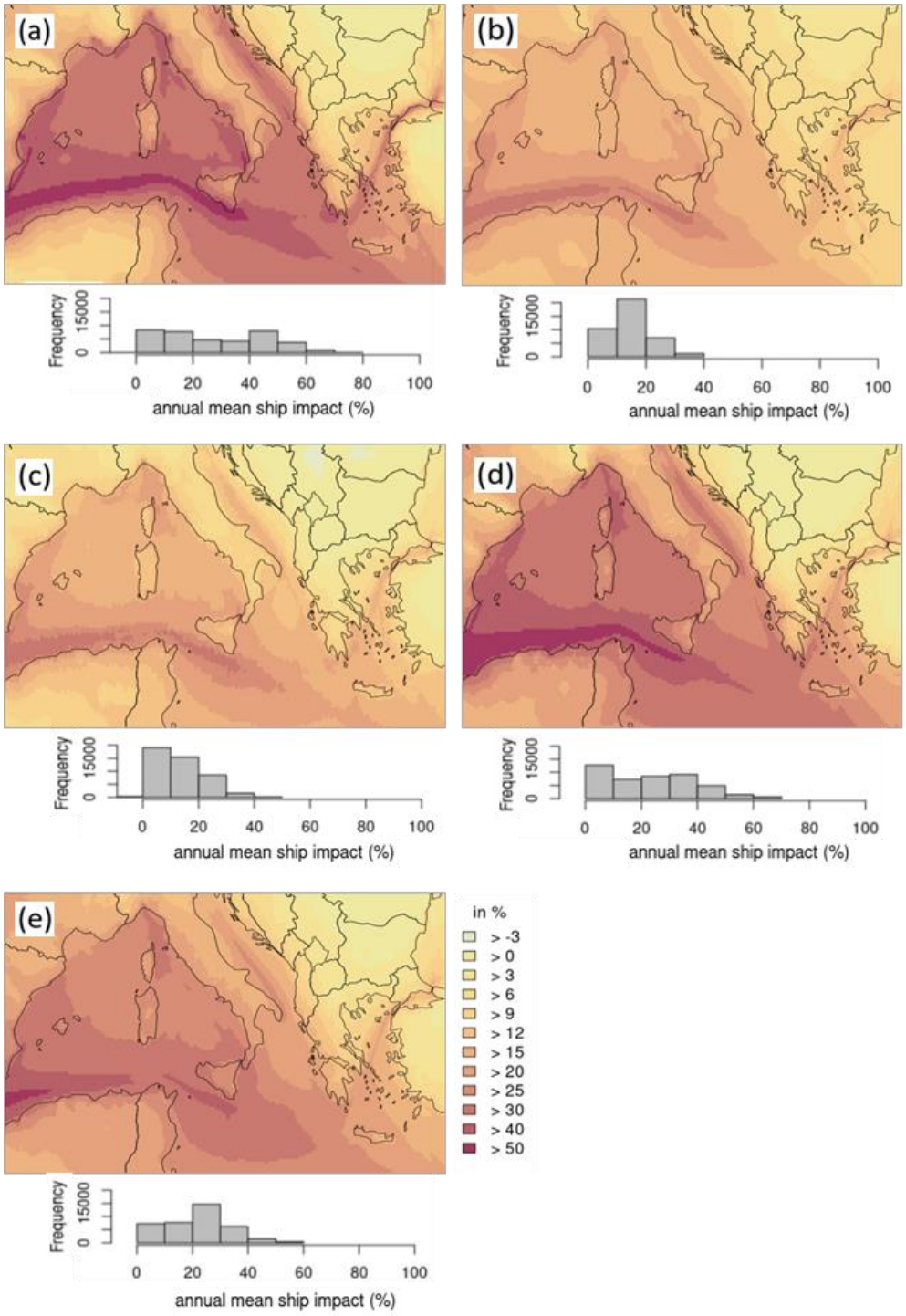

Figure 30: Annual mean SO_4^{2-} relative potential ship impact. (a) = CAMx, (b) = CHIMERE, (c) = CMAQ, (d) = EMEP, (e) = LOTOS-EUROS. Below the domain figure is the respective frequency distribution displayed for the annual mean SO_4^{2-} potential ship impact, referred to the whole model domain.

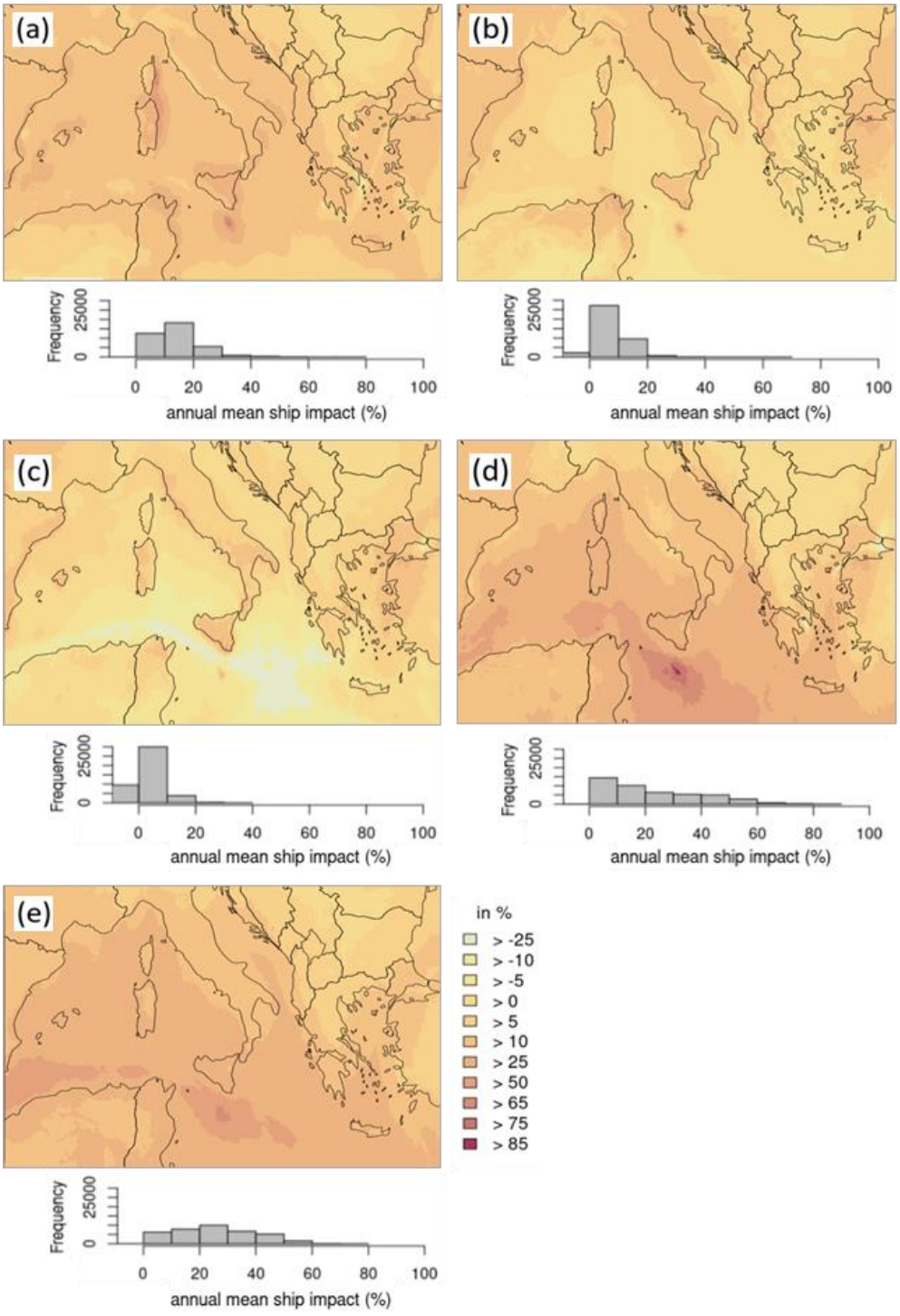

Figure 31: Annual mean NO_3^- relative potential ship impact. (a) = CAMx, (b) = CHIMERE, (c) = CMAQ, (d) = EMEP, (e) = LOTOS-EUROS. Below the domain figure is the respective frequency distribution displayed for the annual mean NO_3 potential ship impact, referred to the whole model domain.

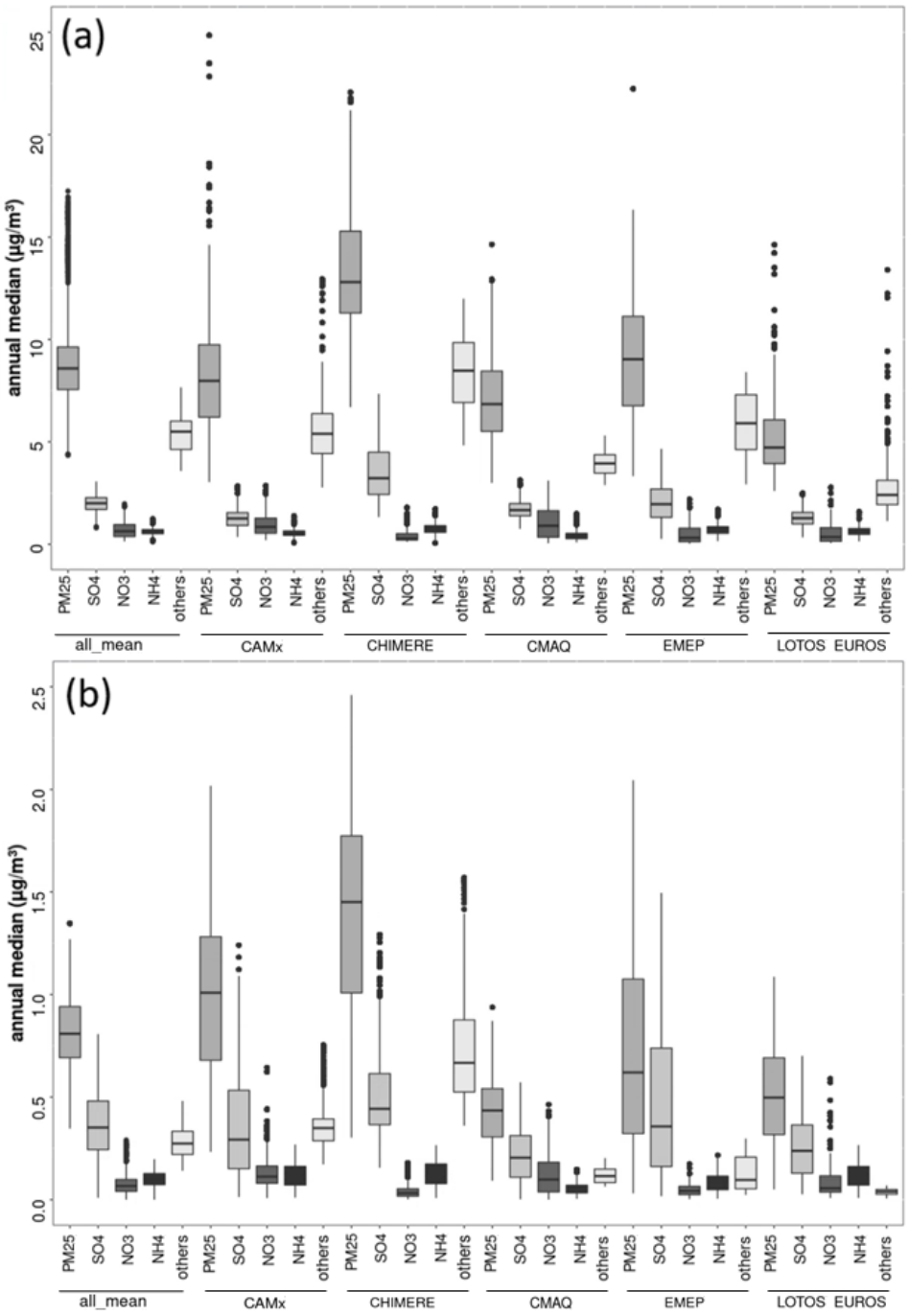

Figure 32: (a) Boxplots for concentrations of $PM_{2.5}$, and the PM2.5 components SO_4^{2-}, NO_3, NH_4^+ and "others" as simulated by the five CTMs. The ensemble mean is "all_mean". Others is calculated as $PM_{2.5}$ minus the sum of SO_4^{2-}, NO_3 and NH_4^+. Data is based on the whole domain (all grid cells) and hourly data for all emission sources ("emisbase"). (b) Same as (a) but for ships only.

Table 12: Relative particle species of total $PM_{2.5}$ emissions.

	Ensemble mean	CAMx	CHIMERE	CMAQ	EMEP	LOTOS-EUROS
SO_4^{2-}	22.8	14.6	27.0	23.8	22.5	24.8
NO_3	8.0	11.1	3.1	14.5	5.6	10.6
NH_4^+	7.1	6.5	5.6	6.2	7.8	12.2
Other	62.1	67.8	64.3	55.5	64.1	52.4

Table 13: Relative particle species of total shipping-related $PM_{2.5}$.

	Ensemble mean	CAMx	CHIMERE	CMAQ	EMEP	LOTOS-EUROS
SO_4^{2-}	44.6	37.0	36.0	48.5	63.9	51.8
NO_3	8.6	13.1	2.5	11.9	6.6	16.9
NH_4^+	12.4	11.7	9.1	12.6	11.8	23.5
Other	24.4	38.2	52.4	27.0	17.7	7.8

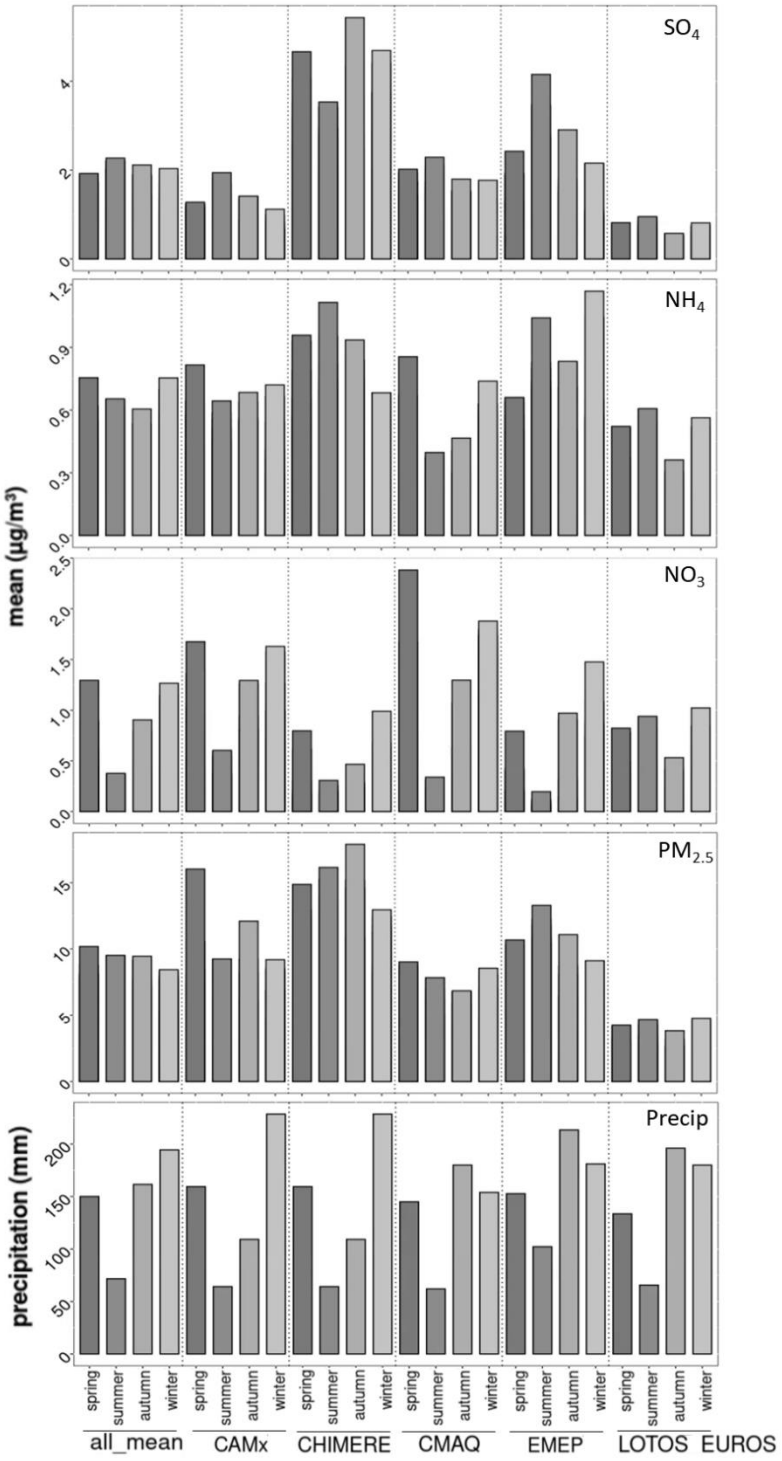

Figure 33: Concentration of particle species and precipitation divided by seasons and CTMs. "all_mean" displays the model ensemble. Spring = March, April, May; summer = June, July, August; autumn = September, October, November; winter = December, January, February. Concentration is based on the annual median over the whole domain. Precipitation displays the seasonal sum (in mm).

5.2.4.2 Wet Deposition

Wet deposition can provide hints about the fate of particles. EMEP does not deliver separate deposition files for individual particle species but for reduced and oxidized nitrogen. Thus, EMEP is not considered when analyzing wet deposition in this study.

Regarding spatial distribution of NH_4^+ wet deposition, highest annual sums are displayed by CMAQ and LOTOS-EUROS (up to 250 mg/m²/year over land; up to 50 mg/m²/year over water; Supplements 2, S23). CAMx and CHIMERE show a similar spatial distribution with values mainly between 10 mg/m²/year and 25 mg/m²/year. CAMx and CHIMERE used the same meteorology data, but despite of this the seasonal distribution of wet deposition differs (Figure 34). An explanation of this differing behavior might be provided by the scavenging mechanisms. In CHIMERE the incloud mechanism for deposition of particles is assumed to be proportional to amount of water lost by precipitation. In CAMx, the incloud scavenging coefficient for aqueous aerosols is the same as for the scavenging of cloud droplets. Below the cloud, CHIMERE uses a polydisperse distribution following Henzig et al. (2006) whereas in CAMx for rain or graupel the collection efficiency is calculated as in Seinfeld and Pandis (1998). The other possible explanation is that all the emissions in CAMx are emitted in the first layer and in CHIMERE, it depends on the emissions distribution.

Regarding the wet deposition of sulfate, the annual totals for all emission sources are highest over the Balkan Peninsula in the CMAQ and LOTOS-EUROS model outputs (300 mg/m²/year to 800 mg/m²/year; Supplements 2, S24). For CAMx over land areas, the values reach 300 mg/m²/year, and the lowest totals over land can be seen in the CHIMERE results (0.0 mg/m²/year to 50 mg/m²/year). Over water, these values are low in all model outputs (50 mg/m²/year to 150 mg/m²/year), except CHIMERE, contrary to the other models, highest wet deposition was found over water.

The wet deposition of NO_3^- is highest for CMAQ (> 400 mg/m²/year) over the whole domain (Supplements 2, S25). For CAMx and LOTOS-EUROS, it is generally lower, with most areas displaying 25 mg/m²/year to 50 mg/m²/year. Lowest wet deposition of nitrate is shown in CHIMERE outputs with values not exceeding 50 mg/m². Regarding the sum for the whole year, the highest values are found for CMAQ (Northern Italy and the Balkan Peninsula, where the urban-area values reached 400 mg/m²/year). Over water, deposition is lower than over land in the results of all CTMs. Lower wintertime precipitation in CMAQ compared to the other models might lead to high particle concentrations as well as high deposition due to low dilution (Figure 34).

Wet deposition depends mainly on the ability of models to predict the amount, duration, and type of precipitation. The precipitation data show that the lowest values are found for CMAQ input data. CAMx and CHIMERE use the same meteorological input data and thus display the same precipitation results, with the highest values in winter. CMAQ and LOTOS-EUROS have precipitation values within a similar range, with the highest values occurring in autumn and winter.

Although the precipitation results in CAMx and CHIMERE are the same, wet deposition differed among these two models, indicating that the concentration as well as model internal mechanisms caused differences rather than the input data. Additionally, in CMAQ, a lower wet deposition rate is expected for nitrate. There are usually two mechanisms important for scavenging in CMAQ; in-cloud and below-cloud scavenging. High wet deposition for nitrate in CMAQ outputs might be traced back to efficient below cloud scavenging of coarse mode particles containing nitrate, through which the wet deposition can be high despite precipitation in similar ranges as other models. Furthermore, the deposition of particulate nitrate crucially depends on the reactive uptake of HNO_3 to larger particles (Karl et al., 2019b), because coarse-mode particles are removed much faster than fine-mode particles.

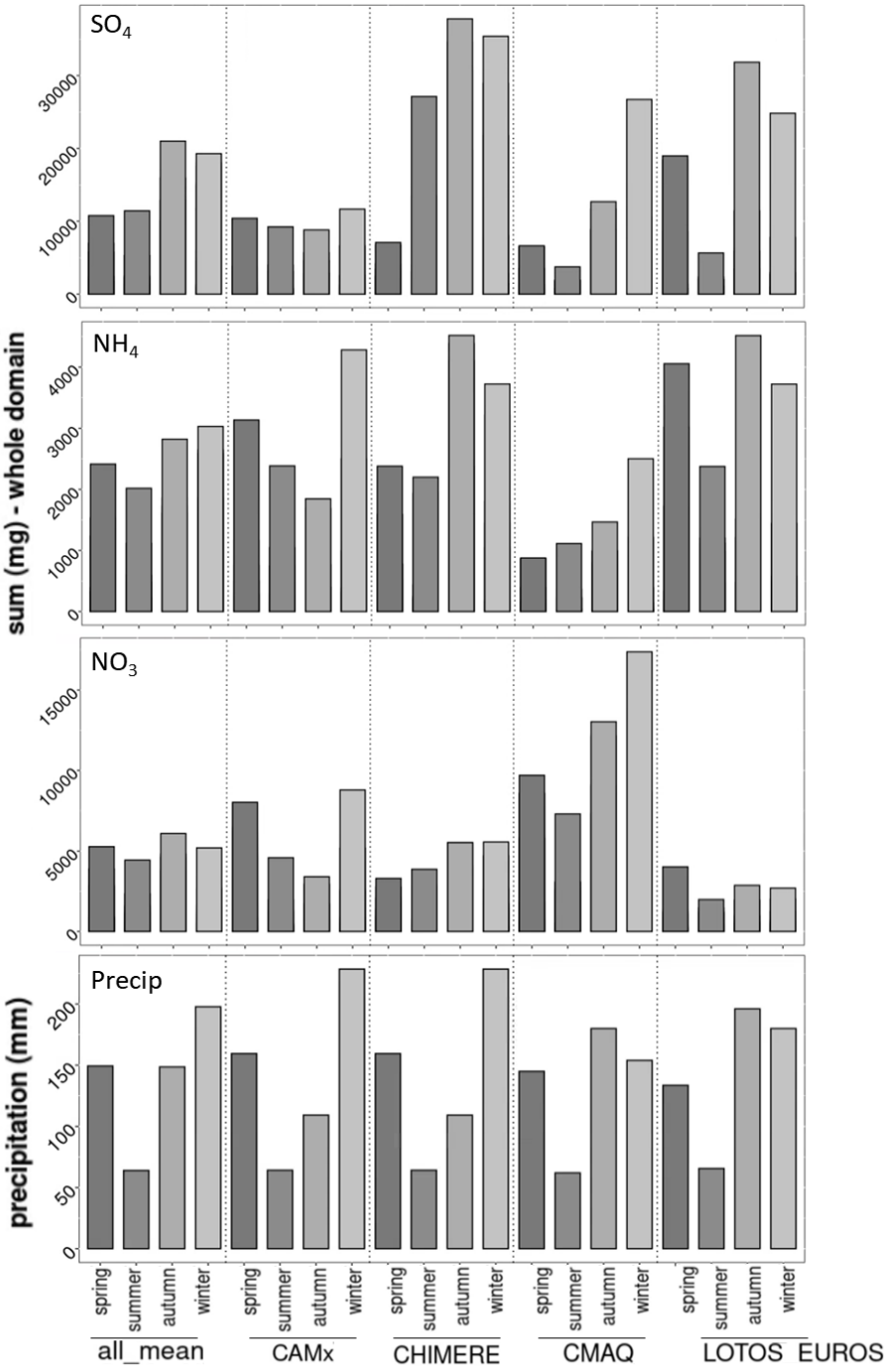

Figure 34: Wet deposition sum (mg/season) of particle species and precipitation divided by seasons and CTMs. "all_mean" displays the model ensemble. Spring = March, April, May; summer = June, July, August; autumn = September, October, November; winter = December, January, February. Wet deposition is based on the annual sum over the whole domain. Precipitation displays the seasonal sum (in mm).

5.2.5 Discussion

Various reasons for deviations of $PM_{2.5}$ concentrations among regional CTM systems might be traced back to model-specific calculations.

Regarding PM (coarse and fine for sea salt), an uncertainty among models might be caused by the differences in calculation of sea salt and dust emissions. Here, both is considered in all CTMs, except for dust in CMAQ. If sodium chloride and dust components are not considered, underestimations of PM and uncertainties in areas near coasts (sea salt) or where dust is important, e.g. Saharan dust in the Mediterranean region, occur, as described in Section 5.2.1. Furthermore, if sea salt and dust are omitted from the pH calculations, it might also cause deviations in sulfur chemistry, as this factor is very sensitive to pH.

In the CMAQ runs dust was considered at the model boundaries but dust emissions were not included. The Mediterranean region is frequently affected by Saharan desert dust (Palacios-Peña, 2019), but the main source region for this dust emission is not included in the model domain, thus the dust coming from the boundary can be seen as sufficient for the CMAQ model run. Generally, the boundary conditions for dust and sea salt in CAMx and CHIMERE were produced by offline models that are running on meteorological fields from GEOS-5, GEOS DAS and MERRA. For CMAQ and LOTOS-EUROS these boundary conditions were produced within the boundary conditions calculations. Boundary conditions of EMEP are developed from climatological ozone-sonde datasets.

All models used offline meteorology in which the ABL heights were calculated. Annual medians of the atmospheric boundary layer heights at 4 PM and 4 AM were compared among the models. The comparison of spatial distribution of ABL heights at 4 PM and 4 AM shows that over water, the ABL heights have not much variability in all models (Supplements 2, S26 & S27). The lowest ABL height over water was used for CHIMERE. This corresponds to the high $PM_{2.5}$ concentrations simulated by this model over water. Over land, the comparison of spatial distribution at 4 PM to 4 AM display more variable ABL heights: during nighttime the ABL heights are up to 200 m whereas during daytime the heights increase to 1000 m or higher (Supplements 2, S26 & S27). Over land the input in CAMx, CHIMERE, CMAQ and LOTOS-EUROS has a higher median ABL at 4 PM whereas in EMEP it is contrary with showing highest median at 4 PM mainly over water areas. Yet, there was no large deviation in $PM_{2.5}$ concentration simulated by EMEP to concentrations received from other models. Generally, due to ABL dynamics deviations from measured to simulated data can be expected because measurement stations were chosen close to the coast, which leads to uncertainties. In these areas, the measurements are influenced by air masses either coming from water or coming from land. In addition, measured data was received from one measurement point, which is hardly representative for a whole grid cell of 12 x 12 km².

The treatment of dust, sea salt and the used boundary conditions have an effect on the analysis and comparison of PM results, because these parameters part of the $PM_{2.5}$ formation but differ among the models.

Regarding the CTMs performance, reasons for underestimations of $PM_{2.5}$ were already discussed in previous studies: For CAMx, Pepe et al. (2019) linked these underestimations to meteorological parameters and to the overestimation of the vertical mixing in the lower atmosphere. Tuccella et al. (2019) found underestimations of $PM_{2.5}$ in the CHIMERE model and explained these by an excess of wet scavenging in the model. An excess of wet scavenging in CHIMERE compared to the other CTM systems is not found in the present study, thus it cannot be used as explanation for deviations here. In EMEP, differing from the other CTM systems, the MARS module was used to calculate the equilibrium between the gas and aerosol phases; this model does not treat sea salt or dust, leading to underestimations of $PM_{2.5}$. Kranenburg et al. (2013) linked the underestimation of particulate matter

in LOTOS-EUROS to the missing descriptions of SOA processes in the model. Thus, various reasons and combinations of reasons can lead to underestimations of $PM_{2.5}$ in the CTM systems used herein. For a better understanding, the inorganic particle species are considered in the present study. Consideration of inorganic as well as organic particles could lead to more uncertainties. Besides, in shipping emissions the inorganic aerosols display a higher share.

Large part of $PM_{2.5}$ is secondary, therefore underestimations can be linked to underestimations of precursors, e.g., NO_2. This was already shown in the first part of this intercomparison study, where all five CTM systems underestimated measured NO_2 (Fink et al., 2023a). Also SO_2 is usually underestimated by CTMs, as shown in previous studies (e.g. Eyring et al., 2007). Four out of five CTM systems underestimate the observed $PM_{2.5}$ concentration in the present study. Gaseous precursors like SO_2 and NO_2 need to be oxidized before they can form particles in reactions with ammonia. The hydroxyl radical (OH) is the main oxidant. The amount of available OH can be analyzed when the NO_2 concentration is set in relation to HNO_3 and NO_3^- (Supplements 2, S23).This gives an indication about the OH availability. In ship plumes OH is consumed fast, therefore values are low along the shipping lanes. In regions with lower NO_2 concentration more OH is available and HNO_3 is efficiently formed. In the present study, the HNO_3 was similar within all five CTM systems (Supplements 2, S4).

One reason for the differences in HNO_3 might be traced back to the amount of cloud droplets, since HNO_3 is resolved in it. The dissolution of gases in droplets is usually assumed to be irreversible for HNO_3 and NH_3 in CTMs; thus, the amount of formed ammonium nitrate mass depends on the amount of HNO_3 or the cloud droplets. This could lead in the end to the deviation among the CTMs simulated HNO_3.

The preference of NH_4^+ to bind to SO_4^{2-} in atmospheric aerosols to form $(NH_4)_2SO_4$ explains why in some models NO_3^- displays relatively low values when the SO_4^{2-} concentration is high. CHIMERE, for instance, has a NO_3^- share of 3.1 % to total $PM_{2.5}$ and a SO_4^{2-} share of 27.0 %, whereas in the CAMx results, NO_3^- had a share of 11.1 % to total $PM_{2.5}$ and a SO_4^{2-} share of 14.6 %. This can be confirmed by the low SO_2 concentration and high SO_4^{2-} concentration in CHIMERE (Supplements 2, S11 & S19), indicating that sulfate is formed more efficiently compared to CAMx. Furthermore, this leads to lower NO_3^- concentration in CHIMERE output (Supplements 2, S21). Also for SO_2 and SO_4^{2-} concentration cloud water and amount of cloud droplets plays an important role.

Regarding the thermodynamic equilibrium within the models, ISORROPIA and ISORROPIA II mechanisms are used in all CTM systems except EMEP, meaning similar results can be assumed to be obtained from this mechanism. Despite this similarity, differences in concentrations may be a result of differences in available cloud water, vertical mixing, the spatiotemporal distribution of emissions or aerosol size distributions. EMEP uses the MARS module to calculate the equilibrium between the gas and the aerosol phase. Although four of five models use the ISORROPIA or ISORROPIA II mechanisms for inorganic secondary aerosol formation, many factors within these models still cause significant differences among the model outputs.

The aerosol size distribution also has an impact on the particle species distribution. As displayed in Table 2 (Section 4.1.1), there are two concepts how the aerosol size distribution is represented within the models, either the distribution in bins or in log-normal modes. As already discussed in Solazzo et al. (2012) the PM chemical composition differs greatly with the particle size. Consequently, differences in modelling the aerosol size distribution also affects the chemical composition. In CMAQ, for example, large fractions of nitrate and ammonium can be found in the coarse mode where they undergo other removal processes than in the fine mode.

Although there is harmonization in terms of the input emission data in the present study, the internal model mechanisms used to calculate particulate matter lead to differences in the particle species distribution, as discussed in Sect. 5.2.1. In addition, the calculations how to determine $PM_{2.5}$ vary among CTM systems or even within one CTM. As an example, there are two possibilities for calculating $PM_{2.5}$ within CMAQ: either online during the model run with the $PM_{2.5}$ module or subsequently by calculating the value as the sum of two modes. These different options lead to different results (as shown by Jiang et al., 2006) and will also affect the particle composition. In the present study, the sum of two modes is used in CMAQ.

Model simulations with relatively high $PM_{2.5}$ concentrations display higher absolute shipping impacts on $PM_{2.5}$, as presented in Sect. 5.2.2. Consequently, relatively low variability in the relative potential ship impacts among the models compared to that of the absolute values could be expected. For a more quantitative evaluation, relative potential ship impact is plotted against absolute potential impact. A larger incline of the regression line can be explained by a higher background $PM_{2.5}$ concentration, thus relative ship impact is lower for the same concentration increase (e.g. EMEP and CHIMERE; Supplements 2, S29).

From the ISORROPIA and ISORROPIA II mechanism, it can be expected that the molar ratios between the acids on the one side (NO_3^- and SO_4^{2-}) and the base on the other side (NH_4^+) are in balance. However, the ratio between SO_4^{2-}, NH_4^+ and NO_3^- shows that the balance in all models expect LOTOS-EUROS is not given for $PM_{2.5}$; sulfate plus nitrate is much higher compared to ammonium (Supplements 2, S30). This balance is almost perfectly given in LOTOS-EUROS, although both, CMAQ and LOTOS-EUROS, used the ISORROPIA II mechanism. Especially at the shipping lanes, an imbalance among the inorganic particle species is present. Differences of particle species ratio among the models can be traced back to the differences in particle size distribution. Contrary to the other models, CAMx has only three species in the coarse mode: coarse others primary, coarse crustal and reactive gaseous mercury. For NO_3^- and SO_4^{2-}, the ratio between the fine and coarse mode is calculated for the CTMs (Supplements 2, S31 & S32). NH_4^+ was not considered here since it is only in present in coarse mode in CMAQ. These ratios show that CHIMERE and LOTOS-EUROS have only a small proportion of particles in coarse mode. For SO_4^{2-} in LOTOS-EUROS the coarse particle concentration is zero and for EMEP no SO_4^{2-} is present in coarse mode. In CMAQ a higher concentration of particles is assigned to the coarse mode, also for NH_4^+.

The present study has shown that different reasons can cause deviations among the simulated $PM_{2.5}$ CTM outputs. Major reasons are the differences in size distribution and how models distribute chemical species among the coarse and fine mode ($PM_{2.5}$ and PM_{10}). Differences among the modeled $PM_{2.5}$ concentrations can also be a result of the differences in the height of the lowest model layer and the way in which ship emissions are distributed among the layers. As shown in Fink et al. (2023a) the vertical distribution of $PM_{2.5}$ precursor emissions varies among the models, e.g. in CAMx all shipping emissions are assigned to the lowest layer. This leads to differences in chemical transformations because of different concentration levels close to the source and consequently to deviations among the particle distributions. Furthermore, precipitation differences lead to variations among the model outputs for wet deposition.

Limitations of the present study are that only the chemistry of the lowest layer is evaluated. The model input was standardized as far as possible, but meteorological input data varied and is not compared in detail here. Interactions between fine and coarse particles are only studied to a limited extent, the same holds for aqueous chemistry, which has an impact on oxidation mechanisms of sulfur species.

5.3 Publication III: Determining improved VOC emission factors of ship plumes with the aerosol box model MAFOR

The following chapter corresponds to results and discussion in the preliminary manuscript of the same name authored by:

Lea Fink, Matthias Karl, Andreas Weigelt, Pauli Simonen

and will be submitted in the near future.

5.3.1 Dilution of gases and particles between ships and background

To obtain more representative ship emissions, the emission process from the stack to the background air should be considered. Therefore, the emission process, e.g., in-plume chemistry and aerosol dynamics, should be addressed due to the extremely nonlinear reactions among gases and particle coagulation (Karl et al., 2020).
As described in Sect. 4.2.2, the initial dilution of gases with fast cooling and expansion of the initial plume volume was performed as that described in Karl et al. (2020) by using a dilution ratio of 1:8. This initial expansion ends with the initiation of the MAFOR model at one second after the plume leaves the stack. The dilution after MAFOR model initiation follows the parametrization of Chosson et al. (2008) for the convective boundary layer to match the modeled concentrations in the ship plume. The parameters for plume dispersion were not adjusted and used as provided in the MAFOR model. The parameters for plume dispersion in the MAFOR model and the original parameters of Chosson et al. (2008) are listed in Table G1 in Appendix G. In addition to particle nucleation, condensation, and coagulation, dry deposition of particles and gas-phase chemistry inside the plume, the model considers the mixing of air parcels with gases and particles in the background air.

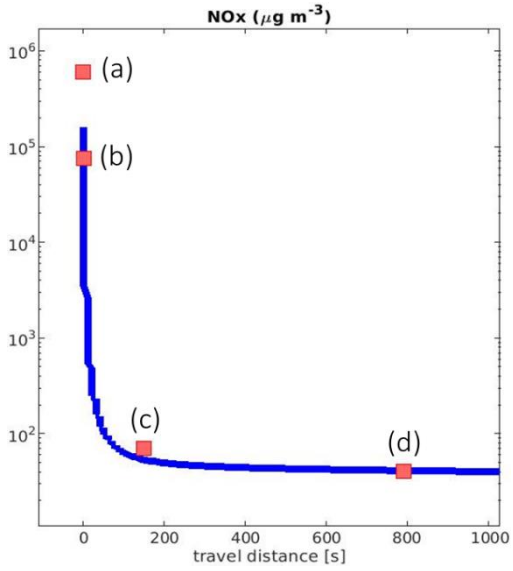

Figure 35: Dilution of NO_x, dark red dots are the measured NO_x values. (a) = Stack, (b) = Stack with 1:8 dilution, (c) = Sniffer, (d) = Background.

NO_x dilution simulated by MAFOR suitably agrees with the observations at the sniffer location and the background concentrations (Figure 35). The dilution curve of NO_x serves as a base for the dilution of other chemicals. Particles in the MAFOR model evolve at the model starting time one second after the exhaust leaves the stack.
As described in Sect. 4.2.1, the peaks of the NO_x concentration and the particle number concentration at the shore-based sniffer station were measured at 17:41:00 UTC (Appendix A). There was one additional peak of the NO_x concentration observed at 17:42:00 UTC. Additionally, in regard to the particle number concentration, two peaks were observed at 17:41:37 and 17:42:42 UTC. The aerosol measurements were obtained at a high temporal resolution, and the aerosol instrument response time was shorter than that of the NO_x sensor. Thus, the exact peak time could be slightly shifted and recorded. The explanation of the two peaks is the meandering behavior of the ship plume. In addition, the ship is moving, and the plume released one minute after the first plume may follow a different path.

5.3.2 Aerosol size distribution

MAFOR was used to calculate the changes in the exhaust particle size distribution over time with increasing downwind distance from the ship stack. MAFOR was adopted to simulate the particle size distribution starting with the input mass concentrations. The measured particle background concentrations were observed at the same station as the plume measurements but at a different time. The station was located 530 m from the shipping lane. As shown in Fig. 36, there is a number concentration peak in the Aitken mode for the measured background particles, indicating a certain influence of shipping-related emissions or other sources of UFPs.

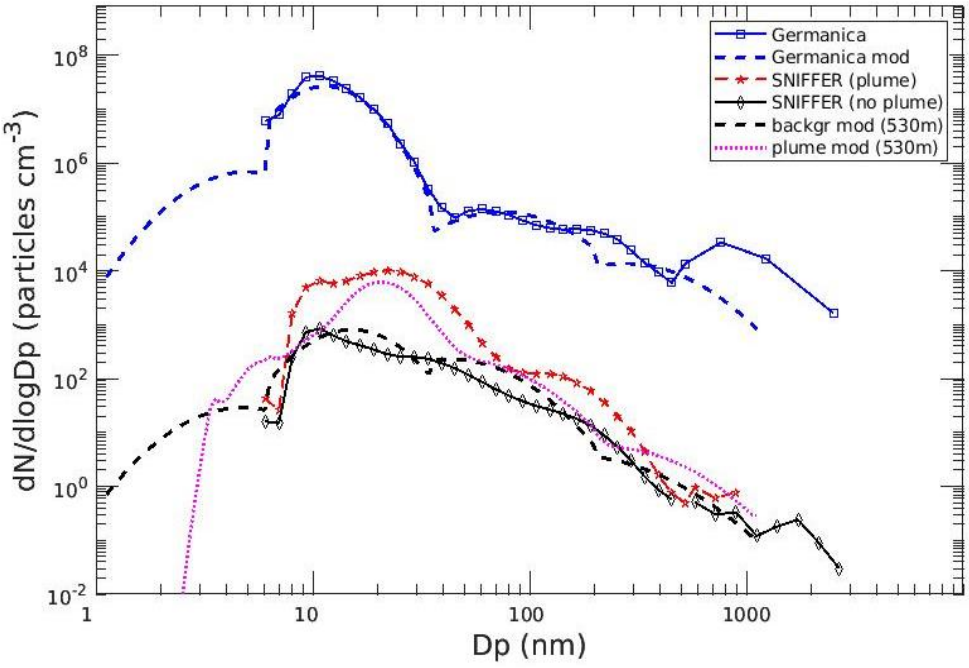

Figure 36: Comparison of the modeled particle size distributions with the observed particle size distributions. "Germanica" = measured particle size distribution at the stack. "Germanica mod" = simulated particle size distribution at the stack. "SNIFFER (plume)" = particle size distributions recorded at the Sniffer at the plume arrival. "SNIFFER (no plume)" = particle size distributions recorded at the Sniffer without a plume event. "backgr mod (530 m)" = simulated particle size distribution at the Sniffer without a plume event. "plume mod (530 m)" = particle size distributions simulated at the Sniffer at the plume arrival.

In this study, one peak was found at 15 nm (Figure 36). The 25th and 75th percentiles of the median of each bin for the measured data at the ship location and at the sniffer location without a plume are provided in Appendix H. Regarding the plume at the sniffer location, only the measurement with the highest concentration was considered; thus, no percentiles are displayed.
The EF for VOCs was adjusted as described in Sect. 2.2, and the amount of converted H_2SO_4 from SO_2 was set according to the concentrations retrieved from Karl et al. (2020). With these settings, the simulated plume particle size distribution at a 530 m distance (Figure 36, magenta line) was optimized to narrow the discrepancy with the measured data at the sniffer location (Figure 36, red line). This was done to obtain a correction factor by comparing several scenarios of the modeled output against the measured data from the sniffer station in regard to the number concentration and size distribution (Sect. 5.3.3; Table 14). Only slight variations in the measurements on Germanica and at the measurement station were found, as the revealed by the 25th and 75th percentiles (Appendix H).

It has been previously shown that the particle number size distribution of fresh diesel exhaust exhibits a bimodal character (Karl et al., 2020). The measured size distribution at the sniffer station (Figure 36) exhibits a bimodal structure, indicating that the plume concentration has not yet reached the background concentration. Similar to this study, Pirjola et al. (2014) found one dominating peak for the number size distribution in the Aitken mode, with one predominant size distribution in two modes and the dominating mode peaking from 20 nm to 30 nm. Nevertheless, the position of the maximum varied between 30 and 50 nm depending on the type of vessel; thus, comparing the results of this work with those of previous studies is hardly possible.
Karl et al. (2020) applied the emission factor for the particle number concentration obtained by Moldanova et al. (2013) directly to exhaust flow. However, no data were obtained from measurements on the ship at the same time as those on land, as was done in the considered investigations.

5.3.3 Comparison between simulated and measured data

Numerous particle size distributions with different VOC emission factors were calculated by the MAFOR model to simulate the particle concentration in the plume at the sniffer station. All the model results were evaluated by comparing them to the measured particle size distribution. In this comparison, particle size classes were defined following the size class distribution reported by Karl et al. (2022) by fitting the modeled size distribution with the size classes (bins) of the measured size distribution. In the common classes, the integral number concentration and mean diameter of the modeled data were compared to those of the measured data (Table 14).

The best fit was selected based on the differences in size classes S2 to S5. Larger size classes were not used because of the high uncertainty caused by the fluctuations in the effective density of soot particles that could generate a systematic error of approximately 20 % in PM estimation using ELPI (Maricq et al., 2006). Regarding the small size classes (< 15 nm), particle measurements suffer higher uncertainty due to the lower particle charging efficiency or higher diffusion loss (Wang et al., 2016). The smallest total difference between the measured and modeled values was found when multiplying the initial EFs for all VOCs by a factor of 1.7 (Table 14). The best match for the number concentration and mean diameter could yield different CFs. Thus, the smallest total difference was based on the sum of the absolute difference of the relative deviation for the number concentration plus the sum of the difference of the relative deviation for the mean diameter in size classes S2 to S5 under the respective scenario.

The original VOC EF from the previous measurements was adopted and multiplied by the NO_x EF change factor in the first step to approximate the magnitude of VOC EF change. However, the changes in the NO_x and VOC EFs might not be of the same magnitude, and the factors might not be adopted directly. This explained the necessity to correct via several correction factors relative to the measurements, and the factor with the best agreement was used then for further the calculations.

The relative differences between the simulated and measured data could either be positive (simulated values < measured values) or negative (measured values < simulated values). If there was under- or overestimation of the VOCs, there could be a shift in the peak and a change in the distribution of the particles in the various size ranges. This occurs because all VOC EFs were adjusted, i.e., all volatility classes were adjusted. This also resulted in different deviations (positive or negative) in size classes S1 to S7.

Table 14: Size ranges of the size classes S1:1nm -10 nm; S2: 10nm -20 nm; S3: 20nm -50 nm; S4: 50nm -100 nm; S5: 100nm -300 nm; S6: 300nm -600 nm; S7: > 600 nm; differences are referring to the relative deviations of the modeled and measured data. CF = correcting factor. 1.0 means no changes, because the CF is 1.

Difference in number concentrations compared to measurements (in %)								
CF	**S1**	**S2**	**S3**	**S4**	**S5**	**S6**	**S7**	**|S2|+|S3|+ |S4|+|S5|**
0.50	7.78	36.69	-115.56	3.66	-6.59	77.82	82.96	162.50
0.60	-0.29	35.35	-92.83	3.78	-6.03	77.87	83.01	137.99
0.70	-11.34	33.61	-74.69	3.88	-5.47	77.92	83.06	117.65
0.80	-20.56	31.56	-59.88	4.00	-4.92	77.97	83.11	100.36
0.90	-28.19	29.24	-47.53	4.10	-4.34	78.03	83.16	85.21

1.00	-34.37	26.73	-37.30	4.21	-3.78	78.07	83.21	72.03
1.10	-39.52	24.06	-28.67	4.33	-3.23	78.12	83.26	60.29
1.20	-44.01	21.16	-21.16	4.46	-2.67	78.17	83.31	49.45
1.30	-47.90	18.19	-14.84	4.61	-2.11	78.22	83.36	39.75
1.40	-51.44	15.04	-9.26	4.77	-1.56	78.27	83.41	30.62
1.50	-54.82	11.68	-4.33	4.97	-1.00	78.31	83.46	21.99
1.60	-57.95	8.24	-0.04	5.19	-0.46	78.36	83.50	13.93
1.70	-60.94	4.65	3.76	5.45	0.06	78.41	83.55	13.92
1.80	-63.89	0.91	7.16	5.75	0.57	78.46	83.60	14.39
1.90	-66.68	-2.96	10.19	6.10	1.05	78.50	83.65	20.30
2.00	-69.42	-6.97	12.91	6.47	1.53	78.55	83.70	27.89

Difference in mean diameter compared to measurements (in %)

CF	**S1**	**S2**	**S3**	**S4**	**S5**	**S6**	**S7**	**|S2|+|S3|+ |S4|+|S5|**
0.50	17.48	3.13	12.32	-12.29	7.86	-3.34	6.21	35.60
0.60	21.45	1.92	12.47	-12.30	7.84	-3.35	6.20	34.54
0.70	22.54	0.81	12.51	-12.33	7.83	-3.35	6.19	33.48
0.80	23.22	-0.20	12.48	-12.35	7.81	-3.36	6.18	32.84
0.90	23.51	-1.14	12.37	-12.36	7.79	-3.37	6.17	33.66
1.00	23.51	-1.96	12.21	-12.38	7.77	-3.37	6.17	34.32
1.10	23.31	-2.71	12.00	-12.39	7.75	-3.38	6.16	34.85
1.20	22.98	-3.38	11.75	-12.39	7.73	-3.39	6.15	35.26
1.30	22.56	-3.97	11.48	-12.38	7.71	-3.40	6.14	35.54
1.40	22.12	-4.50	11.19	-12.36	7.68	-3.40	6.13	35.74
1.50	21.62	-4.97	10.87	-12.33	7.66	-3.41	6.12	35.83
1.60	21.12	-5.37	10.54	-12.29	7.63	-3.42	6.11	35.84
1.70	20.62	-5.73	10.19	-12.24	7.60	-3.42	6.10	35.76
1.80	20.09	-6.04	9.83	-12.18	7.56	-3.43	6.10	35.61
1.90	19.59	-6.30	9.47	-12.10	7.52	-3.44	6.09	35.39
2.00	19.06	-6.52	9.09	-12.02	7.48	-3.45	6.08	35.11

5.3.4 CMAQ with adjusted VOC emissions

With the help of the adjusted VOC emissions derived from the smallest-difference fit between the modeled and observed particle size distributions (Sect. 3.3), the ship emissions for the CTM run were modified. The MAFOR model contains three volatility classes for primary organic aerosols represented by PIOV (intermediate volatile), PSOV (semivolatile) and PELV (extremely low-volatile; Karl et al., 2022).

The volatilities of organic compounds in the CMAQ model are calculated internally in this model based on the volatility basis set (VBS) approach (Donahue et al., 2006; Robinson et al., 2007), providing a framework for gas aerosol partitioning and chemical aging of both POAs and SOAs. The CMAQ model has two basis sets for freshly emitted organic aerosols, with each set containing five volatility bins (Koo et al., 2014; Murphy et al., 2017).

The same adjustment factor (Eq. 4.5) was used to adjust the VOC emissions in all volatility classes. VOC emissions enter the CMAQ model as POCs. Although in the CMAQ model, many more (nonmethane) VOCs are included in the CB05 mechanism, regarding the connection with the MAFOR model, only POCs are used, including semi- and low-volatile VOCs.

During the preprocessing of CMAQ emissions, the derived STEAM ship emissions are added to the land-based emissions, and the pollutants are assigned to the chemical species of CB05 in the CMAQ model. In this process, the STEAM VOC emissions are multiplied by the adjustment factor *f_STEAM* with a value of 60.5. There was only one EF for the VOCs, which was not divided into the VOC groups provided by the STEAM. The other substances derived from the STEAM, as listed in Sect. 4.1.4.2, remained unchanged.

The CMAQ simulations with adjusted VOC ship emissions are compared to simulations without VOC emissions adjusted for the effect on $PM_{2.5}$. The increase in VOC ship emissions by a factor of 60.5 causes an increase in the $PM_{2.5}$ concentration along the major shipping routes by up to 5 % (Figure 37).

VOCs react with nitrogen oxides (NO_x) originating from various emission sources to form ozone (O_3) under sunlight. Most primary organic-particulate emissions are semivolatile; thus, to a certain extent, they evaporate accompanied with atmospheric dilution, generating large amounts of low-volatility gas-phase material. Photooxidation initiates the formation of particles, as it results in the generation of abundant precursors for the nucleation and growth of fine particles in air (Wang et al., 2015, Guo et al., 2020). Experiments in the laboratory indicate that photooxidation of diesel exhaust rapidly produces organic aerosols (Robinson et al., 2007). Particularly in summer, the aerosol mixing ratios in the Mediterranean area are higher than those in most continental European regions (Debevec et al., 2018).

In this study, the highest increase was found in June (Figure 37 c), with a growth in the total $PM_{2.5}$ mass ranging from 3 % to 5 % over water. In the colder months of December and March with less solar radiation, the increase in the $PM_{2.5}$ concentration varied between 0 % and 2 % (Figure 37 a, d). This indicates that the impact of VOCs on the concentration of $PM_{2.5}$ is relatively limited in the winter and early spring, which is similar to the results of the sensitivity study of Lee et al. (2023) and can explained by increased speed of chemical reactions at high temperatures .

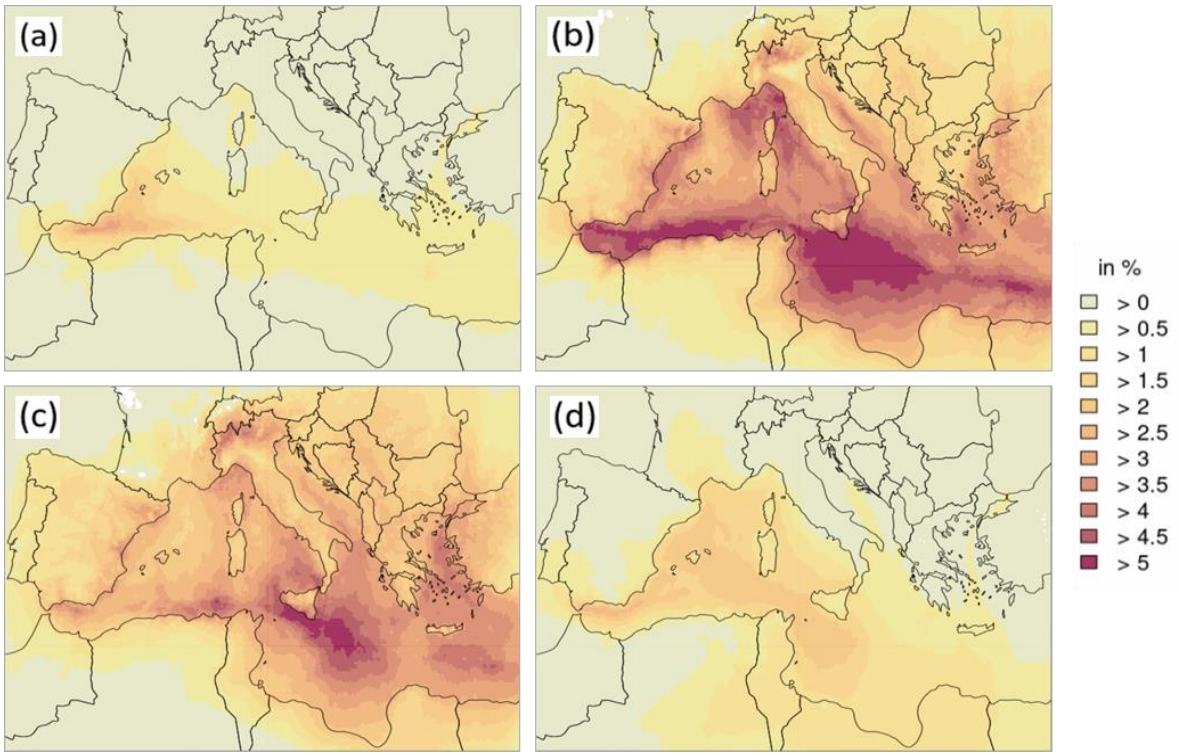

Figure 37: Change in $PM_{2.5}$ for the CTM run with adjusted ship emissions to initial ship emissions, displayed as mean values for (a) = March 2015; (b) = June 2015; (c) = September 2015; (d) = December 2015.

6 Summarizing conclusions

As the final part of this work, the research questions raised in Sect. 2.1 are answered, and an overall conclusion and outlook are given.

In this thesis, the magnitude of the impact of ships on the concentrations of air pollutants NO_2, O_3 and particles was examined, the difference between regional scale CTMs was determined, and plume and aerosol formation were analyzed in detail. Furthermore, possible limitations as well as over- and underestimation of the model outputs were noted through model intercomparison. The $PM_{2.5}$ model performance and detailed investigation of inorganic particle species and the in-plume particle formation process were investigated, as aerosols and their formation are the focus of this thesis.

The research results of this work indicated that the data obtained with regional scale chemical transport models deviated from measured air pollutant concentrations and could cause underestimation of the measured concentrations of NO_2 (a particle precursor) and $PM_{2.5}$. This could be traced back to the dilution of emissions on a large scale, where important processes in terms of aerosol formation could not be considered. For a detailed investigation of the in-plume processes, simulations with a box model were conducted. The ship emissions of regional scale CTMs were adjusted based on the box model output. The subsequent evaluation of the simulation results of a regional scale CTM showed an increase in $PM_{2.5}$ ship emissions after emission adjustment.

(1) What is the influence of ships on air pollution in coastal areas concerning the photooxidants NO_2 and O_3 as well as $PM_{2.5}$ and inorganic aerosol species?

This question was addressed in the research reported in the first and second publications (refer to the results in Sect. 5.1 and 5.2).

The influence on coastal areas differed depending on the considered air pollutants. The potential impact of ships on NO_2 at several stations in one area, as shown in Supplements 1, S3-S10, indicated a mean value up to 48.1 %. The influence of ships on NO_2 in most coastal regions reached 25 %. As it is strongly connected to NO_2, secondary air pollutant O_3 was considered as well. NO_x originating from ships led to a decrease in the O_3 concentration by down to -20 % in areas close to emission sources. The results indicated values mainly between 6 % and 9 % for the total O_3 concentration in coastal areas.

The relative ship impact on $PM_{2.5}$ simulated by the CTMs was 15 % of the total $PM_{2.5}$ concentration in most coastal regions.

Secondary inorganic particle species SO_4^{2-}, NH_4^+ and NO_3^- represented a large fraction of the overall $PM_{2.5}$ composition. They were investigated to determine how the respective models calculate each species to obtain an indication regarding the composition of the total $PM_{2.5}$ concentration. SO_4^{2-} was the main contributor to the total $PM_{2.5}$ concentration stemming from shipping. In coastal areas, the potential impact of ships on SO_4^{2-} ranged from 6 % to 20 %. The spatial distribution of the NH_4^+ ship impact pattern was similar across the CTMs; in coastal regions, the models yielded values of up to 10 %. The relative potential impact of ships on NO_3^- in coastal areas and Italy varied between 10 % and 25 %, whereas along the main shipping routes, it ranged from 50 % to 65 % or even reached 85 %.

Overall, the results of this research showed that ships could greatly impact the air quality in coastal regions in the whole investigated domain, independent of the air pollutants. This could entail a positive (e.g., NO_2, $PM_{2.5}$, and SO_4^{2-}) or negative (O_3 and NO_3^- in some models) impact.

a. How much do regional scale CTMs deviate from each other when simulating air pollutants and deposition, and how well do they perform compared with observed data?

To answer this question, model performance analysis and comparison of CTMs are crucial to obtain the range in which the various models simulate air pollution and to determine how well they can mirror the observed concentrations (refer to the results in Sect. 5.1 & 5.2). Concerning the results for NO_2, the model performance showed differences in the time series among the various models for several reasons. The difference could be traced back to i) the large grid size, ii) the differences in meteorology, iii) the small-scale heterogeneity, which can hardly be captured by regional CTMs, leading to excessively high dry deposition or underestimation of natural emissions at remote stations. All five CTMs underestimated the observed NO_2 concentration data at most stations.
A relatively favorable model performance for O_3 was obtained by all five CTMs, as shown in the correlation when comparing modeled and observed data (R = 0.38 to 0.69). Nevertheless, the outputs differed in the spatial distribution and potential ship impact over water. In contrast to NO_2, overestimation of the simulated O_3 concentrations was found at almost all stations.
Contrary to the photooxidants, the spatial and temporal resolutions of the $PM_{2.5}$ model results showed a more diverse pattern and higher deviations among the CTMs. This was indicated by the correlation between the models: the correlation for the O_3 model results was moderate to high, whereas that for NO_2 and $PM_{2.5}$ was mostly low, with a moderate correlation only in some cases (R = 0.02 to 0.54). Furthermore, the results showed that the observed $PM_{2.5}$ concentrations were underestimated by four of the five CTMs.
Another aim of this thesis was a detailed investigation of inorganic particle species because they play an important role in ship emissions. The share of inorganic particle species in the total $PM_{2.5}$ concentration mirrored the diverse pattern of $PM_{2.5}$ among the various models. In general, it was found that in models simulating high SO_4^{2-} concentrations, the NO_3^- concentrations were lower. There were no measurements to assess the model performance by comparing measurement data of inorganic particle species with observational data.
Further evaluation in this thesis was performed of dry and wet deposition mechanisms, as they are linked to atmospheric concentration of air pollutants in CTM systems. The model results for dry deposition showed a higher variability between the model outputs relative to the air concentrations of the respective pollutants. Dry deposition was higher over land areas than over water areas due to the higher deposition rates over land. Wet deposition is usually closely linked to the precipitation amount. In the present investigations, wet deposition differed among the various models even for the same meteorological data, indicating that the concentration and model internal mechanisms caused differences rather than the input data.
When answering the first question regarding the impact of shipping on coastal regions and the second question on model performance and deviations, the next point was raised on why the models differ although they use the same emission data:

b. What is causing the uncertainty in regional scale models when one uncertainty factor, namely, emissions, is the same across all models?

Emissions were harmonized to exclude the source of uncertainty originating from the emission input dataset. This was done to shed light on what factors other than the emission data could lead to differences between individual model results. Different CTM systems should simulate the impact of shipping based on the same emissions as input data as well as the same domain and grid resolution.

For all investigated air pollutants, the results in this thesis indicated that the large grid size, meteorology, vertical distribution and boundary conditions led to uncertainties and deviations between the model outputs. In addition, dry and wet deposition influenced atmospheric concentrations because air pollutants are sensitive to the deposition velocity and the precipitation amount.

It could be shown that the large grid size is an uncertainty factor mainly leading to underestimation of the measured concentrations of air pollutants. Important to mention is the direct dilution of emissions from the point source to the scale of the grid. Regional scale models with relatively coarse grid resolutions usually cannot describe chemical transformation mechanisms and physical processes (e.g., condensation, evaporation, and coagulation) within ship exhaust gas plumes. Typically, they assume the direct dilution of emissions and disregard the in-plume chemistry at high pollutant concentration levels.

The ABL height as part of the meteorological data was found to cause uncertainties in the performance of the CTMs. In coastal areas, the observations are influenced by air masses either coming from water or coming from land. This might not be represented well in the CTM systems due to the coarse resolution.

Several reasons for uncertainties and differences between the CTMs outputs were found and investigated within this work. Although in the model simulations emissions were harmonized, the vertical distribution of the emissions differed and only the lowest model layer was evaluated during the intercomparison. Dust and sea salt emissions were not harmonized and calculated differently within the CTMs, thus leading to uncertainties in total PM (coarse and fine for sea salt).

In the present thesis, it was shown that higher uncertainties could be expected for $PM_{2.5}$ concentrations compared to concentrations of NO_2 and O_3 due to the underlying particle formation processes. In Sect. 5.2.5 the reasons leading to variable outputs regarding $PM_{2.5}$ were discussed, but the complexity of particle treatments within the models, as well as the large number of causes of these changes made it difficult to find a single reason. One point causing uncertainties were the differing aerosol-formation mechanisms of the CTMs. The detailed investigation of $PM_{2.5}$ and its chemical composition has demonstrated that differences among the particle species might be traced back to the aerosol size distribution. This was shown especially for CMAQ regarding the balance of the inorganic particle species NO_3^- and SO_4^{2-} on the one side and NH_4^+ on the other side. CMAQ and EMEP tend to assign a higher particle mass to the coarse mode compared to the other three CTMs. This has implications for particle deposition because both, wet and dry deposition are more efficient for larger particles.

All these uncertainties display that using only one chemical transport model can result in underestimated model uncertainty and overconfidence in the conclusions. Particularly in terms of the policy point of view, one ensemble model mean or median is important: If model simulations are used to support in decision-making regarding shipping regulations, the uncertainty of individual models must be considered. Additionally, CTM runs with a smaller grid resolution might give a more detailed concentration distribution. Considering the particles and the aerosol formation in detail, one could use another type of atmospheric models, such as the Lagrangian models or box models.

To obtain more precise information regarding effects of shipping on particle concentrations, the particle size distribution and the interaction mechanisms from plume to background concentrations, as well as chemical transformations within ship plumes will be answered in the following.

(2) How large is the influence on results of regional scale CTM simulations when the plume development is considered?

This question was raised because the previous points have shown the limitations of regional scale CTMs with regard to underestimations of $PM_{2.5}$ and the lack of detailed particle formation processes. The early stage of plume dispersion can have a large impact on the chemistry within the plume. However, regional scale CTMs usually do not use parametrization of plume dispersion and particle formation for the sub-grid ship plumes.

a. How can ship plumes be represented in atmospheric chemical models?

In the present thesis, the plume representation focused on the particulate matter and particle formation. This representation was done by using measured data from a ship plume on shore and in-plume measurements. Based on data from these measurements, the aerosol box model MAFOR calculated the nucleation, coagulation, condensation and dry deposition to receive information on number and mass size distribution as well as composition distribution. In MAFOR, NO_x serves as conservation quantity that makes it possible to characterize the plumes properties independently from the location of observation. This conservation quantity was represented well by MAFOR when the simulated output was compared against measurements. Subsequently, the dilution of particles from the ship stack to the measurement station was investigated. This was evaluated by comparing the mean diameter and number concentration of measured against the modelled values. Especially for size ranges between 10 nm to 300 nm the ship plume could be represented well by the MAFOR model.
This investigation has shown that the appropriate model can give a good representation of the ship plume. Nevertheless, the used model approach has the limitation that it is based on several adjustments: A large number of processing steps have to be carried out manually, which makes it highly time-consuming and practically unsuitable to apply the MAFOR model for a large number of ships.
Information received on the plume development should be applied within a larger scale CTM for the aspects of automation in the calculation process and for the spatial distribution. This leads to the last question raised within this work:

b. How can the output of a box model be implemented in a 3-D regional scale CTM?

The approach in the present thesis was to adjust the ship emissions with help of a sectional aerosol box model to prevent from a loss of information on the in-plume chemistry.

This was done by implementing the output of a sectional aerosol box model into a 3-D regional scale CTM by adjusting the EF for the VOCs as particle precursors in ship emissions. The link between the MAFOR output and the ship emissions was the VOC EF, which was used because the VOCs are important in the formation of particles. This makes the VOCs crucial for the simulation of actual emitted particle mass on a larger scale. The information on the VOC EF were available for the ship emission inventory and it was used as input in MAFOR.
As a first step, several sensitivity runs for MAFOR VOC EFs were carried out to receive an EF with which the measured particle size distribution in 530 m distance was best represented by the model simulation. The corrected EF served as a basis for adjustments in the ship emissions by using the same adjustment factor for VOCs in all volatility classes.

The next step after running the aerosol box model was to adjust the ship emissions, which was done by correcting the VOC emission factor.
In the third step, the simulation with the regional scale CTM with the adjusted ship emissions were carried out. The CTM run with adjusted ship emissions resulted in increased $PM_{2.5}$ concentrations, especially in summer at main shipping lanes with a maximum increase of 5 % at main shipping lanes for the mean change in June.
In the present thesis, the box model was not implemented directly into the 3-D regional scale CTM, but with the corrected VOC EF and the adjusted ship emissions as an intermediate step. In future studies, other methods for including the box model into a regional scale model could be applied to compare different methods, such as diluting the box-model output to the size of a regional CTM grid cell. For implementation of box model in larger scale model, Karl et al. (2022) mentioned some specifications that need to be prepared in the large-scale model. There should be a consistency between the number and mass calculations as well as consistency in the structure of the aerosol modes and their division into size sections.
Another implementation of the box model into the regional scale CTM would be to use the dilution of particles. When the grid sizes in the regional scale model are reduced or a city scaled model is used and the MAFOR plume is diluted on this grid size, this could also lead to a change in particle concentrations in the regional scale CTM. This approach might be carried out in future investigations.

The possibilities and limitations of the implementation of the output of MAFOR into CMAQ were shown in the present study and give an insight into the link between the representation of VOCs at small scales with MAFOR and the particle formation processes and $PM_{2.5}$ concentrations in CMAQ. Limiting factor of the used approach is that the VOC EF adjustments are based on only one ship plume.

Generally, the measurements showed a wide range of temporal and spatial variability and so does the concentration and particle count. In upcoming studies, more sampling points and continuous plume measurements should be considered, e.g. with a measurement device remaining on board for a longer time period. Besides, measurements in different heights on the shore could be carried out. This might be achieved by using an observation tower at the coastline that takes measurements in different heights. Another option to measure would be by using manned aircraft to track the ship plume and get detailed information on particle number or mass in the ship plume. For indication of total rather than specific emission of gaseous pollutants, satellites can be used.

References

Agrawal, H., Welch, W. A., Henningsen, S., Miller, J. W., and Cocker, D. R.: Emissions from main propulsion engine on container ship at sea, J. Geophys. Res, 115, D23205, https://doi.org/10.1029/2009JD013346, 2010.

Agrawal, H., Welch, W. A., Miller, J. W., and Cockert, D. R.: Emission measurements from a crude oil tanker at sea, Environ. Sci. Technol. 2008, 42(19), 7098–7103, https://doi.org/10.1021/es703102y, 2008.

Aksoyoglu, S., Baltensperger, U., and Prévôt, A. S. H.: Contribution of ship emissions to the concentration and deposition of air pollutants in Europe, Atmos. Chem. Phys., 16, 1895–1906, https://doi.org/10.5194/acp-16-1895-2016, 2016.

Alfaro, S. D. and Gomes, L.: Modeling mineral aerosol production by wind erosion: Emission intensities and aerosol size distributions in source areas, J. Geophys. Res., 106, 18075–18084, doi:10.1029/2000jd900339, 2001.

Anav, A., Proietti, C., Menut, L., Carnicelli, S., De Marco, A., and Paoletti, E.: Sensitivity of stomatal conductance to soil moisture: implications for tropospheric ozone, Atmos. Chem. Phys., 18, 5747–5763, https://doi.org/10.5194/acp-18-5747-2018, 2018.

Anderson, J.O., Thundiyil, J.G. and Stolbach, A. Clearing the Air: A Review of the Effects of Particulate Matter Air Pollution on Human Health. J. Med. Toxicol. 8, 166–175. https://doi.org/10.1007/s13181-011-0203-1, 2012.

Appel, K. W., Napelenok, S. L., Foley, K. M., Pye, H. O. T., Hogrefe, C., Luecken, D. J., Bash, J. O., Roselle, S. J., Pleim, J. E., Foroutan, H., Hutzell, W. T., Pouliot, G. A., Sarwar, G., Fahey, K. M., Gantt, B., Gilliam, R. C., Heath, N. K., Kang, D., Mathur, R., Schwede, D. B., Spero, T. L., Wong, D. C., and Young, J. O.: Description and evaluation of the Community Multiscale Air Quality (CMAQ) modeling system version 5.1, Geosci. Model Dev., 10, 1703–1732, https://doi.org/10.5194/gmd-10-1703-2017, 2017.

Astitha, M., Lelieveld, J., Abdel Kader, M., Pozzer, A., and Meij, A. de: Parameterization of dust emissions in the global atmospheric chemistry-climate model EMAC: impact of nudging and soil properties, Atmos. Chem. Phys., 12, 11057–11083, https://doi.org/10.5194/acp-12-11057-2012, 2012.

Baldasano, J. M., Pay, M. T., Jorba, O., Gassó, S., and Jiménez-Guerrero, P.: An annual assessment of air quality with the CALIOPE modeling system over Spain, Sci. Total Environ., 409(11), 2163-2178, https://doi.org/10.1016/j.scitotenv.2011.01.041, 2011.

Banzhaf, S., Schaap, M., Kerschbaumer, A., Reimer, E., Stern, R., van der Swaluw, E., and Builtjes, P.: Implementation and evaluation of pH-dependent cloud chemistry and wet deposition in the chemical transport model REM-Calgrid, Atmos. Environ., 49, 378-390, https://doi.org/10.1016/j.atmosenv.2011.10.069, 2012.

Barbu, A. L., Segers, A. J., Schaap, M., Heemink, A. W., and Builtjes, P.J.H.: A multi-component data assimilation experiment directed to sulphur dioxide and sulphate over Europe, Atmos. Environ., 43(9), 1622-1631, https://doi.org/10.1016/j.atmosenv.2008.12.005, 2009.

Behera, S.N., Sharma, M., Aneja, V.P. et al. Ammonia in the atmosphere: a review on emission sources, atmospheric chemistry and deposition on terrestrial bodies. Environ Sci. Pollut. Res. 20, 8092–8131, https://doi.org/10.1007/s11356-013-2051-9, 2013

Beltman, J. B., Hendriks, C., Tum, M., and Schaap, M.: The impact of large scale biomass production on ozone air pollution in Europe, Atmos. Environ., 71, 352-363, https://doi.org/10.1016/j.atmosenv.2013.02.019, 2013.

Berge, E and Jakobsen, H.A.:A regional scale multilayer model for the calculation of long-term transport and deposition of air pollution in Europe, Tellus B: Chemical and Physical Meteorology, 50:3, 205-223, 10.3402/tellusb.v50i3.16097, 1998.

Bergström, R., Denier van der Gon, H. A. C., Prévôt, A. S. H., Yttri, K. E., and Simpson, D.: Modelling of organic aerosols over Europe (2002–2007) using a volatility basis set (VBS) framework: application of different assumptions regarding the formation of secondary organic aerosol, Atmos. Chem. Phys., 12, 8499–8527, https://doi.org/10.5194/acp-12-8499-2012, 2012.

Bessagnet, B., Pirovano, G., Mircea, M., Cuvelier, C., Aulinger, A., Calori, G., Ciarelli, G., Manders, A., Stern, R., Tsyro, S., García Vivanco, M., Thunis, P., Pay, M.-T., Colette, A., Couvidat, F., Meleux, F., Rouïl, L., Ung, A., Aksoyoglu, S., Baldasano, J. M., Bieser, J., Briganti, G., Cappelletti, A., D'Isidoro, M., Finardi, S., Kranenburg, R., Silibello, C., Carnevale, C., Aas, W., Dupont, J.-C., Fagerli, H., Gonzalez, L., Menut, L., Prévôt, A. S. H., Roberts, P., and White, L.: Presentation of the EURODELTA III intercomparison exercise – evaluation of the chemistry transport models' performance on criteria pollutants and joint analysis with meteorology, Atmos. Chem. Phys., 16, 12667–12701, https://doi.org/10.5194/acp-16-12667-2016, 2016.

Bieser, J., Aulinger, A., Matthias, V., Quante, M., and Builtjes, P.: SMOKE for Europe – adaptation, modification and evaluation of a comprehensive emission model for Europe, Geosci. Model Dev., 4, 47–68, https://doi.org/10.5194/gmd-4-47-2011, 2011a.

Bieser, J., Aulinger, A., Matthias, V., Quante, M., and van der Denier Gon, H. A. C.: Vertical emission profiles for Europe based on plume rise calculations, Environ. Pollut., 159(10), 2935-2946, https://doi.org/10.1016/j.envpol.2011.04.030, 2011b.

Binkowski, F. S. and Roselle, S. J.: Models-3 Community Multiscale Air Quality (CMAQ) model aerosol component 1. Model description, J. Geophys. Res., 108(D6), https://doi.org/10.1029/2001JD001409, 2003.

Binkowski, F. S. and Shankar, U.: The Regional Particulate Matter Model: 1. Model description and preliminary results, J. Geophys. Res., 100(D12), 26,191-26,209, https://doi.org/10.1029/95JD02093, 1995.

Bobbink, R. and Hettelingh, J.-P.: Review and revision of empirical critical loads and dose-response relationships, Report, https://www.rivm.nl/bibliotheek/rapporten/680359002.pdf, 2011.

Byun, D. and Schere, K. L.: Review of the Governing Equations, Computational Algorithms, and Other Components of the Models-3 Community Multiscale Air Quality (CMAQ) Modeling System, Appl. Mech. Rev., 2, https://doi.org/10.1115/1.2128636, 2006.

Carlton, A. G., Bhave, P. V., Napelenok, S. L., Edney, E. O., Sarwar, G., Pinder, R. W., Pouliot, G. A., and Houyoux, M.: Model representation of secondary organic aerosol in CMAQv4.7, Appl. Mech. Rev., 59(2), 51–77, https://doi.org/10.1021/es100636q, 2010.

Celik, S., Drewnick, F., Fachinger, F., Brooks, J., Darbyshire, E., Coe, H., Paris, J.-D., Eger, P. G., Schuladen, J., Tadic, I., Friedrich, N., Dienhart, D., Hottmann, B., Fischer, H., Crowley, J. N., Harder, H., and Borrmann, S.: Influence of vessel characteristics and atmospheric processes on the gas and particle phase of ship emission plumes: In situ measurements in the Mediterranean Sea and around the Arabian Peninsula, Atmos. Chem. Phys., 20, 4713–4734, https://doi.org/10.5194/acp-20-4713-2020, 2020.

Cesaroni, G., Forastiere, F., Stafoggia, M., Andersen, Z. J., Badaloni, C., Beelen, R., Caracciolo, B., Faire, U. de, Erbel, R., Eriksen, K. T., Fratiglioni, L., Galassi, C., Hampel, R., Heier, M., Hennig, F., Hilding, A., Hoffmann, B., Houthuijs, D., Jöckel, K.-H., Korek, M., Lanki, T., Leander, K., Magnusson, P. K. E., Migliore, E., Ostenson, C.-G., Overvad, K., Pedersen, N. L., J, J. P., Penell, J., Pershagen, G., Pyko, A., Raaschou-Nielsen, O., Ranzi, A., Ricceri, F., Sacerdote, C., Salomaa, V., Swart, W., Turunen, A. W., Vineis, P., Weinmayr, G., Wolf, K., Hoogh, K. de, Hoek, G., Brunekreef, B., and Peters, A.: Long term exposure to

ambient air pollution and incidence of acute coronary events: prospective cohort study and meta-analysis in 11 European cohorts from the ESCAPE Project, BMJ 2014; 348 :f7412 doi:10.1136/bmj.f7412, 2014.

Chen, R., Hu, B., Liu, Y., Xu, J., Yang, G., Xu, D., and Chen, C.: Beyond PM2.5: The role of ultrafine particles on adverse health effects of air pollution, Biochim Biophys Acta, 1860(12), 2844-2855, https://doi.org/10.1016/j.bbagen.2016.03.019, 2016.

Chipperfield, M. P. and Arnold, S. R.: NUMERICAL MODELS | Chemistry Models, CrossRef 4, 135-143, 10.1016/B978-0-12-382225-3.00249-8, 2015.

Cholakian, A.; Mailler, S.; Pennel, R.; Valari, M.; Couvidat, F.; Menut., L., Siour, G.: CHIMERE v2020r3 version (+ WRF 3.7.1 + OASIS-MCT3), model code, https://www.lmd.polytechnique.fr/chimere/2020_getcode.php, (accessed: 19.01.2023).

Chosson, F., Paoli, R., and Cuenot, B.: Ship plume dispersion rates in convective boundary layers for chemistry models, Atmos. Chem. Phys., 8, 4841–4853, https://doi.org/10.5194/acp-8-4841-2008, 2008.

Clapp, L. J. and Jenkin, M. E.: Analysis of the relationship between ambient levels of O3, NO2 and NO as a function of NOx in the UK, Atmos. Environ., 35, 6391-6405, http://dx.doi.org/10.1016/S1352-2310(01)00378-8, 2001.

Clappier, A., Thunis, P., Beekmann, M., Putaud, J. P., and Meij, A. de: Impact of SOx, NOx and NH3 emission reductions on PM2.5 concentrations across Europe: Hints for future measure development, Environ. Int.,156, 106699, https://doi.org/10.1016/j.envint.2021.106699, 2021.

Clifton, O. E., Fiore, A. M., Massman, W. J., Baublitz, C. B., Coyle, M., Emberson, L., Fares, S., Farmer, D. K., Gentine, P., Gerosa, G., Guenther, A. B., Helmig, D., Lombardozzi, D. L., Munger, J. W., Patton, E. G., Pusede, S. E., Schwede, D. B., Silva, S. J., Sörgel, M., Steiner, A. L., and Tai, A. P. K.: Dry Deposition of Ozone over Land: Processes, Measurement, and Modeling, Rev. Geophys., 58, https://doi.org/10.1029/2019RG000670, 2020.

Cofala., J., Amann, M., Borken-Kleefeld, J., Gomez-Sanabria, A., Heyes, C., Kiesewetter, G., Sander, R., Schoepp, W., Holland, M., Fagerli, H., and Nyiri, A.: Final Report. The potential for cost-effective air emission reductions from international shipping through designation of further Emission Control Areas in EU waters with focus on the Mediterranean Sea, Report, https://previous.iiasa.ac.at/web/home/research/researchPrograms/air/Shipping_emissions_reductions_main.pdf, 2018.

Colette, A., Andersson, C., Manders, A., Mar, K., Mircea, M., Pay, M.-T., Raffort, V., Tsyro, S., Cuvelier, C., Adani, M., Bessagnet, B., Bergström, R., Briganti, G., Butler, T., Cappelletti, A., Couvidat, F., D'Isidoro, M., Doumbia, T., Fagerli, H., Granier, C., Heyes, C., Klimont, Z., Ojha, N., Otero, N., Schaap, M., Sindelarova, K., Stegehuis, A. I., Roustan, Y., Vautard, R., van Meijgaard, E., Vivanco, M. G., and Wind, P.: EURODELTA-Trends, a multi-model experiment of air quality hindcast in Europe over 1990–2010, Geosci. Model Dev., 10, 3255–3276, https://doi.org/10.5194/gmd-10-3255-2017, 2017.

Corbett, J. J. and Fischbeck, P.: Emissions from ships, Science 278, 823- 824, DOI: 10.1126/science.278.5339.823, 1997.

Corbett, J. J., Fischbeck, P., and Pandis, S.: Global nitrogen and sulfur inventories for oceangoing ships, Journal of Geophysical Research-Atmospheres 104, 3457-3470, https://doi.org/10.1029/1998JD100040, 1999.

Corbin, J. C., Peng, W., Yang, J., Sommer, D. E., Trivanovic, U., Kirchen, P., Miller, J. W., Rogak, S., Cocker, D. R., Smallwood, G. J., Lobo, P., and Gagné, S.: Characterization of particulate matter emitted by a marine

engine operated with liquefied natural gas and diesel fuels, Atmos. Environ. 220, https://doi.org/10.1016/j.atmosenv.2019.117030, 2020.

COSMO Consortium: Models Supported by COSMO - COSMO Model, https://www.cosmo-model.org/content/support/software/default.htm#models (accessed: 07.09.2023).

Crutzen, P. J.: The Role of NO and NO2 in the Chemistry of the Troposphere and Stratosphere, Annu Rev Earth Planet Sci 7 (1), 443–472. DOI: 10.1146/annurev.ea.07.050179.002303, 1979.

Debevec, C., Sauvage, S., Gros, V., Sellegri, K., Sciare, J., Pikridas, M., Stavroulas, I., Leonardis, T., Gaudion, V., Depelchin, L., Fronval, I., Sarda-Esteve, R., Baisnée, D., Bonsang, B., Savvides, C., Vrekoussis, M., and Locoge, N.: Driving parameters of biogenic volatile organic compounds and consequences on new particle formation observed at an eastern Mediterranean background site, Atmos. Chem. Phys., 18, 14297–14325, https://doi.org/10.5194/acp-18-14297-2018, 2018.

Deutscher Wetterdienst (DWD): Schematic multi-modal particle size distribution with typical transformations and example particle types within each mode, Figure 4, https://www.dwd.de/EN/research/observing_atmosphere/composition_atmosphere/aerosol/cont_nav/particle_size_distribution_node.html (accessed: 04.05.2023).

Doche, C., Dufour, G., Foret, G., Eremenko, M., Cuesta, J., Beekmann, M., and Kalabokas, P.: Summertime tropospheric-ozone variability over the Mediterranean basin observed with IASI, Atmos. Chem. Phys., 14, 10589–10600, https://doi.org/10.5194/acp-14-10589-2014, 2014.

Dodge, M. C.: Effect of selected parameters on predictions of a photochemical model.: No. PB-269858; EPA-600/3-77/048., Environmental Protection Agency, Research Triangle Park, NC (USA), 1977.

Donahue, N. M., Robinson, A. L., and Pandis, S. N.: Atmospheric organic particulate matter: From smoke to secondary organic aerosol, Atmos. Environ, 43(1), 94-106, https://doi.org/10.1016/j.atmosenv.2008.09.055, 2009.

Donahue, N. M., Robinson, A. L., Stanier, C. O., and Pandis, S. N.: Coupled partitioning, dilution, and chemical aging of semivolatile organics, Environ. Sci. Technol., 40, 8, 2635–2643, https://doi.org/10.1021/es052297c, 2006.

Donahue, N. M., Epstein, S. A., Pandis, S. N., and Robinson, A. L.: A two-dimensional volatility basis set: 1. organic-aerosol mixing thermodynamics, Atmos. Chem. Phys., 11, 3303–3318, https://doi.org/10.5194/acp-11-3303-2011, 2011.

Donateo, A., Gregoris, E., Gambaro, A., Merico, E., Giua, R., Nocioni, A., and Contini, D.: Contribution of harbour activities and ship traffic to PM2.5, particle number concentrations and PAHs in a port city of the Mediterranean Sea (Italy), Environ. Sci. Pollut. Res., 21, 9415–9429, https://doi.org/10.1007/s11356-014-2849-0, 2014.

ECMWF IFS: ERA-Interim Reanalysis Data, GitHub Repository, data set and code, https://github.com/ecmwf-ifs (accessed: 07.09.2023), 2023.

EEA (European Environmental Agency): Europe's air quality status 2023: Briefing no. 05/2023, https://www.eea.europa.eu/publications/europes-air-quality-status-2023, doi: 10.2800/59526, 2023.

Emberson, L. D., Simpson, D., Tuovinen, J.-P., Ashmore, M. R. and Cambridge, H. M.: 'Towards a Model of Ozone Deposition and Stomatal Uptake over Europe', EMEP/MSC-W Note 6/00, Norwegian Meteorological Institute, Oslo, 57, 2000.

EMEP Status Report 1/2022. "Transboundary particulate matter, photo-oxidants, acidifying and eutrophying components". Joint MSC-W & CCC & CEIP & CIAM Report. https://emep.int/publ/reports/2022/EMEP_Status_Report_1_2022.pdf, 2022.

Emerson, E. W., Hodshire, A. L., DeBolt, H. M., Bilsback, K. R., Pierce, J. R., McMeeking, G. R., and Farmer, D. K.: Revisiting particle dry deposition and its role in radiative effect estimates, PNAS, 117(42) 26076-26082, https://doi.org/10.1073/pnas.2014761117, 2020.

Endresen, Ø., Sørgård, E., Sundet, J. K., Dalsøren, S. B., Isaksen, I. S., Berglen, T. F., and Gravir, G.: Emission from international sea transportation and environmental impact, J. Geophys. Res., 108 (D17), https://doi.org/10.1029/2002JD002898, 2003.

EPA: Health Effects of Ozone Pollution, https://www.epa.gov/ground-level-ozone-pollution/health-effects-ozone-pollution (accessed 23.03.2022), 2021.

Erisman, J. W., van Pul, A., and Wyers, P.: Parametrization of surface resistance for the quantification of atmospheric deposition of acidifying pollutants and ozone, Atmos. Environ., 28(16), 2595-2607, https://doi.org/10.1016/1352-2310(94)90433-2, 1994.

EU Parliament and Council: Directive 2008/50/EC of the European Parliament and of the Council of 21 May 2008 on ambient air quality and cleaner air for Europe, https://eur-lex.europa.eu/eli/dir/2008/50/2015-09-18 (accessed: 25.03.2023), 2015.

European Commission, Directorate-General for Environment, Study to support the impact assessment for a revision of the EU Ambient Air Quality Directives: final report, Publications Office of the European Union, https://data.europa.eu/doi/10.2779/327850, 2022.

European Maritime Safety Agency (EMSA): EMSA Facts & Figures 2022, https://www.emsa.europa.eu/publications/item/4945-emsa-facts-figures-2022.html (accessed 06.09.2023), 2023.

European Parliament: Directive 2008/50/EC of the European Parliament and of the Council of 21 May 2008 on ambient air quality and cleaner air for Europe, http://data.europa.eu/eli/dir/2008/50/oj (accessed: 06.09.2023), 2008.

Eurostat Press Office: World Maritime Day. Half of EU trade in goods is carried by sea, https://ec.europa.eu/eurostat/documents/2995521/7667714/6-28092016-AP-EN.pdf (accessed 03.08.2022), 2016.

Eyring, V., Isaksen, I. S.A., Berntsen, T., Collins, W. J., Corbett, J. J., Endresen, O., Grainger, R. G., Moldanova, J., Schlager, H., and Stevenson, D. S.: Transport impacts on atmosphere and climate: Shipping, Atmos. Environ., 44(37), 4735-4771, https://doi.org/10.1016/j.atmosenv.2009.04.059, 2010.

Eyring, V., Stevenson, D. S., Lauer, A., Dentener, F. J., Butler, T., Collins, W. J., Ellingsen, K., Gauss, M., Hauglustaine, D. A., Isaksen, I. S. A., Lawrence, M. G., Richter, A., Rodriguez, J. M., Sanderson, M., Strahan, S. E., Sudo, K., Szopa, S., van Noije, T. P. C., and Wild, O.: Multi-model simulations of the impact of international shipping on Atmospheric Chemistry and Climate in 2000 and 2030, Atmos. Chem. Phys., 7, 757–780, https://doi.org/10.5194/acp-7-757-2007, 2007.

Farrelly, D. J., Everard, C. D., Fagan, C. C., and McDonnell, K. P.: Carbon sequestration and the role of biological carbon mitigation: A review, Elsevier 21, 712-727, doi: 10.1016/j.rser.2012.12.038, 2013.

Fécan, F., Marticorena, B., and Bergametti, G.: Parameterization of the increase of aeolian erosion threshold wind friction velocity due to soil moisture for arid and semi-arid areas, Ann. Geophys. 17, 149–157, doi:10.1007/s00585-999-0149-7, 1999.

Fink, L., Karl, M., Matthias, V., Oppo, S., Kranenburg, R., Kuenen, J., Moldanova, J., Jutterström, S., Jalkanen, J.-P., and Majamäki, E.: Potential impact of shipping on air pollution in the Mediterranean region – a multimodel evaluation: comparison of photooxidants NO2 and O3, Atmos. Chem. Phys., 23, 1825–1862, https://doi.org/10.5194/acp-23-1825-2023, 2023a.

Fink, L., Karl, M., Matthias, V., Oppo, S., Kranenburg, R., Kuenen, J., Jutterström, S., Moldanova, J., Majamäki, E., and Jalkanen, J.-P.: A multimodel evaluation of the potential impact of shipping on particle species in the Mediterranean Sea, Atmos. Chem. Phys., 23, 10163–10189, https://doi.org/10.5194/acp-23-10163-2023, 2023b.

Finlayson-Pitts, B. J. and Pitts, J. N: Chemistry of the Upper and Lower Atmosphere, Academic Press, ISBN978-0-12-257060-5, https://doi.org/10.1016/B978-0-12-257060-5.X5000-X, 2000.

Folberth, G. A., Hauglustaine, D. A., Lathière, J., and Brocheton, F.: Interactive chemistry in the Laboratoire de Météorologie Dynamique general circulation model: model description and impact analysis of biogenic hydrocarbons on tropospheric chemistry, Atmos. Chem. Phys., 6, 2273–2319, https://doi.org/10.5194/acp-6-2273-2006, 2006.

Foley, K. M., Roselle, S. J., Appel, K. W., Bhave, P. V., Pleim, J. E., Otte, T. L., Mathur, R., Sarwar, G., Young, J. O., Gilliam, R. C., Nolte, C. G., Kelly, J. T., Gilliland, A. B., and Bash, J. O.: Incremental testing of the Community Multiscale Air Quality (CMAQ) modeling system version 4.7, Geosci. Model Dev., 3, 205–226, https://doi.org/10.5194/gmd-3-205-2010, 2010.

Fountoukis, C. and Nenes, A.: ISORROPIA II: A computationally efficient thermodynamic equilibrium model for K+–Ca2+–Mg2+–NH4+–Na+–SO42−–NO3−–Cl−–H2O aerosols, Atmos. Chem. Phys., 7, 4639–4659, https://doi.org/10.5194/acp-7-4639-2007, 2007.

Friedrich, N., Eger, P., Shenolikar, J., Sobanski, N., Schuladen, J., Dienhart, D., Hottmann, B., Tadic, I., Fischer, H., Martinez, M., Rohloff, R., Tauer, S., Harder, H., Pfannerstill, E. Y., Wang, N., Williams, J., Brooks, J., Drewnick, F., Su, H., Li, G., Cheng, Y., Lelieveld, J., and Crowley, J. N.: Reactive nitrogen around the Arabian Peninsula and in the Mediterranean Sea during the 2017 AQABA ship campaign, Atmos. Chem. Phys., 21, 7473–7498, https://doi.org/10.5194/acp-21-7473-2021, 2021.

Frohn, L. M., Ketzel, M., Christensen, J. H., Brandt, J., Im, U., Massling, A., Andersen, C., Plejdrup, M. S., Nielsen, O.-K., van der Gon, H. D., Manders-Groot, A., and Raaschou-Nielsen, O.: Modelling ultrafine particle number concentrations at address resolution in Denmark from 1979-2018 – Part 1: Regional and urban scale modelling and evaluation, Atmos. Environ., 264, https://doi.org/10.1016/j.atmosenv.2021.118631., 2021.

Galmarini, S., Makar, P., Clifton, O. E., Hogrefe, C., Bash, J. O., Bellasio, R., Bianconi, R., Bieser, J., Butler, T., Ducker, J., Flemming, J., Hodzic, A., Holmes, C. D., Kioutsioukis, I., Kranenburg, R., Lupascu, A., Perez-Camanyo, J. L., Pleim, J., Ryu, Y.-H., Jose, R. S., Schwede, D., Silva, S., and Wolke, R.: Technical note: AQMEII4 Activity 1: evaluation of wet and dry deposition schemes as an integral part of regional-scale air quality models, Atmos. Chem. Phys., 21, 15663–15697, https://doi.org/10.5194/acp-21-15663-2021, 2021.

Gao, R. and Sang, N.: Quasi-ultrafine particles promote cell metastasis via HMGB1-mediated cancer cell adhesion, Environ. Pollut., 256, 113390, https://doi.org/10.1016/j.envpol.2019.113390, 2020.

Gašparac, G., Jeričević, A., Kumar, P., and Grisogono, B.: Regional-scale modelling for the assessment of atmospheric particulate matter concentrations at rural background locations in Europe, Atmos. Chem. Phys., 20, 6395–6415, https://doi.org/10.5194/acp-20-6395-2020, 2020.

Ge, Y., Heal, M. R., Stevenson, D. S., Wind, P., and Vieno, M.: Evaluation of global EMEP MSC-W (rv4.34) WRF (v3.9.1.1) model surface concentrations and wet deposition of reactive N and S with measurements, Geosci. Model Dev., 14, 7021–7046, https://doi.org/10.5194/gmd-14-7021-2021, 2021.

Ginoux, P., Chin, M., Tegen, I., Prospero, J. M., Holben, B., Dubovik, O., and Lin, S.-J.: Sources and distributions of dust aerosols simulated with the GOCART model, J. Geophys. Res., 106(D17), 20.255-20.273, https://doi.org/10.1029/2000JD000053, 2001.

Giordano, L., Brunner, D., Flemming, J., Hogrefe, C., Im, U., Bianconi, R., Badia, A., Balzarini, A., Baró, R., Chemel, C., Curci, G., Forkel, R., Jiménez-Guerrero, P., Hirtl, M., Hodzic, A., Honzak, L., Jorba, O., Knote, C., Kuenen, J.J.P., Makar, P. A., Manders-Groot, A., Neal, L., Pérez, J. L., Pirovano, G., Pouliot, G., San José, R., Savage, N., Schröder, W., Sokhi, R. S., Syrakov, D., Torian, A., Tuccella, P., Werhahn, J., Wolke, R., Yahya, K., Žabkar, R., Zhang, Y., and Galmarini, S.: Assessment of the MACC reanalysis and its influence as chemical boundary conditions for regional air quality modeling in AQMEII-2, Atmos. Environ., 115, 371-388, https://doi.org/10.1016/j.atmosenv.2015.02.034, 2015.

Glasow, R von., Lawrence, M. G., Sander, R., and Crutzen, P. J.: Modeling the chemical effects of ship exhaust in the cloud-free marine boundary layer, Atmos. Chem. Phys., 3, 233–250, https://doi.org/10.5194/acp-3-233-2003, 2003.

Gomes, L., Rajot, J. L., Alfaro, S. C., and Gaudichet, A.: Validation of a dust production model from measurements performed in semi-arid agricultural areas of Spain and Niger, Catena, 52, 257-271, https://doi.org/10.1016/S0341-8162(03)00017-1. 52, 2003.

Gong, S. L.: A parameterization of sea-salt aerosol source function for sub- and super-micron particles, Glob. Biogeochem. Cycles, 17(4), 1097, https://doi.org/10.1029/2003gb002079, 2003.

González, Y., Rodríguez, S., Guerra García, J.C., Trujillo, J.L., García, L.:Ultrafine particles pollution in urban coastal air due to ship emissions, Atmos. Environ.,45, 28, 4907-4914, https://doi.org/10.1016/j.atmosenv.2011.06.002, 2011.

Granados-Muñoz, M. J., Sicard, M., Román, R., Benavent-Oltra, J. A., Barragán, R., Brogniez, G., Denjean, C., Mallet, M., Formenti, P., Torres, B., and Alados-Arboledas, L.: Impact of mineral dust on shortwave and longwave radiation: evaluation of different vertically resolved parameterizations in 1-D radiative transfer computations, Atmos. Chem. Phys., 19, 523–542, https://doi.org/10.5194/acp-19-523-2019, 2019.

Granier, C., Darras, S., van der Denier Gon, H., Doubalova, J., Elguindi, N., Galle, B., Gauss, M., Guevara, M., Jalkanen, J.-P., Kuenen, J., Liousse, C., Quack, B., Simpson, D., and Sindelarova, K.: The Copernicus Atmosphere Monitoring Service global and regional emissions: (April 2019 version), Copernicus Atmosphere Monitoring Service (CAMS) report, https://doi.org/10.24380/d0bn-kx16, 2019.

Guenther, A. B., Jiang, X., Heald, C. L., Sakulyanontvittaya, T., Duhl, T., Emmons, L. K., and Wang, X.: The Model of Emissions of Gases and Aerosols from Nature version 2.1 (MEGAN2.1): An extended and updated framework for modeling biogenic emissions, Geosci. Model Dev., 5, 1471–1492., https://doi.org/10.5194/gmd-5-1471-2012, 2012.

Guenther, A., Hewitt, C., Erickson, D., Fall, R., Geron, C., Graedel, T., Harley, P., Klinger, L., Lerdau, M., McKay, W., Pierce, T., Scholes, R., Steinbrecher, R., Tallamraju, R., Taylor, J., and Zimmerman, P.: A global model of natural volatile organic compound emissions, J. Geophys. Res., 100, 8873–8892, https://doi.org/10.1029/94JD02950, 1995.

Guenther, A., Karl, T., Harley, P., Wiedinmyer, C., Palmer, P. I., and Geron, C.: Estimates of global terrestrial isoprene emissions using MEGAN (Model of Emissions of Gases and Aerosols from Nature), Atmos. Chem. Phys., 6, 3181–3210, https://doi.org/10.5194/acp-6-3181-2006, 2006.

Guenther, A., Zimmerman, P., Harley, P., Monson, R., and Fall, R.: Isoprene and monoterpene rate variability: model evaluations and sensitivity analyses, J. Geophys. Res., 98, 12609–12617, https://doi.org/10.1029/93JD00527, 1993.

Guevara, M.: Emissions of Primary Particulate Matter: Sources, atmospheric processes and health, https://doi.org/10.1039/9781782626589-00001, 2016.

Guo, S., Hu, M., Peng, J., Wu, Z., Zamora, M. L., Shang, D., Du, Z., Zheng, J., Fang, X., Tang, R., Wu, Y., Zeng, L., Shuai, S., Zhang, W., Wang, Y., Ji, Y., Li, Y., Zhang, A. L., Wang, W., Zhang, F., Zhao, J., Gong, X., Wang, C., Molina, M. J., and Zhang, R.: Remarkable nucleation and growth of ultrafine particles from vehicular exhaust, PNAS, 117, 3427-3432, DOI: 10.1073/pnas.1916366117, 2020.

Halleux, V.: Revision of EU air quality legislation Setting a zero pollution objective for air, Briefing, EU Legislation in progress, https://www.europarl.europa.eu/RegData/etudes/BRIE/2023/747087/EPRS_BRI%282023%29747087_EN.pdf (accessed: 10.10.2023), 2023.

Hardacre, C., Wild, O., and Emberson, L.: An evaluation of ozone dry deposition in global scale chemistry climate models, Atmos. Chem. Phys., 15, 6419–6436, https://doi.org/10.5194/acp-15-6419-2015, 2015.

Hayden, B. P. and Pielke, R.: planetary boundary layer, https://www.britannica.com/science/planetary-boundary-layer (accessed: 13.03.2023), 2016.

Heusinkveld, H. J., Wahle, T., Campbell, A., Westerink, R. H. S., Tran, L., Johnston, H., Stone, V., Cassee, F. R., and Schins, R. P. F.: Neurodegenerative and neurological disorders by small inhaled particles, NeuroToxicology, 56, 94-106, https://doi.org/10.1016/j.neuro.2016.07.007, 2016.

Hicks, B. B., Baldocchi, D. D., Meyers, T. P., Hosker, R. P., and Matt, D. R.: A preliminary multiple resistance routine for deriving dry deposition velocities from measured quantities, Water Air Soil Pollut., 36, 311–330, https://doi.org/10.1007/BF00229675, 1987.

Hoffmann, B., Boogaard, H., Nazelle, A. de, Andersen, Z. J., Abramson, M., Brauer, M., Brunekreef, B., Forastiere, F., Huang, W., Kan, H., Kaufman, J. D., Katsouyanni, K., Krzyzanowski, M., Kuenzli, N., Laden, F., Nieuwenhuijsen, M., Mustapha, A., Powell, P., Rice, M., Roca-Barceló, A., Roscoe, C. J., Soares, A., Straif, K., and Thurston, G.: WHO Air Quality Guidelines 2021-Aiming for Healthier Air for all: A Joint Statement by Medical, Public Health, Scientific Societies and Patient Representative Organisations, Int. J. Public Health 66, 10.3389/ijph.2021.1604465, 2021.

Im, U., Bianconi, R., Solazzo, E., Kioutsioukis, I., Badia, A., Balzarini, A., Baró, R., Bellasio, R., Brunner, D., Chemel, C., Curci, G., Flemming, J., Forkel, R., Giordano, L., Jiménez-Guerrero, P., Hirtl, M., Hodzic, A., Honzak, L., Jorba, O., Knote, C., Kuenen, J. J.P., Makar, P. A., Manders-Groot, A., Neal, L., Pérez, J. L., Pirovano, G., Pouliot, G., San Jose, R., Savage, N., Schroder, W., Sokhi, R. S., Syrakov, D., Torian, A., Tuccella, P., Werhahn, J., Wolke, R., Yahya, K., Zabkar, R., Zhang, Y., Zhang, J., Hogrefe, C., and Galmarini, S.: Evaluation of operational on-line-coupled regional air quality models over Europe and North America in the context of AQMEII phase 2. Part I: Ozone, Atmos. Environ., 115, 404-420, https://doi.org/10.1016/j.atmosenv.2014.09.042, 2015a.

Im, U., Bianconi, R., Solazzo, E., Kioutsioukis, I., Badia, A., Balzarini, A., Baró, R., Bellasio, R., Brunner, D., Chemel, C., Curci, G., van der Denier Gon, H., Flemming, J., Forkel, R., Giordano, L., Jiménez-Guerrero, P., Hirtl, M., Hodzic, A., Honzak, L., Jorba, O., Knote, C., Makar, P. A., Manders-Groot, A., Neal, L., Pérez, J. L., Pirovano, G., Pouliot, G., San Jose, R., Savage, N., Schroder, W., Sokhi, R. S., Syrakov, D., Torian, A., Tuccella, P., Wang, K., Werhahn, J., Wolke, R., Zabkar, R., Zhang, Y., Zhang, J., Hogrefe, C., and Galmarini, S.: Evaluation of operational online-coupled regional air quality models over Europe and North America in the

context of AQMEII phase 2. Part II: Particulate matter, Atmos. Environ., 115, 421-441, https://doi.org/10.1016/j.atmosenv.2014.08.072, 2015b.

Im, U., Christodoulaki, S., Violaki, K., Zarmpas, P., Kocak, M., Daskalakis, N., Mihalopoulos, N., and Kanakidou, M.: Atmospheric deposition of nitrogen and sulfur over southern Europe with focus on the Mediterranean and the Black Sea, Atmos. Environ., 81, 660-670, https://doi.org/10.1016/j.atmosenv.2013.09.048, 2013.

IMO (International Maritime Organization): Guidelines for consistent implementation of the 0.50 % Sulphur limit under Marpol annex VI. Resolution MEPC.320(74), https://wwwcdn.imo.org/localresources/en/OurWork/Environment/Documents/MEPC.320(74).pdf (accessed: 20.01.2023), 2019.

IMO (International Maritime Organization): Marine Environment Protection Committee (MEPC) – 79th session, 12-16 December 2022, https://www.imo.org/en/MediaCentre/MeetingSummaries/Pages/MEPC-79th-session.aspx (accessed: 16.01.23).

IMO MEPC. MEPC 70/INF.34. Technical report, International Maritime Organization Marine Environment Protection Committee, https://wwwcdn.imo.org/localresources/en/MediaCentre/HotTopics/

Documents/Finland%20study%20on%20health%20benefits.pdf (accessed: 01.08.2023), 2016.

IMO MEPC: Resolution MEPC.75(40) Protocol to the MARPOL Convention with added Annex VI., https://wwwcdn.imo.org/localresources/en/KnowledgeCentre/IndexofIMOResolutions/MEPCDocuments/MEPC.75(40).pdf (accessed: 16.01.2023), 1997.

Inness, A., Ades, M., Agustí-Panareda, A., Barré, J., Benedictow, A., Blechschmidt, A.-M., Dominguez, J. J., Engelen, R., Eskes, H., Flemming, J., Huijnen, V., Jones, L., Kipling, Z., Massart, S., Parrington, M., Peuch, V.-H., Razinger, M., Remy, S., Schulz, M., and Suttie, M.: The CAMS reanalysis of atmospheric composition, Atmos. Chem. Phys., 19, 3515–3556, https://doi.org/10.5194/acp-19-3515-2019, 2019.

Jalkanen, J.-P., Brink, A., Kalli, J., Pettersson, H., Kukkonen, J., and Stipa, T.: A modelling system for the exhaust emissions of marine traffic and its application in the Baltic Sea area, Atmos. Chem. Phys., 9, 9209–9223, https://doi.org/10.5194/acp-9-9209-2009, 2009.

Jalkanen, J.-P., Johansson, L., Kukkonen, J., Brink, A., Kalli, J., and Stipa, T.: Extension of an assessment model of ship traffic exhaust emissions for particulate matter and carbon monoxide, Atmos. Chem. Phys., 12, 2641–2659, https://doi.org/10.5194/acp-12-2641-2012, 2012.

Jiang, W., Smyth, S., Giroux, É., Roth, H., and Yin, D.: Differences between CMAQ fine mode particle and PM2.5 concentrations and their impact on model performance evaluation in the lower Fraser valley, Atmospheric Environment, 40(26), 4973-4985, https://doi.org/10.1016/j.atmosenv.2005.10.069, 2006.

Jimenez, J. L., Canagaratna, M. R., Donahue, N. M., Prevot, A. S. H., Zhang, Q., Kroll, J. H., DeCarlo, P. F., Allan, J. D., Coe, H., Ng, N. L., Aiken, A. C., Docherty, K. S., Ulbrich, I. M., Grieshop, A. P., Robinson, A. L., Duplissy, J., Smith, J. D., Wilson, K. R., Lanz, V. A., Hueglin, C., Sun, Y. L., Tian, J., Laaksonen, A., Raatikainen, T., Rautiainen, J., Vaattovaara, P., Ehn, M., Kulmala, M., Tomlinson, J. M., Collins, D. R., Cubison, M. J., Dunlea, E. J., Huffman, J. A., Onasch, T. B., Alfarra, M. R., Williams, P. I., Bower, K., Kondo, Y., Schneider, J., Drewnick, F., Borrmann, S., Weimer, S., Demerjian, K., Salcedo, D., Cottrell, L., Griffin, R., Takami, A., Miyoshi, T., Hatakeyama, S., Shimono, A., Sun, J. Y., Zhang, Y. M., Dzepina, K., Kimmel, J. R., Sueper, D., Jayne, J. T., Herndon, S. C., Trimborn, A. M., Williams, L. R., Wood, E. C., Middlebrook, A. M., Kolb, C. E., Baltensperger, U., and Worsnop, D. R.: Evolution of organic aerosols in the atmosphere, Science, 326(5959), 1525-1529, https://doi.org/10.1126/science.1180353, 2009.

Johansson, L., Jalkanen, J.-P., and Kukkonen, J.: Global assessment of shipping emissions in 2015 on a high spatial and temporal resolution, Atmos. Environ., 167, 403-415, https://doi.org/10.1016/j.atmosenv.2017.08.042, 2017.

Johansson, L., Jalkanen, J.-P., Kalli, J., and Kukkonen, J.: The evolution of shipping emissions and the costs of regulation changes in the northern EU area, Atmos. Chem. Phys., 13, 11375–11389, https://doi.org/10.5194/acp-13-11375-2013, 2013.

Jutterström, S., Moldan, F., Moldanová, J., Karl, M., Matthias, V., and Posch, M.: The impact of nitrogen and sulfur emissions from shipping on the exceedance of critical loads in the Baltic Sea region, Atmos. Chem. Phys., 15, 783–798, https://doi.org/10.5194/acp-21-15827-2021, 2021.

Kampa, M. and Castanas, E.: Human health effects of air pollution, Environmental pollution (Barking, Essex 1987), 151, 362–367, https://doi.org/10.1016/j.envpol.2007.06.012, 2008.

Karamfilova, E.: BRIEFING Implementation Appraisal, Revision of the EU Ambient Air Quality Directives, EPRS European Parliamentary Research Service, https://www.europarl.europa.eu/RegData/etudes/BRIE/2022/734679/EPRS_BRI(2022)734679_EN.pdf (accessed: 01.08.2023), 2022.

Karjalainen, P., Teinilä, K., Kuittinen, N., Aakko-Saksa, P., Bloss, M., Vesala, H., Pettinen, R., Saarikoski, S., Jalkanen, J.-P., and Timonen, H.: Real-world particle emissions and secondary aerosol formation from a diesel oxidation catalyst and scrubber equipped ship operating with two fuels in a SECA area, Environ. Poll., 292, Part A, 118278, https://doi.org/10.1016/j.envpol.2021.118278, 2022.

Karl, M., Bieser, J., Geyer, B., Matthias, V., Jalkanen, J.-P., Johansson, L., and Fridell, E.: Impact of a nitrogen emission control area (NECA) on the future air quality and nitrogen deposition to seawater in the Baltic Sea region, Atmos. Chem. Phys., 19, 1721–1752, https://doi.org/10.5194/acp-19-1721-2019, 2019b.

Karl, M., Gross, A., Pirjola, L., and Leck, C.: A new flexible multicomponent model for the study of aerosol dynamics in the marine boundary layer, Tellus (2011), 63B, 1001–1025, DOI: 10.1111/j.1600-0889.2011.00562.x, 2011.

Karl, M., Jonson, J. E., Uppstu, A., Aulinger, A., Prank, M., Jalkanen, J.-P., Johansson, L., Quante, M., and Matthias, V.: Effects of ship emissions on air quality in the Baltic Sea region simulated with three different chemistry transport models, Atmos. Chem. Phys., 19, https://doi.org/10.5194/acp-2018-1317, 2019a.

Karl, M., Pirjola, L., Grönholm, T., Kurppa, M., Anand, S., Zhang, X., Held, A., Sander, R., Dal Maso, M., Topping, D., Jiang, S., Kangas, L., and Kukkonen, J.: Description and evaluation of the community aerosol dynamics model MAFOR v2.0, Geosci. Model Dev., 15, 3969–4026, https://doi.org/10.5194/gmd-15-3969-2022, 2022.

Karl, M.; Pirjola, L.; Karppinen, A.; Jalkanen, J.-P.; Ramacher, M.O.P.; Kukkonen, J. Modeling of the Concentrations of Ultrafine Particles in the Plumes of Ships in the Vicinity of Major Harbors. Int. J. Environ. Res. Public Health 17, 777. https://doi.org/10.3390/ijerph17030777, 2020.

Kelly, J. T., Bhave, P. V., Nolte, C. G., Shankar, U., and Foley, K. M.: Simulating emission and chemical evolution of coarse sea-salt particles in the Community Multiscale Air Quality (CMAQ) model, Geosci. Model Dev., 3, 257–273, https://doi.org/10.5194/gmd-3-257-2010, 2010.

Kendall, M. and Holgate, S.: Health impact and toxicological effects of nanomaterials in the lung. Respirology, 17, 743-758. https://doi.org/10.1111/j.1440-1843.2012.02171.x, 2012.

Kerminen, V.-M., Pirjola, L., Boy, M., Eskola, A., Teinilä, K., Laakso, L., Asmi, A., Hienola, J., Lauri, A., Vainio, V., Lehtinen, K., Kulmala, M.: Interaction between SO2 and submicron atmospheric particles, Atmospheric Research, 54, 1, 41-57, https://doi.org/10.1016/S0169-8095(00)00038-7, 2000.

Kiesewetter, G., Schoepp, W., Heyes, C., and Amann, M.: Modelling PM2.5 impact indicators in Europe: Health effects and legal compliance, Environ. Modell Softw., 74, 201-211, https://doi.org/10.1016/j.envsoft.2015.02.022, 2015.

Klimont, Z., Kupiainen, K., Heyes, C., Purohit, P., Cofala, J., Rafaj, P., Borken-Kleefeld, J., and Schöpp, W.: Global anthropogenic emissions of particulate matter including black carbon, Atmos. Chem. Phys., 17, 8681–8723, https://doi.org/10.5194/acp-17-8681-2017, 2017.

Klingmüller, K., Metzger, S., Abdelkader, M., Karydis, V. A., Stenchikov, G. L., Pozzer, A., and Lelieveld, J.: Revised mineral dust emissions in the atmospheric chemistry–climate model EMAC (MESSy 2.52 DU_Astitha1 KKDU2017 patch), Geosci. Model Dev., 11, 989–1008, https://doi.org/10.5194/gmd-11-989-2018, 2018.

Knote, C., Tuccella, P., Curci, G., Emmons, L., Orlando, J. J., Madronich, S., Baró, R., Jiménez-Guerrero, P., Luecken, D., Hogrefe, C., Forkel, R., Werhahn, J., Hirtl, M., Pérez, J. L., San José, R., Giordano, L., Brunner, D., Yahya, K., and Zhang, Y.: Influence of the choice of gas-phase mechanism on predictions of key gaseous pollutants during the AQMEII phase-2 intercomparison, Atmos. Environ., 115, 553-568, https://doi.org/10.1016/j.atmosenv.2014.11.066, 2015.

Köhler, I., Sausen, R., and Klenner, G.: NOx production from lightning, the impact of NOx emissions from aircraft upon the atmosphere at flight altitudes 8–15 km (AERONOX), edited by U. Schumann, final report to the Comm. of the Eur. Commun., Dtsch. Luft und Raumfahrt, Oberpfaffenhofen, Germany, 1995.

Kok, J. F., Ridley, D. A., Zhou, Q., Miller, R. L., Zhao, C., Heald, C. L., Ward, D. S., Albani, S., and Haustein, K.: Integrative analysis of desert dust size and abundance suggests less dust climate cooling, Nat. Geosci., 10, 274-278, doi:10.1038/ngeo2912, 2017.

Koo, B., Knipping, E., and Yarwood, G.: 1.5-Dimensional volatility basis set approach for modeling organic aerosol in CAMx and CMAQ, Atmos. Environ. 95, 158-164, https://doi.org/10.1016/j.atmosenv.2014.06.031, 2014.

Koziel, J. A., Aneja, V. P., Baek, B.-H.: Gas-to-particle conversion process between ammonia, acid gases, and fine particles in the atmosphere. in Animal Agriculture and the Environment: National Center for Manure and Animal Waste Management White Papers, 201-224, doi:10.13031/2013.20254, 2006.

Kranenburg, R., Segers, A. J., Hendriks, C., and Schaap, M.: Source apportionment using LOTOS-EUROS: module description and evaluation, Geosci. Model Dev., 6, 721–733, https://doi.org/10.5194/gmd-6-721-2013, 2013.

Kulmala, M., Vehkamäki, H., Petäjä, T., Dal Maso, M., Lauri, A., Kerminen, V.-M., Birmili, W., and McMurry, P. H.: Formation and growth rates of ultrafine atmospheric particles: a review of observations, J. Aerosol Sci., 35, 143–176, https://doi.org/10.1016/j.jaerosci.2003.10.003, 2004.

Lee, B.-K., Choi, S.-D., Shin, B., Kim, S.-J., Lee, S.-J., Kim, D.-G., Lee, G., Kang, H.-J., Kim, H.-S., and Park, D.-Y.: Sensitivity analysis of volatile organic compounds to PM2.5 concentrations in a representative industrial city of Korea, Asian J. Atmos. Environ 17, https://doi.org/10.1007/s44273-023-00003-y, 2023.

Levy, H.: Normal atmosphere: large radical and formaldehyde concentrations predicted, Science 173,141-143, DOI:10.1126/science.173.3992.141, 1971.

Liu, J. J., Jones, D. B. A., Worden, J. R., Noone, D., Parrington, M., and Kar, J.: Analysis of the summertime buildup of tropospheric ozone abundances over the Middle East and North Africa as observed by the Tropospheric Emission Spectrometer instrument, J. Geophys. Res., 114(D05304), https://doi.org/10.1029/2008JD010993, 2009.

Loosmore, G. A. and Cederwall, R. T.: Precipitation scavenging of atmospheric aerosols for emergency response applications: testing an updated model with new real-time data, Atmospheric Environment, 38(7), 993-1003, https://doi.org/10.1016/j.atmosenv.2003.10.055, 2004.

Mallet, M. D., D'Anna, B., Même, A., Bove, M. C., Cassola, F., Pace, G., Desboeufs, K., Di Biagio, C., Doussin, J.-F., Maille, M., Massabò, D., Sciare, J., Zapf, P., di Sarra, A. G., and Formenti, P.: Summertime surface PM1 aerosol composition and size by source region at the Lampedusa island in the central Mediterranean Sea, Atmos. Chem. Phys., 19, 11123–11142, https://doi.org/10.5194/acp-19-11123-2019, 2019.

Manahan, S. E.: Green Chemistry and the Ten Commandments of Sustainability, ChemChar Research; third Edition, ISBN 0615433839, 2011.

Manders, A. M. M., Builtjes, P. J. H., Curier, L., van der Denier Gon, H. A. C., Hendriks, C., Jonkers, S., Kranenburg, R., Kuenen, J. J. P., Segers, A. J., Timmermans, R. M. A., Visschedijk, A. J. H., Wichink Kruit, R. J., van Pul, W. A. J., Sauter, F. J., van der Swaluw, E., Swart, D. P. J., Douros, J., Eskes, H., van Meijgaard, E., van Ulft, B., van Velthoven, P., Banzhaf, S., Mues, A. C., Stern, R., Fu, G., Lu, S., Heemink, A., van Velzen, N., and Schaap, M.: Curriculum vitae of the LOTOS–EUROS (v2.0) chemistry transport model, Geosci. Model Dev., 10, 4145–4173, https://doi.org/10.5194/gmd-10-4145-2017, 2017.

Manders-Groot, A., Segers, A., and Jonkers, S.: LOTOS-EUROS v2.0 Reference Guide, Report, https://lotos-euros.tno.nl/media/10360/reference_guide_v2-0_r10898.pdf, 2016.

Manisalidis, I., Stavropoulou, E., Stavropoulos, A., and Bezirtzoglou, E.: Environmental and Health Impacts of Air Pollution: A Review, Front Public Health, 8, doi: 10.3389/fpubh.2020.00014, 2020.

Maricq, M. M., Xu, N., and Chase, R. E.: Measuring Particulate Mass Emissions with the Electrical Low Pressure Impactor, Aerosol Science and Technology, 40, 68-79, DOI: 10.1080/02786820500466591, 2006.

Marmer, E. and Langmann, B.: Impact of ship emissions on the Mediterranean summertime pollution and climate: A regional model study, Atmos. Environ., 39(26), 4659-4669, https://doi.org/10.1016/j.atmosenv.2005.04.014, 2005.

Mårtensson, E. M., Nilsson, E. D., Leeuw, G. de, Cohen, L. H., and Hansson, H.-C.: Laboratory simulations and parameterization of the primary marine aerosol production, J. Geophys. Res., 108(D9), 4297, https://doi.org/10.1029/2002JD002263, 2003.

Marticorena, B. and Bergametti, G.: Modelling the atmospheric dust cycle: 1. Design of a soil drived dust emission scheme, J. Geophys. Res., 100, 16415–16430, doi:10.1029/95jd00690, 1995.

Marticorena, B., Bergametti, G., Aumont, B., Callot, Y., N'Doumé, C., and Legrand, M.: Modelling the atmospheric dust cycle: 2. Simulation of Saharan dust sources, J. Geophys. Res., 102, 4387–4404, doi:10.1029/96JD02964, 1997.

Matthias, V., Bewersdorff, I., Aulinger, A., and Quante, M.: The contribution of ship emissions to air pollution in the North Sea regions, Environ. Pollut., 158(6), 2241-2250, https://doi.org/10.1016/j.envpol.2010.02.013, 2010.

Matthias, V.: The aerosol distribution in Europe derived with the Community Multiscale Air Quality (CMAQ) model: comparison to near surface in situ and sunphotometer measurements, Atmos. Chem. Phys., 8, 5077–5097, https://doi.org/10.5194/acp-8-5077-2008, 2008.

Matthias, V., Arndt, J. A., Aulinger, A., Bieser, J., van der Gon,H. D., Kranenburg, R., Kuenen, J., Neumann, D., Pouliot, G., Quante, M.: Modeling emissions for three-dimensional atmospheric chemistry transport models, J Air Waste Manag Assoc., 68:8, 763-800, DOI: 10.1080/10962247.2018.1424057, 2018.

Meloni, D., di Sarra, A., Brogniez, G., Denjean, C., De Silvestri, L., Di Iorio, T., Formenti, P., Gómez-Amo, J. L., Gröbner, J., Kouremeti, N., Liuzzi, G., Mallet, M., Pace, G., and Sferlazzo, D. M.: Determining the infrared radiative effects of Saharan dust: a radiative transfer modelling study based on vertically resolved measurements at Lampedusa, Atmos. Chem. Phys., 18, 4377–4401, https://doi.org/10.5194/acp-18-4377-2018, 2018.

Menut, L., Bessagnet, B., Khvorostyanov, D., Beekmann, M., Blond, N., Colette, A., Coll, I., Curci, G., Foret, G., Hodzic, A., Mailler, S., Meleux, F., Monge, J.-L., Pison, I., Siour, G., Turquety, S., Valari, M., Vautard, R., and Vivanco, M. G.: CHIMERE 2013: A model for regional atmospheric composition modelling, Geosci. Model Dev., 6, 981–1028, https://doi.org/10.5194/gmd-6-981-2013, 2013.

Merico, E., Donateo, A., Gambaro, A., Cesari, D., Gregoris, E., Barbaro, E., Dinoi, A., Giovanelli, G., Masieri, S., and Contini, D.: Influence of in-port ships emissions to gaseous atmospheric pollutants and to particulate matter of different sizes in a Mediterranean harbour in Italy, Atmos. Environ.,139, 1-10, https://doi.org/10.1016/j.atmosenv.2016.05.024, 2016.

Merico, E., Gambaro, A., Argiriou, A., Alebic-Juretic, A., Barbaro, E., Cesari, D., Chasapidis, L., Dimopoulos, S., Dinoi, A., Donateo, A., Giannaros, C., Gregoris, E., Karagiannidis, A., Konstandopoulos, A. G., Ivošević, T., Liora, N., Melas, D., Mifka, B., Orlić, I., Poupkou, A., Sarovic, K., Tsakis, A., Giua, R., Pastore, T., Nocioni, A., and Contini, D.: Atmospheric impact of ship traffic in four Adriatic-Ionian port-cities: Comparison and harmonization of different approaches, Transp. Res. D: Transp. Environ., 50, 431-445, https://doi.org/10.1016/j.trd.2016.11.016, 2017.

Miller, M. R., Raftis, J. B., Langrish, J. P., McLean, S. G., Samutrtai, P., Connell, S. P., Wilson, S., Vesey, A. T., Fokkens, P. H. B., Boere, A. J. F., Krystek, P., Campbell, C. J., Hadoke, P. W. F., Donaldson, K., Cassee, F. R., Newby, D. E., Duffin, R., and Mills, N. L.: Inhaled Nanoparticles Accumulate at Sites of Vascular Disease, ACS Nano, 11, 10623-10624, doi: 10.1021/acsnano.6b08551, 2017.

Mokhtari, M., Gomes, L., Tulet, P., and Rezoug, T.: Importance of the surface size distribution of erodible material: an improve[1]ment on the Dust Entrainment And Deposition (DEAD) Model, Geosci. Model Dev., 5(3), https://doi.org/10.5194/gmd-5- 581-2012, 2012.

Moldanova, J., Fridell, E., Winnes, H., Holmin-Fridell, S., Boman, J., Jedynska, A., Tishkova, V., Demirdjian, B., Joulie, S., Bladt, H., Ivleva, N. P., and Niessner, R.: Physical and chemical characterisation of PM emissions from two ships operating in European Emission Control Areas, Atmos. Meas. Tech., 6, 3577–3596, https://doi.org/10.5194/amt-6-3577-2013, 2013.

Monahan, E. C., Spiel, D. E., and Davidson, K. L.: A Model of Marine Aerosol Generation Via Whitecaps and Wave Disruption, OCSL, 2,https://doi.org/10.1007/978-94-009-4668-2_16, 1986.

Murphy, B. N., Woody, M. C., Jimenez, J. L., Carlton, A. M. G., Hayes, P. L., Liu, S., Ng, N. L., Russell, L. M., Setyan, A., Xu, L., Young, J., Zaveri, R. A., Zhang, Q., and Pye, H. O. T.: Semivolatile POA and parameterized total combustion SOA in CMAQv5.2: impacts on source strength and partitioning, Atmos. Chem. Phys., 17, 11107–11133, https://doi.org/10.5194/acp-17-11107-2017, 2017.

National Research Council: Rethinking the Ozone Problem in Urban and Regional Air Pollution, The National Academies Press., Washington, DC: The National Academies Press. https://doi.org/10.17226/1889, 1991.

Nenes, A., Pandis, S. N., and Pilinis, C.: ISORROPIA: A New Thermodynamic Equilibrium Model for Multiphase Multicomponent Inorganic Aerosols, Aquat. Geochem., 4, 123–152, https://doi.org/10.1023/A:1009604003981, 1998.

Novak, J. H. and Pierce, T. E.: Natural emissions of oxidant precursors, Water Air Soil Poll., 67, 57–77, https://doi.org/10.1007/BF00480814, 1993.

Nordic Drones: AEROMON BH-12, Real-time data from the air, https://nordicdrones.fi/en/products/product-information/aeromon-bh-12/ (accessed: 20.09.2023), 2023.

Nunes, R. A. O., Alvim-Ferraz, M. C. M., Martins, F. G., Calderay-Cayetano, F., Durán-Grados, V., Moreno-Gutiérrez, J., Jalkanen, J.-P., Hannuniemi, H., and Sousa, S. I. V.: Shipping emissions in the Iberian Peninsula and the impacts on air quality, Atmos. Chem. Phys., 20, 9473–9489, https://doi.org/10.5194/acp-20-9473-2020, 2020.

Oberdörster, G., Oberdörster, E., and Oberdörster, J.: Nanotoxicology: an emerging discipline evolving from studies of ultrafine particles, Environ Health Perspect, 113, 823-39. doi: 10.1289/ehp.7339, 2005.

Olivier, J.G.J. and Berdowski, J.J.M.: Global Emissions Sources and Sinks, in the Climate System, in: Berdowski, J., Guicherit, R., Heij, B.J. and Lisse, Eds., The Climate System, A.A. Balkema Publishers/Swets and Zeitlinger Publishers, The Netherlands, 33-78, 2001.

Ordóñez, C., Richter, A., Steinbacher, M., Zellweger, C., Nüß, H., Burrows, J. P., and Prévôt, A. S. H.: Comparison of 7 years of satellite-borne and ground-based tropospheric NO2 measurements around Milan, Italy, J. Geophys. Res., 111(D5), https://doi.org/10.1029/2005JD006305, 2006.

Otto, S., de Reus, M., Trautmann, T., Thomas, A., Wendisch, M., and Borrmann, S.: Atmospheric radiative effects of an in situ measured Saharan dust plume and the role of large particles, Atmos. Chem. Phys., 7, 4887–4903, https://doi.org/10.5194/acp-7-4887-2007, 2007.

Ovadnevaite, J., Manders, A., Leeuw, G. de, Ceburnis, D., Monahan, C., Partanen, A.-I., Korhonen, H., and O'Dowd, C. D.: A sea spray aerosol flux parameterization encapsulating wave state, Atmos. Chem. Phys., 14, 1837–1852, https://doi.org/10.5194/acp-14-1837-2014, 2014.

Pacyna, J.M.: Atmospheric Deposition, in Encyclopedia of Ecology, Academic Press, 275-285, ISBN 9780080454054, https://doi.org/10.1016/B978-008045405-4.00258-5, 2008.

Palacios-Peña, L.; Lorente-Plazas, R.; Montávez, J.P.; Jiménez-Guerrero, P.: Saharan Dust Modeling Over the Mediterranean Basin and Central Europe: Does the Resolution Matter? Front. Earth Sci., 7(290), doi: 10.3389/feart.2019.00290, 2019.

Pandolfi, M., Gonzalez-Castanedo, Y., Alastuey, A., La Rosa, J. D. de, Mantilla, E., La Campa, A. S. de, Querol, X., Pey, J., Amato, F., and Moreno, T.: Source apportionment of PM(10) and PM(2.5) at multiple sites in the strait of Gibraltar by PMF: impact of shipping emissions, Environ. Sci. Pollut. Res.18, 260–269, https://doi.org/10.1007/s11356-010-0373-4, 2011.

Pepe, N., Pirovano, G., Balzarini, A., Toppetti, A., Riva, G. M., Amato, F., and Lonati, G.: Enhanced CAMx source apportionment analysis at an urban receptor in Milan based on source categories and emission regions, Atmos. Environ. X, 2,100020, https://doi.org/10.1016/j.aeaoa.2019.100020, 2019.

Petrik, R., Geyer, B., and Rockel, B.: On the diurnal cycle and variability of winds in the lower planetary boundary layer: evaluation of regional reanalyses and hindcasts, Dyn. Meteorol. Oceanogr., 73(1), 1804294, https://doi.org/10.1080/16000870.2020.1804294, 2021.

Pirjola, L., Pajunoja, A., Walden, J., Jalkanen, J.-P., Rönkkö, T., Kousa, A., and Koskentalo, T.: Mobile measurements of ship emissions in two harbour areas in Finland, Atmos. Meas. Tech., 7, 149–161, https://doi.org/10.5194/amt-7-149-2014, 2014.

Pleim, J. and Ran, L.: Surface Flux Modeling for Air Quality Applications, Atmosphere, 2(3), 271-302, https://doi.org/10.3390/atmos2030271, 2011.

Pleim, J. E., Xiu, A., Finkelstein, P. L., and Otte, T. L.: A Coupled Land-Surface and Dry Deposition Model and Comparison to Field Measurements of Surface Heat, Moisture, and Ozone Fluxes, Water Air Soil Pollut.: Focus, 1, 243–252, https://doi.org/10.1023/A:1013123725860, 2001.

Prati, M. V., Costagliola, M. A., Quaranta, F., and Murena, F.: Assessment of ambient air quality in the port of Naples, J. Air Waste Manag. Assoc., 65, 970-979, https://doi.org/10.1080/10962247.2015.1050129, 2015.

Prigent, C., Jiménez, C., and Catherinot, J.: Comparison of satellite microwave backscattering (ASCAT) and visible/near-infrared reflectances (PARASOL) for the estimation of aeolian aerodynamic roughness length in arid and semi-arid regions, Atmos. Meas. Tech. Discuss., 5, 2933–2957, https://doi.org/10.5194/amtd-5-2933-2012, 2012.

Pun, B. K., Seigneur, C., and Lohman, K.: Modeling secondary organic aerosol formation via multiphase partitioning with molecular data, Environ. Sci. Technol., 40, 4722–4731, doi: 10.1021/es0522736, 2006.

Pye, H. O. T. and Pouliot, G. A.: Modeling the role of alkanes, polycyclic aromatic hydrocarbons, and their oligomers in secondary organic aerosol formation, Environ. Sci. Technol., 6041-6047, https://doi.org/10.1021/es300409w, 2012.

Pye, H. O. T., Murphy, B. N., Xu, L., Ng, N. L., Carlton, A. G., Guo, H., Weber, R., Vasilakos, P., Appel, K. W., Budisulistiorini, S. H., Surratt, J. D., Nenes, A., Hu, W., Jimenez, J. L., Isaacman-VanWertz, G., Misztal, P. K., and Goldstein, A. H.: On the implications of aerosol liquid water and phase separation for organic aerosol mass, Atmos. Chem. Phys., 17, 343–369, https://doi.org/10.5194/acp-17-343-2017, 2017.

Ramboll Environment and Health: CAMx Source Code and Documentation, CAMx v6.50 (April 30, 2018) https://camx-wp.azurewebsites.net/download/source/, (accessed: 07.09.2023).

Ramboll Environment and Health: User's Guide COMPREHENSIVE AIR QUALITY MODEL WITH EXTENSIONS: Version 7.10, User's Guide, https://camx-wp.azurewebsites.net/Files/CAMxUsersGuide_v7.10.pdf, 2020.

Reichle, L. J., Cook, R., Yanca, C. A., and Sonntag, D. B.: Development of organic gas exhaust speciation profiles for nonroad spark-ignition and compression-ignition engines and equipment, J. Air Waste Manag. Assoc., 65(10), 1185–1193, https://doi.org/10.1080/10962247.2015.1020118, 2015.

Robinson, A. L., Donahue, N. M., Shrivastava, M. K., Weitkamp, E. A., Sage, A. M., Grieshop, A. P., Lane, T. E., Pierce, J. R., and Pandis, S. N.: Rethinking organic aerosols: semivolatile emissions and photochemical aging, Science, 315(5816), https://doi.org/10.1126/science.1133061, 2007.

Roselle, S. J. and Binkowski, F. S.: Cloud Dynamics and Chemistry: Chapter 11, https://www.cmascenter.org/cmaq/science_documentation/pdf/ch11.pdf, 1999.

Rückerl, R., Schneider, A., Breitner, S., Cyrys, J., and Peters, A.: Health effects of particulate air pollution: A review of epidemiological evidence, Inhal Toxicol., 23, 555-92. doi: 10.3109/08958378.2011.593587, 2011.

Safieddine, S., Boynard, A., Coheur, P.-F., Hurtmans, D., Pfister, G., Quennehen, B., Thomas, J. L., Raut, J.-C., Law, K. S., Klimont, Z., Hadji-Lazaro, J., George, M., and Clerbaux, C.: Summertime tropospheric ozone assessment over the Mediterranean region using the thermal infrared IASI/MetOp sounder and the WRF-Chem model, Atmos. Chem. Phys., 14, 10119–10131, https://doi.org/10.5194/acp-14-10119-2014, 2014.

Schaap, M., Manders, A.M.M., Hendriks, E.C.J., Cnossen, J.M., Segers, A.J.S., Denier van der Gon, H.A.C., Jozwicka, M., Sauter, F., Velders, G., Matthijsen, J., Builtjes, P.J.H.: Regional modelling of particulate matter for the Netherlands. Tech.rep. Netherlands Environmental Assessment Agency (PBL). https://www.pbl.nl/sites/default/files/downloads/500099008_0.pdf, 2009.

Schaap, M., Timmermans, R. M.A., Roemer, M., Boersen, G.A.C., Builtjes, P. J.H., Sauter, F. J., Velders, G. J.M., and Beck, J. P.: The LOTOS EUROS model: Description, validation and latest developments, Int J Environ Pollut., 32(2), 270-290, https://doi.org/10.1504/IJEP.2008.017106, 2008.

Schaap, M., van Loon, M., ten Brink, H. M., Dentener, F. J., and Builtjes, P. J. H.: Secondary inorganic aerosol simulations for Europe with special attention to nitrate, Atmos. Chem. Phys., 4, 857–874, https://doi.org/10.5194/acp-4-857-2004, 2004.

Schack, K. J., Pratsinis, S. E., Friedlander, S.K.: A general correlation for deposition of suspended particles from turbulent gases to completely rough surfaces, Atmospheric Environment (1967),19, 6, 953-960, https://doi.org/10.1016/0004-6981(85)90240-9, 1985.

Schembari, C., Cavalli, F., Cuccia, E., Hjorth, J., Calzolai, G., Pérez, N., Pey, J., Prati, P., and Raes, F.: Impact of a European directive on ship emissions on air quality in Mediterranean harbours, Atmospheric Environment, 61, 661-669, https://doi.org/10.1016/j.atmosenv.2012.06.047, 2012.

Schneider, A., Cyrys, J., Breitner, S., Kraus, U., Peters, A., Diegmann, V., and Neunhäuserer, L.: Quantifizierung von umweltbedingten Krankheitslasten aufgrund der Stickstoffdioxid-Exposition in Deutschland, Umweltbundesamt Deutschland, https://www.umweltbundesamt.de/sites/default/files/medien/421/publikationen/abschlussbericht_no2_krankheitslast_final_2018_03_05.pdf (accessed: 01.08.2023), 2018.

Schober, P., Boer, C., and Schwarte, L. A.: Correlation Coefficients: Appropriate Use and Interpretation, Anesth. Analg., 126(5), 1763-1768, https://doi.org/10.1213/ANE.0000000000002864, 2018.

Schultze, M. and Rockel, B.: Direct and semi-direct effects of aerosol climatologies on long-term climate simulations over Europe, Clim Dyn, 50, 3331–3354, https://doi.org/10.1007/s00382-017-3808-5, 2018.

Schulz, M., Cozic, A., Szopa, S.: LMDzT-INCA Dust Forecast Model Developments and Associated Validation Efforts, Earth Environ. Sci. 7, http://iopscience.iop.org/1755-1315/7/1/012014, 2009.

Seinfeld, J.H. and Pandis, S.N. (2006) Atmospheric Chemistry and Physics: From Air Pollution to Climate Change. 2nd Edition, John Wiley & Sons, New York, 2006.

Seinfeld, J.H. and Pandis, S.N.: Atmospheric Chemistry and Physics. John Wiley and Sons, New York, 1998.

Simpson, D., Benedictow, A., Berge, H., Bergström, R., Emberson, L. D., Fagerli, H., Flechard, C. R., Hayman, G. D., Gauss, M., Jonson, J. E., Jenkin, M. E., Nyíri, A., Richter, C., Semeena, V. S., Tsyro, S., Tuovinen, J.-P., Valdebenito, Á., and Wind, P.: The EMEP MSC-W chemical transport model – technical description, Atmos. Chem. Phys., 12, 7825–7865, https://doi.org/10.5194/acp-12-7825-2012, 2012.

Simpson, D., Bergström, R., Briolat, A., Imhof, H., Johansson, J., Priestley, M., and Valdebenito, A.: GenChem v1.0 – a chemical pre-processing and testing system for atmospheric modelling, Geosci. Model Dev., 13, 6447–6465, https://doi.org/10.5194/gmd-13-6447-2020, 2020.

Simpson, D., Fagerli, H., Jonson, J. E., Tsyro, S., and Wind, P.: Transboundary Acidification, Eutrophication and Ground Level Ozone in Europe. PART I. Unified EMEP Model Description, Rort, https://www.emep.int/publ/reports/2003/emep_report_1_part1_2003.pdf, 2003.

Sippula, O., Stengel, B., Sklorz, M., Streibel, T., Rabe, R., Orasche, J., Lintelmann, J., Michalke, B., Abbaszade, G., Radischat, C., Gröger, T., Schnelle-Kreis, J., Harndorf, H., and Zimmermann, R.: Particle emissions from a marine engine: chemical composition and aromatic emission profiles under various operating conditions, Environ. Sci. Technol., 48(19), 11721–11729, https://doi.org/10.1021/es502484z, 2014.

Solazzo, E., Bianconi, R., Pirovano, G., Matthias, V., Vautard, R., Moran, M. D., Wyat Appel, K., Bessagnet, B., Brandt, J., Christensen, J. H., Chemel, C., Coll, I., Ferreira, J., Forkel, R., Francis, X. V., Grell, G., Grossi, P., Hansen, A. B., Miranda, A. I., Nopmongcol, U., Prank, M., Sartelet, K. N., Schaap, M., Silver, J. D., Sokhi, R. S., Vira, J., Werhahn, J., Wolke, R., Yarwood, G., Zhang, J., Rao, S. T., and Galmarini, S.: Operational model evaluation for particulate matter in Europe and North America in the context of AQMEII, Atmos. Environ., 53, 75-92, https://doi.org/10.1016/j.atmosenv.2012.02.045, 2012.

Sotiropoulou, R. E. P. and Tagaris, E.: Impact of Shipping Emissions on European Air Quality, In: Karacostas, T., Bais, A., Nastos, P. (eds) Perspectives on Atmospheric Sciences, Springer Atmospheric Sciences, https://doi.org/10.1007/978-3-319-35095-0_149, 2017.

Strader, R., F. Lurmann, and S.N. Pandis: Evaluation of secondary organic aerosol formation in winter. Atmos. Environ., 33, 4849-4863, DOI:10.1016/S1352-2310(99)00310-6, 1999.

Sun, W., Berasategui, M., Pozzer, A., Lelieveld, J., and Crowley, J. N.: Kinetics of OH + SO2 + M: temperature-dependent rate coefficients in the fall-off regime and the influence of water vapour, Atmos. Chem. Phys., 22, 4969–4984, https://doi.org/10.5194/acp-22-4969-2022, 2022.

Tadic, I., Crowley, J. N., Dienhart, D., Eger, P., Harder, H., Hottmann, B., Martinez, M., Parchatka, U., Paris, J.-D., Pozzer, A., Rohloff, R., Schuladen, J., Shenolikar, J., Tauer, S., Lelieveld, J., and Fischer, H.: Net ozone production and its relationship to nitrogen oxides and volatile organic compounds in the marine boundary layer around the Arabian Peninsula, Atmos. Chem. Phys., 20, 6769–6787,, https://doi.org/10.5194/acp-20-6769-2020, 2020.

Timonen, H., Teinilä, K., Barreira, L. M. F., Saarikoski, S., Simonen, P., Dal Maso, M., Keskinen, J., Kalliokoski, J., Moldanova, J., Salberg, H., Merelli, L., D'Anna, B., Temime-Roussel, B., Lanzafame, G. M., Mellqvist., J.: SCIPPER Project D3.3 - Ship on-board emissions characterisation. https://www.scipper-project.eu/wp-content/uploads/2023/02/scipper-d3.3_s.pdf (accessed: 20.09.2023), 2022.

Tuccella, P., Menut, L., Briant, R., Deroubaix, A., Khvorostyanov, D., Mailler, S., Siour, G., and Turquety, S.: Implementation of Aerosol-Cloud Interaction within WRF-CHIMERE Online Coupled Model: Evaluation and Investigation of the Indirect Radiative Effect from Anthropogenic Emission Reduction on the Benelux Union, Atmosphere, 10(1), 20, https://doi.org/10.3390/atmos10010020, 2019.

Tysro, S. G. and Berge, E.: The Contribution of Ship Emission from the North Sea and the North-eastern Atlantic Ocean to Acidification in Europe, EMEP/MSC-W Note 4/97. EMEP. Meteorol. Synthesizing Centre e West, Norwegian Meteorological Institute, Oslo. Report, https://emep.int/publ/reports/1997/EMEP_1997_N4.pdf, 1997.

UCAR/NCAR Earth System Laboratory: WRF - Weather Research and Forecasting Model Users' Page, MMM/WRF model code, https://doi.org/10.5065/D6MK6B4K (accessed: 07.09.2023).

USEPA (United States Environmental Protection Agency): Nitrogen Oxides (NOx), Why and How They Are Controlled: EPA-456/F-99-006R, 1999.

Večeřa, Z., Mikuška, P., Smolík, J., Eleftheriadis, K., Bryant, C., Colbeck, I., and Lazaridis, M.: Shipboard Measurements of Nitrogen Dioxide, Nitrous Acid, Nitric Acid and Ozone in the Eastern Mediterranean Sea, Water Air Soil Pollut: Focus, 8, 117–125, https://doi.org/10.1007/s11267-007-9133-y, 2008.

Viana, M., Amato, F., Alastuey, A., Querol, X., Moreno, T., Dos Santos, S. G., Herce, M. D., and Fernández-Patier, R.: Chemical tracers of particulate emissions from commercial shipping, Environ. Sci. Technol., 43(19), 7472–7477, https://doi.org/10.1021/es901558t, 2009.

Viana, M., Hammingh, P., Colette, A., Querol, X., Degraeuwe, B., Vlieger, I. d., and van Aardenne, J.: Impact of maritime transport emissions on coastal air quality in Europe, Atmos. Environ., 90, 96-105, https://doi.org/10.1016/j.atmosenv.2014.03.046, 2014.

Viana, M., Rizza, V., Tobías, A., Carr, E., Corbett, J., Sofiev, M., Karanasiou, A., Buonanno, G., and Fann, N.: Estimated health impacts from maritime transport in the Mediterranean region and benefits from the use of cleaner fuels, Environ. Internat., 138,105670, https://doi.org/10.1016/j.envint.2020.105670, 2020.

Vivanco, M. G., Theobald, M. R., García-Gómez, H., Garrido, J. L., Prank, M., Aas, W., Adani, M., Alyuz, U., Andersson, C., Bellasio, R., Bessagnet, B., Bianconi, R., Bieser, J., Brandt, J., Briganti, G., Cappelletti, A., Curci, G., Christensen, J. H., Colette, A., Couvidat, F., Cuvelier, C., D'Isidoro, M., Flemming, J., Fraser, A., Geels, C., Hansen, K. M., Hogrefe, C., Im, U., Jorba, O., Kitwiroon, N., Manders, A., Mircea, M., Otero, N., Pay, M.-T., Pozzoli, L., Solazzo, E., Tsyro, S., Unal, A., Wind, P., and Galmarini, S.: Modeled deposition of nitrogen and sulfur in Europe estimated by 14 air quality model systems: evaluation, effects of changes in emissions and implications for habitat protection, Atmos. Chem. Phys., 18, 10199–10218, https://doi.org/10.5194/acp-18-10199-2018, 2018.

Wang, X., Grose, M. A., Caldow, R., Osmondson, B. L., Swanson, J. J., Chow, J. C., Watson, J. G., Kittelson, D. B., Li, Y., Xue, J., Jung, H., and Hu, S.: Improvement of Engine Exhaust Particle Sizer (EEPS) size distribution measurement – II. Engine exhaust particles, J. Aerosol Sci., 92, 83-94, 10.1016/j.jaerosci.2015.11.003, 2016.

Wesely, M. L.: Parameterization of surface resistances to gaseous dry deposition in regional-scale numerical models, Atmos. Environ., 23 (6), 1293-1304, https://doi.org/10.1016/0004-6981(89)90153-4, 1989.

Whitten, G. Z., H. Hogo, and J.P. Killus, The carbon-bond mechanism: A condensed kinetic mechanism for photochemical smog, Environ. Sci. Technol., 18, 280-87, DOI: 10.1021/es60166a008, 1980.

Whitten, G. Z., Heo, G., Kimura, Y., McDonald-Buller, E., Allen, D. T., Carter, W. P.L., and Yarwood, G.: A new condensed toluene mechanism for Carbon Bond: CB05-TU☆, Atmos. Environ., 44(40), 5346-5355, https://doi.org/10.1016/j.atmosenv.2009.12.029, 2010.

WHO: Air quality guidelines for Europe, Regional Office for Europe, WHO regional publications, European series, Copenhagen: ISBN 92-890-1114-9. https://apps.who.int/iris/handle/10665/107364 (accessed: 23.08.2023), 1987.

WHO: Ambient (outdoor) air pollution, https://www.who.int/news-room/fact-sheets/detail/ambient-(outdoor)-air-quality-and-health (accessed: 24.05.2023), 2022.

WHO: global air quality guidelines. Particulate matter (PM¬2.5 and PM10), ozone, nitrogen dioxide, sulphur dioxide and carbon monoxide, Geneva: World Health Organization, https://apps.who.int/iris/bitstream/handle/10665/345329/9789240034228-eng.pdf, 2021.

Wichink Kruit, R. J., Schaap, M., Sauter, F. J., van Zanten, M. C., and van Pul, W. A. J.: Modeling the distribution of ammonia across Europe including bi-directional surface-atmosphere exchange, Biogeosciences Discuss., 9, 4877–4918, https://doi.org/10.5194/bgd-9-4877-2012, 2012.

Wichink Kruit, R. W., Schaap, M., Segers, A., Heslinga, D., Builtjes, P., Branzhaf, S., and Scheuschner, T.: Modelling and mapping of atmospheric nitrogen and sulphur deposition and critical loads for ecosystem specific assessment of threats to biodiversity in Germany – PINETI (Pollutant INput and EcosysTem Impact) Substudy Report 1., https://www.umweltbundesamt.de/sites/default/files/medien/1410/publikationen/2017-08-15_texte_62-2017_pineti2-teil1.pdf, 2014.

Wiedinmyer, C., Akagi, S. K., Yokelson, R. J., Emmons, L. K., Al-Saadi, J. A., Orlando, J. J., and Soja, A. J.: The Fire INventory from NCAR (FINN): A high resolution global model to estimate the emissions from open burning, Geosci. Model Dev., 4, 625–641, https://doi.org/10.5194/gmd-4-625-2011, 2011.

Wild, O.: Modelling the global tropospheric ozone budget: Exploring the variability in current models, Atmos. Chem. Phys., 7, 2643–2660, https://doi.org/10.5194/acp-7-2643-2007, 2007.

Williams, J. and Koppmann, R.: Volatile organic compounds in the atmosphere: an overview. Volatile Organic Compounds in the Atmosphere 1, Blackwell Publishing Ltd, Oxford, UK, ISBN 0470994150, 2007.

Winnes, H. and Fridell, E.: Particle emissions from ships: dependence on fuel type, J Air Waste Manag Assoc, 59, 12, 1391-1398, https://doi.org/10.3155/1047-3289.59.12.1391, 2009.

WRF Model, WPS: The Weather Research and Forecasting (WRF) Preprocessing System. GitHub Repository. https://github.com/wrf-model/WPS.git (accessed: 07.09.2023).

Yarwood, G., Rao, S., Yocke, M. and Whitten, G.Z.: Updates to the Carbon Bond Chemical Mechanism: CB05. Final Report Prepared for the United States Environmental Protection Agency, http://www.camx.com/publ/pdfs/CB05_Final_Report_120805.pdf, 2005.

Zannetti, P., Dry and Wet Deposition. Air Pollution Modeling. Springer, Boston, MA. https://doi.org/10.1007/978-1-4757-4465-1_10, 1990.

Zanten, M. C. van, Sauter, F. J., Wichink Kruit, R. J., van Jaarsveld, J. A., and van Pul, W.A.J.: Description of the DEPAC module: Dry deposition modelling with DEPAC_GCN2010, RIVM Report 680180001/2010, https://www.rivm.nl/bibliotheek/rapporten/680180001.pdf, 2010.

Zender, C., Bian, H., and Newman, D.: Mineral Dust Entrainmentand Deposition (DEAD) model: Description and 1990s dust climatology., J. Geophys. Res., 108, 4416–4437, doi:10.1029/2002jd002775, 2003.

Zhang, L., Brook, J. R., and Vet, R.: A revised parameterization for gaseous dry deposition in air-quality models, Atmos. Chem. Phys., 3, 2067–2082, https://doi.org/10.5194/acp-3-2067-2003, 2003.

Zhong, Q., Shen, H., Yun, X., Chen, Y., Ren, Y.'a., Xu, H., Shen, G., Du, W., Meng, J., Li, W., Ma, J., and Tao, S.: Global Sulfur Dioxide Emissions and the Driving Forces, Environ. Sci. Technol., 54(11), 6508–6517, https://doi.org/10.1021/acs.est.9b07696, 2020.

Appendix

Appendix A

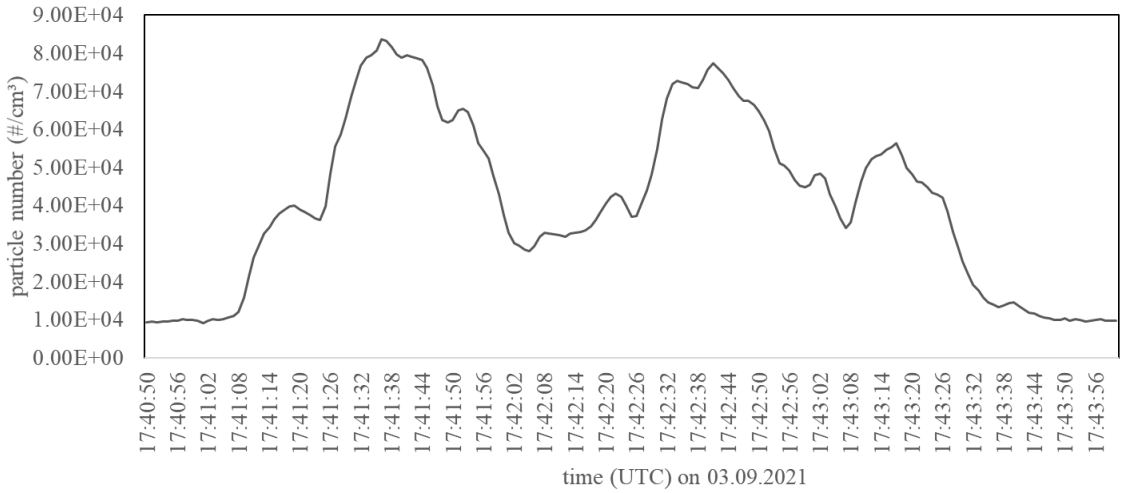

Figure A1: Total particle count measured by the Sniffer during the SCIPPER measurement campaign on 03.09.2021 in Laboe at the Kieler Förde (54.392809, 10.209186). The plume arrived the measurement station at 17:41:37 UTC and the plume peak was determined when the total concentration was highest.

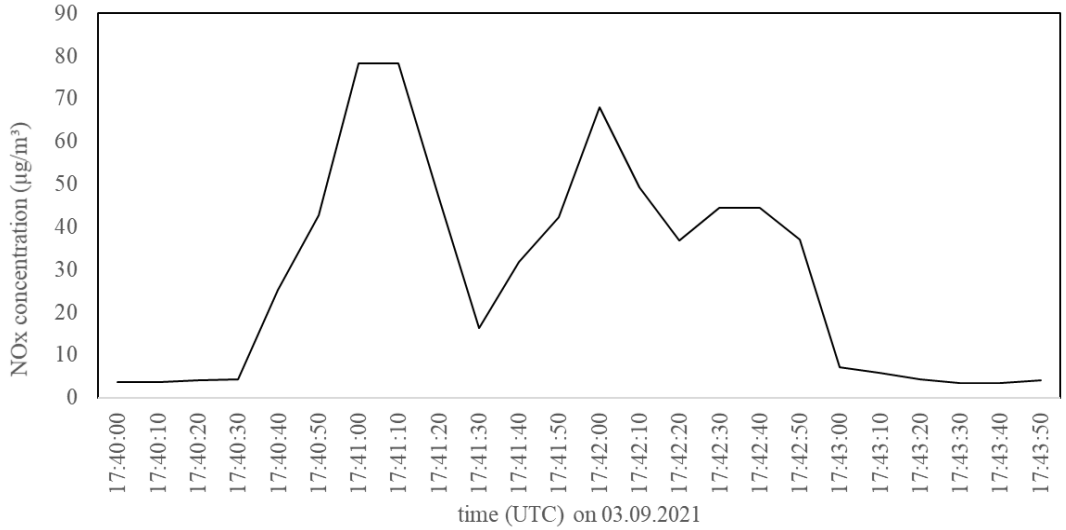

Figure A2: NO_x concentrations after the Germanica passed the measurement station. Gases and meteorological parameters were measured by an airpointer 4D measurement system for NO_x, O_3, SO_2 and a weather station during the SCIPPER measurement campaign on 03.09.2021 in Laboe at the Kieler Förde (54.392809, 10.209186).

Appendix B:

Table B1: Detailed overview of monitoring stations.

Name	Code	Country	Latitude	Longitude	Elevation	Station Type	Data Points	Measured Pollutants
Vlora	al0204a	Albania	40.40309	19.4862	25	urban background	6850	benzene, CO, NO_2, NO_x, O_3, PM_{10}, $PM_{2.5}$, SO_2
Shkoder	al0206a	Albania	42.3139	19.52342	13	urban background	7536	CO, NO_2, NO_x, O_3, PM_{10}, $PM_{2.5}$, SO_2
Els Torms	es0014r	Spain	41.39389	0.73472	470	rural background	8549	NO, NO_2, NO_x, O_3, SO_2
Vila-seca (RENFE)	es1117a	Spain	41.11209	1.151824	41	suburban background	8594	NO, NO_2, NO_x
Sant Celoni (Carles Damm)	es1275a	Spain	41.68905	2.495747	145	suburban background	7180	NO, NO_x, NO_2, SO_2
Barcelona (Ciutadella)	es1679a	Spain	41.38641	2.187417	7	urban background	8565	NO, NO_2, NO_x
Mataró (passeig dels Molins)	es1816a	Spain	41.54716	2.443254	40	urban background	8484	NO, NO_x, NO_2, O_3, CO
Barcelona (Palau Reial)	es1992a	Spain	41.38748	2.11515	81	urban background	8393	NO, NO_2, NO_x, SO_2, CO
Marseille 5 Avenues	fr03043	France	43.30607	5.395794	73	urban background	8585	NO_2, O_3, PM_{10}, $PM_{2.5}$, SO_2
Esterel	fr03070	France	43.43786	6.768366	5	suburban background	1820	NO_2, O_3
Agathois-piscénois	fr08022	France	43.28776	3.504831	20	suburban background	8382	NO_2, O_3
Gauzy	fr08614	France	43.8344	4.374219	40	urban background	8406	NO_2, O_3, PM_{10}, $PM_{2.5}$

Rigaud	fr08713	France	42.68402	2.903453	50	urban background	8419	NO_2, PM_{10}
Cannes Broussilles	fr24009	France	43.5625	7.007222	71	urban background	8587	NO_2, O_3, PM_{10}, $PM_{2.5}$
Manosque	fr24018	France	43.83527	5.785831	385	urban background	8517	NO_2, O_3, PM_{10}, $PM_{2.5}$
Nice Arson	fr24036	France	43.70207	7.286264	11	urban background	8701	NO_2, O_3, PM_{10}, $PM_{2.5}$
Ajaccio Sposata	fr41007	France	41.94923	8.757586	60	suburban background	8497	NO_2, O_3
Bastia Montesoro	fr41017	France	42.67134	9.434644	47	rural background	8626	NO_2, O_3, $PM_{2.5}$
Lykovrysi	gr0035a	Greece	38.06963	23.77689	210	suburban background	6719	NO_2, NO_2, O_3
Neochoroud a	gr0045a	Greece	40.73984	22.87623	229	suburban background	8725	NO_2, NO, O_3
Finokalia	gr0002r	Greece	35.315871	25.666216	250	rural background	6825	PM_{10}, O_3
NA	hr0025a	Croatia	44.86247	13.81686	0	suburban background	8293	NO_2, NO_x, O_3
Melilli	it0611a	Italy	37.18237	15.12883	300	urban background	7964	NO_2, O_3, SO_2
Priolo	it0614a	Italy	37.15612	15.19087	35	urban background	7902	NO_2, benzene, SO_2
SR - Via Gela	it0620a	Italy	37.10247	15.26564	60	suburban background	6958	NO_2, O_3, SO_2
Gela-Enimed	it0815a	Italy	37.06222	14.28422	13	suburban background	8052	NO_2, SO_2, benzene
Aprilia	it0865a	Italy	41.59528	12.65361	83	urban background	8169	NO_2

Leonessa	it0989a	Italy	42.5725	12.96194	948	urban background	8207	NO_2, O_3
Gherardi	it1179a	Italy	44.83972	11.96111	-2	rural background	8269	NO_x, NO_2, O_3
Adria	it1213a	Italy	45.04667	12.06194	4	urban background	8306	NO_2, NO_x, O_3
Cennm1	it1375a	Italy	39.44361	9.015278	124	rural background	7595	NO_2, SO_2
Teatro d'Annunzio	it1423a	Italy	42.45639	14.23472	4	urban background	8135	NO_2, O_3, PM_{10}, $PM_{2.5}$, SO_2, benzene, CO
Cenps7	it1576a	Italy	39.20333	8.386111	25	suburban background	7968	CO, NO_2, SO_2
Taranto San Vito	it1610a	Italy	40.42333	17.22528	10	urban background	7871	NO_2
Lecce - S.M. Cerrate	it1665a	Italy	40.45889	18.11611	10	rural background	7290	NO_2, O_3
Brindisi Via Magellano	it1702a	Italy	40.65083	17.94361	10	suburban background	7904	NO_2, PM_{10}
Genga - Parco Gola della Rossa	it1773a	Italy	43.46806	12.95222	550	rural background	5310	NO_2, O_3, PM_{10}, $PM_{2.5}$, SO_2, benzene, CO
Civitanova Ippodromo S. Marone	it1796a	Italy	43.33556	13.67472	110	rural background	6699	NO_2, NO_x, O_3, PM_{10}, $PM_{2.5}$, benzene
Guardiaregia	it1806a	Italy	41.41889	14.52556	884	rural background	7892	NO_2, NO_x, O_3, SO_2
Ancona Cittadella	it1827a	Italy	43.61167	13.50861	100	urban background	5985	NO_2, O_3, PM_{10}, $PM_{2.5}$, benzene, CO, SO_2
Schivenoglia	it1865a	Italy	44.99694	11.07083	16	rural background	8325	NO_2, NO_x, O_3, SO_2, benzene

Trapani	it1898a	Italy	38.01237	12.54689	40	urban background	7396	NO_2, O_3, benzene, CO
San Rocco	it1914a	Italy	44.87306	10.66389	22	rural background	8398	NO_2, NO_x, O_3
Locri	it1940a	Italy	38.22976	16.25518	11	urban background	8509	NO_2, O_3, SO_2, benzene, CO
GR - Maremma	it1942a	Italy	42.67056	11.09417	40	rural background	7784	NO_2, O_3
Censa3	it1947a	Italy	39.06667	9.008889	56	urban background	8169	NO_2, SO_2, benzene
Milazzo - Termica	it1997a	Italy	38.19061	15.24911	28	suburban background	8329	NO_2, O_3, CO, benzene
Stadio Casardi	it2003a	Italy	41.31667	16.28611	15	urban background	8391	NO_2, O_3, benzene
Cenqu1	it2040a	Italy	39.23278	9.188056	8	urban background	8181	NO_2, O_3, SO_2, benzene
Carbonara	it2051a	Italy	41.07694	16.86583	130	suburban background	7505	NO_2, PM_{10}
Ceglie Messapica	it2148a	Italy	40.64917	17.5125	100	suburban background	8393	NO_2, PM_{10}, $PM_{2.5}$, SO_2, CO, benzene
LI - Piombino-Parco-VIII-Marzo	it2154a	Italy	42.93194	10.52417	40	urban background	8228	NO_2, benzene
Gela - Biviere	it2206a	Italy	37.02249	14.34497	0	rural background	8277	NO_2, O_3, SO_2
Bar2	me0008a	Montenegro	42.10035	19.10348	12	urban background	7721	CO, NO, NO_2, NO_x, O_3, SO_2
Niskic2	me0009a	Montenegro	42.78121	18.94291	629	urban background	7693	CO, NO, NO_2, NO_x, O_3, SO_2
Koper	si0038a	Slovenia	45.54297	13.71354	56	urban background	8198	NO_2, NO_x, O_3

Balikesir-Bandirma	tr100241	Turkey	40.34795	27.97496	38	urban background	8509	NO_2
Canakkale-Lapseki	tr170313	Turkey	40.40307	26.77063	12	rural background	8170	NO_2, NO_x, O_3, $PM_{2.5}$, SO_2
Istanbul-Esenyurt	tr340241	Turkey	41.02028	28.66955	36	urban background	7915	NO_2, NO_x, SO_2
Istanbul-Sultangazi	tr340841	Turkey	41.10197	28.87202	128	urban background	8304	NO_2, NO_x, SO_2
Kirkareli-Luleburgaz-	tr390441	Turkey	41.39841	27.34588	56	rural background	8393	NO_2, SO_2

Appendix C: Example time series for NO_2

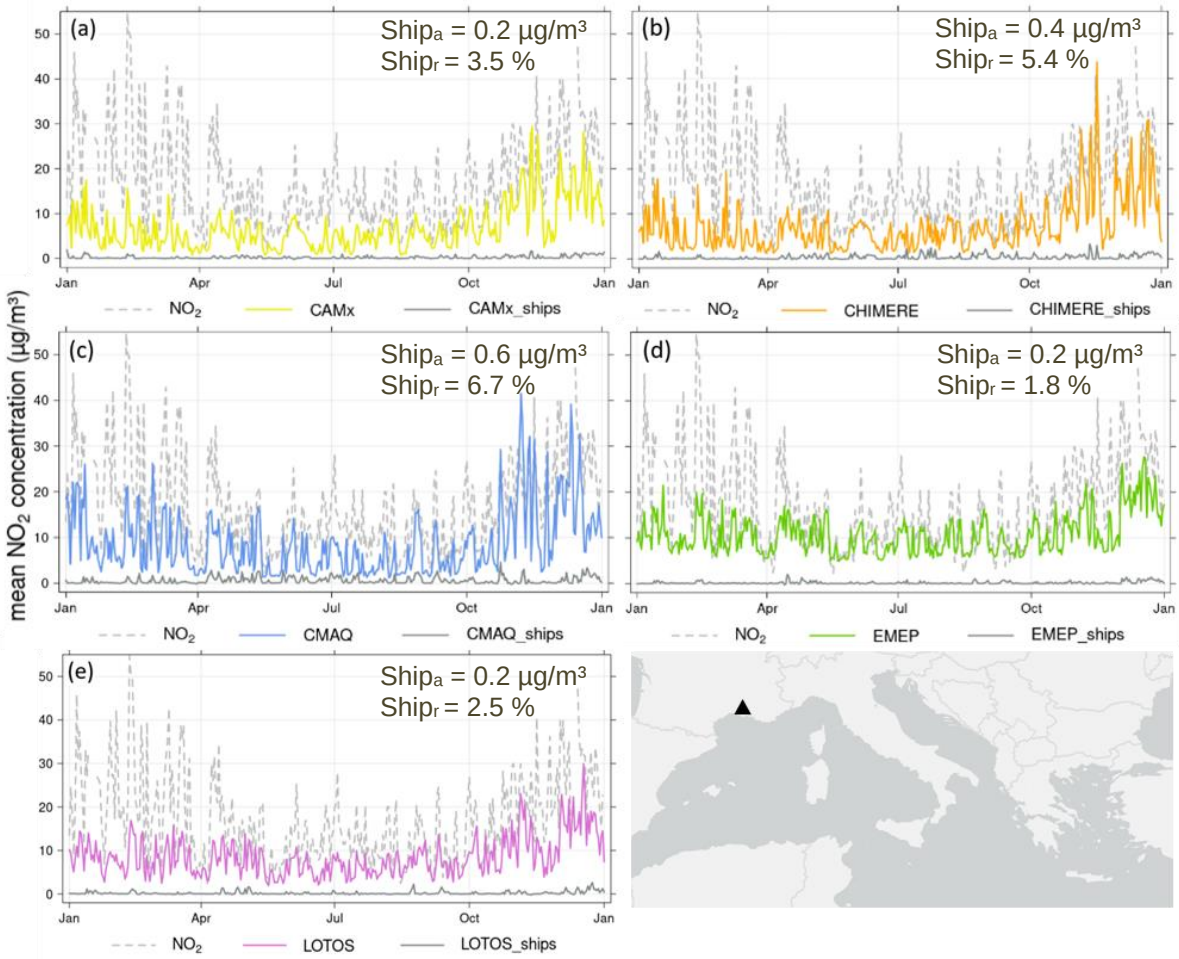

Figure C1: Time series with daily mean NO_2 concentrations in 2015 at station fr08614 in France. The black triangle on the map (bottom right) displays the location of the station. (a) = CAMx, (b) = CHIMERE, (c) = CMAQ, (d) = EMEP, (e) = LOTOS-EUROS. Dashed grey line = measured data, colored lines = modeled data, grey line = modeled potential ship impact. Correlation between modeled and measured data for hourly total emission data for 2015: CAMx = 0.23, CHIMERE = 0.20, CMAQ = 0.60, EMEP = 0.02, LOTOS-EUROS = 0.65. Ship$_a$ displays potential absolute ship impact, Ship$_r$ potential relative ship impact of the respective model.

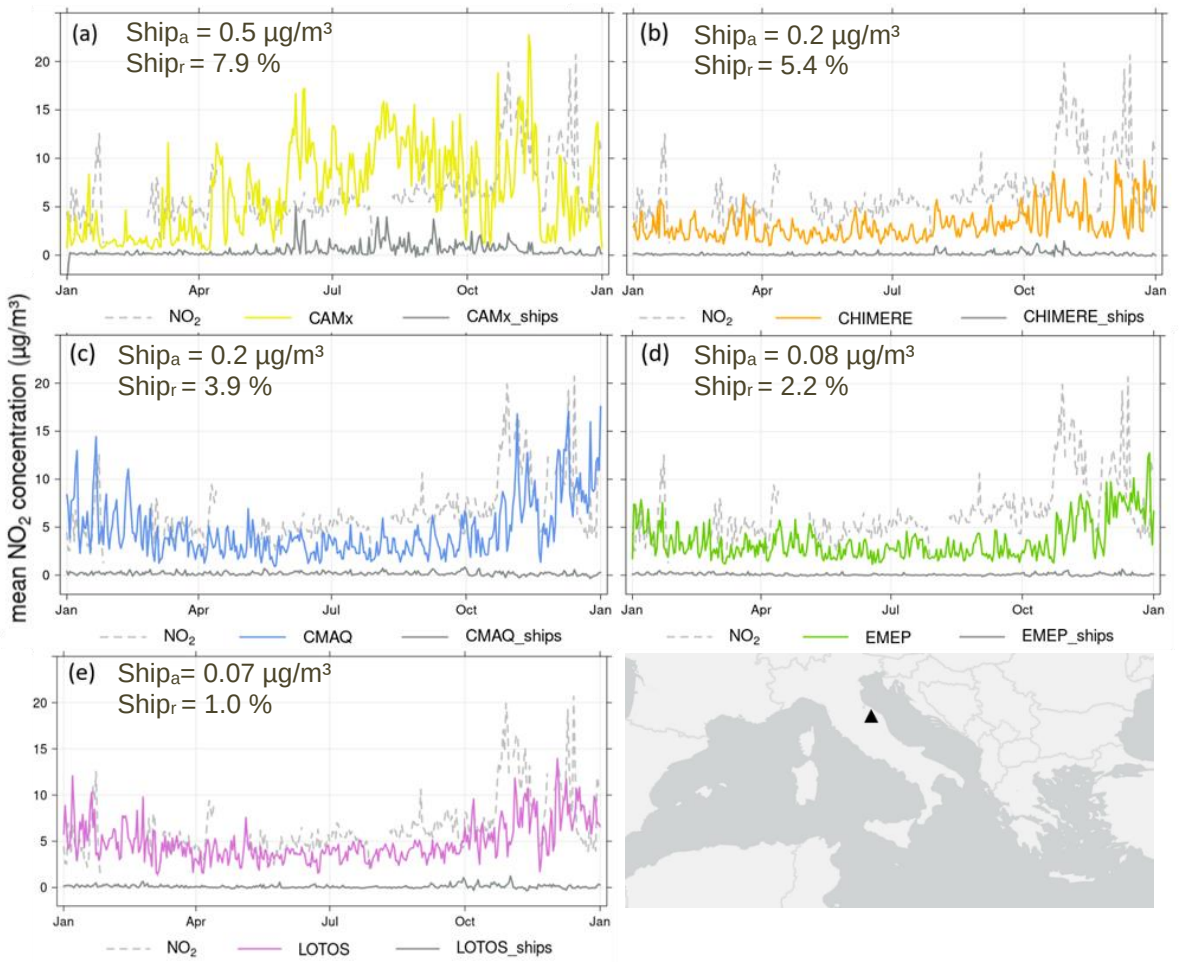

Figure C2: Time series with daily mean NO_2 concentration in 2015 at station it1773a in Italy. The black triangle on the map (bottom right) displays the location of the station. (a) = CAMx, (b) = CHIMERE, (c) = CMAQ, (d) = EMEP, (e) = LOTOS-EUROS. Dashed grey line = measured data, colored lines = modeled data, grey line = modeled ship potential impact. Correlation between modeled and measured data for hourly total emission data for 2015: CAMx = 0.03; CHIMERE = 0.03; CMAQ = 0.20; EMEP = -0.09; LOTOS-EUROS = 0.14 $Ship_a$ displays potential absolute ship impact, $Ship_r$ potential relative ship impact of the respective model.

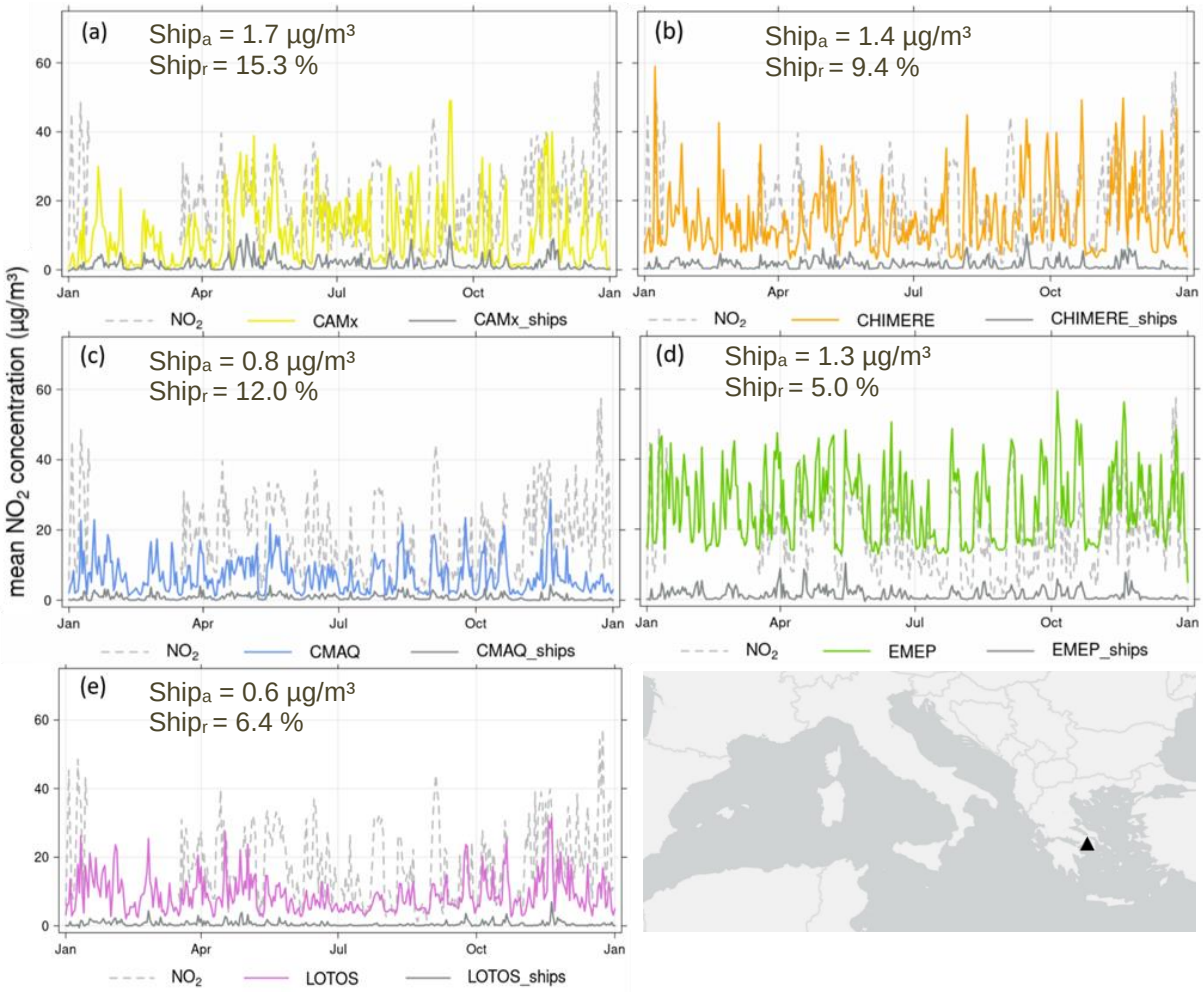

Figure C3: Time series with daily mean NO_2 concentration in 2015 at station gr0035a in Greece. The black triangle on the map (bottom right) displays the location of the station. (a) = CAMx, (b) = CHIMERE, (c) = CMAQ, (d) = EMEP, (e) = LOTOS-EUROS. Dashed grey line = measured data, colored lines = modeled data, grey line = modeled potential ship impact. Correlation between modeled and measured data for hourly total emission data for 2015: CAMx = 0.15; CHIMERE = 0.20; CMAQ = 0.28; EMEP = 0.55; LOTOS-EUROS = 0.38. Ship$_a$ displays potential absolute ship impact, Ship$_r$ potential relative ship impact of the respective model.

Appendix D: Example time series for O_3

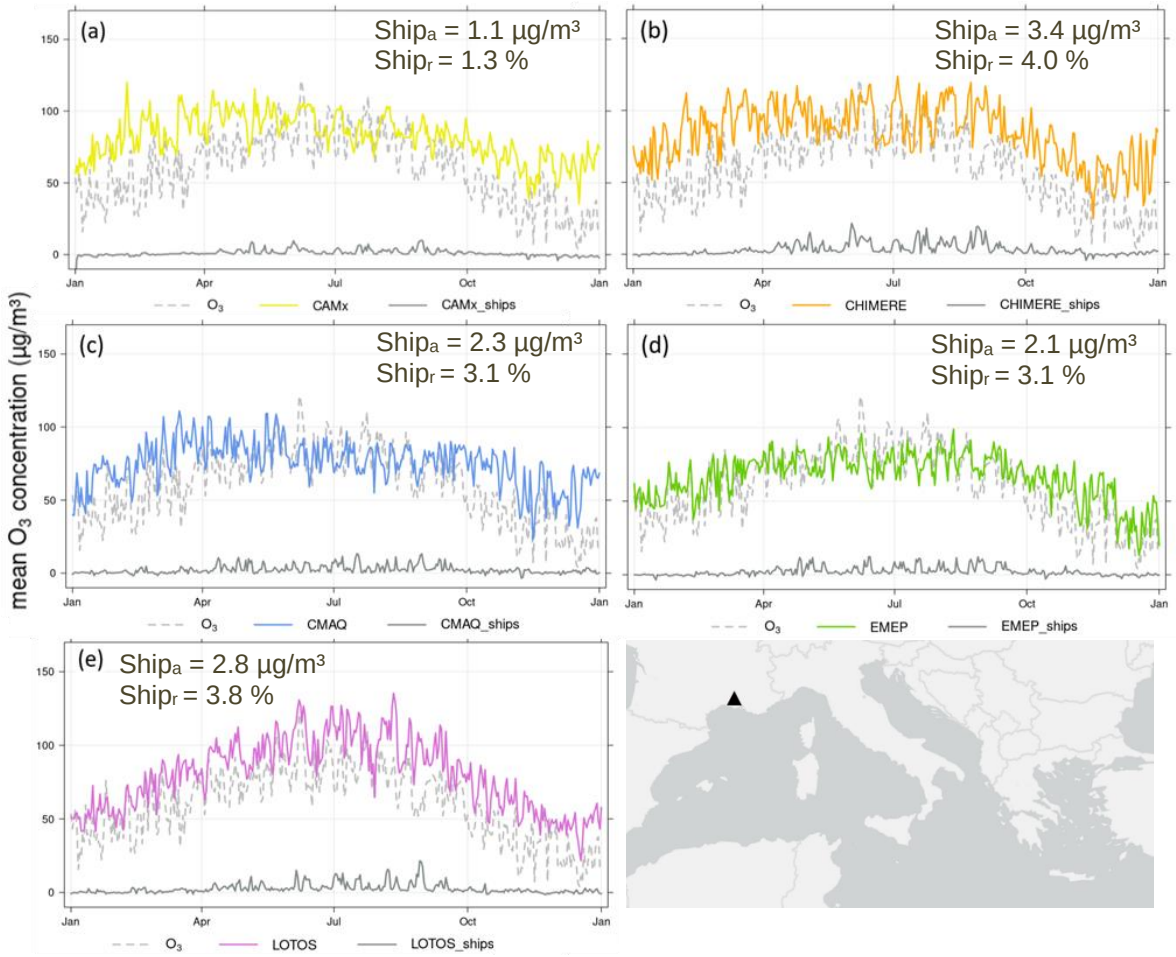

Figure D1: Time series with daily mean O_3 concentration in 2015 at station fr08614 in France. The black triangle on the map (bottom right) displays the location of the station. (a) = CAMx, (b) = CHIMERE, (c) = CMAQ, (d) = EMEP, (e) = LOTOS-EUROS. Dashed gray line = measured data, colored lines = modeled data, gray line = modeled potential ship impact. Correlation between modeled and measured data for hourly total emission data for 2015: CAMx= 0.57; CHIMERE = 0.6; CMAQ = 0.71; EMEP = 0.39; LOTOS-EUROS = 0.78. Ship$_a$ displays potential absolute ship impact, Ship$_r$ potential relative ship impact of the respective model.

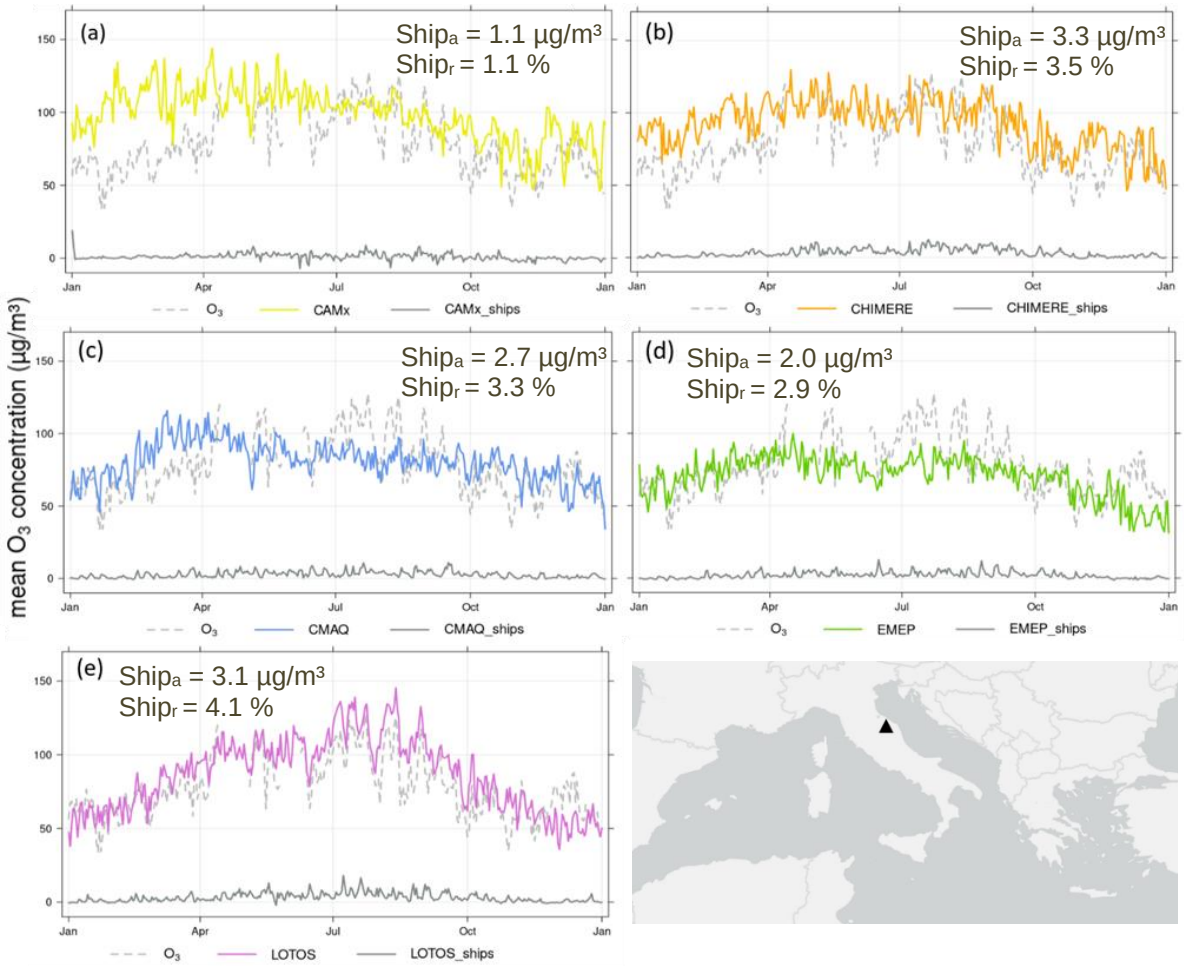

Figure D2: Time series with daily mean O_3 concentration in 2015 at station it1773a in Italy. The black triangle on the map (bottom right) displays the location of the station. (a) = CAMx, (b) = CHIMERE, (c) = CMAQ, (d) = EMEP, (e) = LOTOS-EUROS. Dashed gray line = measured data, colored lines = modeled data, gray line = modeled potential ship impact. Correlation between modeled and measured data for hourly total emission data for 2015: CAMx = 0.37; CHIMERE = 0.4; CMAQ = 0.58; EMEP = 0.35; LOTOS-EUROS = 0.7. $Ship_a$ displays potential absolute ship impact, $Ship_r$ potential relative ship impact of the respective model.

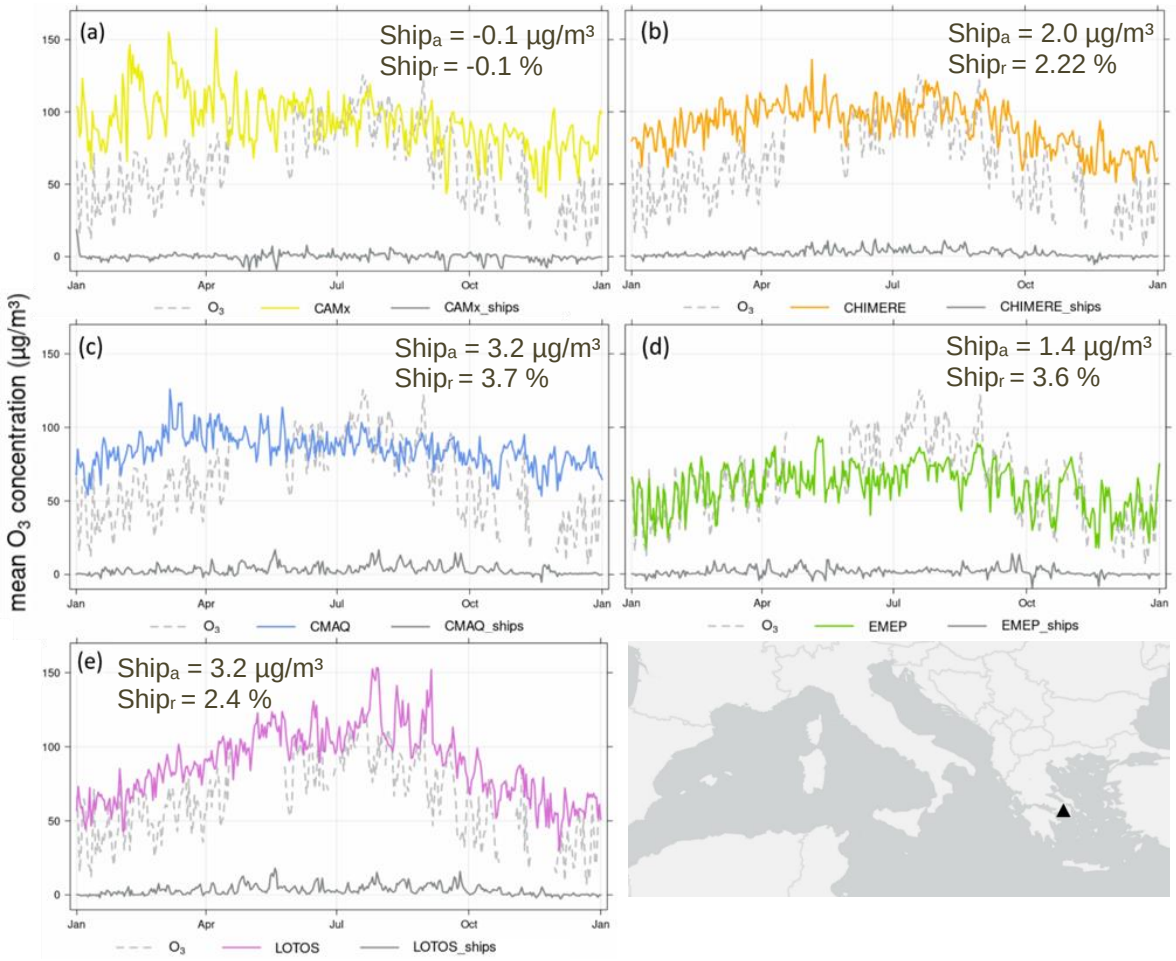

Figure D3: Time series with daily mean O_3 concentration in 2015 at station gr0035a in Greece. The black triangle on the map (bottom right) displays the location of the station. (a) = CAMx, (b) = CHIMERE, (c) = CMAQ, (d) = EMEP, (e) = LOTOS-EUROS. Dashed gray line = measured data, colored lines = modeled data, gray line = modeled potential ship impact. Correlation between modeled and measured data for hourly total emission data for 2015: CAMx = 0.29; CHIMERE = 0.46; CMAQ = 0.50; EMEP = 0.71; LOTOS-EUROS = 0.57. $Ship_a$ displays potential absolute ship impact, $Ship_r$ potential relative ship impact of the respective model.

Appendix E: NO_x Spatial Distribution

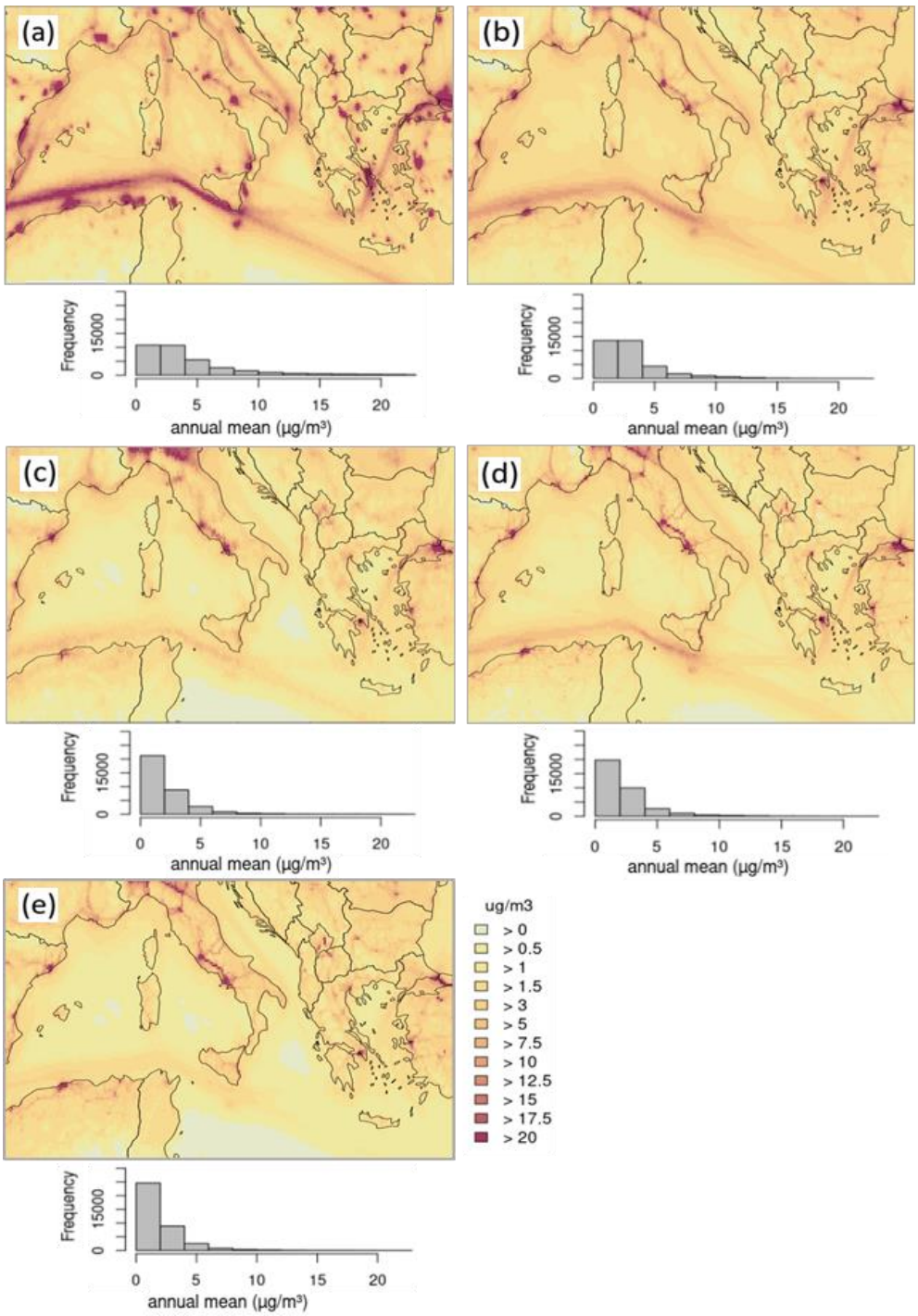

Figure E1: Annual mean of NO_x total concentration. (a) = CAMx, (b) = CHIMERE, (c) = CMAQ, (d) = LOTOS-EUROS. Below the domain figure, the respective frequency distribution is displayed for the annual mean NO_x concentration, referred to the whole model domain.

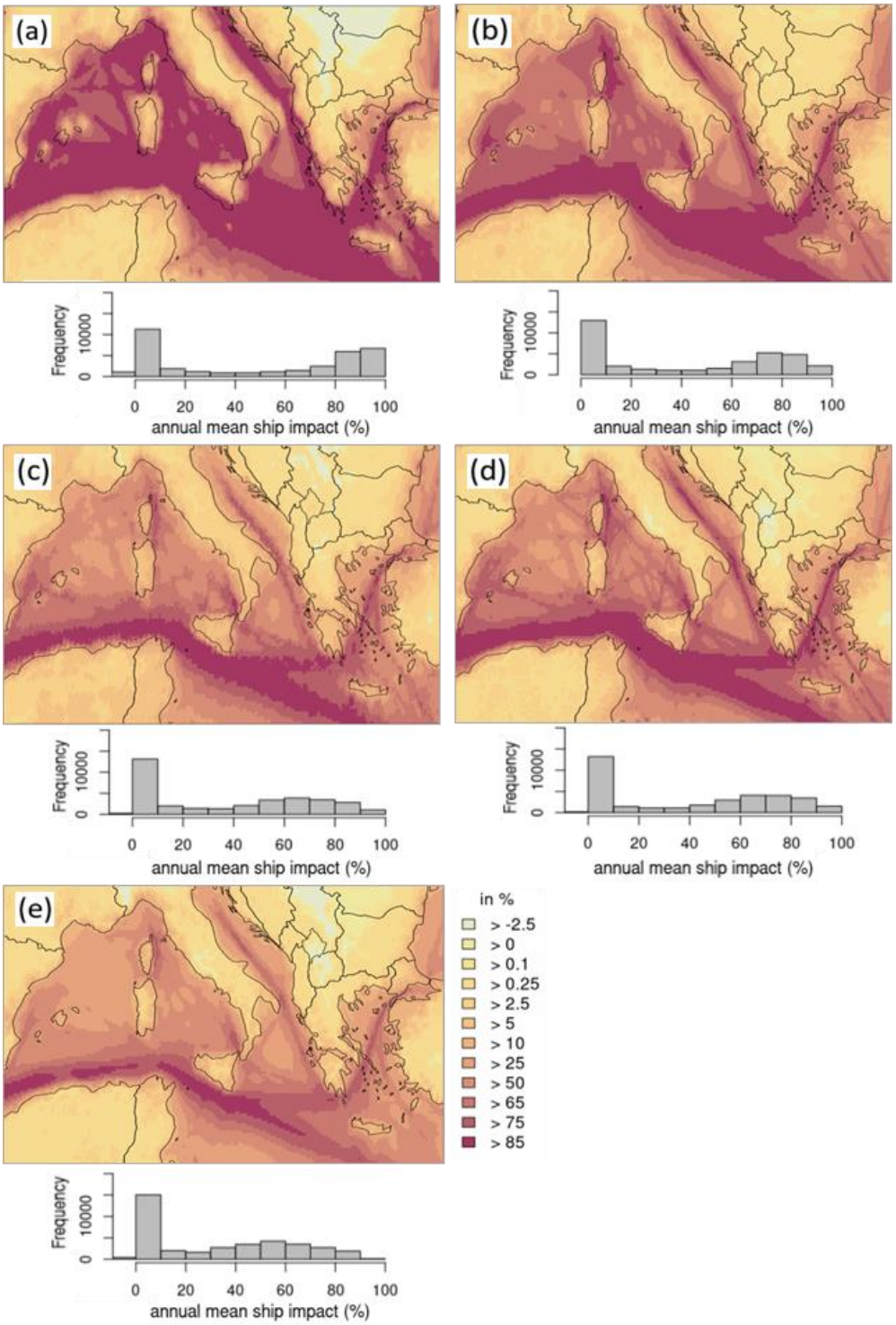

Figure E2: Annual mean relative potential ship impact of NO_x. (a) = CAMx, (b) = CHIMERE, (c) = CMAQ, (d) = LOTOS-EUROS. Below the domain figure the respective frequency distribution is displayed for the annual mean relative potential ship impact of NO_x, referred to the whole model domain.

Appendix F: annual total dry deposition of N

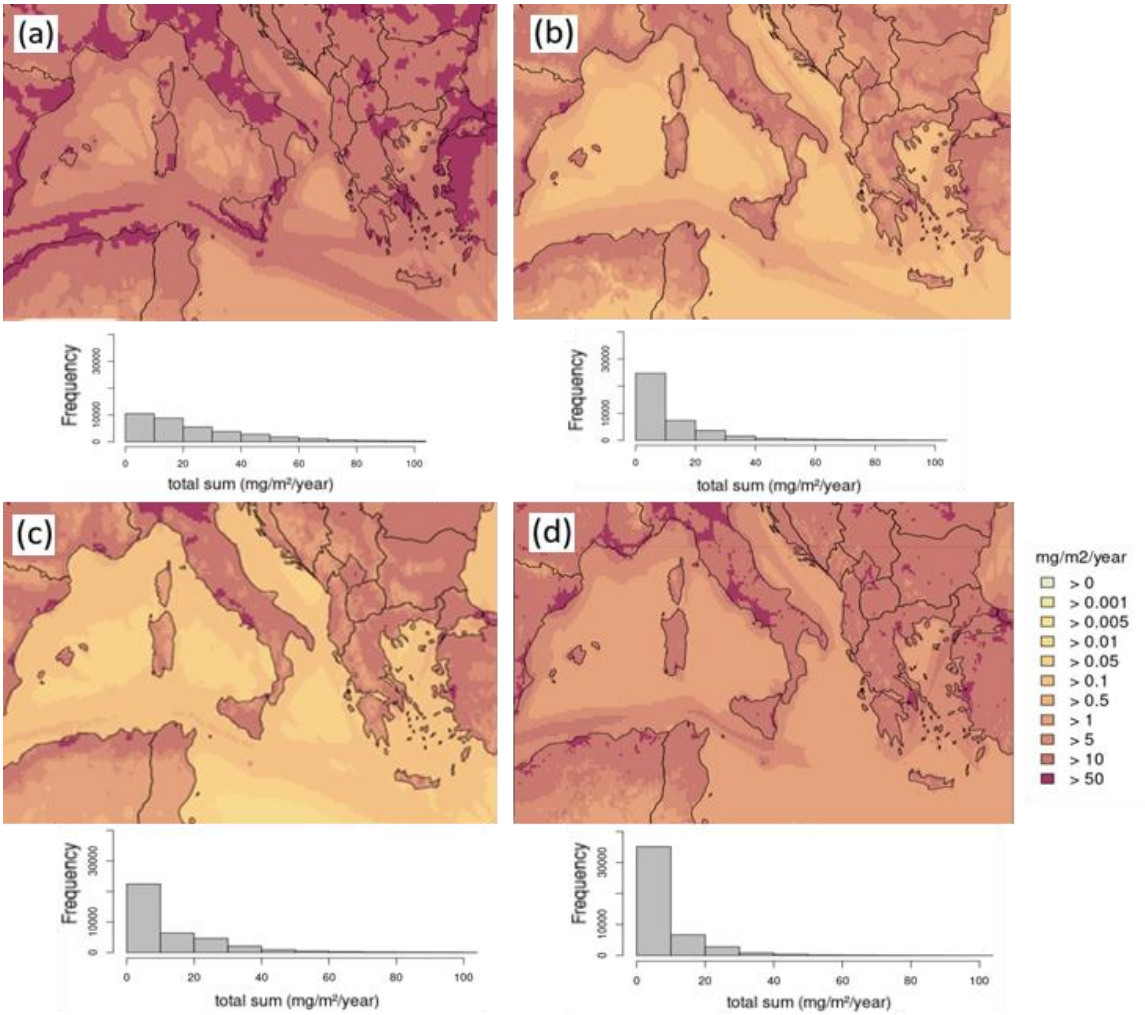

Figure F1: Annual total dry deposition of N. (a) = CAMx, (b) = CHIMERE, (c) = CMAQ, (d) = LOTOS-EUROS.

Appendix G

Table G1: Comparison plume dispersion in MAFOR and Chosson et al. (2008).

MAFOR		Chosson et al. (2008)	
Calculation	Parameters[1]	Calculation	Parameters[2]
$\boldsymbol{dil\_rate = (\frac{a}{dil\_time})^b}$	a = 1.659 b = 1.133 dil_time = input: time passed in plume [s]	$dil\_rate = a\,(\frac{t*}{t})^b$	a = 0.051 [min^{-1}] b = 1.08 t* = turn-over time scale [min] t = time passed in plume [min]

[1] based on adjustments from Moldanova, J. (personal communication)

[2] Parameters are for a buoyancy flux of 250 m^4/s^3

Appendix H:

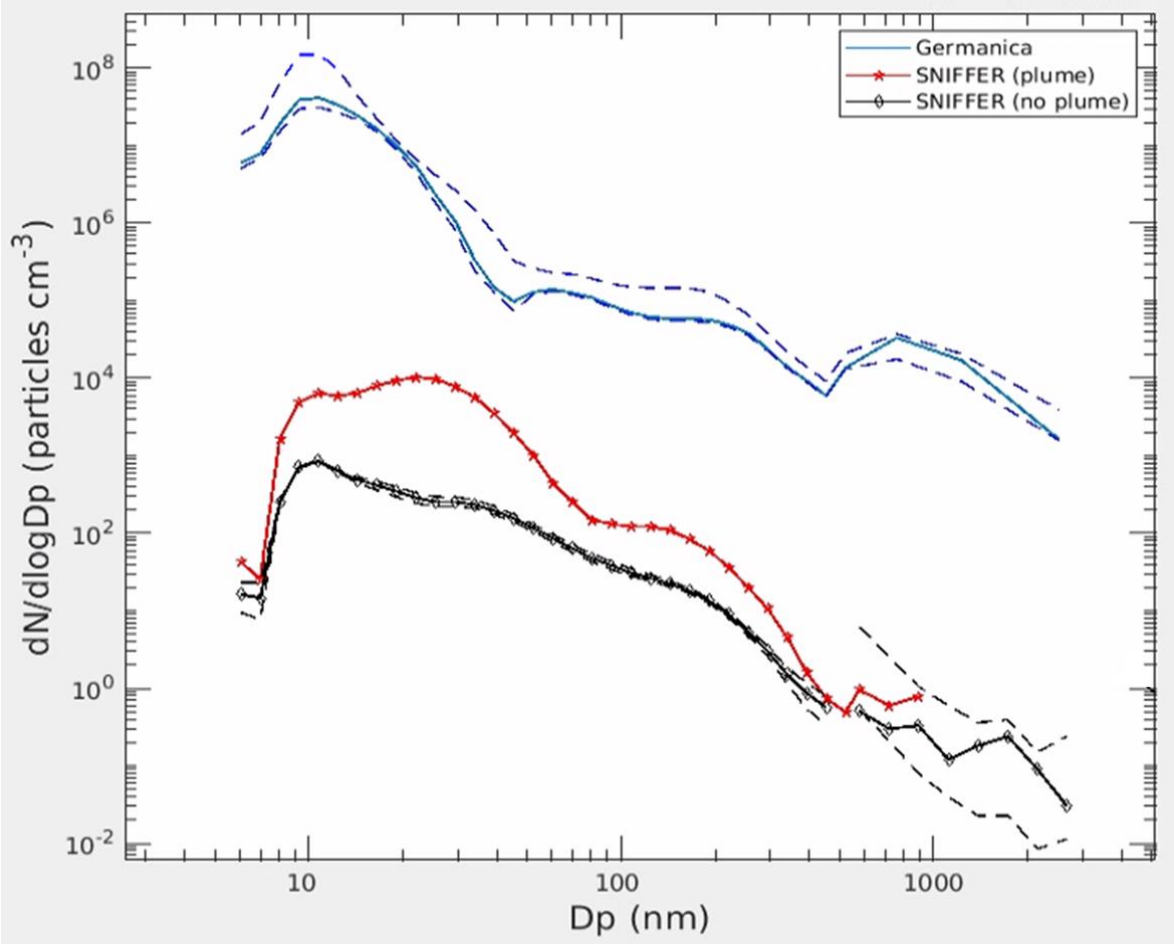

Figure H1: Measurements with 25th and 75th percentile. Comparison of the modeled particle size distributions with the observed particle size distributions. "Germanica" = measured particle size distribution at the stack. "SNIFFER (plume)" = particle size distributions recorded at the Sniffer at the plume arrival. "SNIFFER (no plume)" = particle size distributions recorded at the Sniffer without a plume event.

Supplements 1

Supplements 1, Table S1: Extent of computational domains.

Model	Longitudes	Latitudes
CAMx	-1.1323 to 30.0677	33.8102 to 45.8102
CHIMERE	-1.52724 to 30.07276	33.3787 to 45.8787
CMAQ	-1.0 to 31.1	32.8 to 46.7
EMEP	-0.95 to 31.15	32.85 to 46.75
LOTOS-EUROS	-0.95 to 29.95	32.85 to 44.95

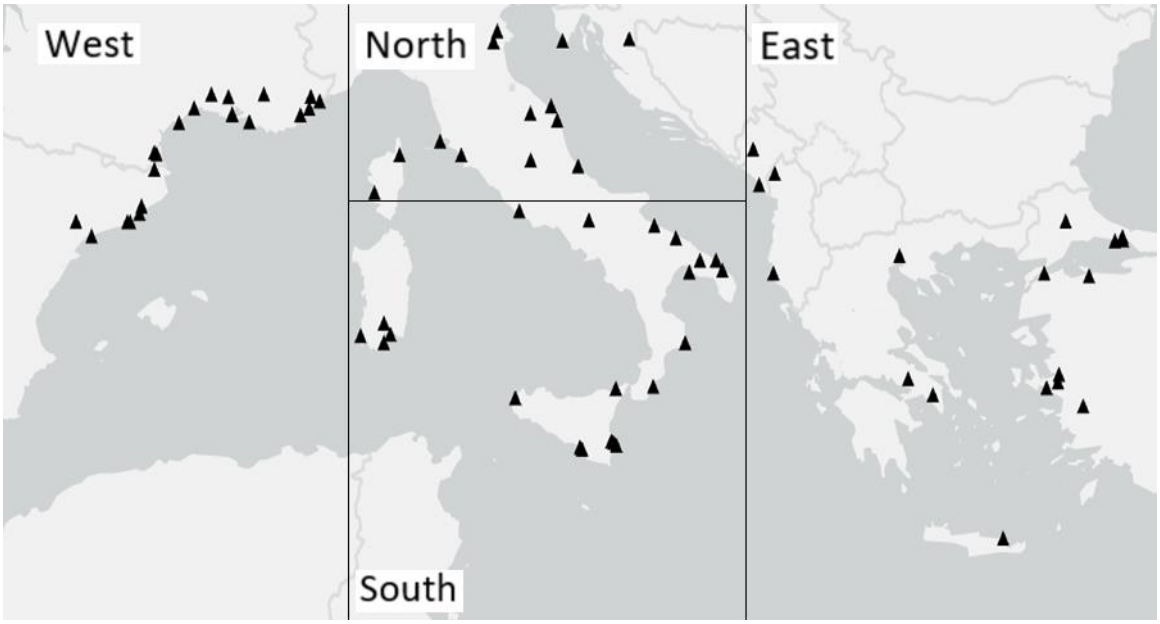

Supplements 1, S2: Time series display mean values of all stations in the respective region and the mean value of each model in this region in the grid cells of the stations.

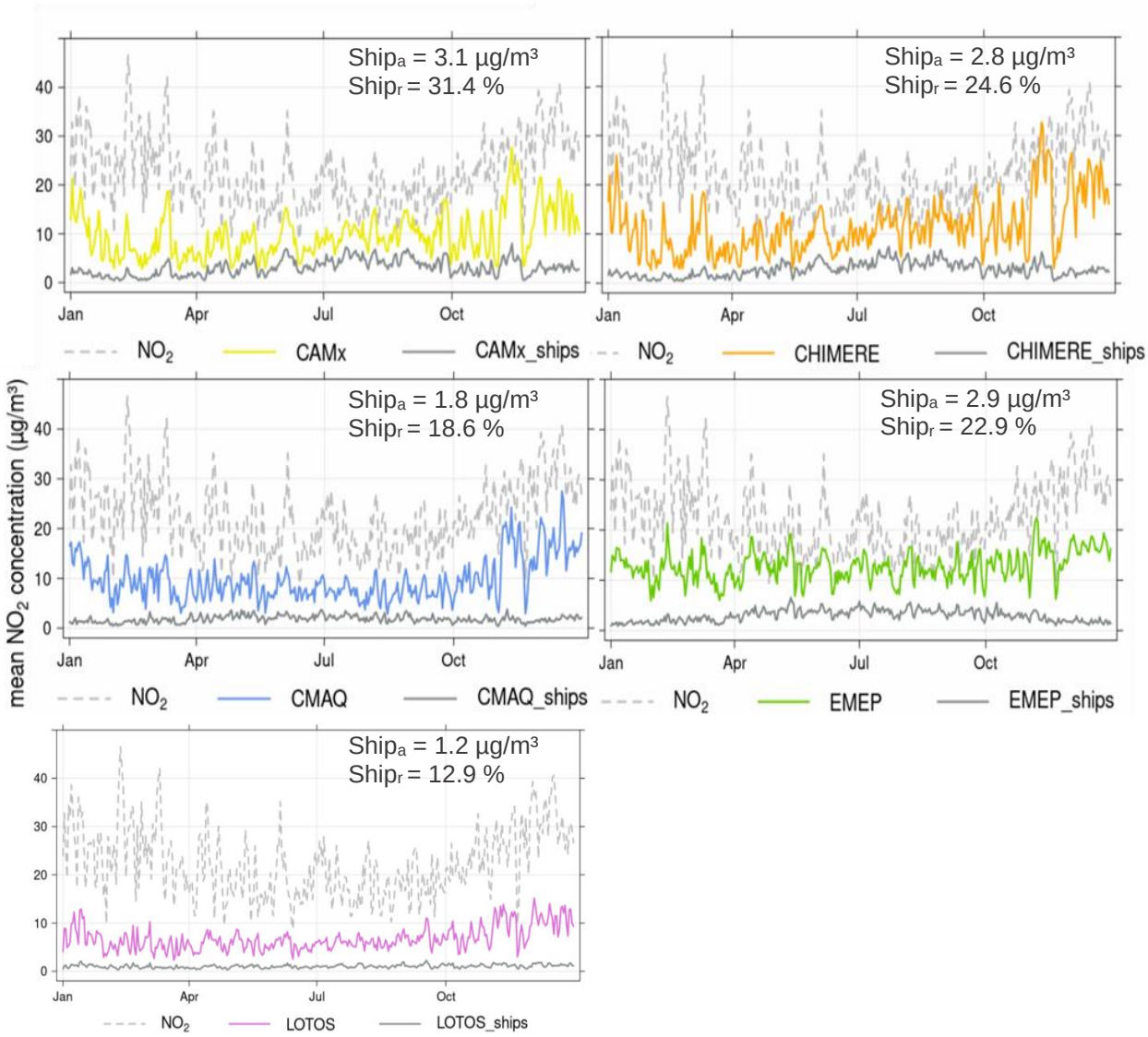

Supplements 1, S3: Time series with daily mean values of NO_2 for 2015 in panel "west". (a) = CAMx, (b) = CHIMERE, (c) = CMAQ, (d) = EMEP, (e) = LOTOS-EUROS. Dashed grey line = measured data, colored lines = modeled data, grey line = modeled ship contribution. Correlation between modeled and measured data for hourly total emission data for 2015: CAMx: R = 0.23, CHIMERE: R = 0.25, CMAQ: R = 0.2, EMEP: R = 0.23, LOTOS-EUROS: R = 0.26.

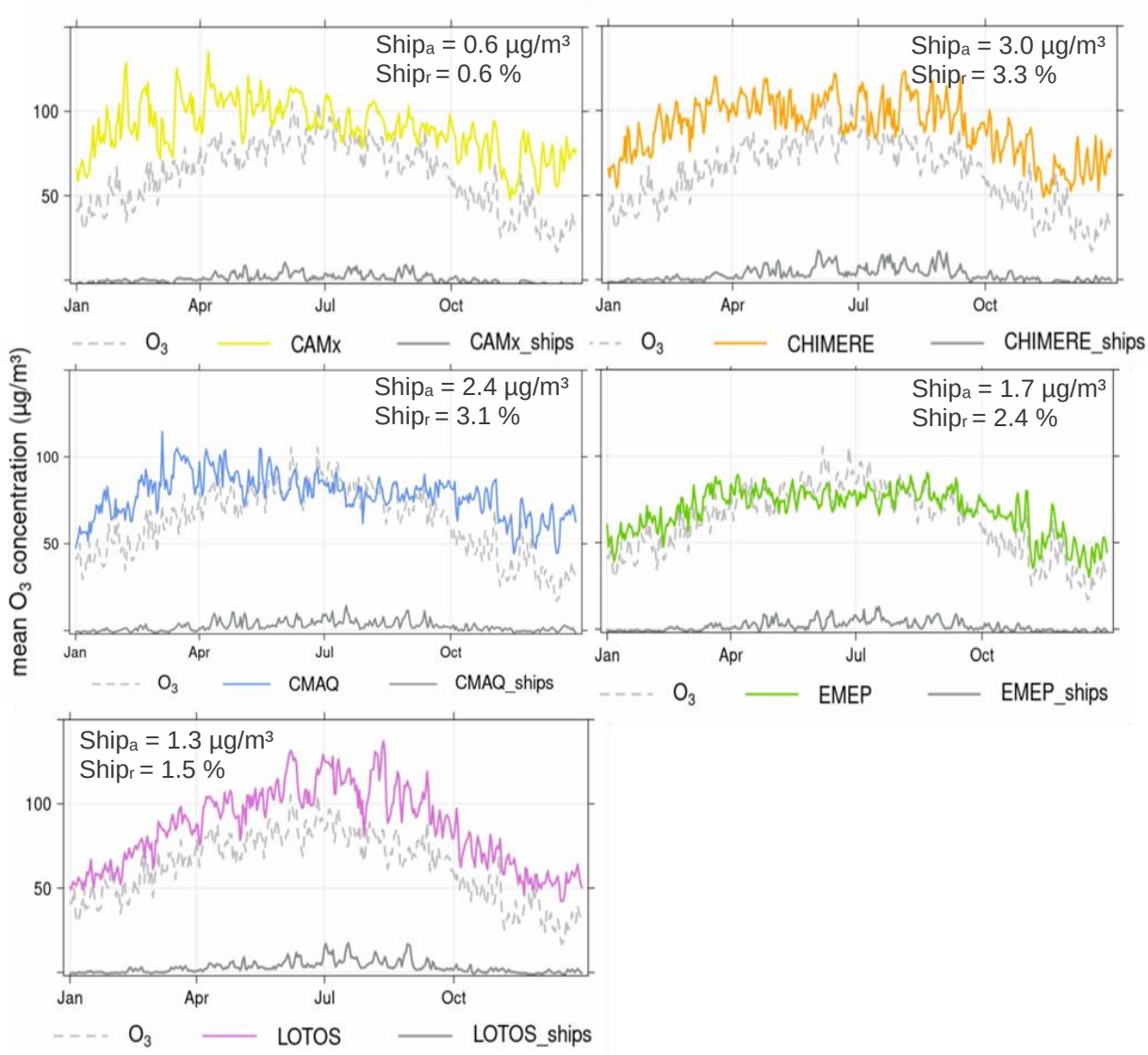

Supplements 1, S4: Time series with daily mean values of O_3 for 2015 in panel "west". (a) = CAMx, (b) = CHIMERE, (c) = CMAQ, (d) = EMEP, (e) = LOTOS-EUROS. Dashed grey line = measured data, colored lines = modeled data, grey line = modeled ship contribution. Correlation between modeled and measured data for hourly total emission data for 2015: CAMx R = 0.57, CHIMERE R = 0.60, CMAQ: R = 0.58, EMEP: R = 0.23, LOTOS-EUROS: R = 0.65.

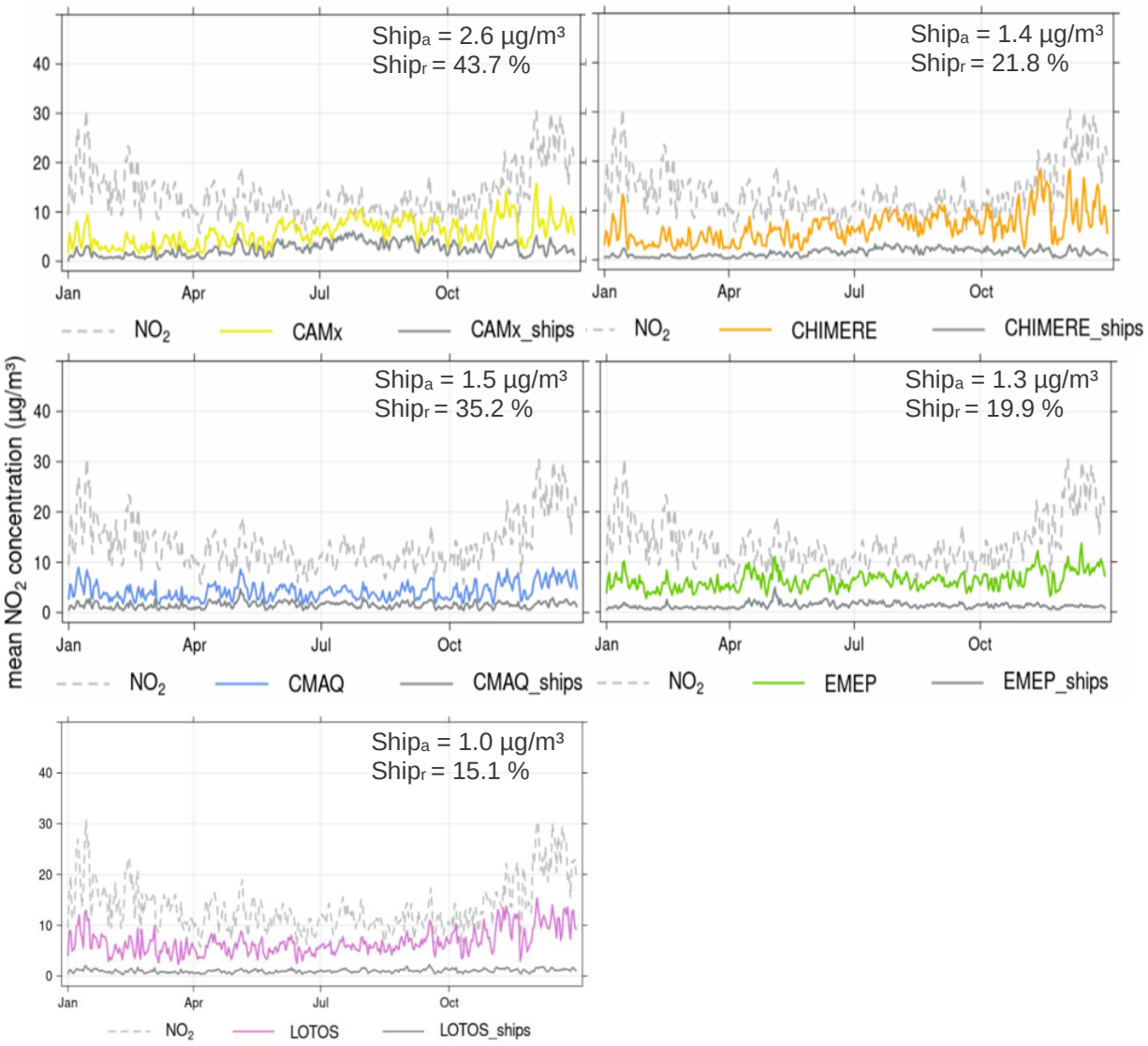

Supplements 1, S5: Time series with daily mean values of NO_2 for 2015 in panel "south". (a) = CAMx, (b) = CHIMERE, (c) = CMAQ, (d) = EMEP, (e) = LOTOS-EUROS. Dashed grey line = measured data, colored lines = modeled data, grey line = modeled ship contribution. Correlation between modeled and measured data for hourly total emission data for 2015: CAMx: R = 0.20, CHIMERE: R = 0.26, CMAQ: R = 0.15, EMEP: R = 0.24, LOTOS-EUROS: R = 0.22.

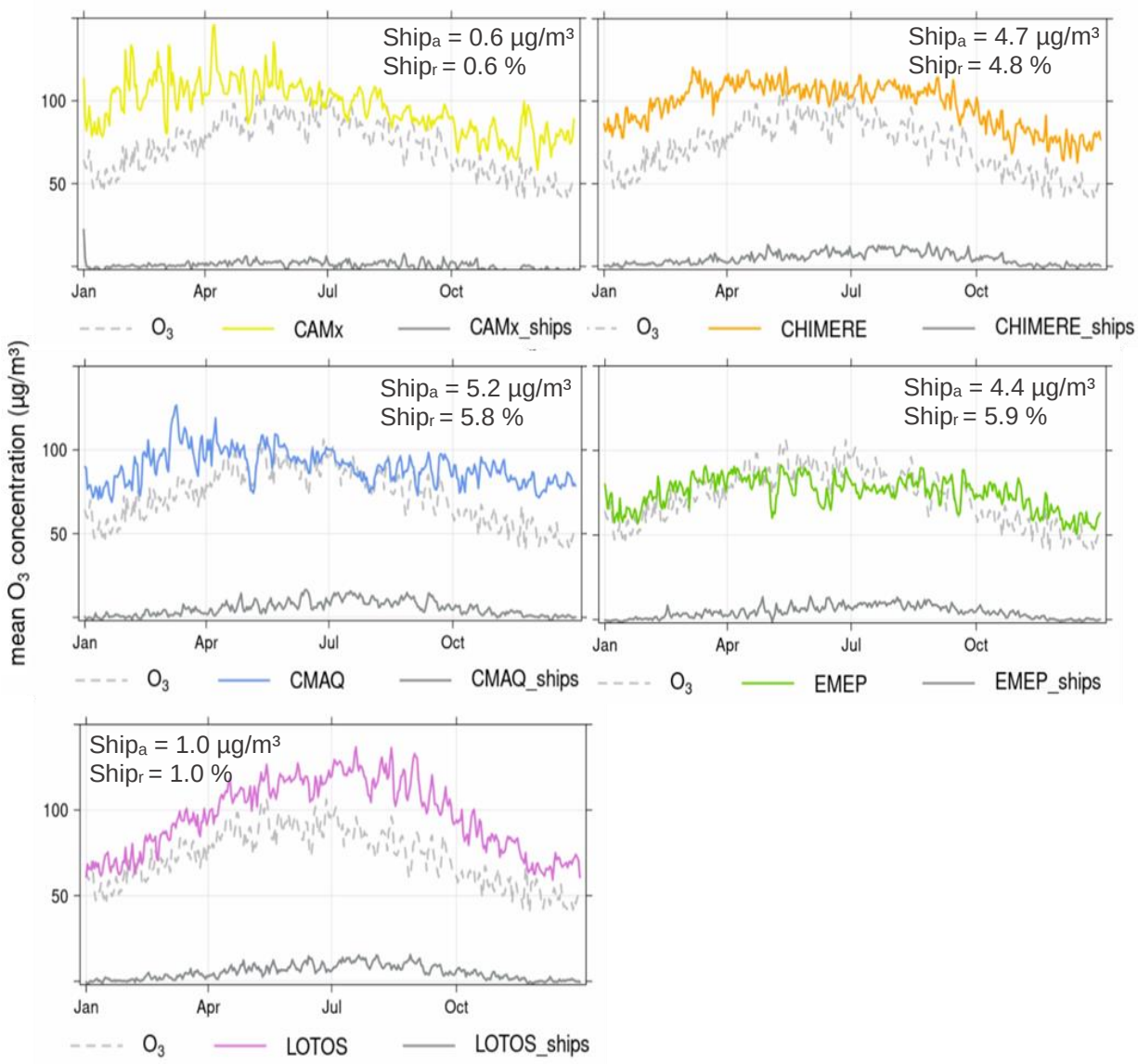

Supplements 1, S6: Time series with daily mean values of O_3 for 2015 in panel "south". (a) = CAMx, (b) = CHIMERE, (c) = CMAQ, (d) = EMEP, (e) = LOTOS-EUROS. Dashed grey line = measured data, colored lines = modeled data, grey line = modeled ship contribution. Correlation between modeled and measured data for hourly total emission data for 2015: CAMx: R = 0.47, CHIMERE: R = 0.56, CMAQ: R = 0.44, EMEP: R = 0.52, LOTOS-EUROS: R = 0.53.

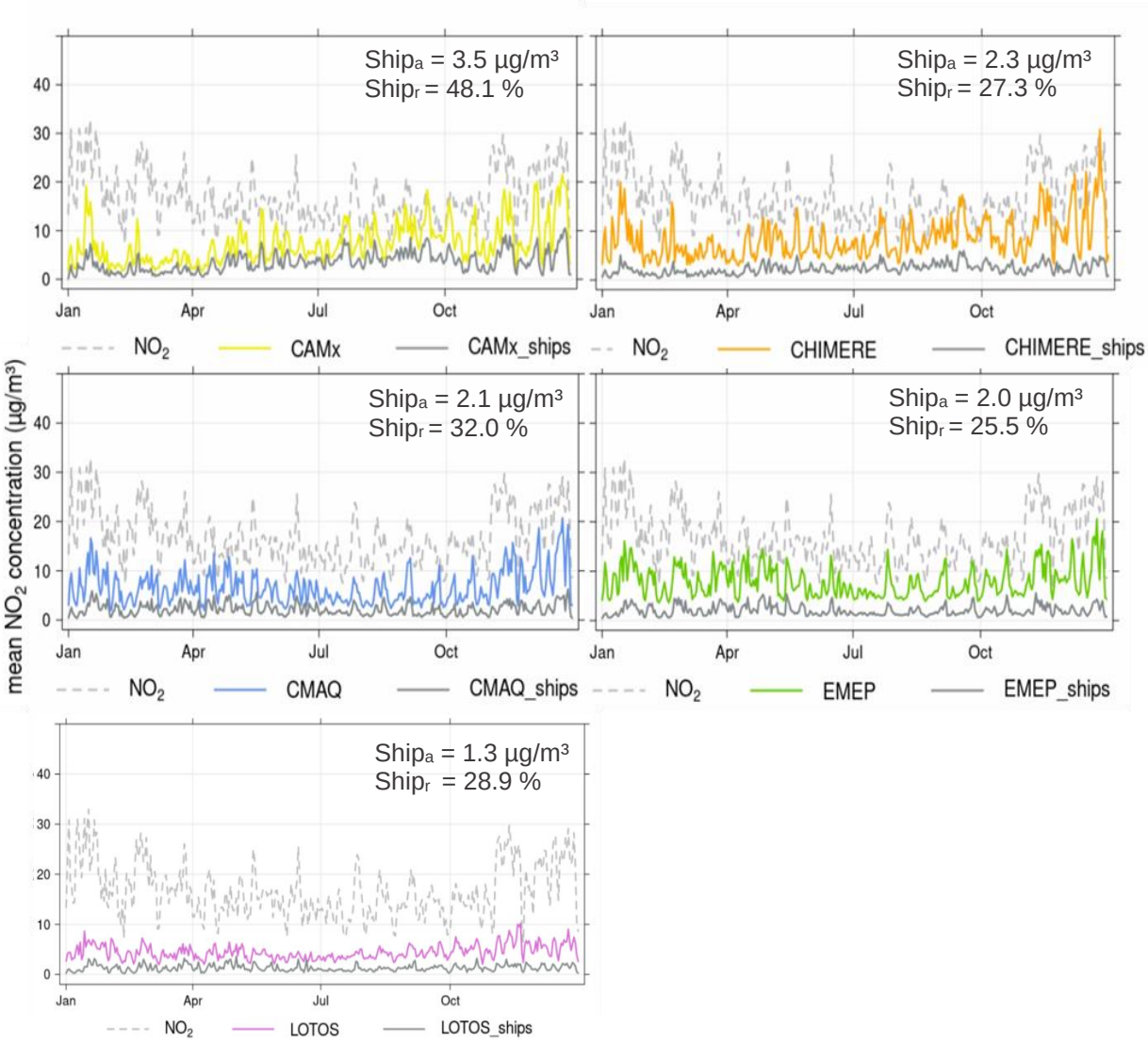

Supplements 1, S7: Time series with daily mean values of NO_2 for 2015 in panel "east". (a) = CAMx, (b) = CHIMERE, (c) = CMAQ, (d) = EMEP, (e) = LOTOS-EUROS. Dashed grey line = measured data, colored lines = modeled data, grey line = modeled ship contribution. Correlation between modeled and measured data for hourly total emission data for 2015: CAMx: R = 0.16, CHIMERE: R = 0.22, CMAQ: R = 0.22, EMEP: R = 0.27, LOTOS-EUROS: R = 0.23.

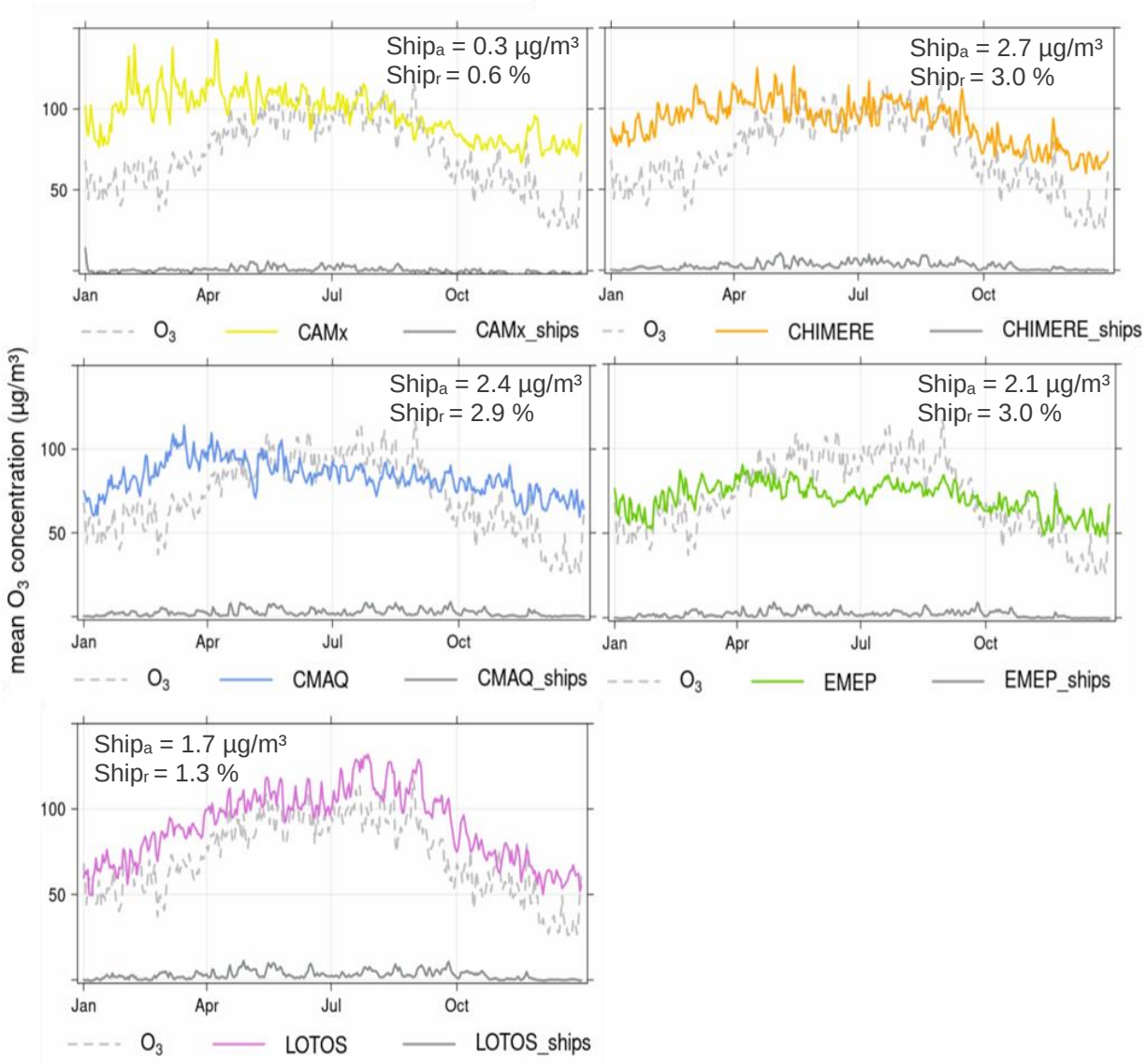

Supplements 1, S8: Time series with daily mean values of O_3 for 2015 in panel "east". (a) = CAMx, (b) = CHIMERE, (c) = CMAQ, (d) = EMEP, (e) = LOTOS-EUROS. Dashed grey line = measured data, colored lines = modeled data, grey line = modeled ship contribution. Correlation between modeled and measured data for hourly total emission data for 2015: CAMx: R = 0.35, CHIMERE: R = 0.46, CMAQ: R = 0.37, EMEP: R = 0.47, LOTOS-EUROS: R = 0.53.

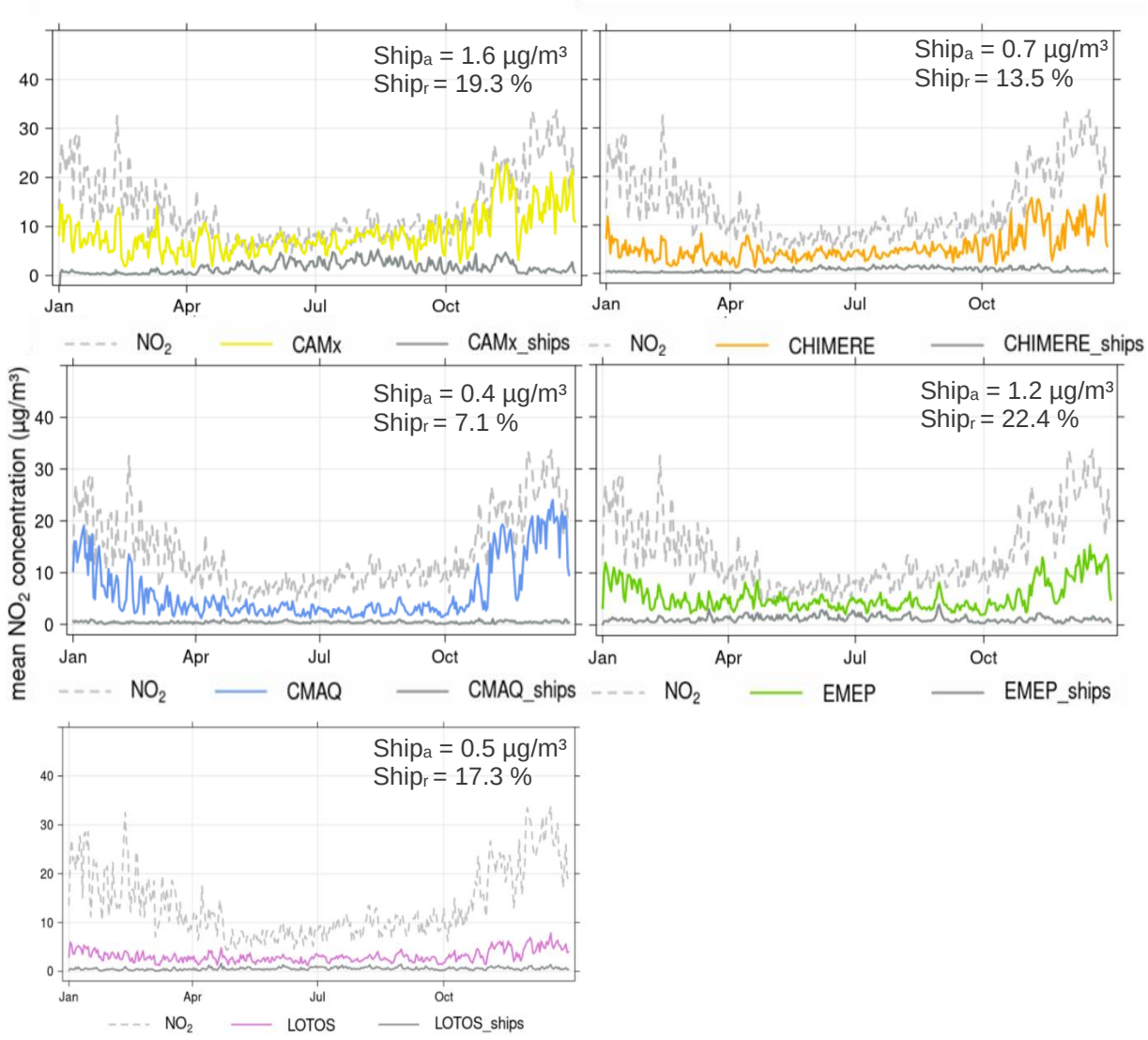

Supplements 1, S9: Time series with daily mean values of NO_2 for 2015 in panel "north". (a) = CAMx, (b) = CHIMERE, (c) = CMAQ, (d) = EMEP, (e) = LOTOS-EUROS. Dashed grey line = measured data, colored lines = modeled data, grey line = modeled ship contribution. Correlation between modeled and measured data for hourly total emission data for 2015: CAMx: R = 0.3, CHIMERE: R = 0.27, CMAQ: R = 0.35, EMEP: R = 0.33, LOTOS-EUROS: R = 0.26.

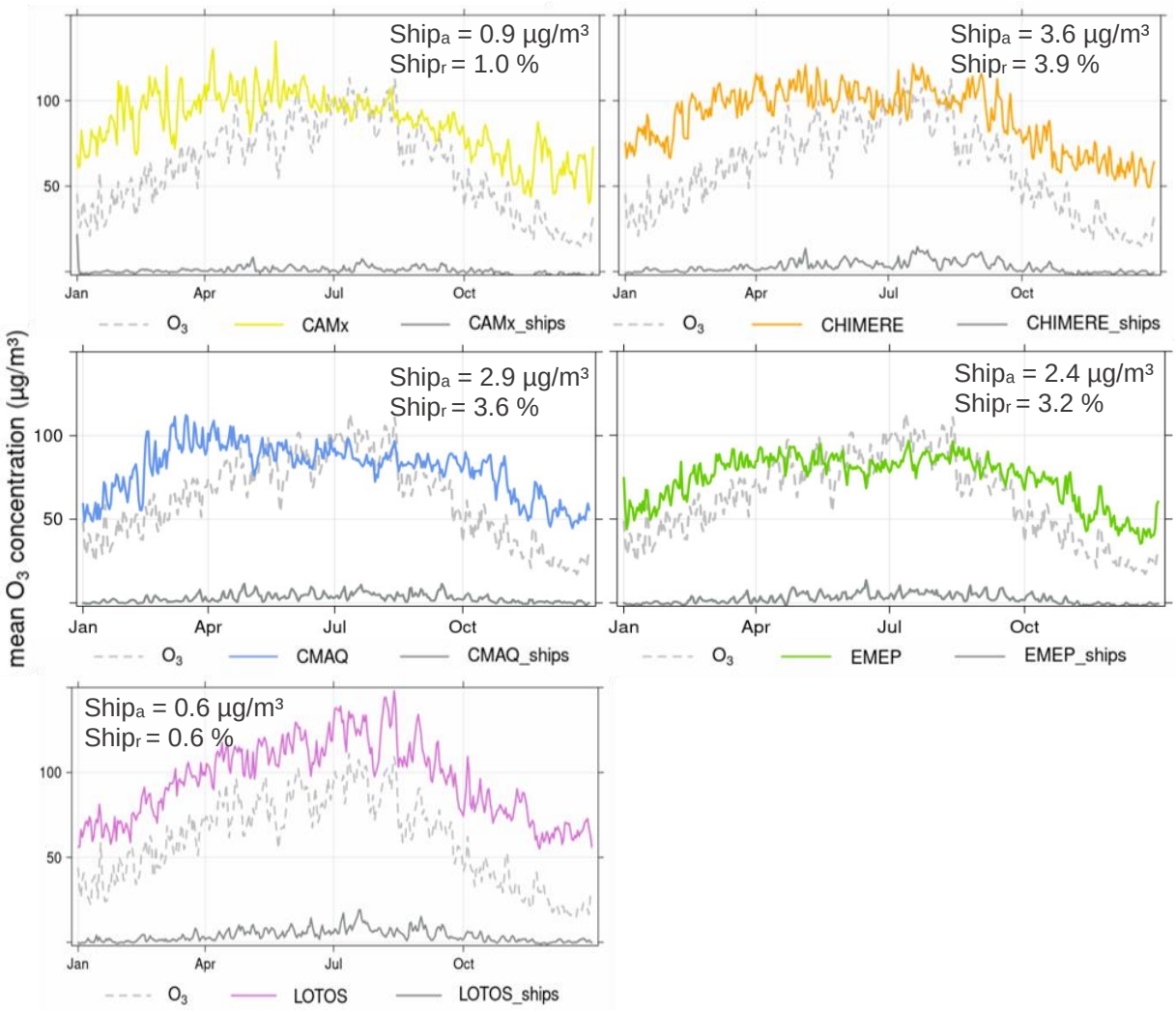

Supplements 1, S10: Time series with daily mean values of O_3 for 2015 in panel "north". (a) = CAMx, (b) = CHIMERE, (c) = CMAQ, (d) = EMEP, (e) = LOTOS-EUROS. Dashed grey line = measured data, colored lines = modeled data, grey line = modeled ship contribution. Correlation between modeled and measured data for hourly total emission data for 2015: CAMx: R = 0.61, CHIMERE: R = 0.70, CMAQ: R = 0.60, EMEP: R = 0.65, LOTOS-EUROS: R = 0.66.

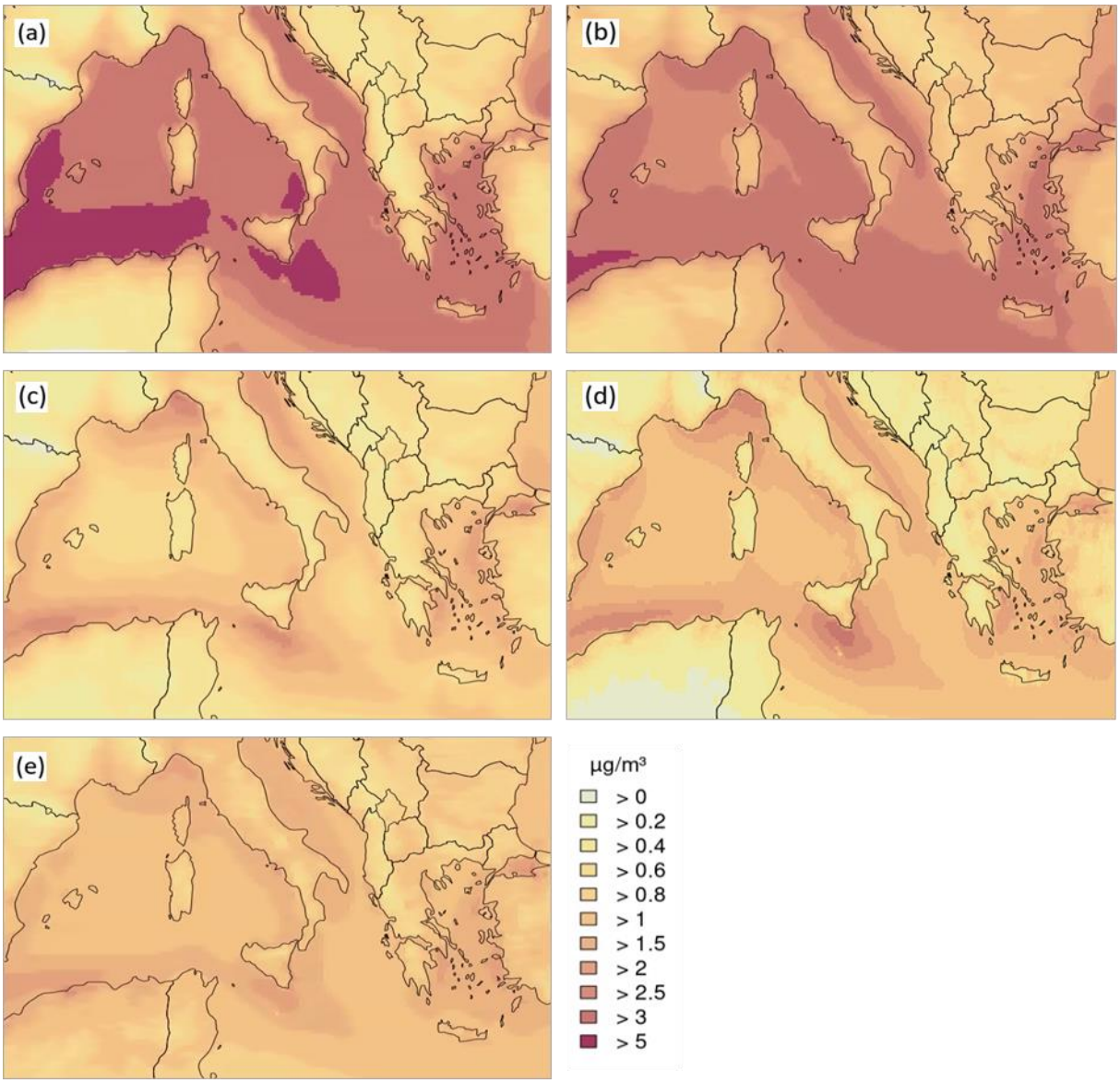

Supplements 1, S11: Annual mean concentration of HNO_3 for emisbase run with all emission sources, based on averaged daily values. (a) = CAMx, (b) = CHIMERE, (c) = CMAQ, (d) = EMEP, (e) = LOTOS-EUROS.

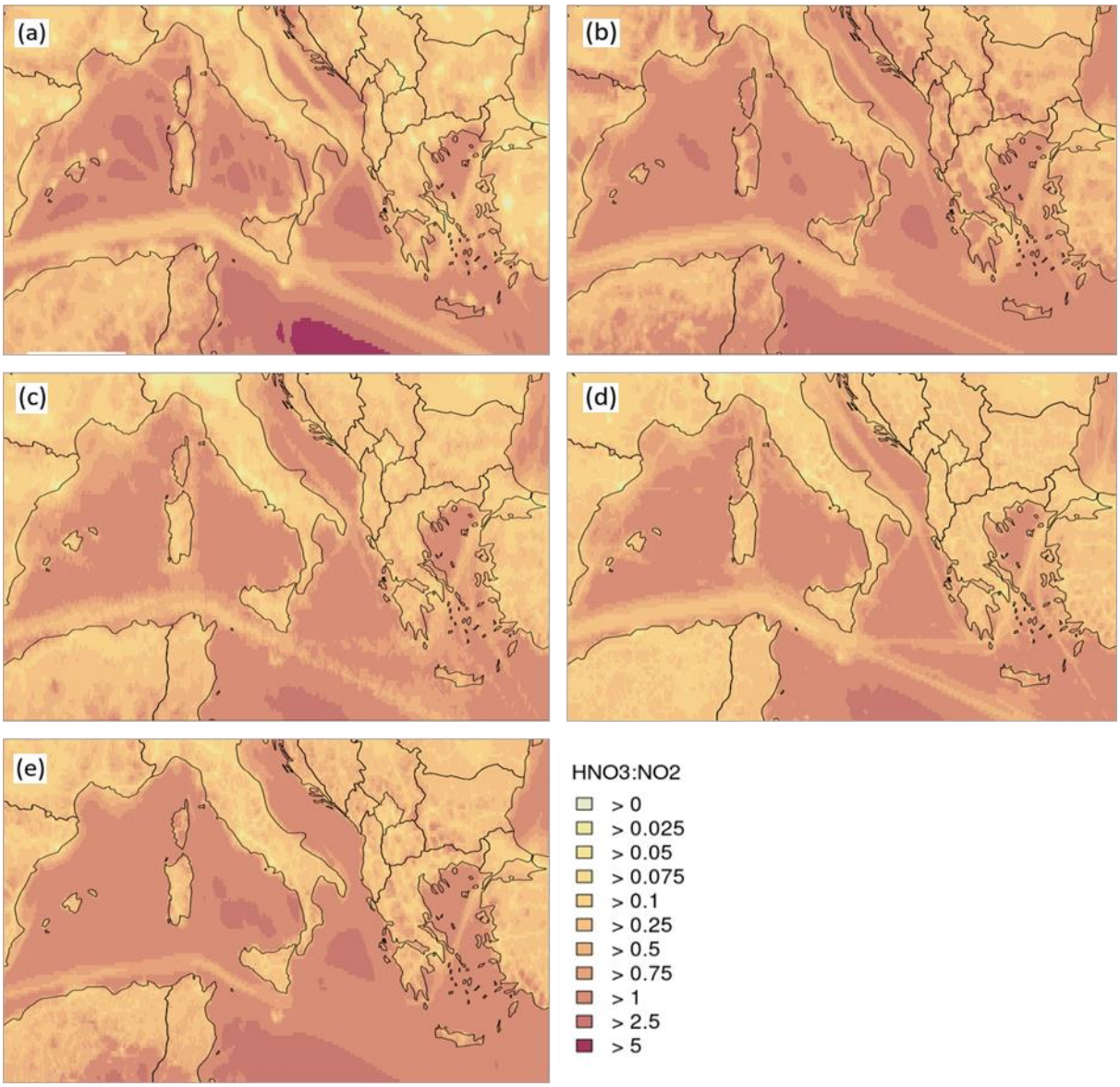

Supplements 1, S12: Annual mean ratio of HNO_3:NO_2 for emisbase run with all emission sources, based on averaged daily values. (a) = CAMx, (b) = CHIMERE, (c) = CMAQ, (d) = EMEP, (e) = LOTOS-EUROS.

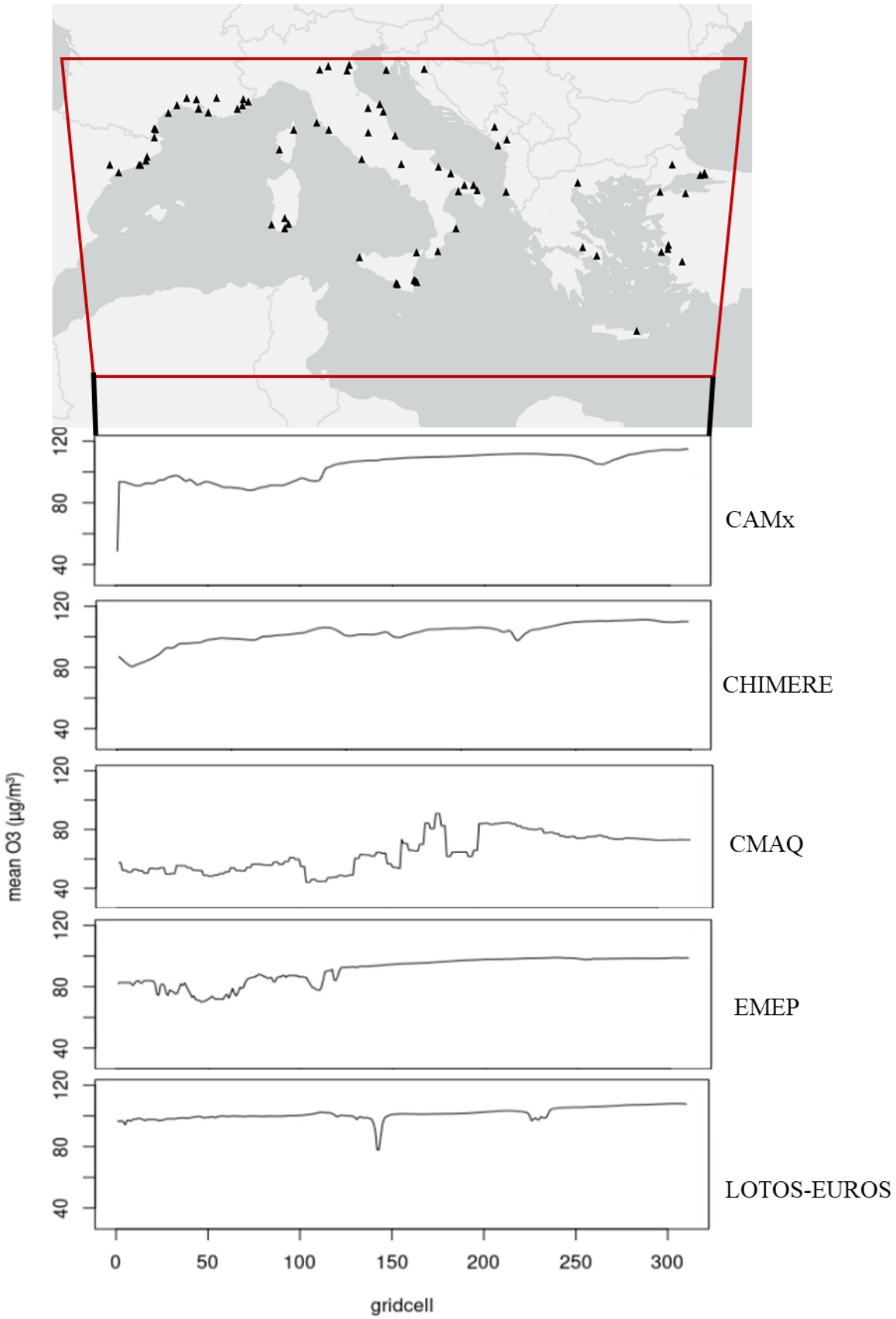

Supplements 1, S13: Boundary conditions of the southern part of the SC12 domain.

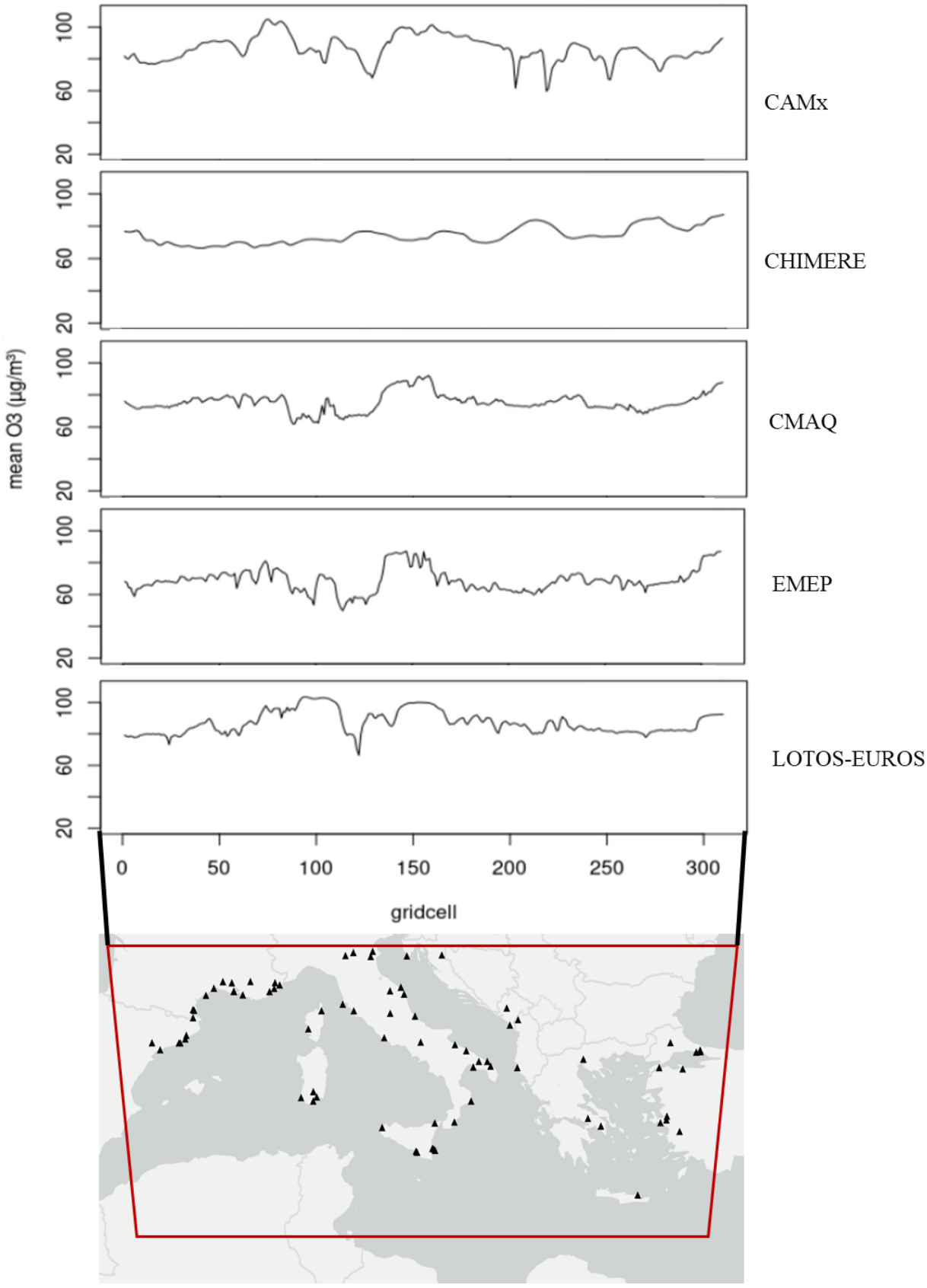

Supplements 1, S14: Boundary conditions of the northern part of the SC12 domain.

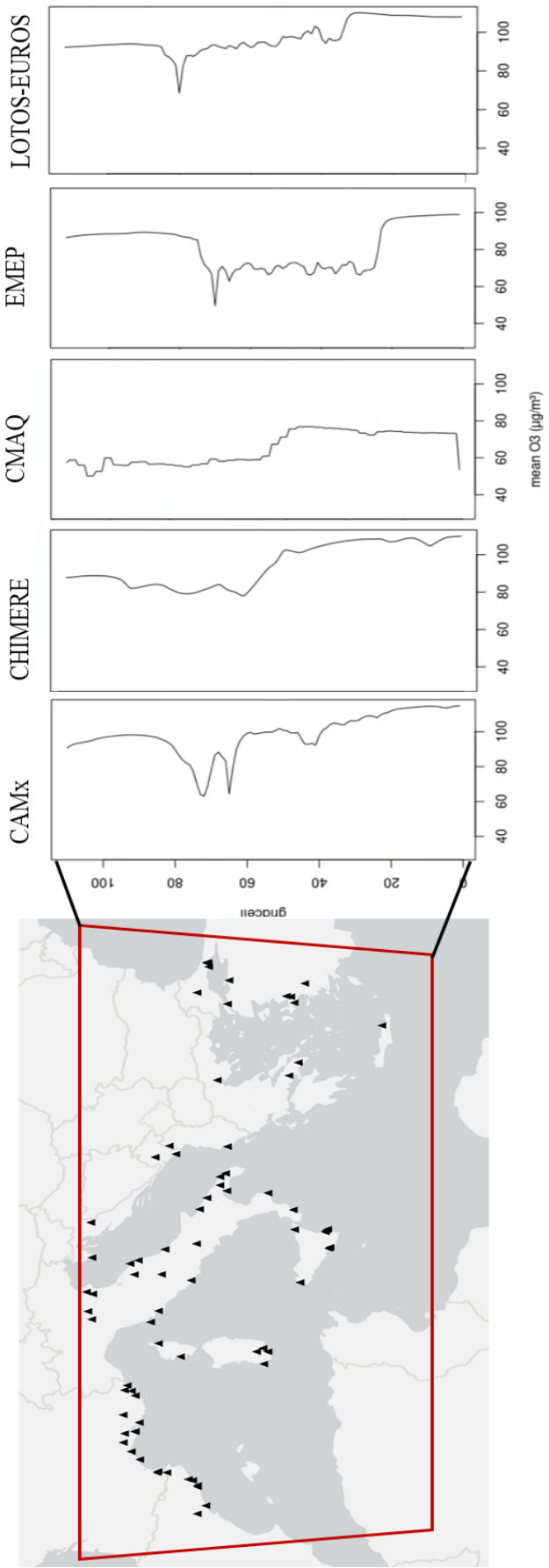

Supplements 1, S15: Boundary conditions of the eastern part of the SC12 domain.

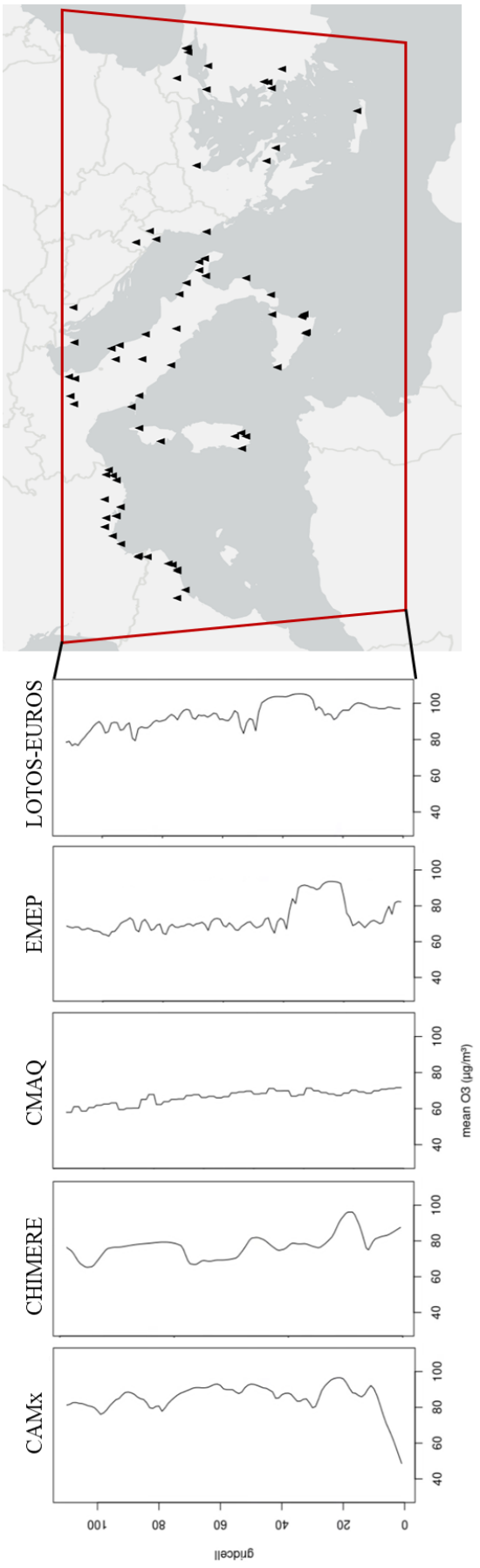

Supplements 1, S16: Boundary conditions of the eastern part of the SC12 domain.

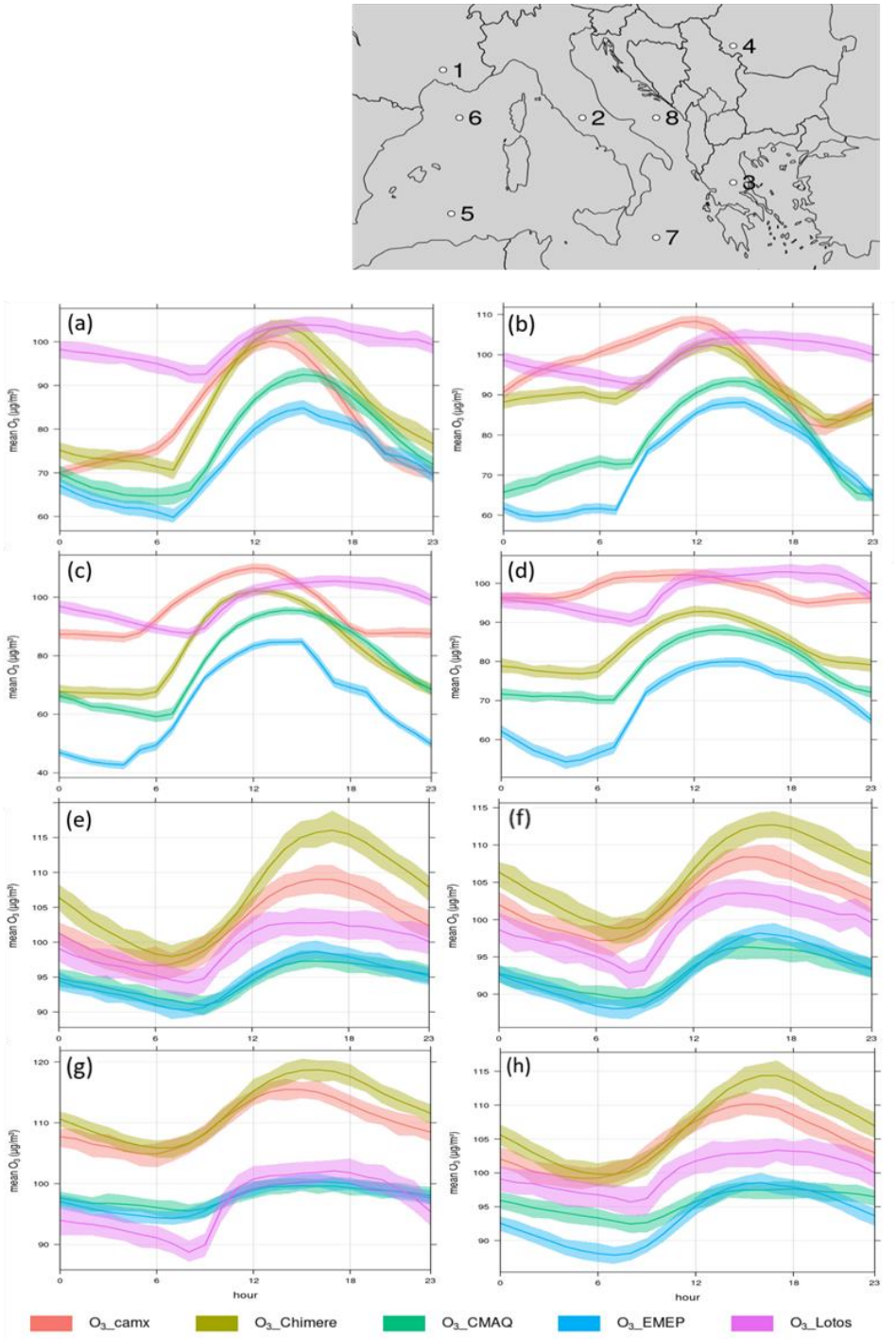

Supplements 1, S17: Diurnal cycle of O_3 in grid cells over land: (a) = Location 1, (b) = Location 2, (c) = Location 3, (d) = Location 4. Diurnal cycle of O_3 in grid cells over water: (e) = Location 5, (f) = Location 6, (g) = Location 7, (h) = Location 8. The map displays the location of the respective chosen grid cell.

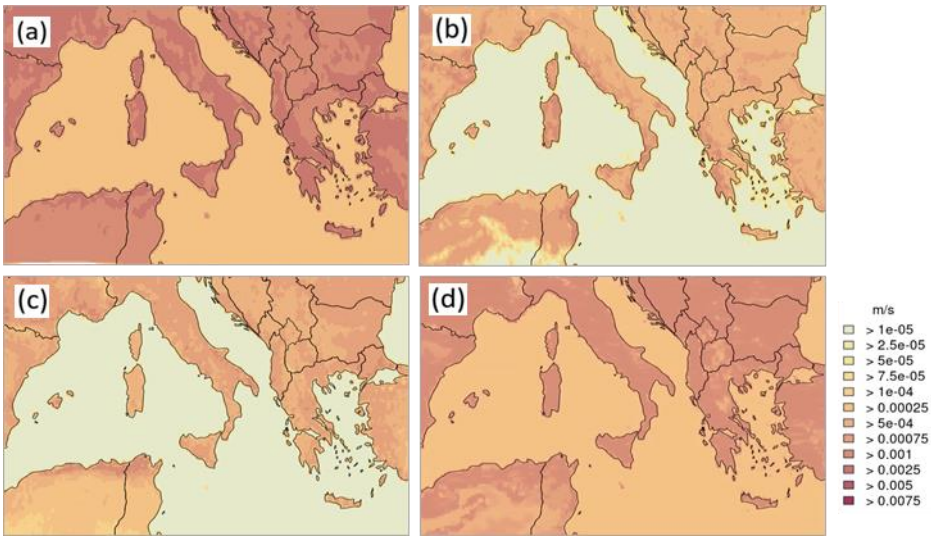

Supplements 1, S18: annual mean NO_2 deposition velocities based on hourly data. (a) = CAMx, (b) = CHIMERE, (c) = CMAQ, (d) = LOTOS-EUROS.

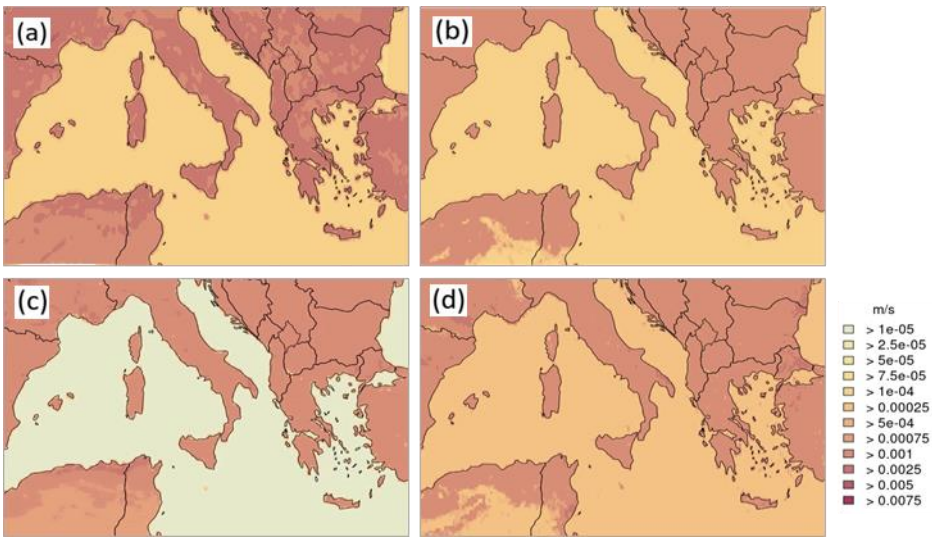

Supplements 1, S19: annual mean O_3 deposition velocities based on hourly data. (a) = CAMx, (b) = CHIMERE, (c) = CMAQ, (d) = LOTOS-EUROS.

Supplements 1, Table S20: annual total of biogenic emissions (in g).

	CAMx	CHIMERE	CMAQ	EMEP	LOTOS-EUROS
ISOP	2.08E+08	3.05E+12	2.19E+12	1.835E+12	2.3753E+12
TERP	5.67E+07	0.00E+00	1.14E+12	1.696E+12	1.2652E+12
PAR	1.10E+06		1.27E+11		
XYL	4.40E+03		0.00E+00		
OLE	1.36E+05		2.32E+11		
MEOH	1.08E+05		5.71E+11		
CH4	2.41E+04		2.39E+08		
NH3	0.00E+00		0.00E+00		
NO	3.60E+06	7.17E+10	7.25E+11	1.06E+11	2.5184E+11
ALD2	5.99E+04		8.05E+10		
ETOH	6.00E+04		7.96E+10		
FORM	2.22E+04		1.37E+10		
ALDX	2.06E+04		0.00E+00		
TOL	2.71E+03		0.00E+00		
IOLE	2.77E+04		1.78E+10		
CO	4.46E+05		3.13E+11		
ETHA	1.49E+03		3.69E+10		
ETH	9.65E+04		6.46E+10		
AACD			1.16E+10		
FACD			4.39E+10		
HCN			4.84E+09		
ISPD			1.22E+11		
N2O			0.00E+00		
SESQ			9.50E+10		
TRS			0.00E+00		
CH3BR			1.41E+08		
CH3CL			6.03E+08		
CH3I			5.40E+09		
HONO	0.00E+00				
NO2	0.00E+00				
TRP	5.66E+07				
POA	0.00E+00				
SO2	0.00E+00				
PEC	0.00E+00				
PSO4	1.34E+12				
NA	6.93E+09	2.88E+09			
PCL	9.64E+09				
ISP	2.08E+08				
CPRM (DUST)	5.33E+11	9.90E+11			
FPRM (SEASALT)	1.79E+11	9.28E+11			
DMS				1.85E+11	
APINEN	4.64E+11	4.71E+10			

BPINEN	2.06E+11	2.93E+11			
OCIMEN	1.29E+11	1.67E+11			
H2SO4		7.61E+11			
Limonene		1.43E+11			
total sum	2.07E+12	5.04E+12	5.87E+12	3.64E+12	3.89E+12

Supplements 2

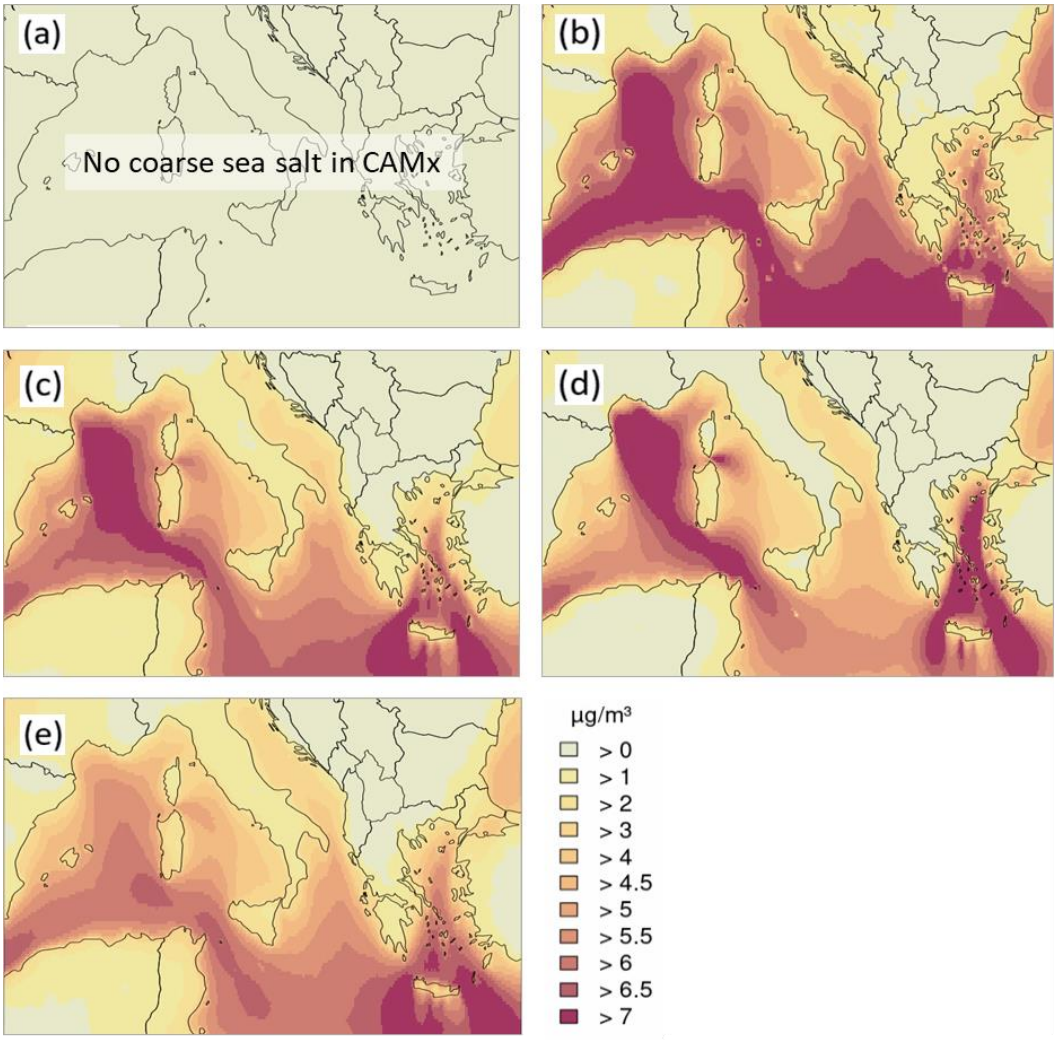

Supplements 2, S1: Annual mean sea salt (NaCl) total concentration. (a) = CAMx, (b) = CHIMERE, (c) = CMAQ, (d) = EMEP, (e) = LOTOS-EUROS.

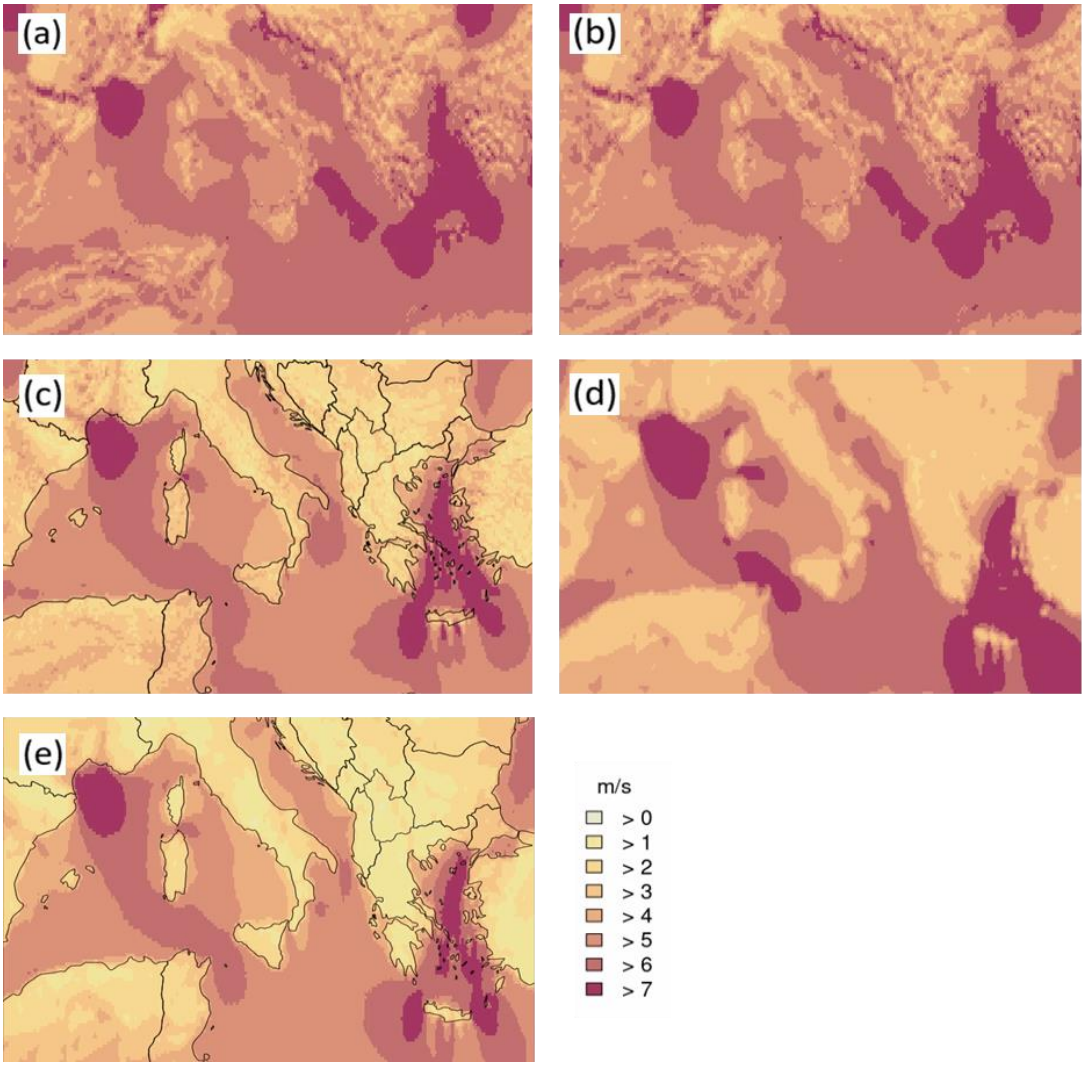

Supplements 2, S2: Annual mean wind speed (m/s). (a) = CAMx, (b) = CHIMERE, (c) = CMAQ, (d) = EMEP, (e) = LOTOS-EUROS.

Supplements 2, S3: Overview of points the wind speed and sea salt correlation was tested was compared, latitude and longitude values are in table S1. Map source: ArcGIS Pro 2.7.1 © 2020 Esri Inc.

Supplements 2, Table S1: Latitudes, longitudes, and correlation at these points based on hourly values in CMAQ, EMEP and LOTOS-EUROS and daily values in CHIMERE.

			Correlation (r) wind speed and sea salt			
ID	**latitude**	**longitude**	**CHIMERE**	**CMAQ**	**EMEP**	**LOTOS-EUROS**
1	42.778684	4.00158	0.59	0.72	0.48	0.62
2	38.663892	4.00158	0.72	0.72	0.53	0.62
3	39.549332	6.587002	0.75	0.79	0.59	0.67
4	35.720838	12.907362	0.7	0.78	0.58	0.7
5	37.014137	17.641123	0.67	0.77	0.60	0.66
6	42.832907	15.678871	0.62	0.75	0.55	0.64
7	36.179274	25.391863	0.34	0.71	0.48	0.57
8	39.267262	25.102001	0.31	0.78	0.60	0.71

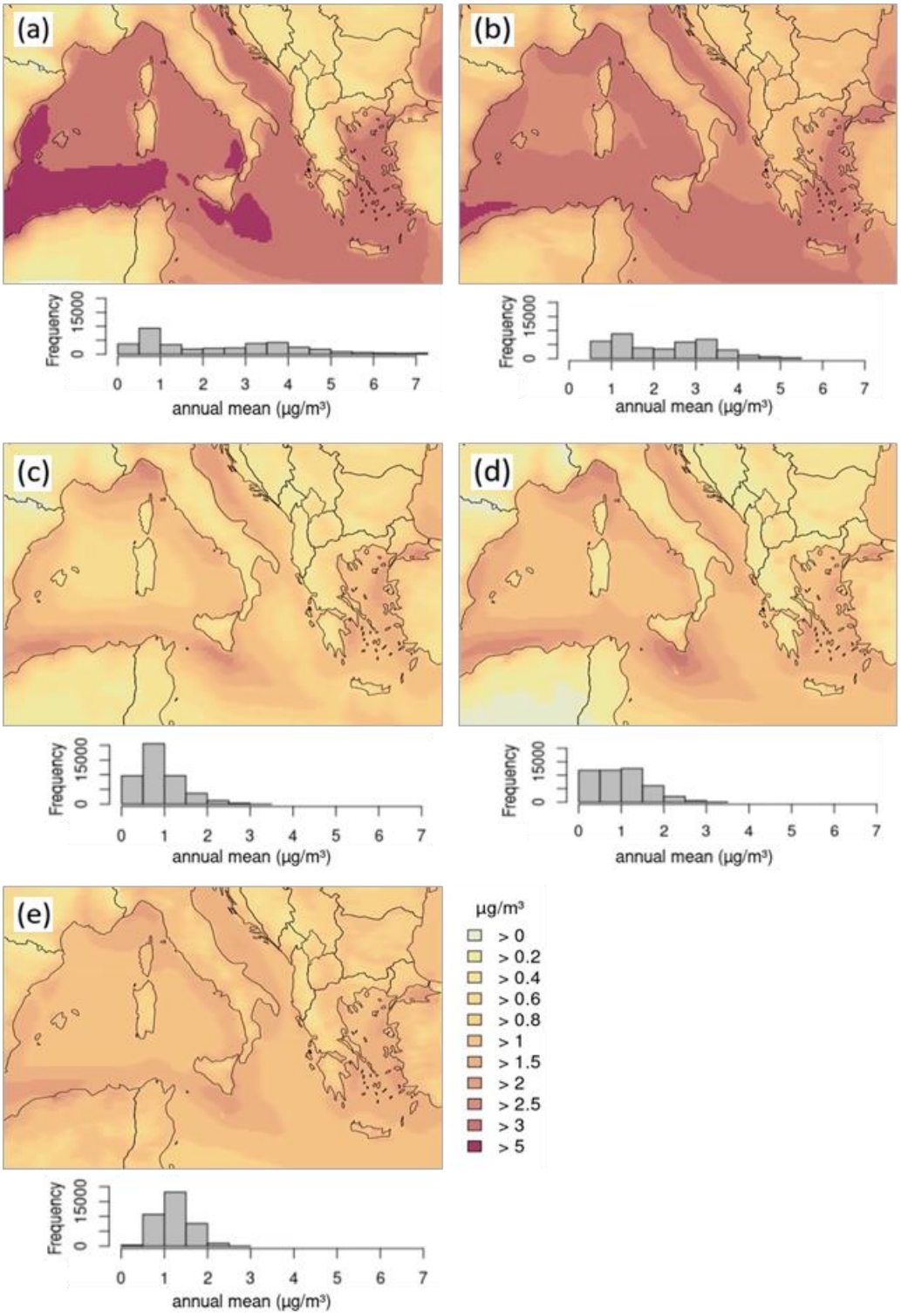

Supplements 2, S4: Annual mean HNO_3 total concentration. (a) = CAMx, (b) = CHIMERE, (c) = CMAQ, (d) = EMEP, (e) = LOTOS-EUROS. Below the domain figure is the respective frequency distribution displayed for the annual mean HNO_3 concentration, referred to the whole model domain.

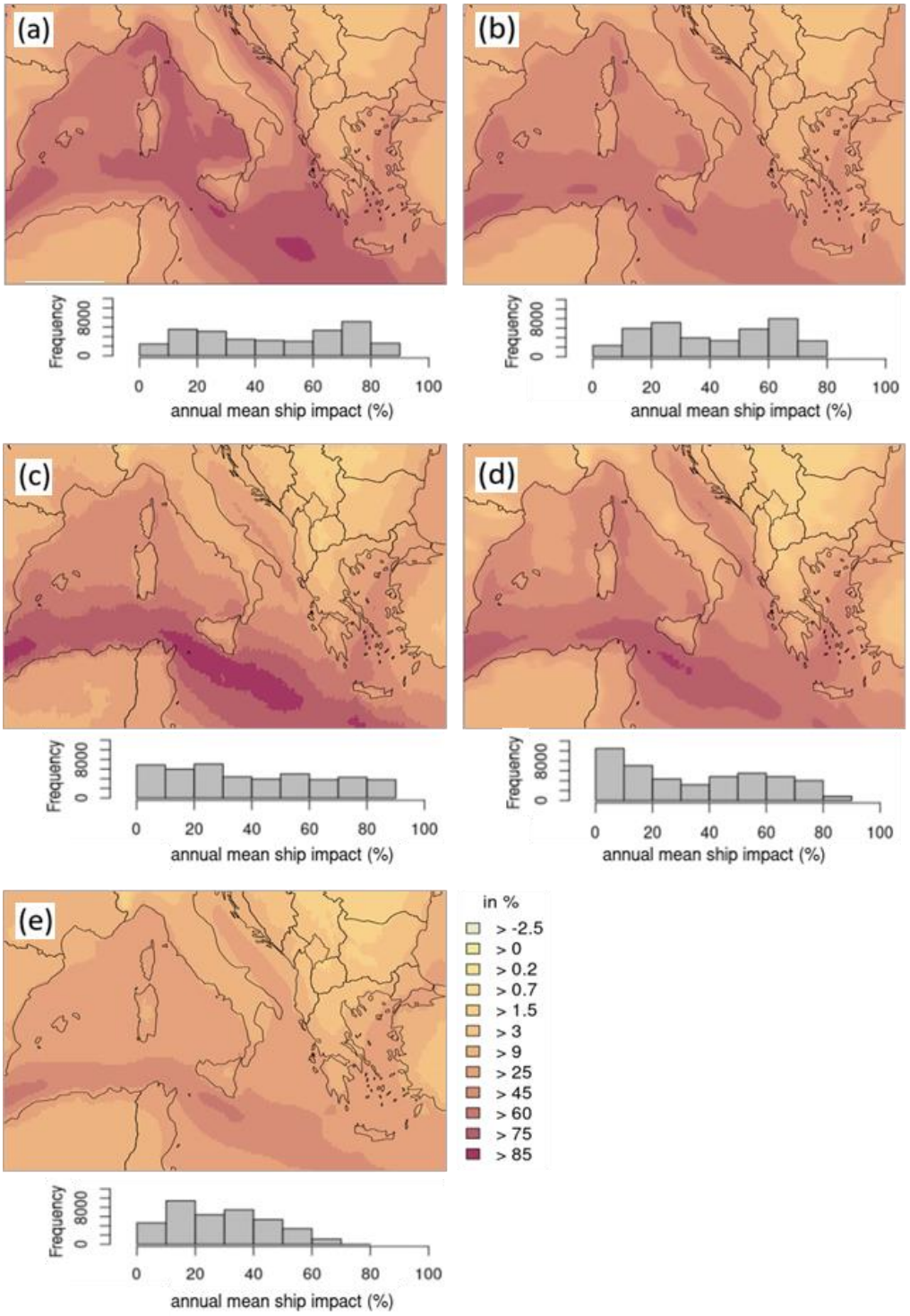

Supplements 2, S5: Annual mean HNO_3 relative potential ship impact. (a) = CAMx, (b) = CHIMERE, (c) = CMAQ, (d) = EMEP, (e) = LOTOS-EUROS. Below the domain figure is the respective frequency distribution displayed for the annual mean HNO_3 potential ship impact, referred to the whole model domain.

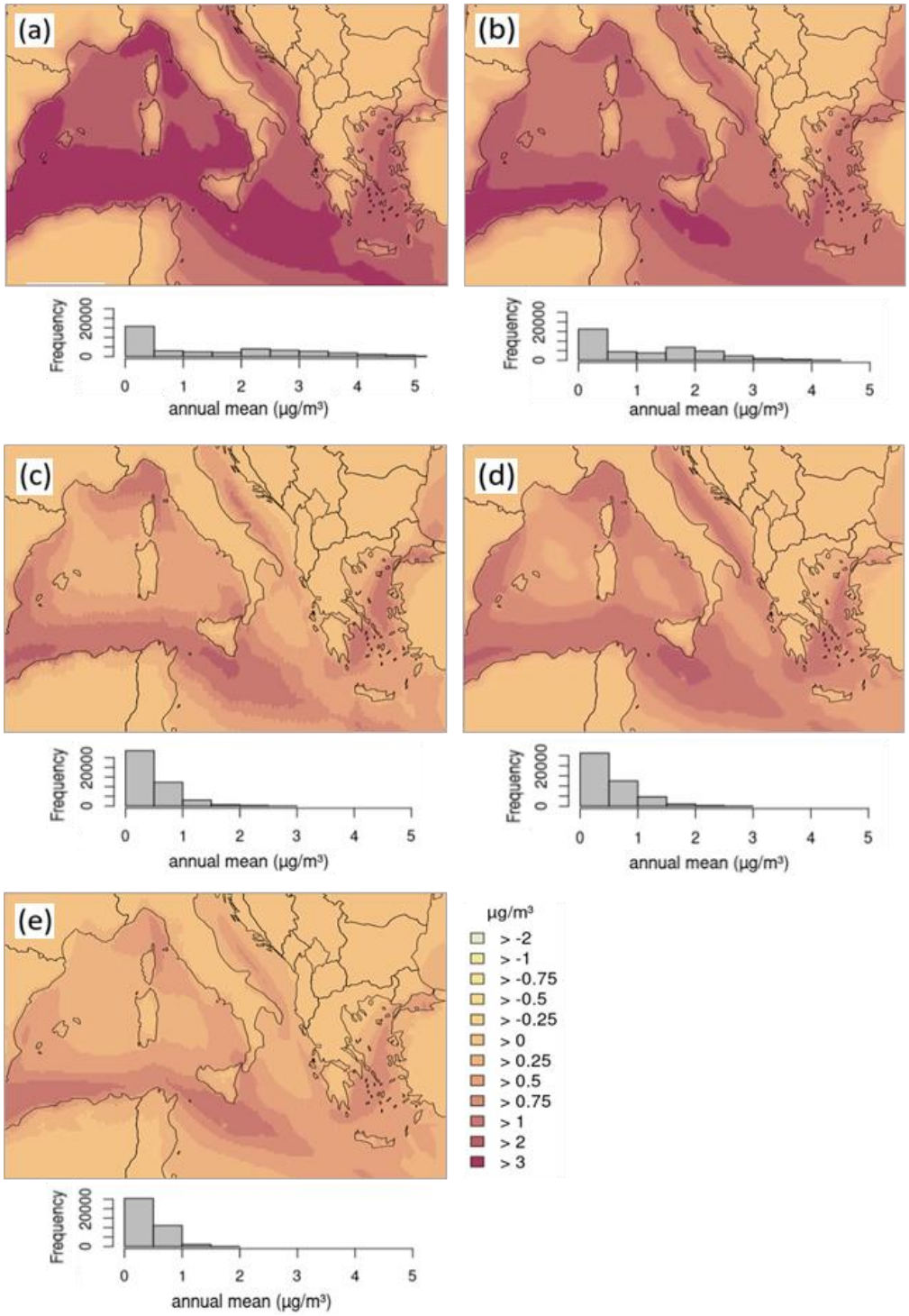

Supplements 2, S6: Annual mean HNO_3 absolute potential ship impact. (a) = CAMx, (b) = CHIMERE, (c) = CMAQ, (d) = EMEP, (e) = LOTOS-EUROS. Below the domain figure is the respective frequency distribution displayed for the annual mean HNO_3 potential ship impact, referred to the whole model domain.

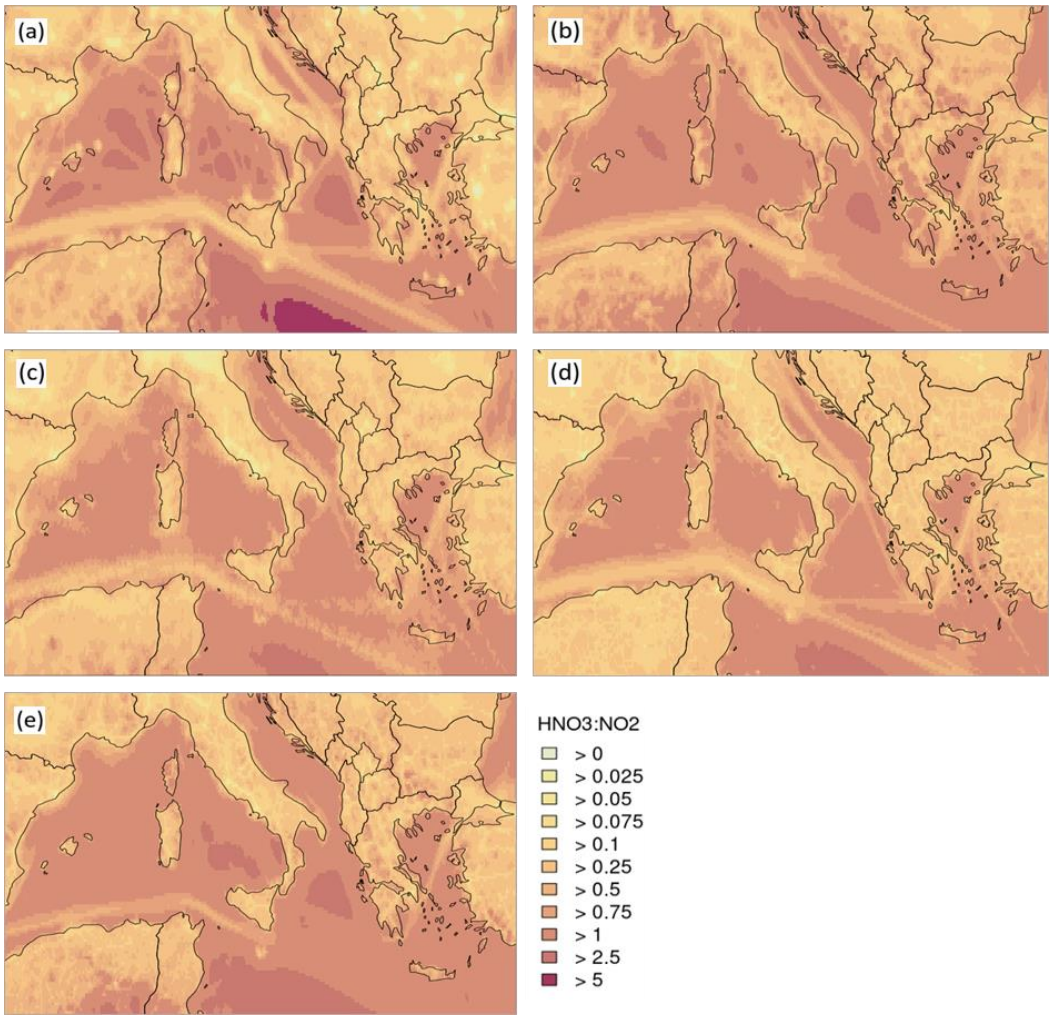

Supplements 2, S7: Annual mean ratio of HNO_3:NO_2 for emisbase run with all emission sources, based on averaged daily values. (a) = CAMx, (b) = CHIMERE, (c) = CMAQ, (d) = EMEP, (e) = LOTOS-EUROS.

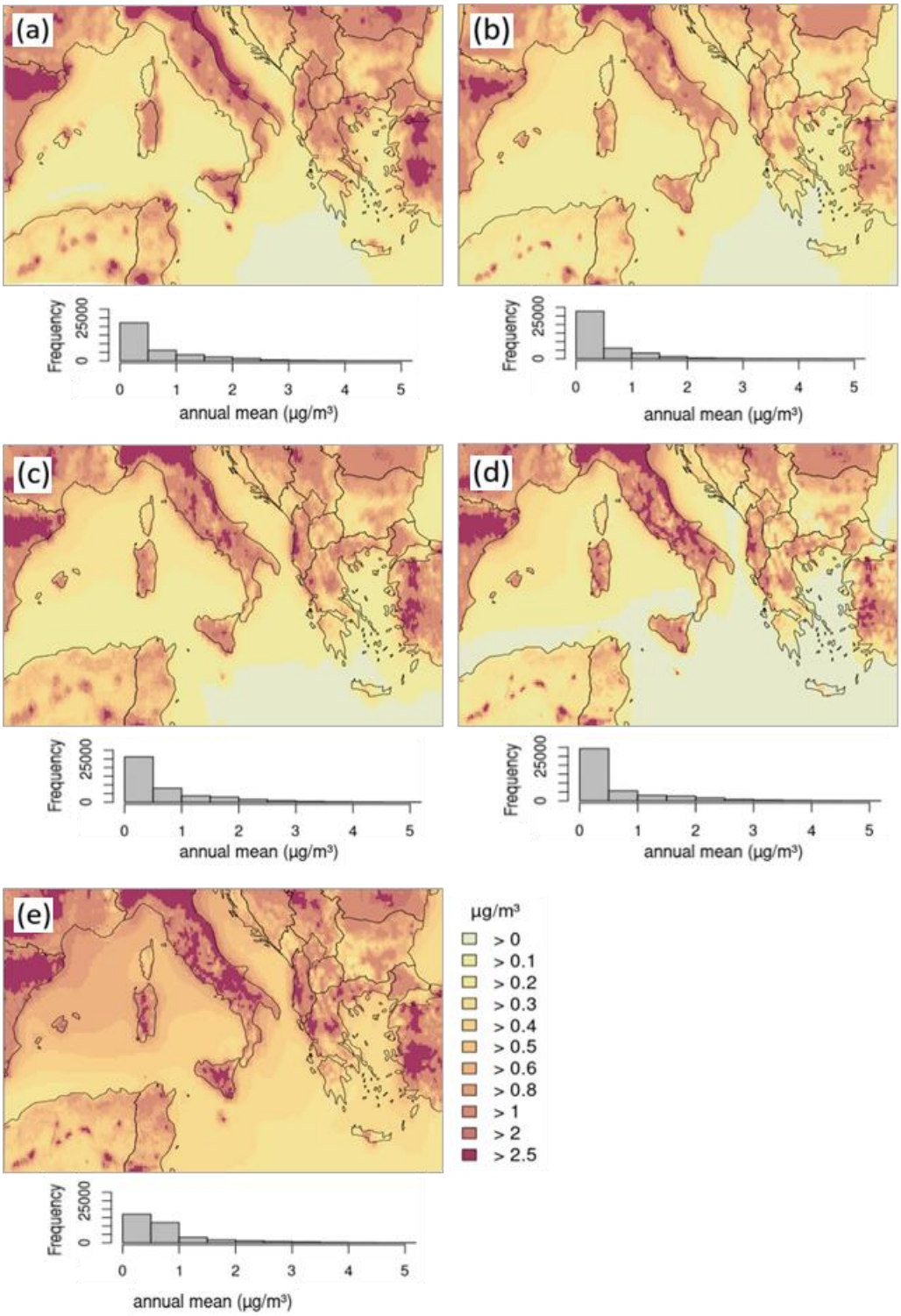

Supplements 2, S8: Annual mean NH_3 total concentration. (a) = CAMx, (b) = CHIMERE, (c) = CMAQ, (d) = EMEP, (e) = LOTOS-EUROS. Below the domain figure is the respective frequency distribution displayed for the annual mean NH_3 concentration, referred to the whole model domain.

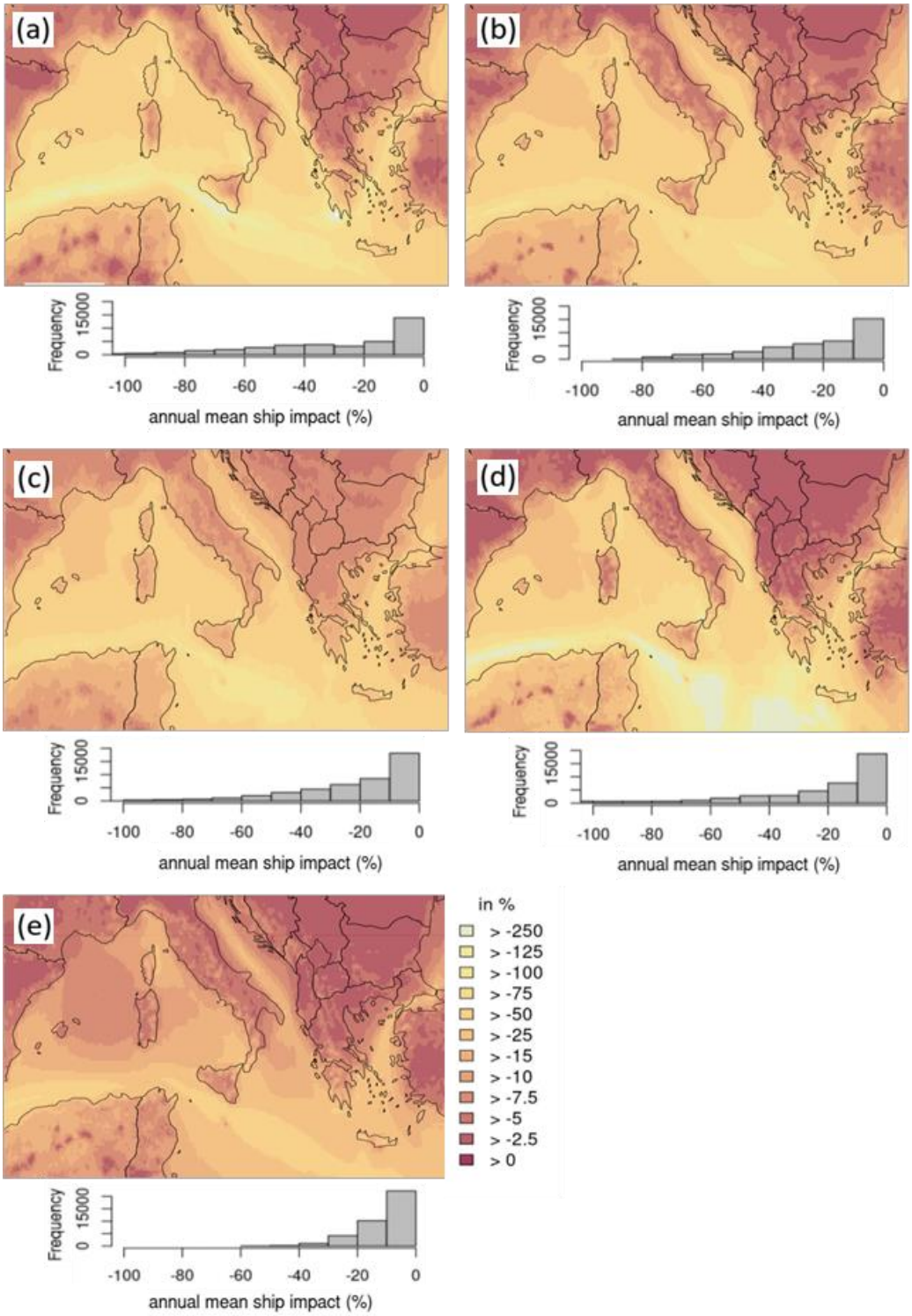

Supplements 2, S9: Annual mean NH_3 relative potential ship impact. (a) = CAMx, (b) = CHIMERE, (c) = CMAQ, (d) = EMEP, (e) = LOTOS-EUROS. Below the domain figure is the respective frequency distribution displayed for the annual mean NH_3 potential ship impact, referred to the whole model domain.

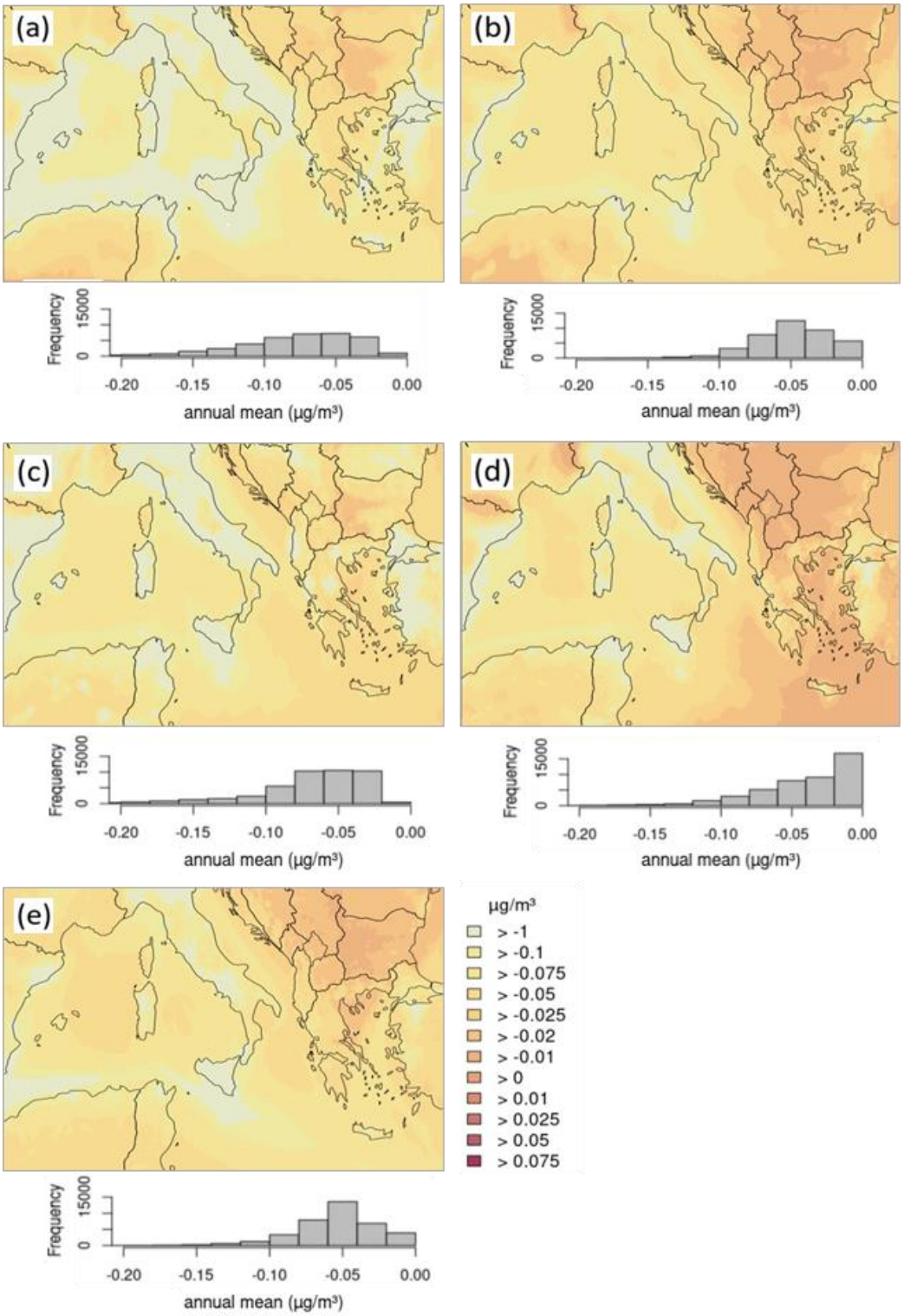

Supplements 2, S10: Annual mean NH_3 absolute potential ship impact. (a) = CAMx, (b) = CHIMERE, (c) = CMAQ, (d) = EMEP, (e) = LOTOS-EUROS. Below the domain figure is the respective frequency distribution displayed for the annual mean NH_3 potential ship impact, referred to the whole model domain.

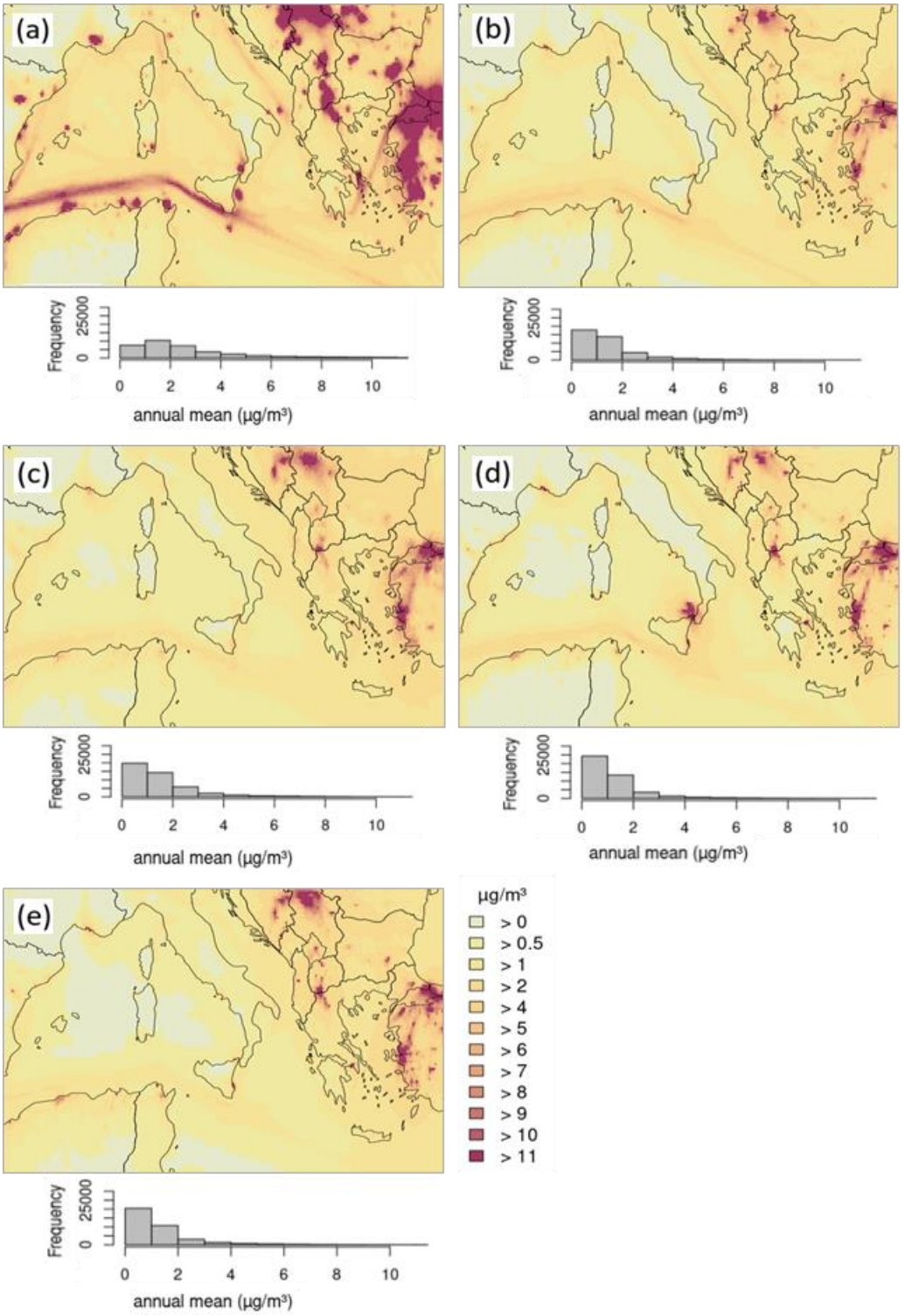

Supplements 2, S11: Annual mean SO_2 total concentration. (a) = CAMx, (b) = CHIMERE, (c) = CMAQ, (d) = EMEP, (e) = LOTOS-EUROS. Below the domain figure is the respective frequency distribution displayed for the annual mean SO_2 concentration, referred to the whole model domain.

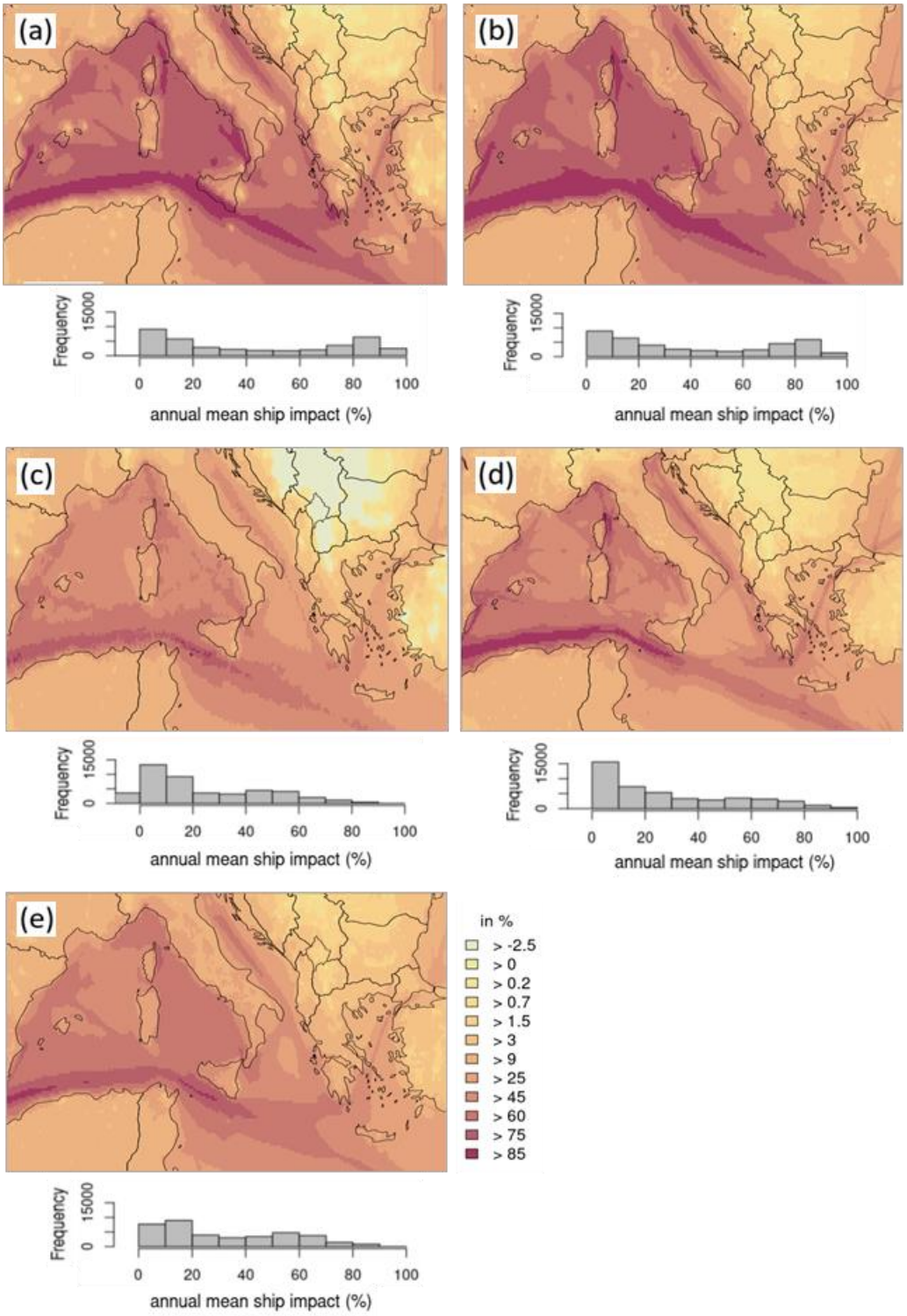

Supplements 2, S12: Annual mean SO_2 relative potential ship impact. (a) = CAMx, (b) = CHIMERE, (c) = CMAQ, (d) = EMEP, (e) = LOTOS-EUROS. Below the domain figure is the respective frequency distribution displayed for the annual mean SO_2 potential ship impact, referred to the whole model domain.

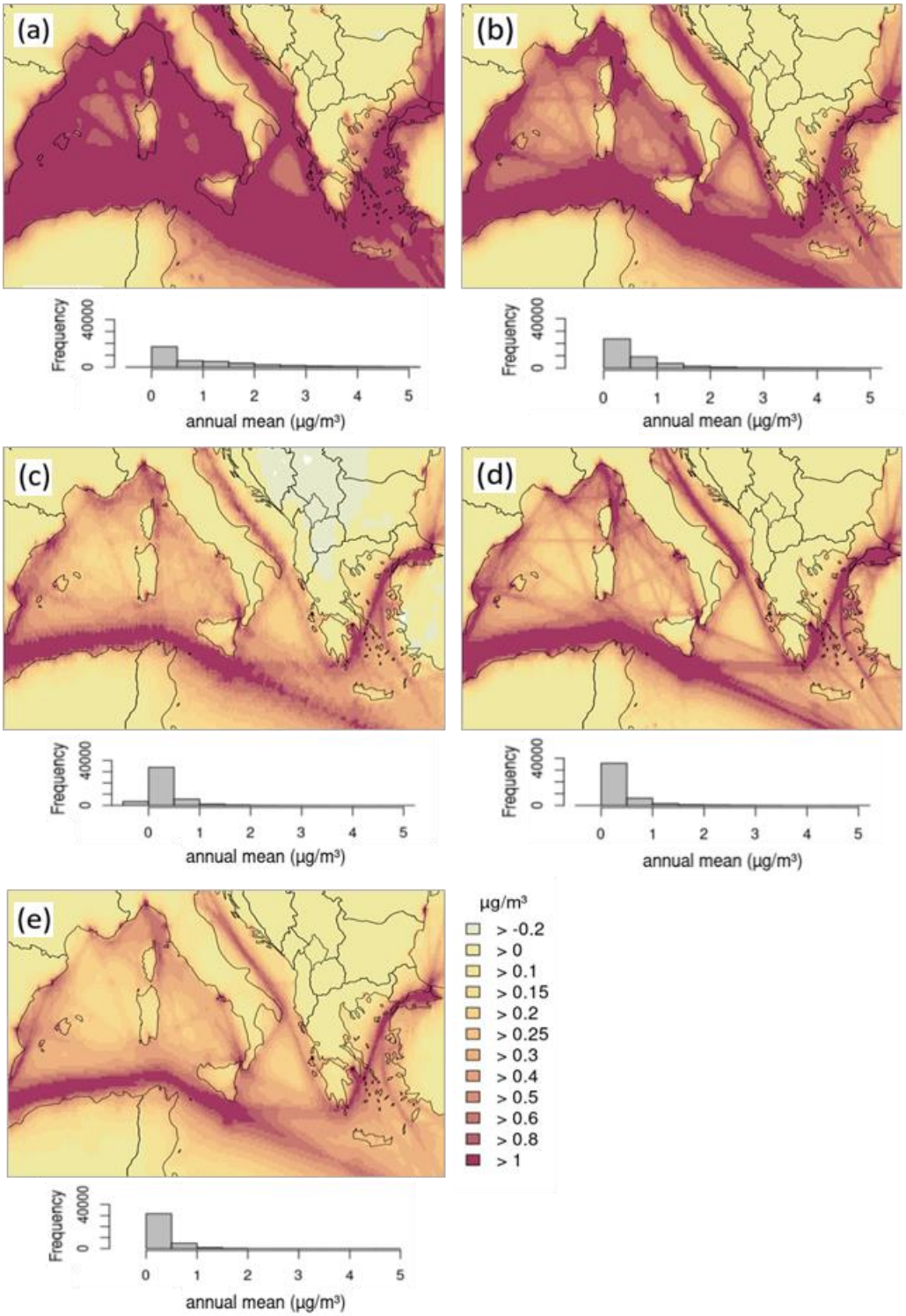

Supplements 2, S13: Annual mean SO_2 absolute potential ship impact. (a) = CAMx, (b) = CHIMERE, (c) = CMAQ, (d) = EMEP, (e) = LOTOS-EUROS. Below the domain figure is the respective frequency distribution displayed for the annual mean SO_2 potential ship impact, referred to the whole model domain.

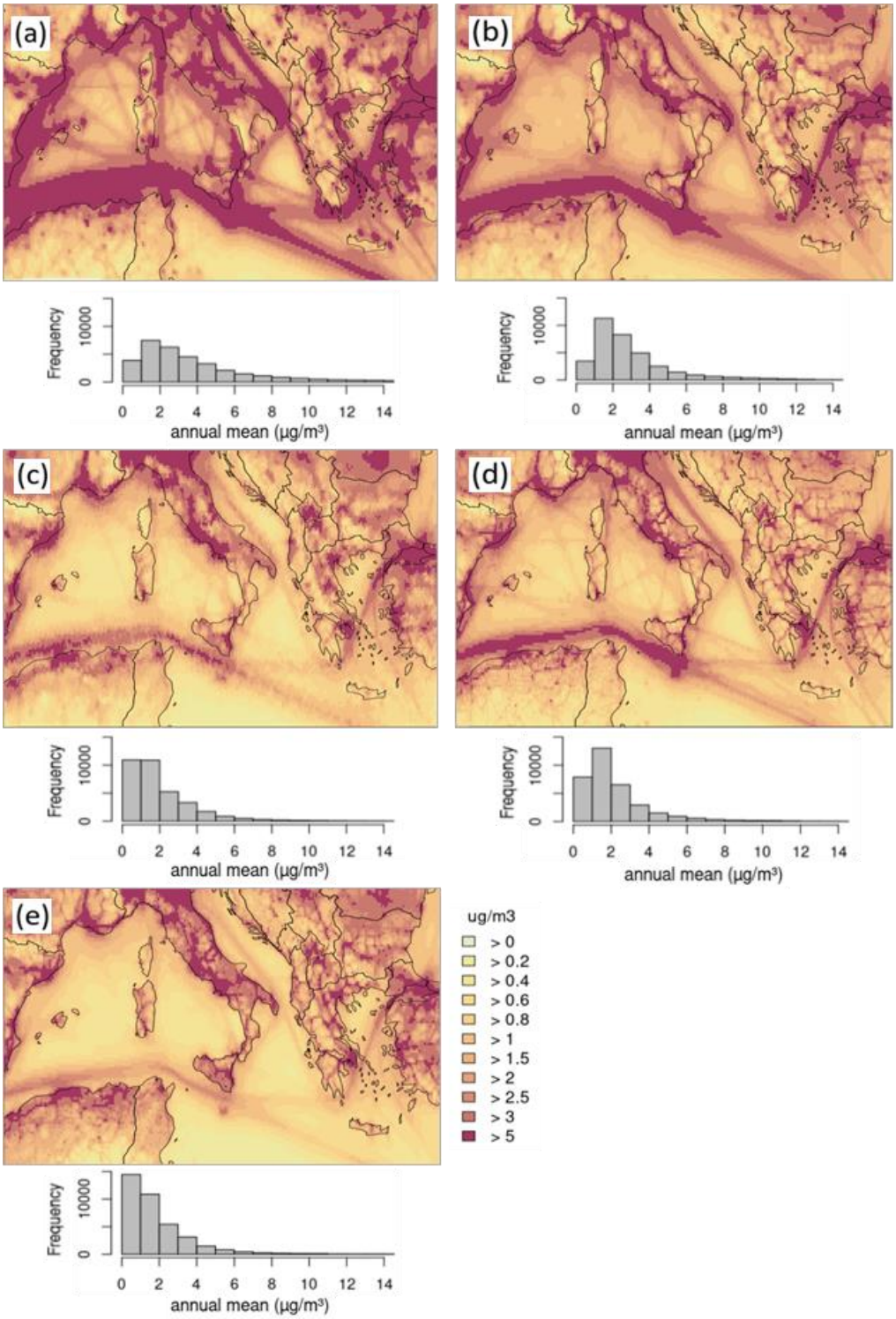

Supplements 2, S14: Annual mean NO_2 total concentration. (a) = CAMx, (b) = CHIMERE, (c) = CMAQ, (d) = EMEP, (e) = LOTOS-EUROS. Below the domain figure is the respective frequency distribution displayed for the annual mean NO_2 concentration, referred to the whole model domain.

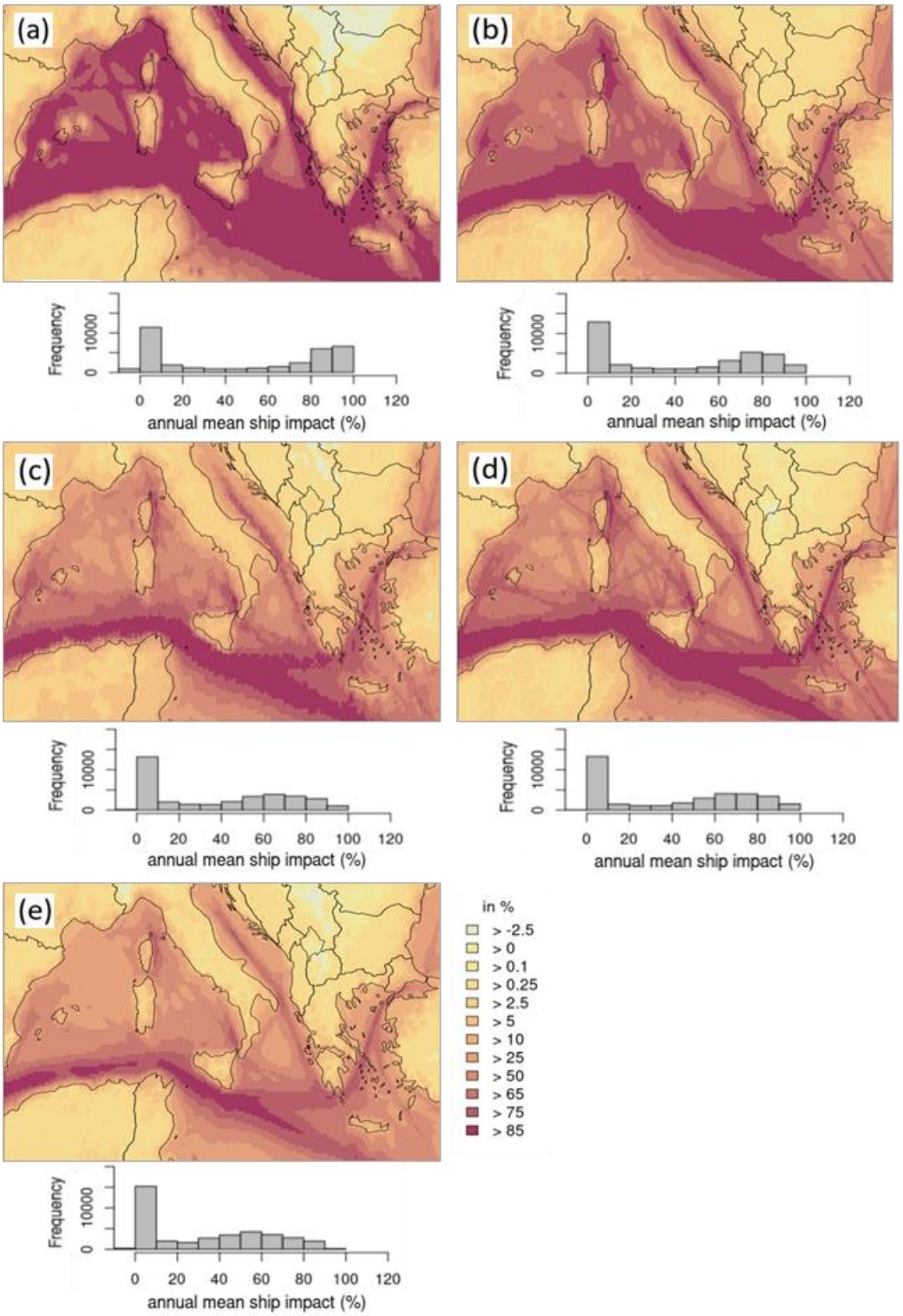

Supplements 2, S15: **Annual mean NO_2 relative potential ship impact. (a) = CAMx, (b) = CHIMERE, (c) = CMAQ, (d) = EMEP, (e) = LOTOS-EUROS. Below the domain figure is the respective frequency distribution displayed for the annual mean NO_2 potential ship impact, referred to the whole model domain.**

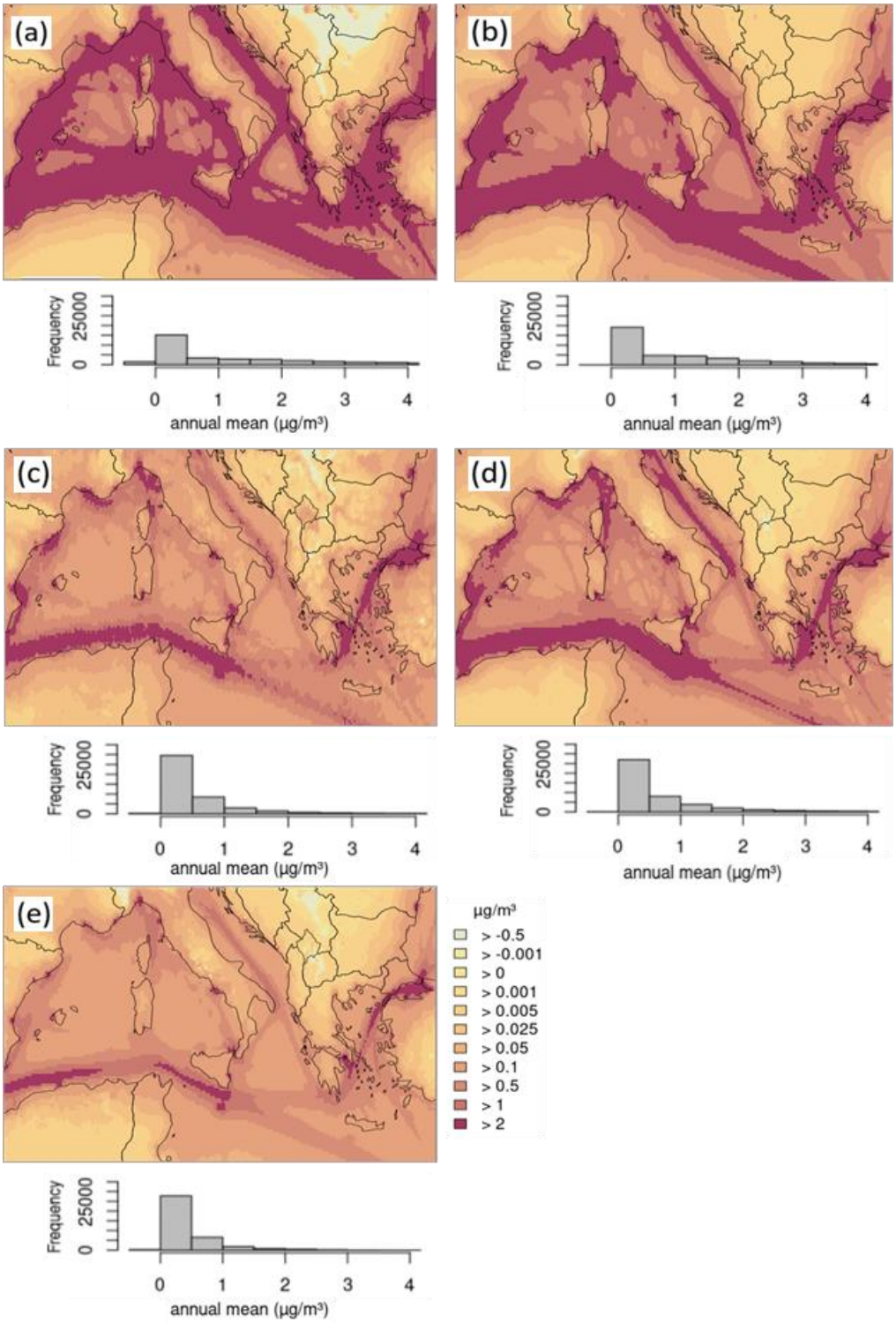

Supplements 2, S16: Annual mean NO_2 absolute potential ship impact. (a) = CAMx, (b) = CHIMERE, (c) = CMAQ, (d) = EMEP, (e) = LOTOS-EUROS. Below the domain figure is the respective frequency distribution displayed for the annual mean NO_2 potential ship impact, referred to the whole model domain.

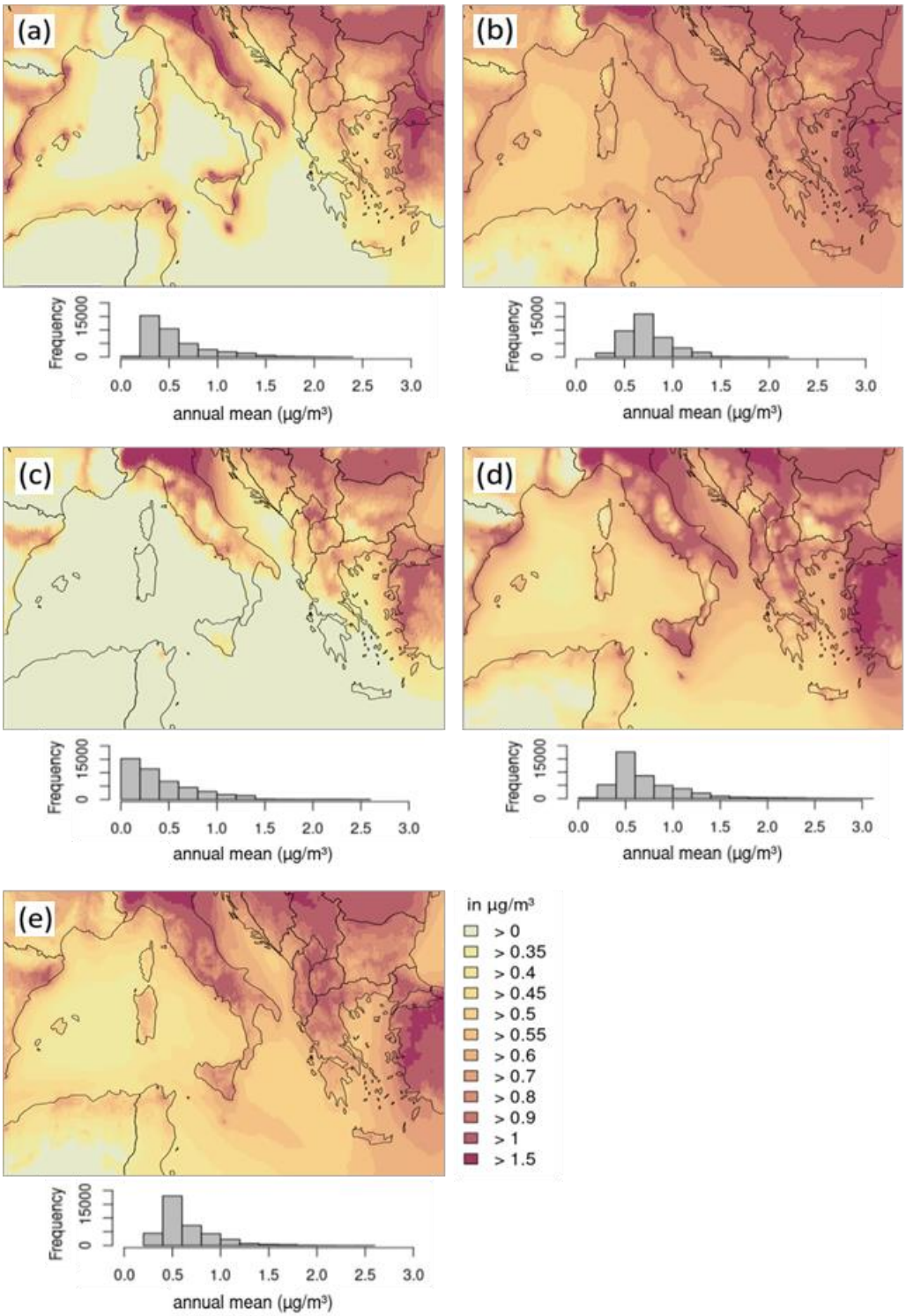

Supplements 2, S17: Annual mean NH_4^+ total concentration. (a) = CAMx, (b) = CHIMERE, (c) = CMAQ, (d) = EMEP, (e) = LOTOS-EUROS. Below the domain figure is the respective frequency distribution displayed for the annual mean NH_4^+ concentration, referred to the whole model domain.

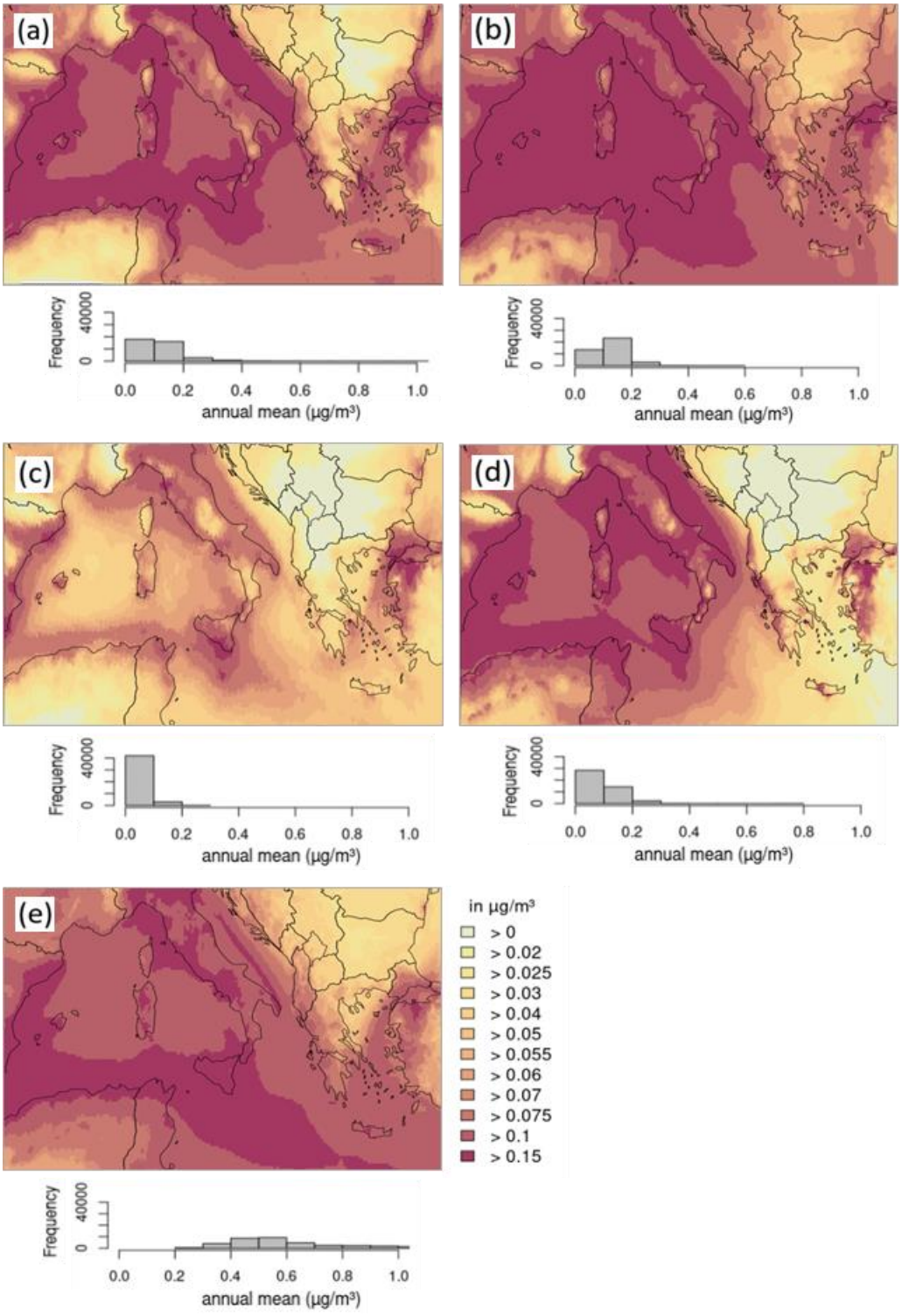

Supplements 2, S18: Annual mean NH_4^+ absolute potential ship impact. (a) = CAMx, (b) = CHIMERE, (c) = CMAQ, (d) = EMEP, (e) = LOTOS-EUROS. Below the domain figure is the respective frequency distribution displayed for the annual mean NH_4^+ potential ship impact, referred to the whole model domain.

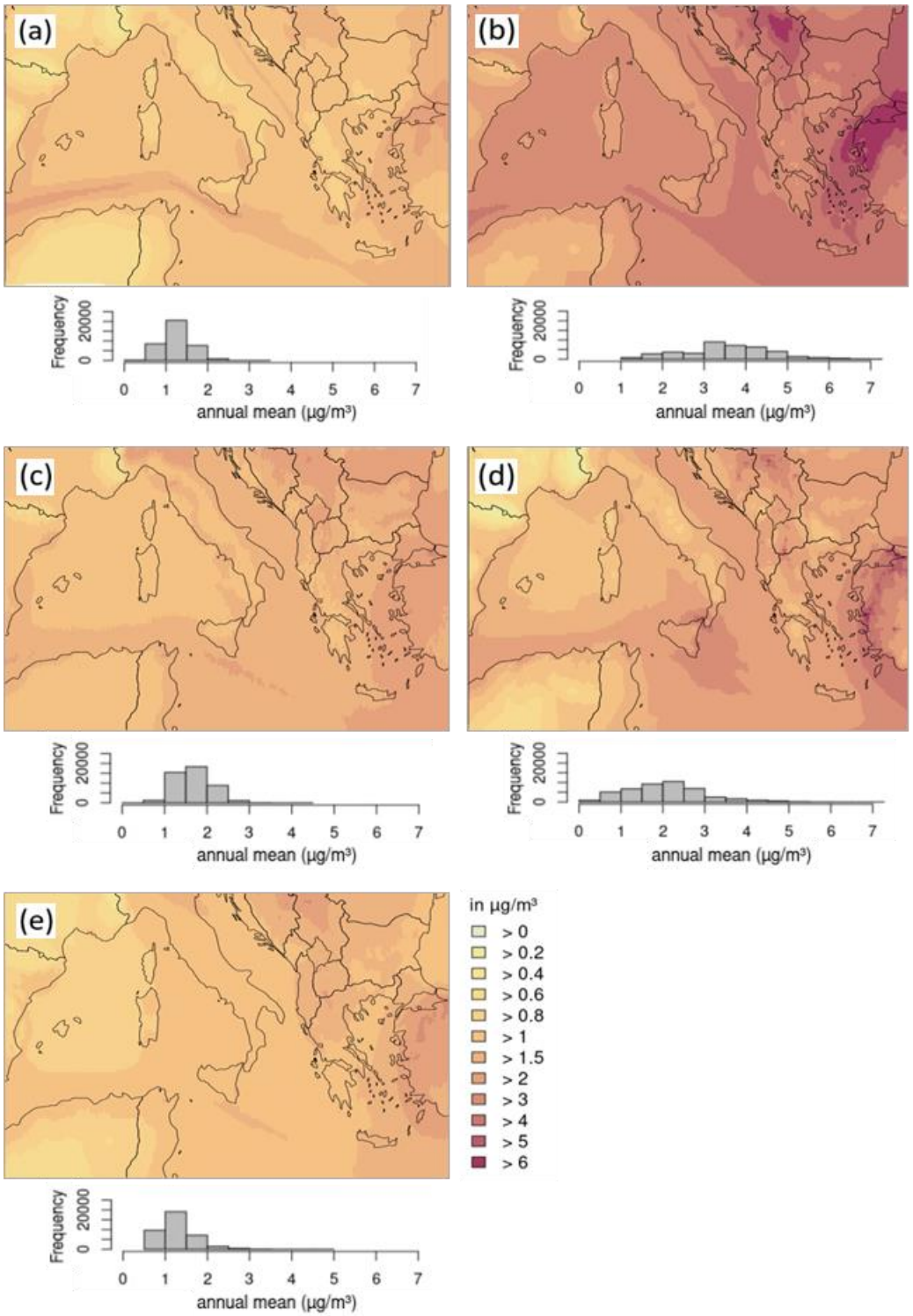

Supplements 2, S19: Annual mean SO_4^{2-} total concentration. (a) = CAMx, (b) = CHIMERE, (c) = CMAQ, (d) = EMEP, (e) = LOTOS-EUROS. Below the domain figure is the respective frequency distribution displayed for the annual mean SO_4^{2-} concentration, referred to the whole model domain.

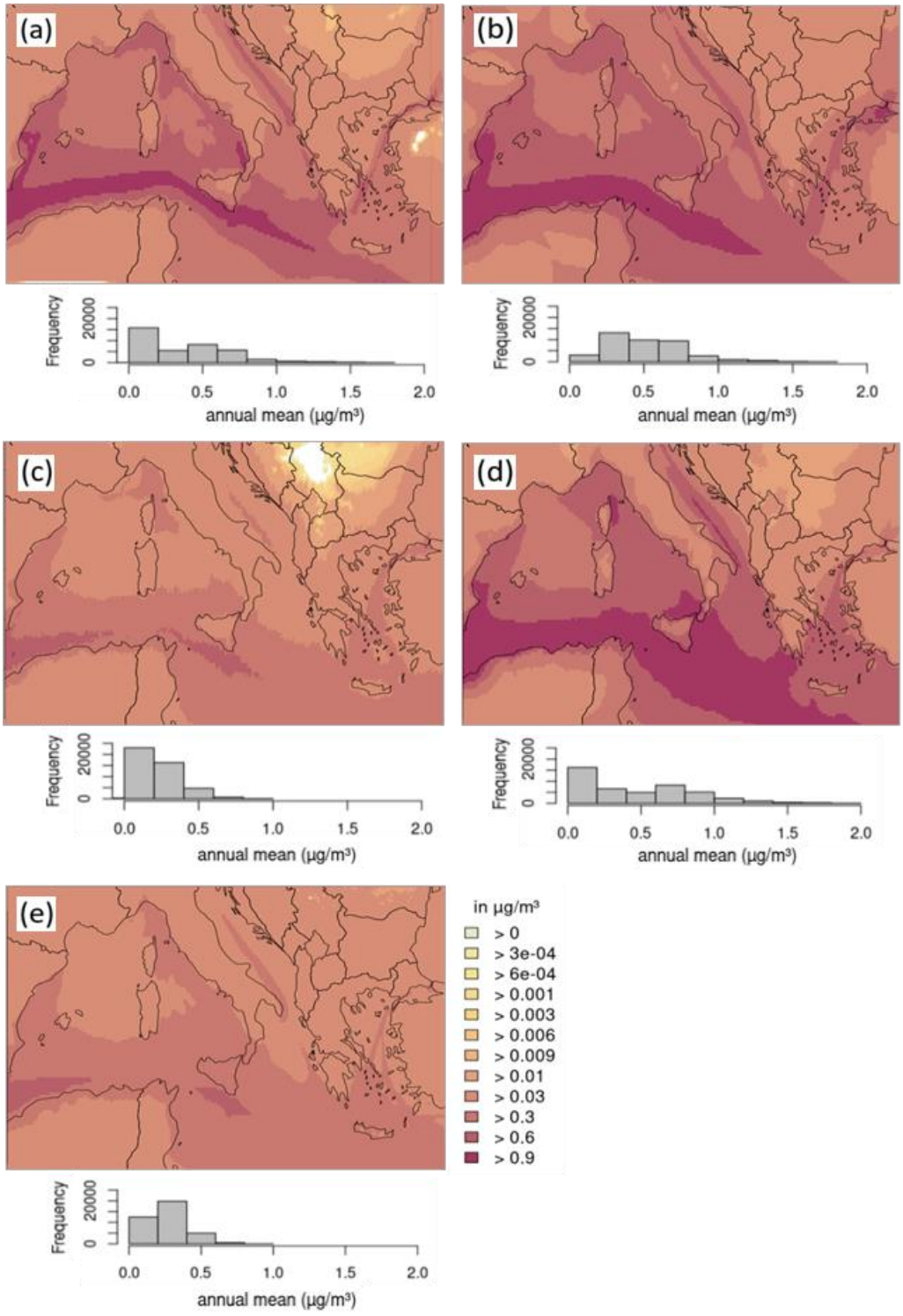

Supplements 2, S20: Annual mean SO_4^{2-} absolute potential ship impact. (a) = CAMx, (b) = CHIMERE, (c) = CMAQ, (d) = EMEP, (e) = LOTOS-EUROS. Below the domain figure is the respective frequency distribution displayed for the annual mean SO_4^{2-} potential ship impact, referred to the whole model domain.

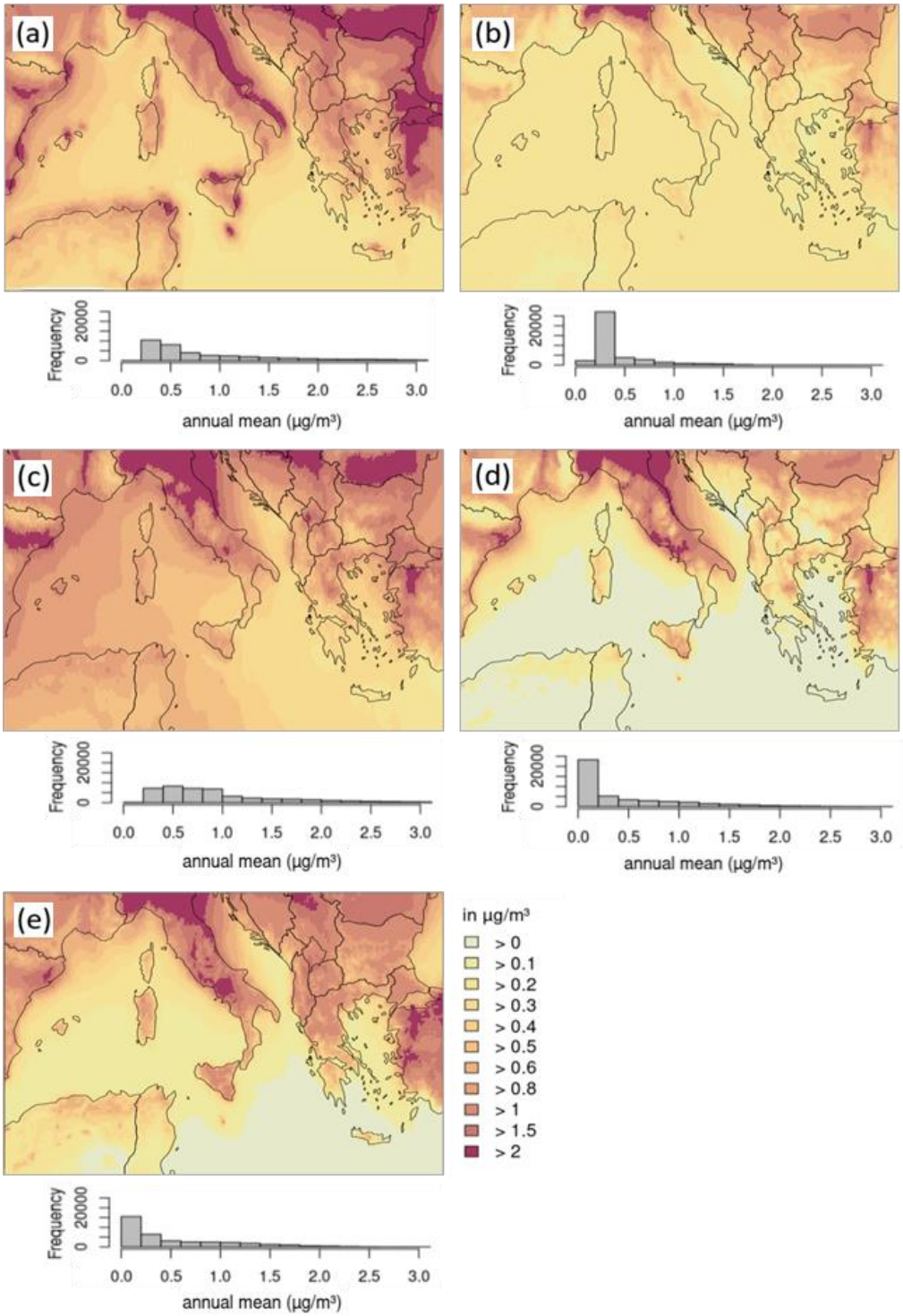

Supplements 2, S21: Annual mean NO_3^- total concentration. (a) = CAMx, (b) = CHIMERE, (c) = CMAQ, (d) = EMEP, (e) = LOTOS-EUROS. Below the domain figure is the respective frequency distribution displayed for the annual mean NO_3^- concentration, referred to the whole model domain.

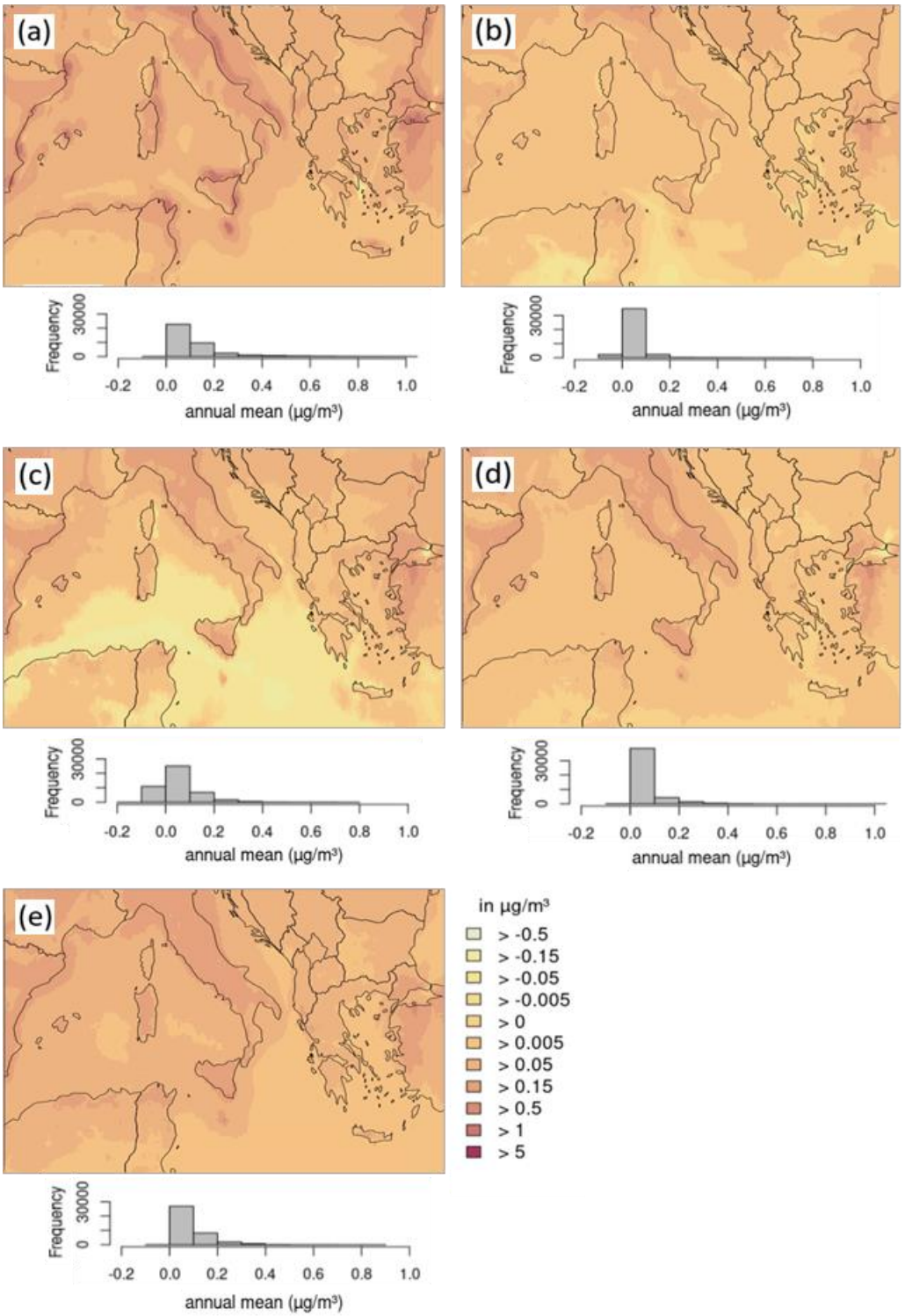

Supplements 2, S22: Annual mean NO_3^- absolute potential ship impact. (a) = CAMx, (b) = CHIMERE, (c) = CMAQ, (d) = EMEP, (e) = LOTOS-EUROS. Below the domain figure is the respective frequency distribution displayed for the annual mean NO_3^- potential ship impact, referred to the whole model domain.

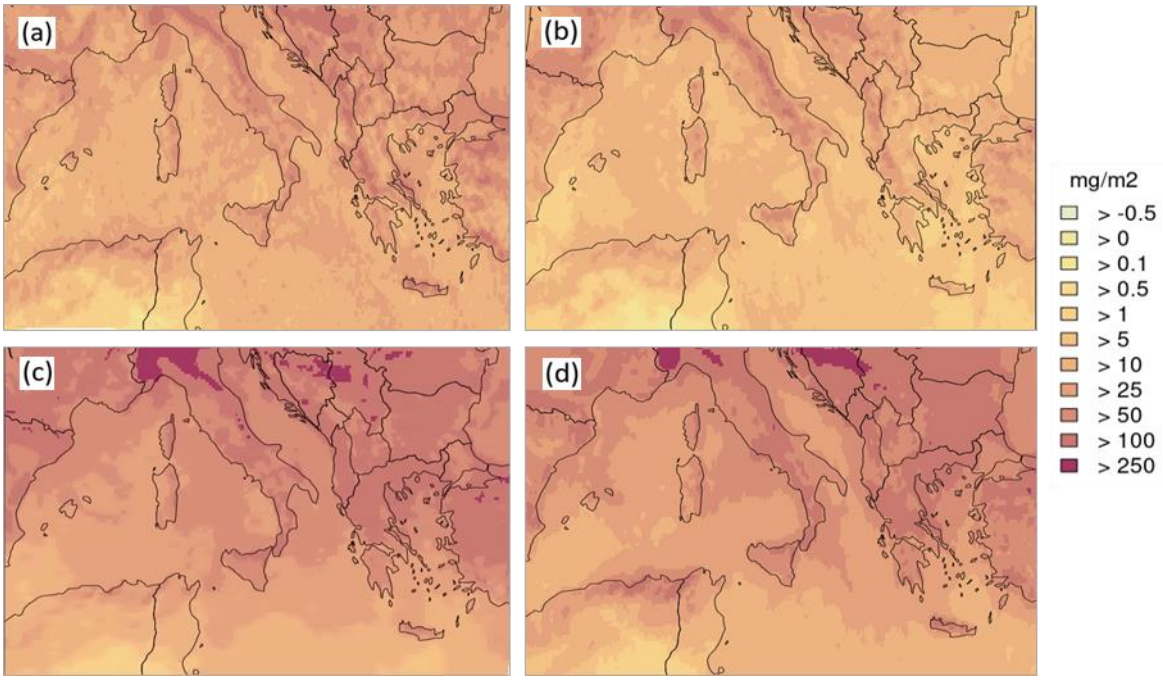

Supplements 2, S23: NH_4^+ wet deposition annual sum. (a) = CAMx, (b) = CHIMERE, (c) = CMAQ, (d) = LOTOS-EUROS.

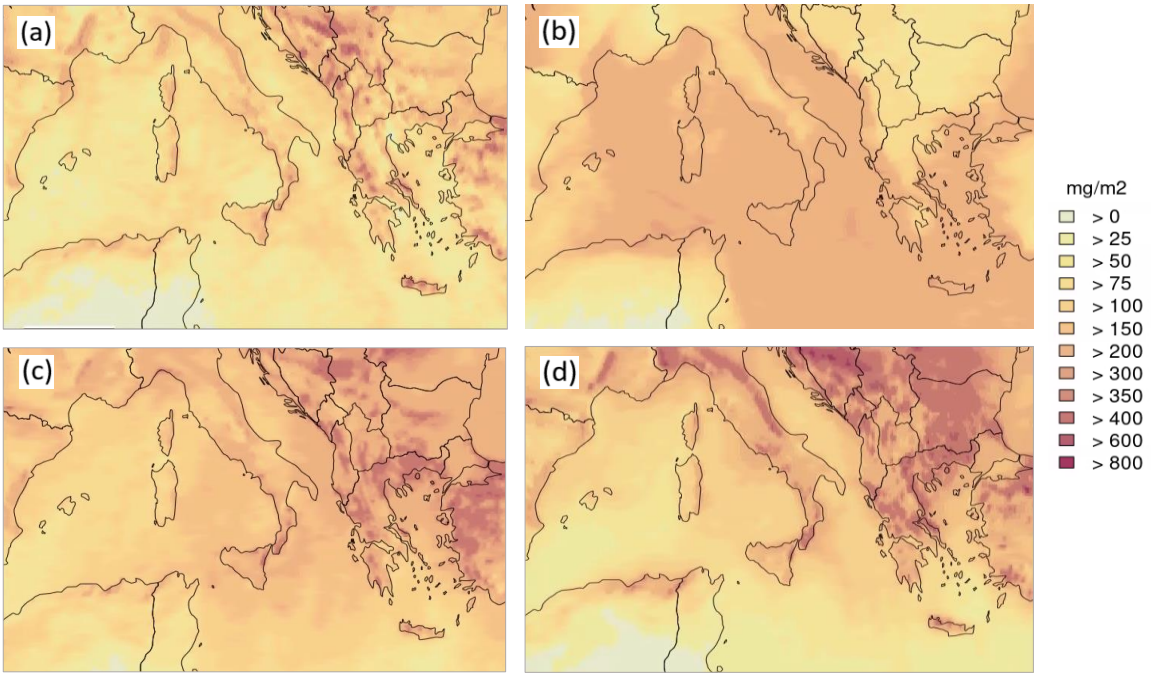

Supplements 2, S24: SO_4^{2-} wet deposition annual sum. (a) = CAMx, (b) = CHIMERE, (c) = CMAQ, (d) = LOTOS-EUROS.

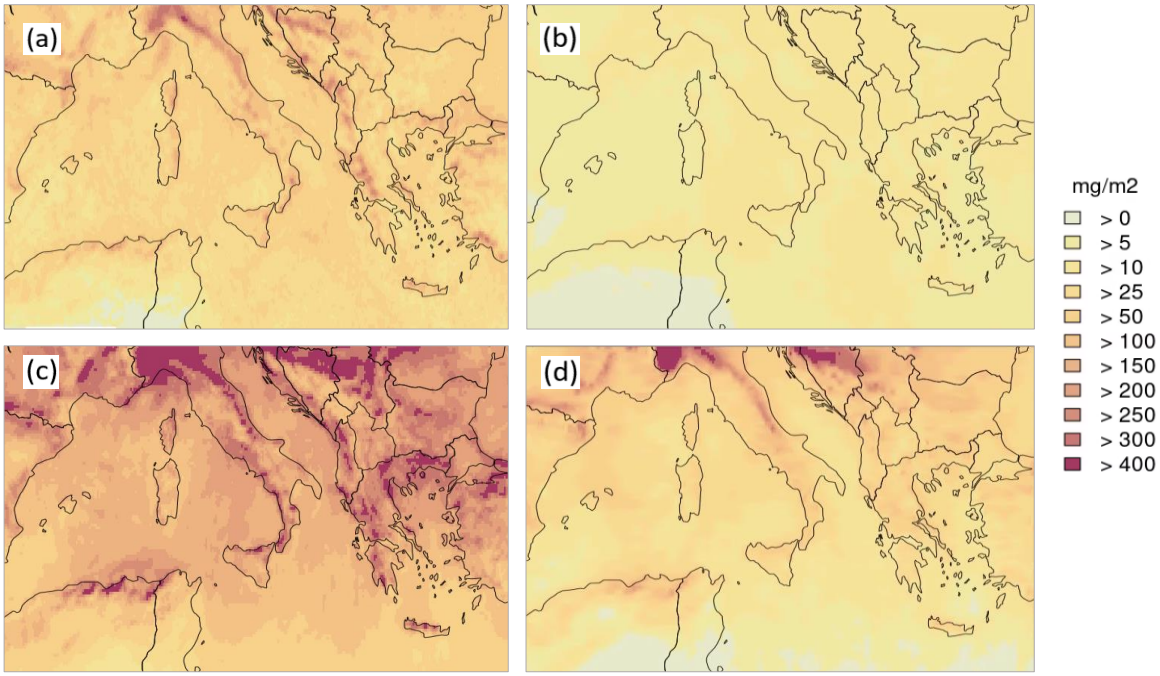

Supplements 2, S25: NO_3^- wet deposition annual sum. (a) = CAMx, (b) = CHIMERE, (c) = CMAQ, (d) = LOTOS-EUROS.

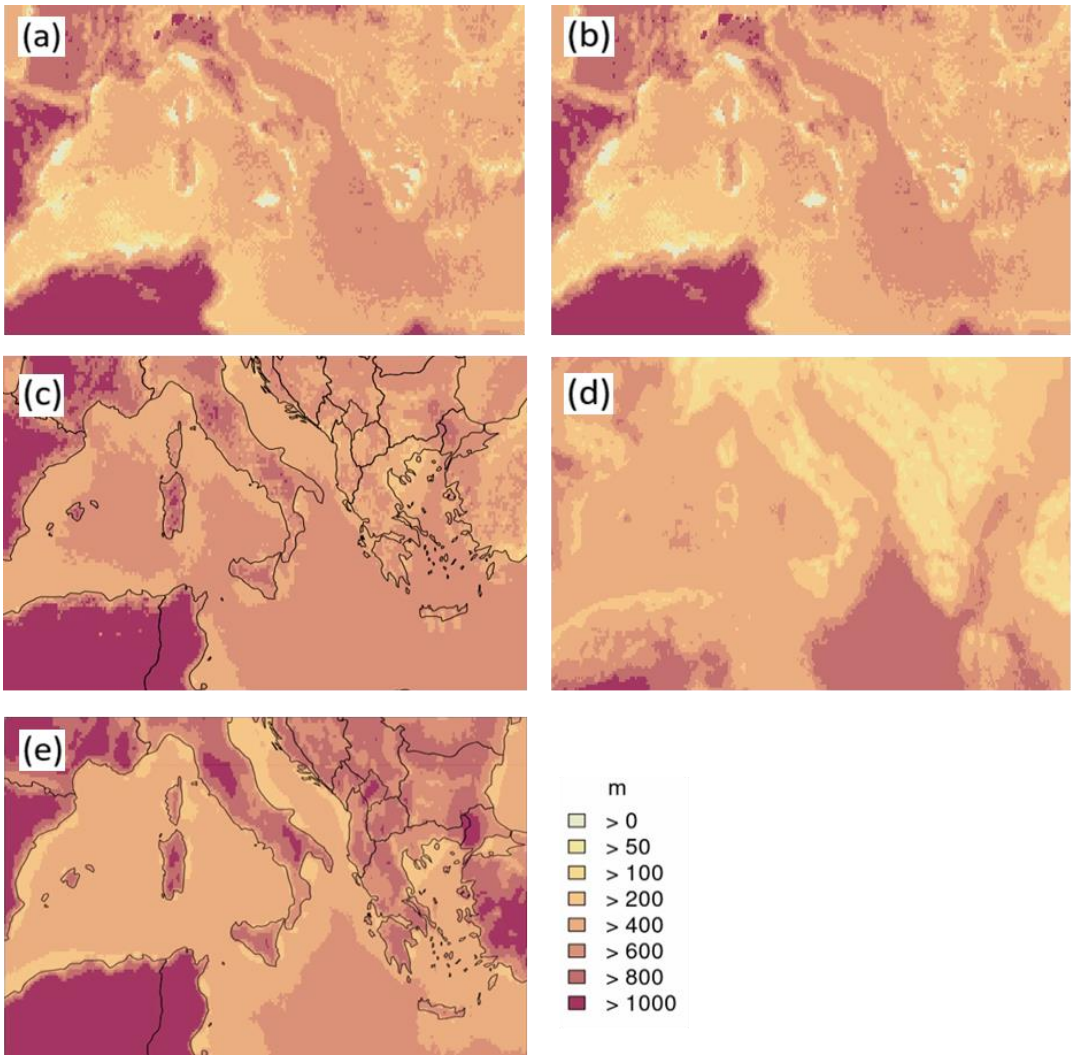

Supplements 2, S26: Median height of ABL at 4PM. (a) = CAMx, (b) = CHIMERE, (c) = CMAQ, (d) = EMEP, (e) = LOTOS-EUROS.

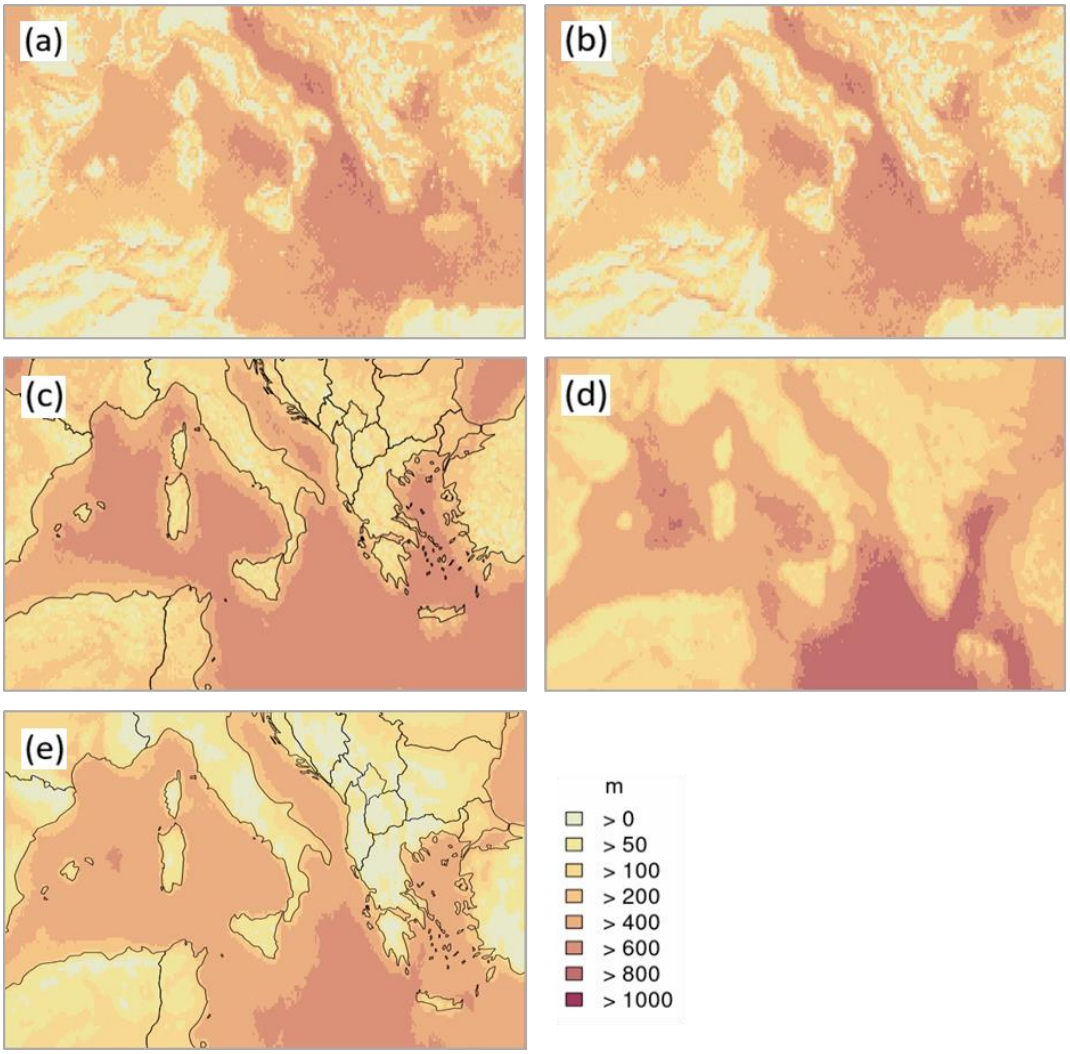

Supplements 2, S27: Median height of ABL at 4AM. (a) = CAMx, (b) = CHIMERE, (c) = CMAQ, (d) = EMEP, (e) = LOTOS-EUROS.

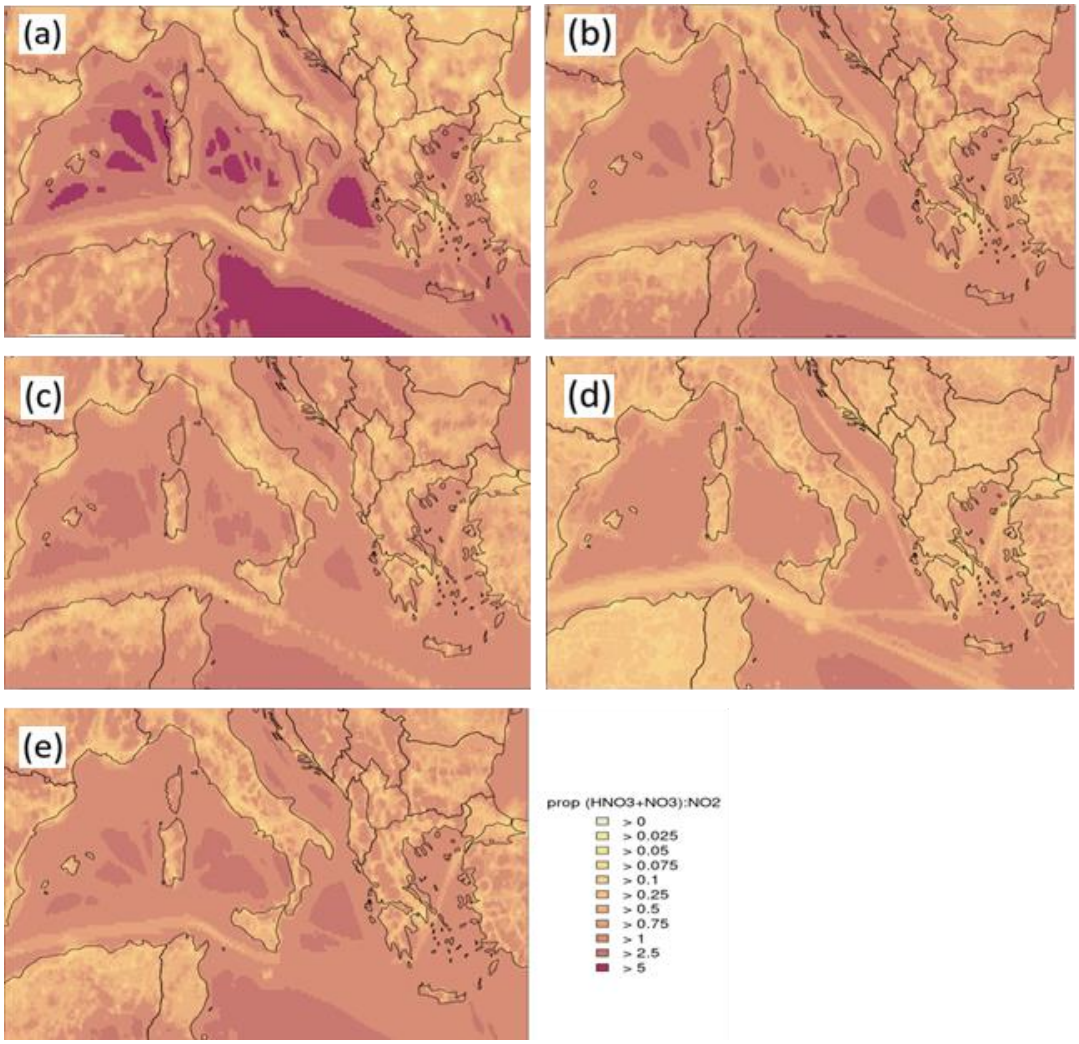

Supplements 2, S28: Ratio (HNO_3+NO_3^-):NO_2. (a) = CAMx, (b) = CHIMERE, (c) = CMAQ, (d) = EMEP, (e) = LOTOS-EUROS.

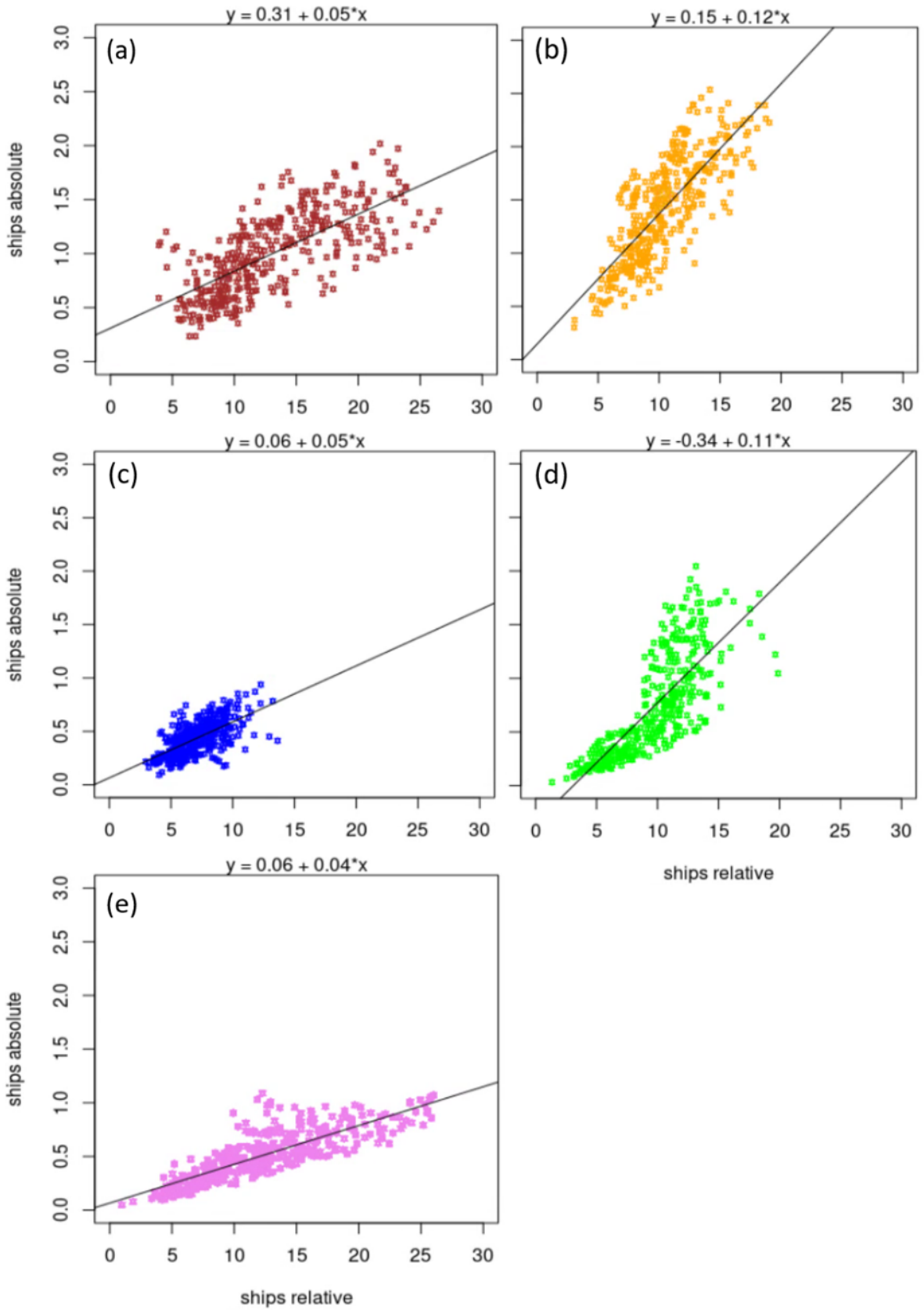

Supplements 2, S29: Relative ship impact plotted against absolute potential ship impact. (a) = CAMx, (b) = CHIMERE, (c) = CMAQ, (d) = EMEP, (e) = LOTOS-EUROS.

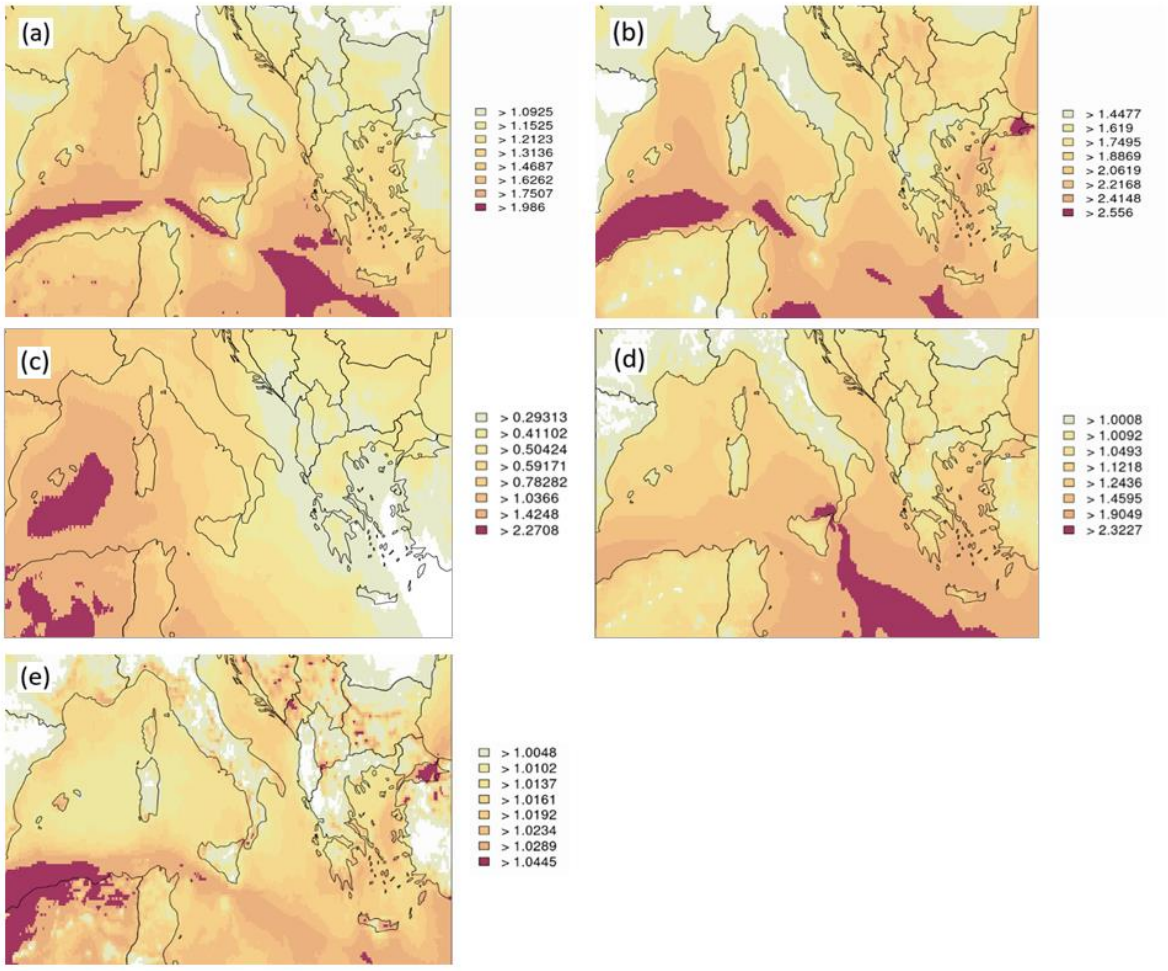

Supplements 2, S30: Maps display the ratio (2*SO_4^{2-} + NO_3^-):NH_4^+; calculated in mol. (a) = CAMx, (b) = CHIMERE, (c) = CMAQ, (d) = EMEP, (e) = LOTOS-EUROS.

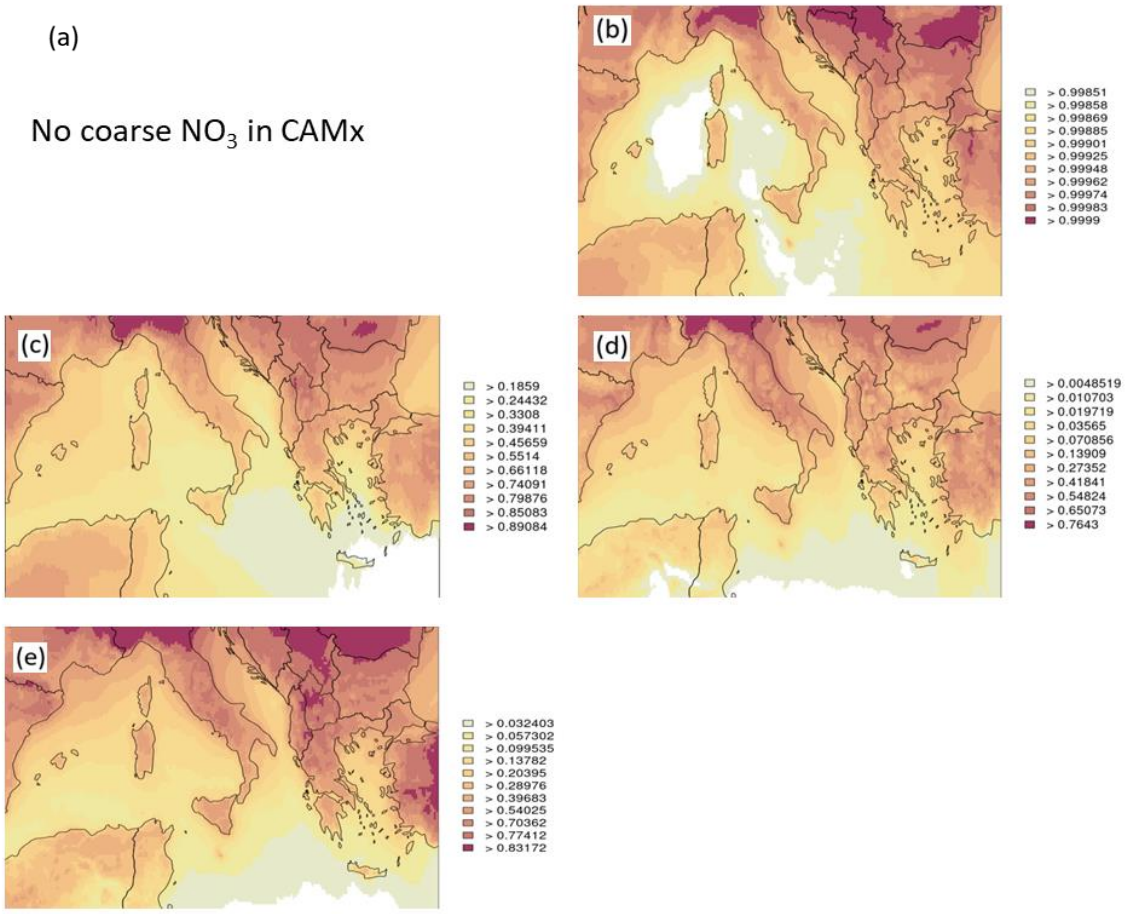

Supplements 2, S31: Maps display the ratio for the concentrations (NO_3^- fine):(NO_3^- fine + NO_3^- coarse). (b) = CHIMERE, (c) = CMAQ, (d) = EMEP, (e) = LOTOS-EUROS.

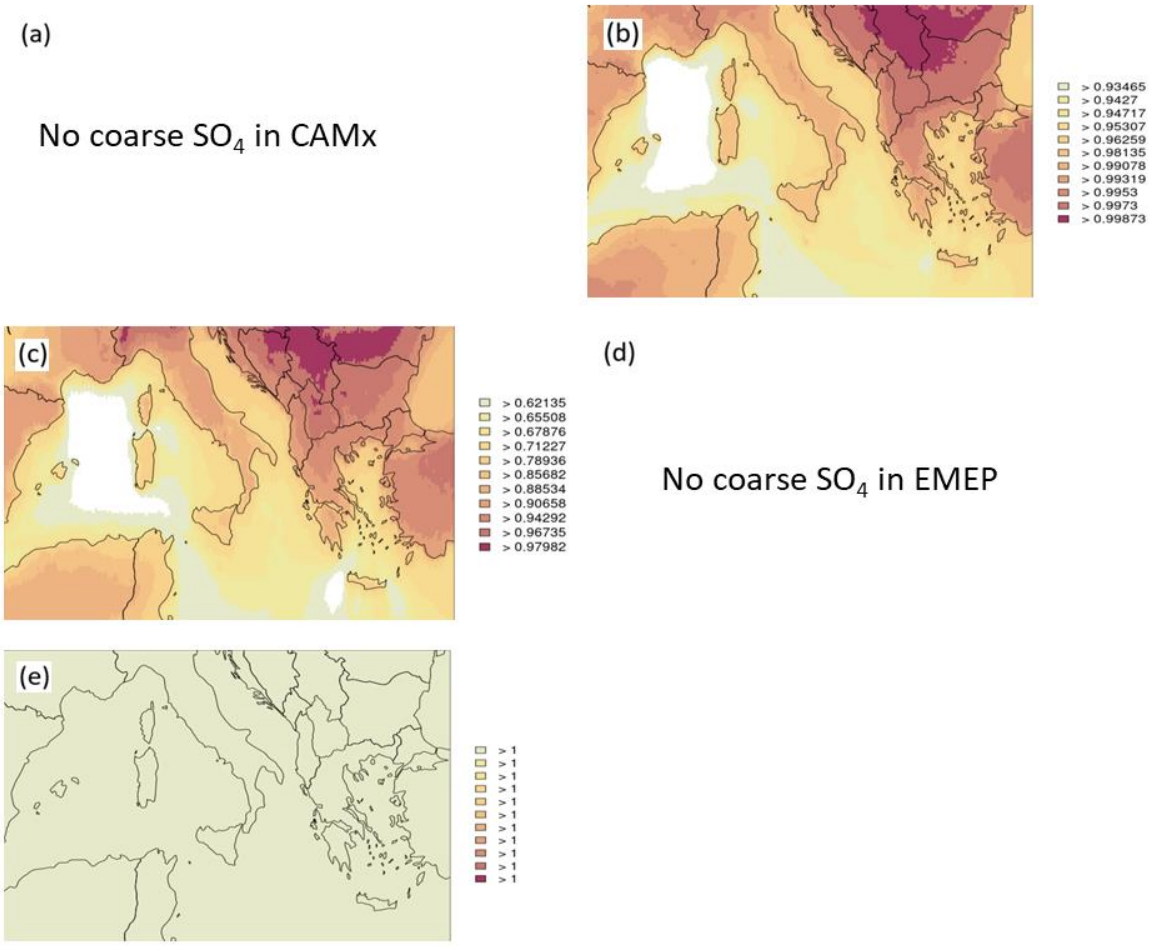

Supplements 2, S32: Maps display the ratio for the concentrations (SO_4^{2-} fine):(SO_4^{2-} coarse). (b) = CHIMERE, (c) = CMAQ, (d) = EMEP, (e) = LOTOS-EUROS.